Clays and Clay Minerals, Vol. 61, No. 3, 165–176, 2013.

FEASIBLE SYNTHESIS OF TiO_2 DEPOSITED ON KAOLIN FOR PHOTOCATALYTIC APPLICATIONS

JIŘÍ HENYCH* AND VÁCLAV ŠTENGL

[1] Department of Solid State Chemistry, Institute of Inorganic Chemistry AS CR v.v.i., 250 68 Husinec-Řež, Czech Republic
[2] Faculty of the Environment, University of Jan Evangelista Purkyně, Králova Výšina 7, 400 96 Ústí nad Labem, Czech Republic

Abstract— The aim of the present study was to synthesize a photocatalyst on the basis of TiO_2 with kaolin as the support material. Properties such as layered structure and a suitable particle size of kaolin could be beneficial in the production of a high-quality and relatively cheap photocatalyst on an industrial scale. Homogeneous hydrolysis with urea as a precipitation agent and kaolin as support material was used to obtain a kaolin surface covered with TiO_2. Samples were characterized by means of X-ray powder diffraction, infrared and Raman spectroscopy, high-resolution transmission electron microscopy, Brunauer-Emmett-Teller surface area, and Barrett-Joyner-Halenda porosity determination. Photocatalytic activity was assessed by a Reactive Black 5 azo dye discoloration in a water suspension and by acetone decomposition on a thin layer of sample in a gas phase. The characterization confirmed that the well crystallized TiO_2 was distributed effectively over the whole surface of a kaolin substrate, and photocatalytic tests revealed that the active surface layer of titania particles on kaolin performed well, suggesting that kaolin acts as a suitable support.

Key Words—Homogeneous Hydrolysis, Kaolin, Photocatalysis, TiO_2, Urea.

INTRODUCTION

Among photocatalysts, titanium dioxide is one of the most popular and widely used in spite of known drawbacks such as low performance under Vis light and agglomeration of the nanoparticles. Its stability, non-toxicity, and relatively small preparation costs can meet growing demands for sustainable, green technologies. A sol-gel route based on the controlled hydrolysis of an alkoxide (Gupta and Tripathi, 2012; Trentler *et al.*, 1999; Wang and Ying, 1999) is one of the methods of synthesis used most often. This is because structure modifications such as doping (Hamal and Klabunde, 2007) or the growth of tailored structures (Choi *et al.*, 2006) are relatively easy to achieve. Aside from alkoxides, the commonly used starting materials are titanium(IV) chloride and titanium(IV) sulfate. For preparation on an industrial scale, organometallic compounds in non-water solvents or high reactivity can be used; exothermal reaction with water and acids of $TiCl_4$ are problematic. Because of these problems, a method of homogeneous hydrolysis of $TiOSO_4$ in the presence of urea (Stengl *et al.*, 2003b) could be used as it provides highly active, well defined anatase crystals suitable for use in photocatalytic applications.

Recent literature has reported a number of attempts at the preparation of composite materials, where the main focus has been to use a highly functional surface layer with proper support, or a composite medium, which can produce the desired effects: change the properties of the materials, reduce the cost of production sufficiently, or even allow application at industrial scale. Titania-pillared clays have been researched extensively (Ding *et al.*, 2008; Mao *et al.*, 2010; Yamanaka *et al.*, 1987). They have a mesoporous structure due to the small TiO_2 particles which are located as pillars between the silicate layers and show significant adsorption ability due to the large specific surface area (Choy *et al.*, 1998; Ding *et al.*, 2001; Hermosin *et al.*, 1993). The combination of the TiO_2 with clay minerals for a photocatalytic purpose has also become an attractive sector of current research. Because the structure properties are crucial for photocatalysis, the effects of clay minerals in composites on the structure have been evaluated (Belessi *et al.*, 2007; Kun *et al.*, 2006) to effectively control the properties. Yang *et al.* (2008) assessed the effect of a desired mesoporous structure of the beidellite clay/TiO_2 composite synthesized under a hydrothermal treatment for phenol photodegradation under UV light. Investigations by Ahn *et al.* (2009) and Jiang *et al*. (2013) showed that the photocatalytic activity could be improved by forming a mesoporous system. Adsorption is another significant phenomenon influencing the activity of titania, and fine-tuning the ability of the new material to adsorb pollutants is the aim of many research groups. Montmorillonite modified with hexadecylpyridinium chloride (HDPM) in TiO_2 suspensions for 2-chlorophenol (2-CP) degradation was used as an adsorption agent (Mogyorosi *et al.*, 2002). Better degradation was observed (Menesi *et al.*, 2008) on TiO_2/Ca-montmorillonite composites prepared by wet grinding in an

* E-mail address of corresponding author:
henych@iic.cas.cz
DOI: 10.1346/CCMN.2013.0610301

agate mill than on pure TiO_2. Vanadium-doped TiO_2-montmorillonite nanocomposites were prepared by Chen *et al.* (2011b) using a simple sol-gel method for the photodegradation of sulforhodamine B under visible light irradiation, where the layer silicate of montmorillonite behaves as a barrier that prevents TiO_2 powders from agglomerating. Composites also have a larger surface area and V doping can improve the photoabsorption. Titania-impregnated kaolinite was synthesized (Chong *et al.*, 2009) in an attempt to solve the problem of separating the photocatalyst from the water after treatment. A TiO_2/clay composite can be separated readily unlike very small particles of pure TiO_2. This composite, prepared by a two-step sol-gel process, was effective for Congo red decomposition in a water suspension. A study of the evaluation of the physical properties and photodegradation capacity was carried out on titania impregnated into modified kaolin by the sol-gel process (Vimonses *et al.*, 2010) where TiO_2 nanocrystallites were deposited uniformly on the kaolin external surface, resulting in a high degree of photon activation. An interesting comparative study of adsorption and degradation on several volatile organic compound sample pollutants by a combined titania-montmorillonite-silica photocatalyst was carried out by Chen *et al.* (2011a). The present study demonstrates the possibility of using alternative cheaper materials which, because of their structure, are more suitable as supports; proper analysis has not been done, however.

The main aim of the present study was to synthesize a highly active photocatalyst based on titania particles using a kaolinite as a support material, which can effectively prevent agglomeration of the small TiO_2 particles, affect the sorption capacity, and, thanks to the price of kaolin, reduce the cost of production. To test whether titania nanocrystals would: preserve their crystallinity without impurities, maintain good photocatalytic performance, and be distributed over all of the kaolinite surface, several materials-characterization methods were used. Finally, because of the growing demands for 'green technologies,' another condition was to use an environmentally benign method for industrial production. A straightforward, cheap, 'one-pot' method for preparing highly active titania nanocrystals, based on the homogeneous hydrolysis of an aqueous solution of $TiOSO_4$ in a suspension of kaolin, is demonstrated here. Titania was deposited effectively on the surface of kaolin, which serves as a support material. The samples with varying amounts of titania were characterized and tested for photocatalytic discoloration of RB5 azo dye in water slurries and for acetone degradation in a gas phase.

EXPERIMENTAL

Synthesis of samples

Chemicals used were titanium oxo-sulfate, $TiOSO_4$; urea, $(NH_2)_2CO$; and H_2SO_4, which were of analytical grade and supplied by Fluka and Sigma-Aldrich Ltd, Germany. The substrate for reaction, kaolin, which was purchased from the Czech industrial producer České lupkové závody, a.s. (ČLUZ), originated from the acclaimed Czech deposits in Eger Graben in the western part of the Czech Republic, used for many decades in the production of ceramics. This kaolin, denoted as KDG, consists almost entirely of kaolinite (see below), with about equal proportions of the particle size fractions of 0.1−2 μm (55%) and 2−20 μm (45%).

The surface layers of TiO_2 nanocrystals were prepared by the hydrolysis of sulfate aqueous solutions using urea as a precipitation agent. The homogeneous precipitation or hydrolysis differs significantly from the more common, simple technique of adding neutralization agents (Li *et al.*, 2010). Solutions prepared by homogenous precipitation contain the precipitating agents (OH^-, SH^-, or H_2S) produced by a chemical reaction in the bulk of the solution without local supersaturation. For instance, urea and thioacetamide can be used as the precipitating agents instead of ammonia and hydrogen sulfide, respectively. A temperature of >60ºC leads to a decomposition of urea to produce OH^- ions:

$$(NH_2)_2CO + 2\ H_2O \rightarrow CO_2\uparrow + NH_4OH + NH_3 \quad (1)$$

$$NH_3 + H_2O \rightarrow NH_4^+ + OH^- \quad (2)$$

$$Me^{2+} + 2\ OH^- \rightarrow Me(OH)_2 \quad (3)$$

$$Ti^{4+} + 4\ OH- \rightarrow Ti(OH)_4 \quad (4)$$

A gradual evolution of ammonium (1) causes a pH increase (2), which leads to the gradual precipitation of hydroxides or oxides of the dissolved metal cations present (3); reaction 4 refers to the case of Ti^{4+}. The products of these reactions are mostly spherical agglomerates with a well developed microstructure and a large surface area (>300 m^2g^{-1}) which can easily be filtered out.

Various amounts of $TiOSO_4$ (see Table 1) were diluted in 500 mL of hot water (70ºC) acidified by 98% H_2SO_4 to pH ~2−3. 100 g of kaolin was added to the pellucid liquid, and the mixture was diluted with

Table 1. Surface area and pore volume of kaolin and prepared TiO_2 and kaolin/TiO_2 from variable amounts of $TiOSO_4$.

Sample	$TiOSO_4$ (g)	$TiOSO_4$ conc. (M)	BET (m^2g^{-1})	Total pore volume (cm^3g^{-1})
KDG	–	–	12	0.065
pure TiO_2	100	1.25	291	0.240
TiKDG25	25	0.31	46	0.084
TiKDG50	50	0.63	64	0.125
TiKDG75	75	0.94	83	0.166
TiKDG100	100	1.25	86	0.199
TiKDG125	125	1.56	92	0.188

distilled water to a total volume of 4 L. To the solution was added 300 g of urea and the mixture was heated at 95−100ºC under stirring for 6 h until pH 7.2−7.5 was reached and ammonia escaped from the solution. The precipitates formed were washed with distilled water, filtered out (using 5 μm filter paper), and the solids were air dried at ambient temperature.

For the photocatalytic tests in a gas phase, the titania/kaolin powder prepared (2 g) was dispersed in a mixture of 5 mL of poly(hydroxyethyl methacrylate) and 10 mL of ethanol. From this suspension, a layer 300 μm thick (~1 g) was deposited on a 100 mm × 150 mm glass plate.

CHARACTERIZATION METHODS

Diffraction patterns were collected with a PANalytical XPert PRO diffractometer equipped with a conventional X-ray tube (CuKα radiation, 40 kV, 30 mA) and a PIXcel linear position-sensitive detector with an antiscatter shield. A programmable divergence slit set to a fixed value of 0.5, Soller slits of 0.02 rad, and a mask (an integral part of the Xpert Pro diffractometer used to define the size of the primary beam on the sample in the perpendicular direction). A programmable antiscatter slit set to a fixed value of 0.5, a Soller slit of 0.02 rad, and a Ni β filter were used in the diffracted beam. Phase identification was performed using the *DiffracPlus Eva* software package (Bruker AXS GmbH, Karlsruhe, Germany) using the JCPDS PDF-2 database (2001).

Transmission electron micrographs were obtained using a JEOL JEM 3010 microscope operated at 300 kV (LaB_6 cathode). A copper-grid coated with a holey carbon support film was used to prepare samples for HRTEM observation. The powdered sample was dispersed in ethanol and the suspension treated in an ultrasonic bath for 10 min.

The specific surface areas of samples were determined from the nitrogen adsorption-desorption isotherms at liquid nitrogen temperature using a Coulter SA3100 instrument with 15 min of outgas at 150ºC. The Brunauer-Emmett-Teller (BET) method (Brunauer *et al.*, 1938) was used for the surface-area calculation and the pore-size distribution (pore diameters, pore volumes, and micropore surface areas of the samples) was determined using the Barrett-Joyner-Halenda (BJH) method (Barrett *et al.*, 1951).

Raman spectra were obtained using a DXR Raman microscope (Thermo Fisher Scientific, Waltham, Massachussets, USA). A 532 nm laser was used at a power of 3 mW. Powdered samples were scanned using a 15 point mapping mode under a 10× objective lens with an automated autofocus at each point to get 15 random measurements.

The photocatalytic activity in solution was assessed from the kinetics of the photocatalytic degradation of RB5 dye in aqueous slurries. The kinetic curves obtained were processed by fitting exponential models using the *Origin* software (OriginLab, Northampton, USA) as described by Stengl *et al*. (2009). In contrast to methylene blue, the azo dyes (Orange II, Methyl Red, RB5, Congo Red, *etc*.) are not adsorbed on titania surfaces and, hence, their photodecomposition is evaluated simply from the concentration of the remaining dissolved dye. Degradation of azo groups −N=N− in azo dyes leads to N_2 (Lachheb *et al.*, 2002 and Guillard *et al.*, 2003), which is ideal for the elimination of pollutants containing nitrogen for environmental photocatalysis or any other physico-chemical method.

The kinetics of photocatalytic degradation of an aqueous RB5 dye solution was measured by using a homemade photoreactor (Stengl *et al.*, 2008a), which consisted of a stainless steel cover and a quartz tube with a Narva fluorescent lamp (UV, Black-light 365 nm) having a power of 13 W and a light intensity of ~3.5 mW cm^{-2}. One liter of a 0.5 mM RB5 dye solution was circulated by means of a membrane pump using a flow-through measuring cell. Before the lamp was switched on, the suspension was mixed in the dark for 30 min to establish the adsorption-desorption equilibrium. The concentration of RB5 dye was determined by measuring the absorbance at 590 nm with a ColorQuestXE visible-light spectrophotometer. A 0.5 g portion of sample was sonicated for 10 min in an ultrasonic bath (300 W and 35 kHz) before the kinetic tests. The pH of the resulting suspension was taken as the initial value for neutral conditions. In the gas phase, the kinetics of the photocatalytic degradation of acetone was examined using a homemade stainless-steel batch photoreactor (which has a different shape, volume, valves, dosing, and detection system) (Ctibor *et al.*, 2011) with a Narva black-light fluorescent lamp at wavelength 365 nm (input power 8 W, light intensity 6.3 mW cm^{-2}). The gas concentration was measured by a quadrupole mass spectrometer JEOL JMS-Q100GC and gas chromatograph Agilent 6890N. A high-resolution gas chromatography column (19091P-QO4, J&W Scientific) was used. Samples were taken from the reactor in a time interval of 2 h automatically through the sampling valve (six-port external volume sample injector from Valco Instruments Co., Inc, Vici AG International, Schenkon, Switzerland).

Blank tests (a layer of poly(hydroxyethyl methacrylate) without titania) were performed to establish the effect of photolysis and catalysis on the conversion of acetone. The UV irradiation detected no measurable conversion of acetone, as a testing substance, into CO and/or CO_2, and no acetone was adsorbed on the poly(hydroxyethyl methacrylate) matrix. The injection volume of acetone into the photoreactor was 2 mL. The total volume of the reactor was 3.5 L, filled with oxygen, at a flow rate of 1 L/min.

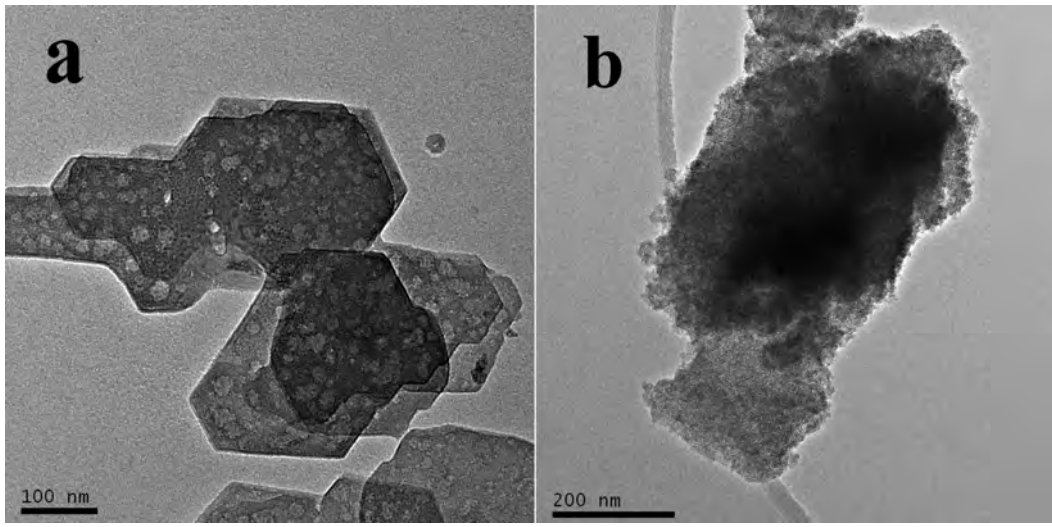

Figure 1. HRTEM images: (a) bare kaolin substrate; (b) kaolin surface covered by TiO_2 nanocrystals.

RESULTS AND DISCUSSION

If the proper composition of the parent solution was found empirically and the correct heating rate was chosen in the presence of a suitable substrate (*i.e*. mica (Stengl *et al.*, 2003a), kaolin, or cellulose) in the reaction mixture, the resulting hydrolysis products have a tendency to cover that substrate with a thin surface layer. In this case, the bare kaolin substrate (Figure 1a) after reaction was coated with small titania particles (Figure 1b). Note that the surface of the kaolin particles depicted was covered by TiO_2 crystals. The uniformity of the distribution of the particles is a desired effect, consequently providing a large specific surface area for photocatalytic reaction. Kaolin was, therefore, shown to be a good supporting material.

The results from XRD analysis of the TiO_2/kaolin composites synthesized (Figure 2) showed the sharp diffraction lines typical of kaolinite (PDF 89-6538) in all samples. A precipitated anatase fraction (PDF 21-1272) was also noted, though the peaks were somewhat less distinct due to the smaller amount and significantly smaller titania particles compared to those of kaolinite. No crystalline phase impurities were observed. Rietveld refinement could not be employed because of the overlapping of the peaks of well crystallized kaolinite and broad, weak peaks of titania. Nevertheless, the size of the coherent domain of the titania particles prepared by homogeneous hydrolysis was a few tens or several nm, as described previously (Stengl *et al*., 2003b, 2008b).

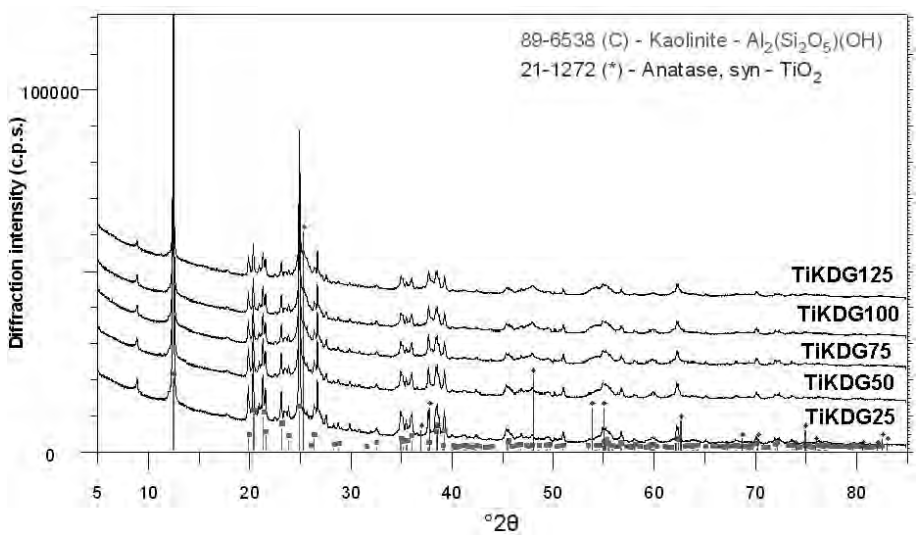

Figure 2. XRD patterns of synthesized TiO_2/kaolin samples.

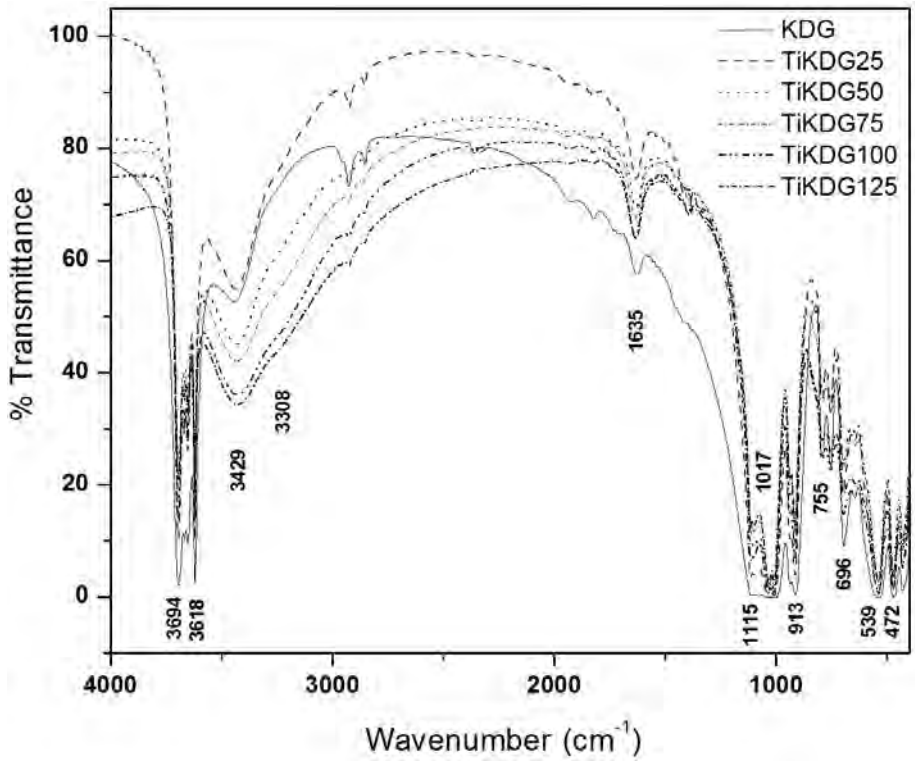

Figure 3. FTIR spectra of kaolin samples coated with TiO_2.

Four characteristic bands for kaolinite in the OH-stretching region at 3694, 3669, 3645, and 3618 cm^{-1} were distinguished in the infrared (IR) spectra of kaolin samples coated with TiO_2 (Figure 3) (Robin *et al*., 2013). Only four OH groups are present in the kaolinite unit cell (Bish, 1993), but because of their dichroic behavior the one-to-one assignment of these bands to the respective individual OH groups is risky (Farmer, 1974; Johnston *et al.*, 1990). The bands observed at positions around 1115 cm^{-1} and 1017 cm^{-1} were attributed to Si−O stretching vibrations. The Al-OH deformation band was observed at 913 cm^{-1}. The band positions at ~755 cm^{-1}, 696 cm^{-1}, and 539 cm^{-1} are part of the Si−O−Al vibrations (Kutlakova *et al.*, 2011; Saikia and Parthasarathy, 2010). Infrared spectroscopy revealed no remnants of anions from the synthesis.

Raman spectroscopy is an established technique for studying crystal structures. Kaolin has only a weak Raman spectrum, whereas anatase has significant specific vibration modes located around 150 cm^{-1} (Eg), 399 cm^{-1} (B1g), 515 cm^{-1} (B1g+A1g), and 638 cm^{-1} (Eg) (Ohsaka *et al.*, 1978). In the spectrum (Figure 4) of kaolin by itself (sample KDG), a peak at 143 cm^{-1} was seen, representing a small admixture of anatase; Raman spectroscopy allows detection of concentrations down to 0.02% of anatase in the kaolin structure (Murad, 1997). With increasing amount of Ti precursor added, the typical vibration modes of anatase became more intense, suggesting well formed crystalline particles of TiO_2 in the samples synthesized. The shift in position and the broadening of the Raman band relative to well crystallized anatase were consistent with the nanocrystalline nature and presence of defects in the anatase structure (Stengl and Matys Grygar, 2011).

The multipoint BET method for the specific surface area and BJH method for pore size and volume determination was employed (Table 1). No micropores were found in any of the samples. Titania prepared by homogeneous hydrolysis (Stengl and Matys Grygar, 2011) possesses the typical type IV isotherm with H2 hysteresis loop, according to IUPAC notation (Sing *et al.*, 1985) which characterizes materials with a good mesoporous structure. The samples of kaolin with titania (Figure 5 inset) had a type II isotherm, suggesting that supporting kaolin had either no pores or only macropores (>50 nm). The H3 hysteresis loop corresponds to aggregates of plate-like particles giving rise to slit-like pores and to solids with very wide pore-size distribution (Chang *et al.*, 2009), which could be expected of a kaolinite surface covered with mesoporous titania. All TiKDG samples had wide pore-size distributions (Figure 6) and an increasing proportion of TiO_2 led to the large volume of N_2 adsorbed, thanks to the large surface area of pure titania crystals. This effect was also seen from the adsorption-desorption isotherms (Figure 7) where, with a larger amount of titania, the isotherm clearly became steeper and closer to the type IV isotherm of the mesoporous surface layer of TiO_2.

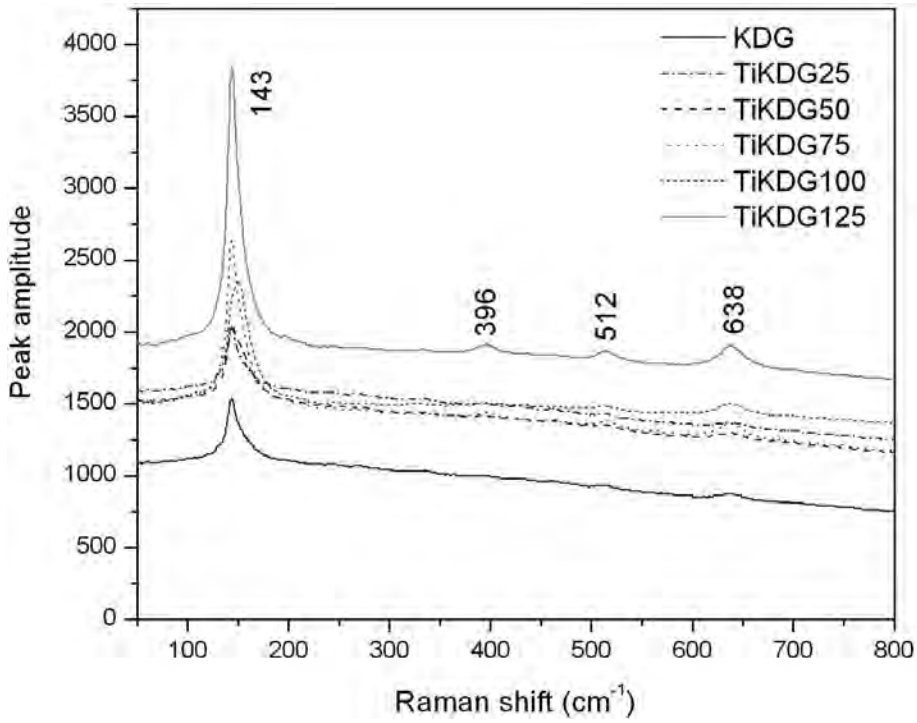

Figure 4. Raman spectra of pure kaolin (KDG) and TiO_2/KDG composites.

With increasing amounts of titania, the surface areas grew linearly, from 46 to 92 m^2g^{-1}. Pure KDG had a surface area of only 12 m^2g^{-1}, but a good covering of the kaolin by a surface layer of TiO_2 particles provided sufficient surface area for adsorption.

The photocatalytic activity of samples prepared in the water phase was determined using the degradation of 0.5 mM RB5 dye aqueous solutions under UV radiation at 365 nm (UV-A, black lamp). As proposed by Zhao *et al.* (2004), the main byproducts formed by the ozonation

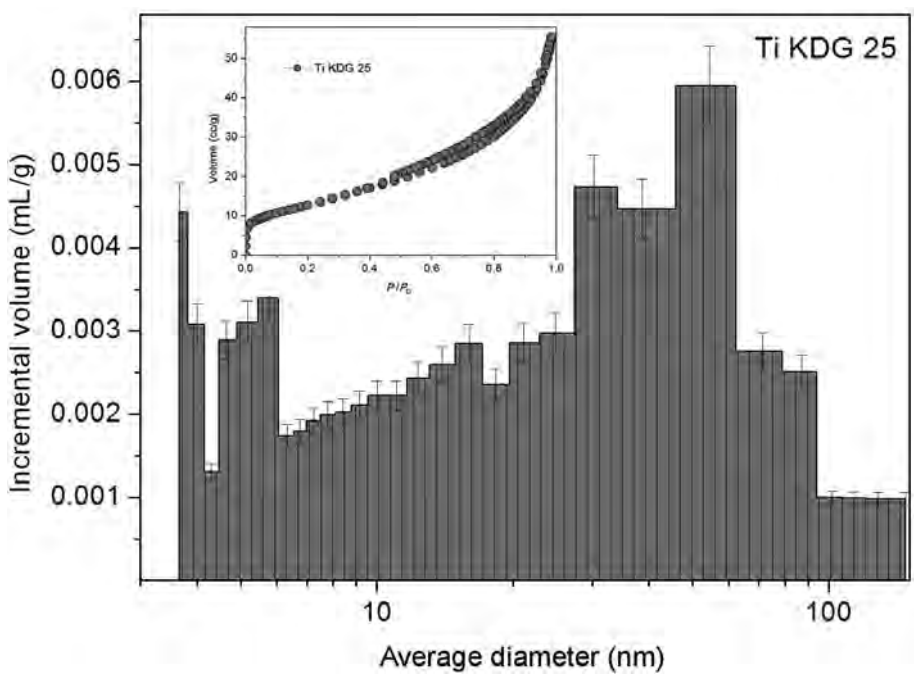

Figure 5. Isotherm (inset) and pore-size distribution of sample TiKDG25.

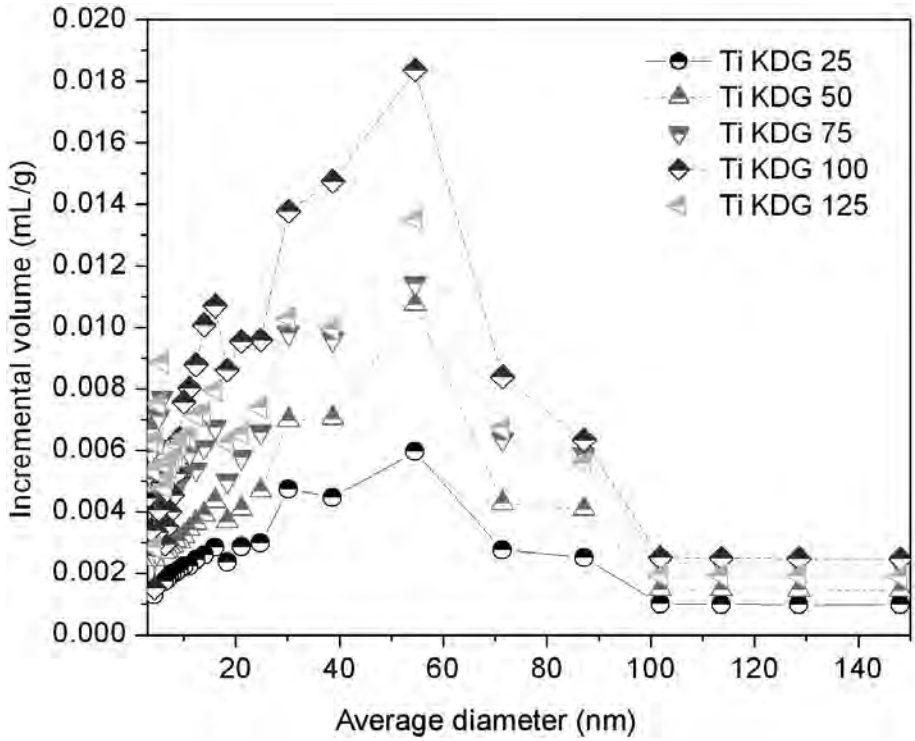

Figure 6. Pore-size distribution of TiO_2/kaolin samples.

or mineralization of azo dyes are organic acids, aldehydes, ketones, and carbon dioxide. According to Demirev and Nenov (2005), the eventual degradation products of azo dyes in the ozonation system are acetic,

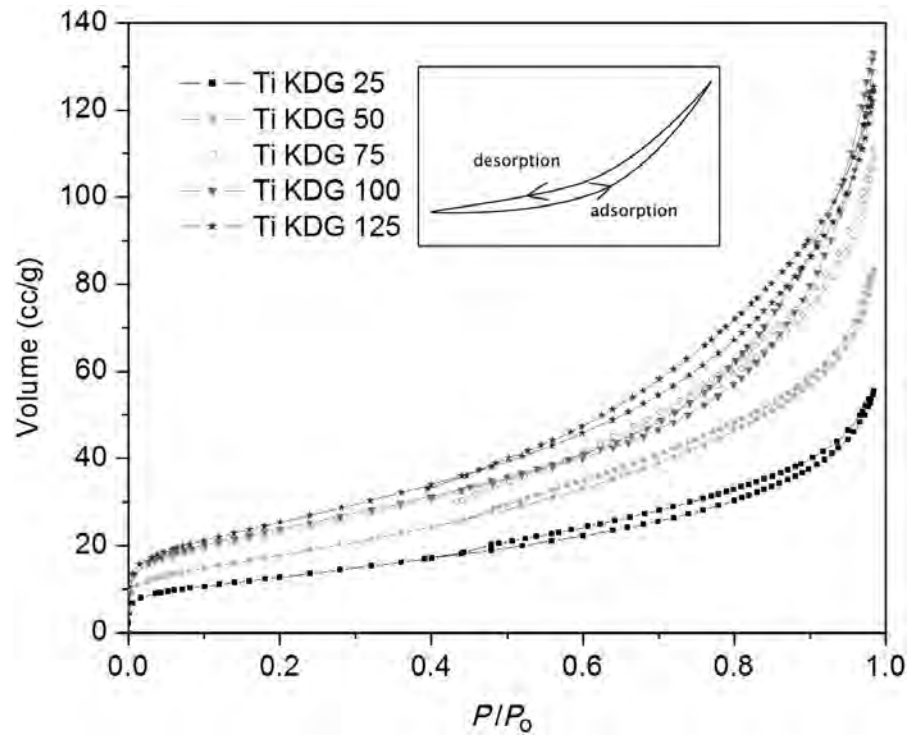

Figure 7. Isotherms of TiO_2/kaolin samples.

Table 2. Rate constants for RB5 discoloration in water slurries and kinetic parameters for acetone degradation in the gas phase under UV light.

Sample	*k* RB5 (min^{-1})	*k* acetone (h^{-1})	*k* O_2 (h^{-1})	CO	CO_2
Pure TiO_2	0.0257	0.0163	0.0068	1.2	14.9
TiKDG25	0.0430	0.0057	0.0112	5.1	13.2
TiKDG50	0.0247	0.0089	0.0131	4.3	18.2
TiKDG75	0.0323	0.0068	0.0126	0.8	5.4
TiKDG100	0.0299	0.0091	0.0121	2.9	10.2
TiKDG125	0.0391	0.0143	0.0118	2.9	9.7

formic, and oxalic acids. The mechanism of mineralization of RB5 dye in heterogeneous photocatalysis on $SrTiO_3/CeO_2$ was proposed by Song *et al.* (2007). The titania catalyzed the RB5 reaction, and mineralization products were mentioned by Sahel *et al.* (2007) and Damodar and You (2010).

For the assessment of the kinetics of a heterogeneous photocatalytic decomposition of model compounds such as RB5 dye, the Langmuir-Hinshelwood equation (Konstantinou and Albanis, 2004) can be used:

$$r = -d[\text{RB5}]/dt = -\,k_r \cdot K \cdot [\text{RB5}]/(1 + K \cdot [\text{RB5}]) \qquad (5)$$

where r is the degree of dye mineralization, k_r the rate constant, t the illumination time, K the adsorption coefficient of the dye, and [RB5] the dye concentration. When the chemical concentration is a millimolar solution (*i.e.* [RB5]0 is small), equation 4 can be simplified to an apparent first-order equation:

$$\ln \cdot([\text{RB5}]_0/[\text{RB5}]) = -k_r \cdot K \cdot t \qquad (6)$$

or:

$$[\text{RB5}] = [\text{RB5}]0 \cdot \exp(-k \cdot t); \quad (k = k_r \cdot K) \qquad (7)$$

As can be seen from the calculated rate constants (Table 2) and the kinetic curves under a UV light (Figure 8), the photoactivity of composite samples was surprisingly high, comparable to or even higher than that of pure titania. This is surprising because all of the TiKDG samples had much smaller surface areas than pure titania and a significant proportion of the particles comprised non-active support, so the presumed result would be a rapid decrease of reactivity, which was observed by Rieder *et al*. (2010). However, for the photocatalyzed reaction, the availability of the surface for the incident light is crucial, alongside the adsorption ability of the surface. Even though the kaolin support has much larger particles than pure titania, it can effectively increase titania activity by hindering the agglomeration

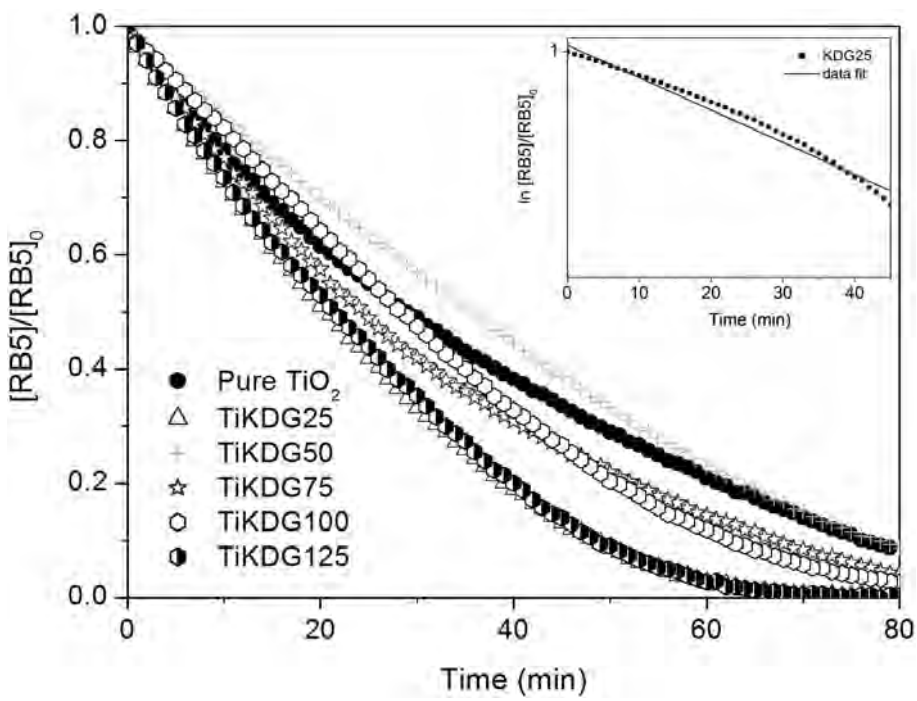

Figure 8. Kinetics of RB5 dye discoloration on TiO_2 and TiO_2/kaolin samples. under UV light.

of very small titania particles as they become more uniformly distributed on the kaolin surfaces. Moreover, the kaolin particles have only large pores which are readily accessible by the light. Last but not least, the sorption ability of clay minerals in soil is well known and this phenomenon surely contributes to good adsorption of the pollutant (azo dye in this case) on the particle surface, where it can be decomposed.

One of the aims of the present study was to estimate the optimum ratio of the concentration of TiO_2 and supporting kaolin. The rate constants for RB5 decomposition were similar to each other and the largest was observed for sample TiKDG25 with the smallest amount of titania, but note that the second largest was TiKDG125 with the most TiO_2 in the structure. From these results an ideal ratio of substrate and TiO_2 cannot be established, but some valuable information can be gleaned. The rather small amount of titania in sample TiKDG25 was sufficient for effective coverage of the substrate to provide an adequate performance of the active surface layer; larger amounts did not guarantee a further increase in terms of the activity. Good homogeneous distribution on particles of the substrate may be the key property governing performance. The larger dosage of titania led to the formation of more layers on the surface of kaolin, but the diffusion in water suspension is not as rapid and the amount of pollutant adsorbed cannot reach the inner surface and exploit the whole surface of active TiO_2.

Rate constants for acetone degradation, O_2 consumption, and normalized total ion current (TIC) for CO and CO_2 evolution after 45 h (Table 2), and the typical corresponding experimental dependencies in time are presented (Figure 9). The rate of degradation was estimated to obey pseudo-first-order kinetics, and hence the rate constant for degradation, k, was obtained from the first-order plot according to equation 8, where c_0 is the initial concentration, c is the concentration of acetone after time (t), and k is the first-order rate constant:

$$\ln(c/c_0) = -\mathrm{k}t \quad (8)$$

Before each measurement the reactor was evacuated and then purged with O_2. When the measured gas chromatogram showed only the oxygen peak, a substance for photocatalytic decomposition (in this case the acetone) could then be injected. The subsequent chromatogram showed the peaks for the O_2 and the acetone, marked with a value of 1. The gases, which were expected to be formed due to a photocatalyzed reaction (CO, CO_2), were assigned zero values. Thus, input data were normalized and measurements over a time period of 2 h could commence.

During the reaction no peaks for intermediates were detected, suggesting that photocatalytic oxidation proceeded not in the gaseous phase but only on the surface layer directly, causing the formation of CO and CO_2.

Sample TiKDG125, which contained the largest amount of titania, had the largest rate constant for acetone degradation; next was sample TiKDG100. However, to evaluate photoactivity, the important parameters are not just the rate but also the degree of mineralization, which is difficult to determine by discoloration of azo dye in water slurries. A gas chromatograph-mass spectroscopy (GC-MS) detection system in a gas-phase identification of the samples

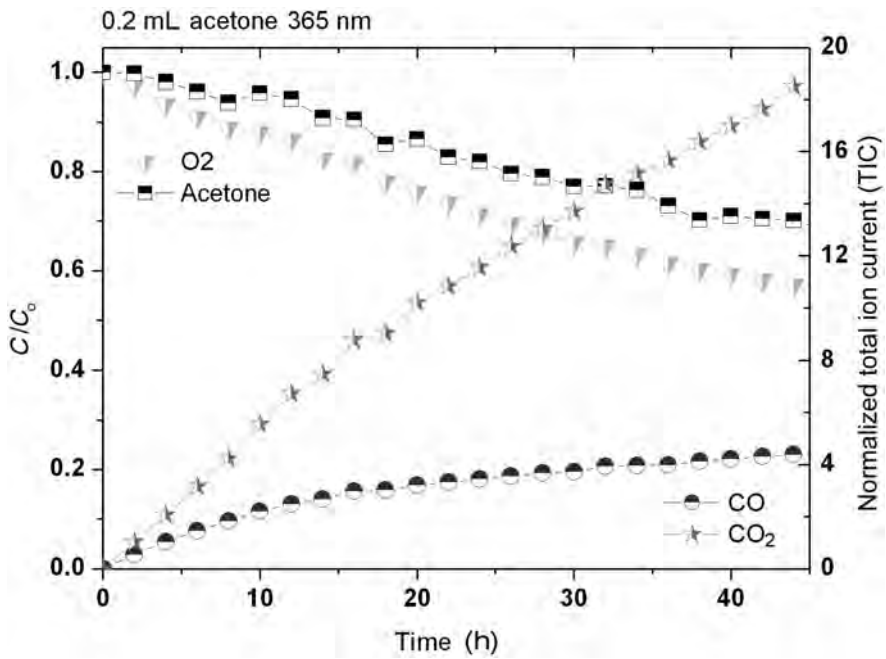

Figure 9. Kinetics of the photocatalytic degradation of acetone on a layer of sample TiKDG50.

which produced the most CO_2 is possible and might be more relevant. Samples TiKDG50 and TiKDG25 had smaller titania contents and the highest degrees of mineralization, consistent with the data obtained from RB5 discoloration in water slurries, where the titania content and a growing surface area did not lead to greater activity. An obvious conclusion is that both the surface area and the availability of the surface for incident light were crucial parameters. Therefore, a perfectly distributed surface layer of well crystallized particles was desired. What was somewhat surprising was the level of activity of sample TiKDG50 on acetone mineralization in the gas phase, in spite of its lesser activity in RB5 discoloration in water. However, the data for one set of samples for different pollutants in different environments are often not perfectly consistent. The many variable aspects, such as different mechanisms of degradation, adsorption, hydrophobicity, diffusion, *etc*., can affect the photocatalytic activity significantly. As a result, one cannot identify with certainty the perfect photocatalyst for all pollutants in different environments so that variability in the results could be expected. This variability should be the subject of further research.

CONCLUSIONS

The kaolin substrate with a surface layer of TiO_2 was synthesized by the simple 'one-pot' method of homogeneous hydrolysis. Analysis by XRD, IR, and Raman spectroscopy proved that the titania formed was nanocrystalline anatase; no impurities or phase admixtures were found. Titania was deposited on kaolin. The photoactivity of the synthesized composite samples was assessed in water slurries and in the gas phase. The tests proved that a thin surface layer of titania on kaolin was sufficient for good photocatalytic performance in comparison with pure TiO_2. Despite a much smaller surface area of kaolin/TiO_2 compared with pure titania, the activity was surprisingly high, which could be the result of a good covering of plate-like particles of kaolinite with only large pores allowing easy approach of incident light.

Kaolin has much larger particles and could be separated easily from water slurries compared to very small particles of titania. Therefore, the TiO_2 deposited on the substrate kaolinite could be a solution for practical difficulties in the separation of particles after treatment. Furthermore, from an economic point of view, the use of a cheap support material with a functional thin surface layer *via* an environmentally benign method promises 'real' application.

ACKNOWLEDGMENTS

This work was supported by the RVO 61388980 and Ministry of Industry and Trade of the Czech Republic (Project No. FR-TI1/006).

REFERENCES

Ahn, B-T., Kim, E-Y, and Kim, D.S. (2009) Synthesis of mesoporous TiO_2 and its application to photocatalytic activation of methylene blue and *E. coli. The Bulletin of the Korean Chemical Society*, **30**,193–196.

Barrett, E.P., Joyner, L.G., and Halenda, P.P. (1951) The determination of pore volume and area distributions in porous substances. 1. Computations from nitrogen isotherms. *Journal of the American Chemical Society*, **73**, 373–380.

Belessi, V., Lambropoulou, D., Konstantinou, I., Katsoulidis, A., Pomonis, P., Petridis, D., and Albanis, T. (2007) Structure and photocatalytic performance of TiO_2/clay nanocomposites for the degradation of dimethachlor. *Applied Catalysis B–Environmental*, **73**, 292–299.

Bish, D.L. (1993) Rietveld refinement of the kaolinite structure at 1.5 K. *Clays and Clay Minerals*, **41**, 738–744.

Brunauer, S., Emmett, P.H., and Teller, E. (1938) Adsorption of gases in multimolecular layers. *Journal of the American Chemical Society*, **60**, 309–319.

Chang, S.S., Clair, B., Ruelle, J., Beauchêne, J., Di Renzo, F., Quignard, F., Zhao, G.J., Yamamoto, H., and Gril, J. (2009) Mesoporosity as a new parameter for understanding tension stress generation in trees. *Journal of Experimental Botany*, **60**, 3023–3030.

Chen, J.Y., Li, G.Y., He, Z.G., and An, T.C. (2011a) Adsorption and degradation of model volatile organic compounds by a combined titania-montmorillonite-silica photocatalyst. *Journal of Hazardous Materials*, **190**, 416–423.

Chen, K., Li, J., Wang, W., Zhang, Y., Wang, X., and Su, H. (2011b) The preparation of vanadium-doped TiO(2)-montmorillonite nanocomposites and the photodegradation of sulforhodamine B under visible light irradiation. *Applied Surface Science*, **257**, 7276–7285.

Choi, H., Sofranko, A.C., and Dionysiou, D.D. (2006) Nanocrystalline TiO_2 photocatalytic membranes with a hierarchical mesoporous multilayer structure: Synthesis, characterization, and multifunction. *Advanced Functional Materials*, **16**, 1067–1074.

Chong, M.N., Vimonses, V., Lei, S., Jin, B., Chow, C., and Saint, C. (2009) Synthesis and characterisation of novel titania impregnated kaolinite nano-photocatalyst. *Microporous and Mesoporous Materials*, **117**, 233–242.

Choy, J.H., Park, J.H., and Yoon, J.B. (1998) Multilayered SiO_2/TiO_2 nanosol particles in two-dimensional aluminosilicate catalyst-support. *Journal of Physical Chemistry B*, **102**, 5991–5995.

Ctibor, P., Ageorges, H., Stengl, V., Murafa, N., Pis, I., Zahoranova, T., Nehasil, V., and Pala, Z. (2011) Structure and properties of plasma sprayed $BaTiO_3$ coatings: Spray parameters versus structure and photocatalytic activity. *Ceramics International*, **37**, 2561–2567.

Damodar, R.A. and You, S.J. (2010) Performance of an integrated membrane photocatalytic reactor for the removal of Reactive Black 5. *Separation and Purification Technology*, **71**, 44–49.

Demirev, A. and Nenov, V. (2005) Ozonation of two acidic azo dyes with different substituents. *Ozone-Science & Engineering*, **27**, 475–485.

Ding, X.J., An, T., Li, G., Zhang, S., Chen, J., Yuan, J., Zhao, H., Chen, H., Sheng, G., and Fu, J. (2008) Preparation and characterization of hydrophobic TiO_2 pillared clay: The effect of acid hydrolysis catalyst and doped Pt amount on photocatalytic activity. *Journal of Colloid and Interface Science*, **320**, 501–507.

Ding, Z., Zhu, H.Y., Greenfield, P.F., and Lu, G.Q. (2001) Characterization of pore structure and coordination of

titanium in TiO_2 and SiO_2-TiO_2 sol-pillared clays. *Journal of Colloid and Interface Science*, **238**, 267–272.

Farmer, V.C. (1974) *The Infrared Spectra of Minerals*. Monograph **4**, The Mineralogical Society, London.

Guillard, C., Disdier, J., Monnet, C., Dussaud, J., Malato, S., Blanco, J., Maldonado, M.I., and Herrmann, J.-M. (2003) Solar efficiency of a new deposited titania photocatalyst: chlorophenol, pesticide and dye removal applications. *Applied Catalysis B–Environmental*, **46**, 319–332.

Gupta, S.M. and Tripathi, M. (2012) A review on the synthesis of TiO_2 nanoparticles by solution route. *Central European Journal of Chemistry*, **10**, 279–294.

Hamal, D.B. and Klabunde, K.J. (2007) Synthesis, characterization, and visible light activity of new nanoparticle photocatalysts based on silver, carbon, and sulfur-doped TiO_2. *Journal of Colloid and Interface Science*, **311**, 514–522.

Hermosin, M.C., Martin, P., and Cornejo, J. (1993) Adsorption mechanisms of monobutyltin in clay minerals. *Environmental Science & Technology*, **27**, 2606–2611.

ICSD Database (2008) ICSD Database, FIZ Karlsruhe, Germany.

Jiang, Z., Kong, L., Alenazey, F.S., Qian, Y. Xiao, T., and Edwards, P.P. (2013) Enhanced visible-light-driven photocatalytic activity of mesoporous TiO_2-xNx derived from ethylenediamine-based complexes. *Nanoscale*, DOI: 10.1039/C3NR00344B

JCPDS PDF-2 (2001) JCPDS PDF-2. *ICDD*, Newtown Square, PA, USA.

Johnston, C.T., Agnew, S.F., and Bish, D.L. (1990) Polarized single-crystal Fourier-transform infrared microscopy of Ouray dickite and Keokuk kaolinite. *Clays and Clay Minerals*, **38**, 573–583.

Konstantinou, I.K. and Albanis, T.A. (2004) TiO_2-assisted photocatalytic degradation of azo dyes in aqueous solution: kinetic and mechanistic investigations – A review. *Applied Catalysis B–Environmental*, **49**, 1–14.

Kun, R., Mogyorosi, K., and Dekany, I. (2006) Synthesis and structural and photocatalytic properties of TiO_2/montmorillonite nanocomposites. *Applied Clay Science*, **32**, 99–110.

Kutlakova, K.M. Tokarsky, J., Kovar, P., Vojteskova, S., Kovarova, A., Smetana, B., Kukutschova, J., Capkova, P., and Matejka, V. (2011) Preparation and characterization of photoactive composite kaolinite/TiO_2. *Journal of Hazardous Materials*, **188**, 212–220.

Lachheb, H., Puzenat, E., Houas, A., Ksibi, M., Elaloui, E., Guillard, C., and Herrmann, J-M. (2002) Photocatalytic degradation of various types of dyes (Alizarin S, Crocein Orange G, Methyl Red, Congo Red, Methylene Blue) in water by UV-irradiated titania. *Applied Catalysis B–Environmental*, **39**, 75–90.

Li, Q., Xu, Z., Gao, S., and Shang, J.K (2010) As(III) removal by hydrous titanium dioxide prepared from one-step hydrolysis of aqueous $TiCl_4$ solution. *Water Research*, **44**, 5713- 5721.

Mao, H.H., Li, B., Li, X., Yue, L., Xu, J., Ding, B., Gao, X., and Zhou, Z. (2010) Facile synthesis and catalytic properties of titanium containing silica-pillared clay derivatives with ordered mesoporous structure through a novel intra-gallery templating method. *Microporous and Mesoporous Materials*, **130**, 314–321.

Menesi, J., Korosi, L., Bazso, E., Zollmer, V., Richardt, A., and Dekany, I. (2008) Photocatalytic oxidation of organic pollutants on titania-clay composites. *Chemosphere*, **70**, 538–542.

Mogyorosi, K., Farkas, A., Dekany, I., Ilisz, I., and Dombi, A. (2002) TiO_2-based photocatalytic degradation of 2-chlorophenol adsorbed on hydrophobic clay. *Environmental Science & Technology*, **36**, 3618–3624.

Murad, E. (1997) Identification of minor amounts of anatase in kaolins by Raman spectroscopy. *American Mineralogist*, **82**, 203–206.

Ohsaka, T., Izumi, F., and Fujiki, Y. (1978) Raman-spectrum of anatase, TiO_2. *Journal of Raman Spectroscopy*, **7**, 321–324.

Rieder, M., Klementova, M., and Szatmary, L. (2010) High-temperature growth of anatase on kaolinite substrate. *Proceedings of the Royal Society A – Mathematical, Physical and Engineering Sciences*, **466**, 721–730.

Robin, V., Petit, S., Beaufort, D., and Prêt, D. (2013) Mapping kaolinite and dickite in sandstone thin sections using infrared microscopy. *Clays and Clay Minerals*, **61**, 141–151.

Sahel, K., Perol, N., Chermette, H., Bordes, C., Derriche, Z., and Guillard C. (2007) Photocatalytic decolorization of Remazol Black 5 (RB5) and Procion Red MX-5B – Isotherm of adsorption, kinetic of decolorization and mineralization. *Applied Catalysis B – Environmental*, **77**, 100–109.

Saikia, B.J. and Parthasarathy, G. (2010) Fourier Transform infrared spectroscopic characterization of kaolinite from Assam and Meghalaya, northeastern India. *Journal of Modern Physics*, **1**, 206–210.

Sing, K.S.W., Everett, D.H., Haul, R.A.W., Moscou, L., Pierotti, R.A., Rouquerol, J., and Siemieniewska, T. (1985) Reporting physisorption data for gas solid systems with special reference to the determination of surface-area and porosity (Recommendations 1984). *Pure and Applied Chemistry*, **57**, 603–619.

Song, S., Xu, L., He, Z., and Chen, J. (2007) Mechanism of the photocatalytic degradation of CI reactive black 5 at pH 12.0 using $SrTiO_3$/CeO_2 as the catalyst. *Environmental Science & Technology*, **41**, 5846–5853.

Stengl, V., Subrt, J., Bakardjieva, S., Kalendova, A., and Kalenda, P. (2003a) The preparation and characteristics of pigments based on mica coated with metal oxides. *Dyes and Pigments*, **58**, 239–244.

Stengl, V., Subrt, J., Bezdicka, P., Marikova, M., and Bakardjieva, S. (2003b) Homogeneous precipitation with urea – An easy process for making spherical hydrous metal oxides. *Solid State Chemistry V*, **90–91**, 121–126

Stengl, V. and Matys Grygar, T. (2011) The simplest way to iodine-doped anatase for photocatalysts activated by visible light. *International Journal of Photoenergy*, doi:10.1155/2011/685935.

Stengl, V., Houskova, V., Bakardjieva, S., Murafa, N., and Havlin, V. (2008a) Optically Transparent Titanium Dioxide Particles Incorporated in Poly(hydroxyethyl methacrylate) Thin Layers. *Journal of Physical Chemistry C*, **112**, 19979–19985.

Stengl, V., Bakardjieva, S., Murafa, N., and Houskova, V. (2008b) Hydrothermal synthesis of titania powders and their photocatalytic properties. *Ceramics-Silikaty*, **52**, 278–290.

Stengl, V., Bakardjieva, S. and Murafa, N. (2009) Preparation and photocatalytic activity of rare earth doped TiO_2 nanoparticles. *Materials Chemistry and Physics*, **114**, 217–226.

Trentler, T.J., Denler, T.E., Bertone, J.F., Agrawal, A., and Colvin, V.L. (1999) Synthesis of TiO_2 nanocrystals by nonhydrolytic solution-based reactions. *Journal of the American Chemical Society*, **121**, 1613–1614.

Vimonses, V., Chong, M.N., and Jin, B. (2010) Evaluation of the physical properties and photodegradation ability of titania nanocrystalline impregnated onto modified kaolin. *Microporous and Mesoporous Materials*, **132**, 201–209.

Wang, C.C. and Ying, J.Y. (1999) Sol-gel synthesis and hydrothermal processing of anatase and rutile titania nanocrystals. *Chemistry of Materials*, **11**, 3113–3120.

Yamanaka, S., Nishihara, T., Hattori, M., and Suzuki, Y. (1987) Preparation and properties of titania pillared clay. *Materials Chemistry and Physics*, **17**, 87–101.

Yang, X., Zhu, H., Liu, J., Gao, X., Martens, W.N., Frost, R.L., and Shen, Y., Yuan, Z. (2008) A mesoporous structure for efficient photocatalysts: Anatase nanocrystals attached to leached clay layers. *Microporous and Mesoporous Materials*, **112**, 32–44.

Zhao, W.R., Shi, H.X., and Wang, D.H. (2004) Ozonation of cationic Red X-GRL in aqueous solution: degradation and mechanism. *Chemosphere*, **57**, 1189–1199.

(*Received 2 July 2012; revised 22 March 2013; Ms. 686; AE: P.B. Malla*)

Clays and Clay Minerals, Vol. 61, No. 3, 177–192, 2013.

ZEOLITES IN MAFIC PYROCLASTIC ROCKS FROM THE SANDIKLI-AFYONKARAHISAR REGION, TURKEY

YAHYA OZPINAR[1], BARIS SEMIZ[1,*], AND PAUL A. SCHROEDER[2]

[1] Pamukkale University, Department of Geological Engineering, TR-20070, Denizli, Turkey
[2] The University of Georgia, Department of Geology, Athens, GA 30602-2501, USA

Abstract—Geologic mapping and crystal-chemical analysis of Middle–Upper Miocene volcanics in the Sandıklı-Afyonkarahisar region of Turkey, coupled with published zeolite analyses has revealed that western Turkey hosts unique zeolitic mineral assemblages with distinct paragenetic sequences. The present investigation focused on pyroclastic deposits, including low to intermediate potassic trachytic/trachyandesitic tuffs (LPT) and high potassic tephriphonolitic, tephritic, and trachybasaltic tuffs (HPT), each of which contains various styles of zeolites. Optical petrography, X-ray powder diffraction, and chemical analyses have revealed varying degrees of lithification, probably related to differences in initial emplacement temperature, depositional mechanism and thickness, chilling rate, and extent of mafic composition. Zeolitization was further influenced by meteoric flushing in a hydrologically open system. Chabazite in the LPT from the Selçik area occurs extensively as coatings and infillings of pores. Phillipsite in the HPT found in the Ballık, Küfeke, and Ömerkuyu areas dominates the assemblage and is accompanied by chabazite and minor amounts of analcime. Analcime was probably generated by alteration of leucite which is found as a pyrogene mineral. Alkali zeolites or Ca-bearing zeolites formed as a consequence of the addition of Ca and/or the removal of Na (*i.e.* dissolution of analcime). The paragenetic sequence may be described as: analcime/phillipsite → chabazite → calcite. The characterization of these assemblages may lead to better exploitation strategies for natural zeolitic resources in the region.

Key Words—Alkaline Pyroclastic Rocks, Chabazite, Phillipsite, Sandıklı, Western Anatolia, Zeolites.

INTRODUCTION

Zeolite occurrences in western Anatolia, Turkey, are normally related to felsic/acidic volcanism formed in saline-alkaline lake basins, which often contain borates, K-feldspar, carbonates, and clay minerals. In Turkey, these occurrences include the regions of Bigadiç, Kırka, Gördes, Simav, Emet, Alaçatı (Çeşme), and Ayvacık-Küçükkuyu (Çanakkale) (Helvacı *et al.*, 1993; Gündoğdu *et al.*, 1996; Kaçmaz and Koktürk, 2004; Esenli and Sirkecioğlu, 2005; Snellings *et al.*, 2008; Semiz *et al.*, 2011; Özen and Göncüoğlu, 2011). Some of these zeolites, such as those in Gördes, are commercially exploited. Commonly, these zeolites are related to felsic and high-silica volcanism and include clinoptilolite, heulandite, analcime, mordenite, erionite, and phillipsite in the mineral assemblages (Bish and Carey, 2001). Zeolite-bearing pyroclastic rocks related to mafic or basaltic volcanism in Turkey are less common and have only recently been recognized (by Özpınar *et al.*, 2002) in the Sandıklı region, and in the Eastern Pontides (by Abdioğlu, 2012). Sandıklı zeolite occurrences are associated with trachytic, trachyandesitic, phonolitic, and tephriphonolitic pyroclastic deposits (Özpınar *et al.*, 2002; Özpınar, 2008, 2011). Similar occurrences are described in other locations around the world such as in Campi Flegrei in southern Italy (de' Gennaro *et al.*, 1999, 2000; Cappelletti *et al.*, 2003); the Canary Islands, Spain (Hernandez *et al.*, 1993); and in the Eifel region of Germany (Bernhard and Barth-Wirsching, 2002). Most of these deposits have been involved in alteration processes that led to the crystallization of phillipsite, chabazite, and analcime (de' Gennaro *et al.*, 1999, 2000). The purpose of the present study was to describe the occurrences of analcime-, chabazite-, and phillipsite-bearing rocks in the southeastern region of Sandıklı–Afyonkarahisar (western Anatolia, Turkey) hosted in mafic volcanics and to compare and contrast the deposits with others in the region and around the world. The broader implication of this work is the constraints these minerals can provide for better understanding of western Turkey geology and the exploitation potential of natural zeolitic resources.

MATERIALS AND METHODS

Detailed geologic field mapping of Sandıklı volcanics was conducted at a scale of 1/25,000 over an area of ~60 km^2 (Figure 1). Thin sections were prepared from 198 representative rock samples. The mineralogy of 58 bulk samples was determined by powder X-ray diffraction (XRD) using a Rigaku D/Max 2200 Ultima/PC diffractometer (in Turkey) and a Bruker D8 Advance diffractometer (in the USA). All powder samples were prepared using an automatic agate mortar. Most of the

* E-mail address of corresponding author:
bsemiz@pau.edu.tr
DOI: 10.1346/CCMN.2013.0610302

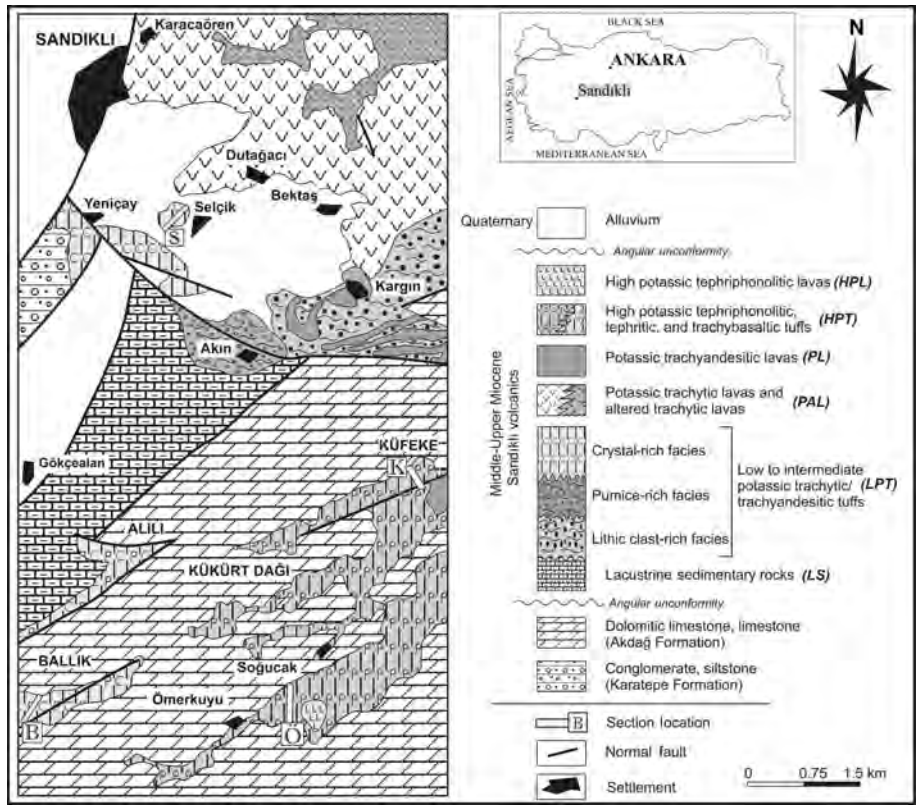

Figure 1. Geologic map of the Sandıklı volcanics.

pressed powders were scanned from 2 to 50º2θ at a rate of 1º/min using CuKα radiation (Ni-filtered). The other samples were measured at a continuous scan rate of 1.00º min^{-1} over a range of 2−70º2θ; counts were collected for 0.600 s at step increments of 0.010º with CoKα radiation (Ni filter).

Scanning electron microscopy and energy-dispersive spectroscopy (SEM-EDX) were used to characterize crystal morphologies. The SEM-EDX work was carried out at the Center for Advanced Ultrastructural Research (CAUR) at the University of Georgia, Athens, Georgia, USA, using a Zeiss 1450EP. Samples for SEM-EDX analysis were prepared by adhering a freshly broken surface of the sample onto an aluminum stub with double-sided tape, which was then coated with a carbon film (~350 Å) using an SPI Module Sputter Coater. Representative minerals of zeolitic tuffs were analyzed chemically by wavelength dispersive spectroscopy (WDS) using a JEOL 8600 electron microprobe at the University of Georgia, USA. Natural and synthetic mineral standards were analyzed as primary standards to monitor accuracy and precision. The WDS running conditions used a 15 kV accelerating voltage, a 15 nA beam current, and an analytical spot size of ~1 μm. The X-ray intensities were corrected using the Phi-Rho-Z matrix correction software of Armstrong (1988).

Bulk chemical analysis of 12 samples for major, trace, and rare earth elements (*REE*) analyses were carried out with fusion inductively coupled plasma (ICP) and fusion inductively coupled plasma-mass spectrometry (ICP-MS) in ACME Laboratories Ltd., Canada. The loss-on-ignition (LOI), representing the weight percentage of total water and volatile components, was determined by heating the samples to 1000ºC after drying them at 105±5ºC.

GEOLOGICAL FRAMEWORK

Basement rocks of the Neogene volcano-sedimentary units in the study area include the Upper Triassic–Lower Jurassic Karatepe Formation and Upper Jurassic−Lower Cretaceous Akdağ Formation. Basement rocks occur unconformably overlain by the Middle−Upper Miocene volcano-sedimentary sequence known as the Sandıklı Volcanics (Figure 1). The Sandıklı volcanic sequence is described as: (1) lacustrine sedimentary rocks (hereafter LS), which include conglomerates, sandstones, marls, and limestones; (2) low-to-intermediate potassic trachytic/ trachyandesitic tuffs (hereafter LPT); (3) trachytic lavas and partly altered trachytic lavas (hereafter PAL); (4) potassic trachyandesitic lavas (hereafter PL); (5) high potassic tephriphonolitic, tephritic, and

trachybasaltic tuffs (hereafter HPT); and (6) high potassic tephriphonolitic lavas (hereafter HPL). They have been dated using the K-Ar method and give model ages of 8.0±0.6 and 14±0.3 Ma (Besang *et al.*, 1977; Ercan, 1986). These Miocene and older units are sporadically overlain by Quaternary alluvium (Figure 1).

Tuffs are divided into two groups on the basis of mineralogical properties and stratigraphic position. The lower group of tuffs (LPT) crops out around the villages of Selçik, Akin, and Yeniçay (Figure 1). The LPT in the Selçik-Akin area are beige in color and can be further divided into three sub-facies which include: (1) lithic clast-rich facies; (2) a pumice-rich facies; and (3) crystal-rich facies (Figure 2a). The lithic clast-rich facies is characterized by poorly sorted beds. These facies contain coarse-grained pyroclastics such as lapilli breccia and lapillistone, which appear as trachytic/trachyandesitic rock and white-gray pumice pieces. According to the classification of Schmid (1981), the upper part of this facies contains tuffaceous conglomerates, tuffaceous sandstones, tuffaceous siltstones, and tuffaceous mudstones. The pumice-rich facies consist of abundant, well rounded pumice clasts with different dimensions set in a poorly sorted ash matrix. This facies has a texture similar to that of ignimbrites and contains coarse-grained trachytic and trachyandesitic pyroclasts. The contacts between the upper and lower facies are gradational. The crystal-rich facies consist chiefly of varicolored, zeolitized, mostly fine-grained, vitric-crystal, and crystal vitric-tuffs. They are beige in color and contain variable amounts of small volcanic rock fragments and a few small epiclasts. Tuffs with zeolite are less lithified and contain chabazite. The zeolite content is greater in the uppermost levels. The depositional characteristics of LPT indicate strongly that they are ash-fall deposits.

The upper group crops out around the villages of Alılı, Ballık, Ömerkuyu, Soğucak, and Küfeke in the southern part of the study area (Figure 1). The HPT in the Ömerkuyu-Soğucak area unconformably overlie the Upper Jurassic to Lower Cretaceous Akdağ Formation (Figure 2b). The HPT have a brown, reddish brown, sometimes light brown color and are very well lithified. They are more dense than the chabazite-bearing trachytic tuffs and often contain volcanic rock fragments (pyroclasts) with fine to coarse sand, as well as a few small, partly rounded radiolarite and limestone fragments. The tuffs in Soğucak contain gravel and coarse sand-sized particles of basaltic and tephriphonolitic composition. Iron alteration appears to be greatest in this suite. Tuffs in Küfeke have fewer pyrogenic minerals and contain microcrystalline limestone "micrite" (Folk, 1962) and pumice (Figure 2c). The HPT contain chabazite and phillipsite near Alılı and Ballık, while phillipsite only occurs near Ömerkuyu, Soğucak, and Küfeke. The HPT appear to be ash-flow deposits.

RESULTS

Petrography-mineralogy

The mineralogical composition of the tuffs was determined by XRD analysis (Table 1). Zeolite minerals occur to a lesser extent in the low to intermediate potassic trachytic and trachyandesitic tuffs (LPT) and more extensively in the high potassic tephriphonolitic, tephritic, and trachybasaltic tuffs (HPT). The LPT contain chabazite, sanidine, and quartz, with minor

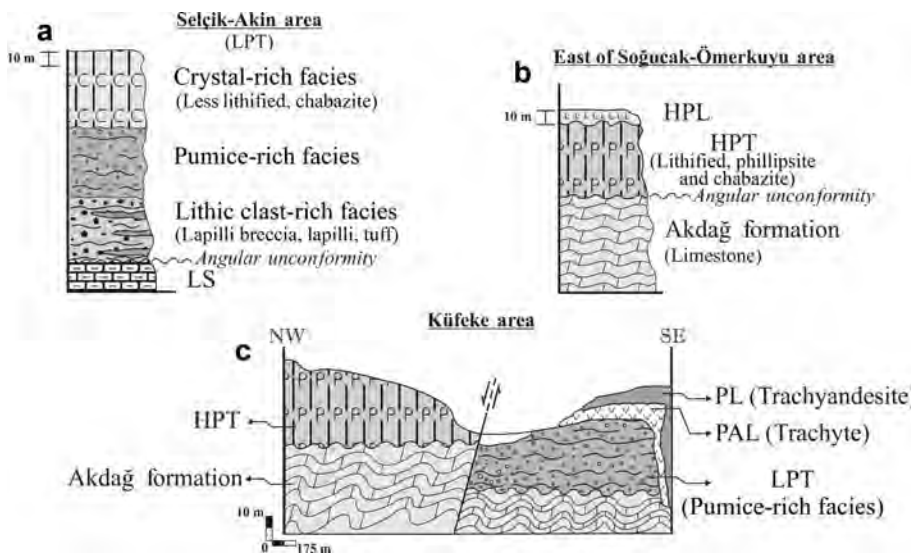

Figure 2. Stratigraphic position of pyroclastic rocks located in the study area: (a) trachytic tuffs (LPT) located in the Selçik and Akin areas; (b) tephriphonolitic tuffs (HPT) located east of the Soğucak-Ömerkuyu areas; and (c) relationship between the trachytic and tephriphonolitic tuffs (LPT and HPT) located in the Küfeke area.

Table 1. Mineralogical composition of the LPT and HPT samples determined by powder XRD.

Rock type	Sample no	Locations	Minerals							
			Cha	Phi	Ana	San	Q	Cal	Bio	Aug
LPT	S11−S19	West of Selçik	+	−	−	+	+	−	−	−
LPT	S3−S4	West of Selçik	+	−	−	+	−	−	−	−
LPT	S34; S36	South of Selçik	+	−	−	+	+	+	−	−
LPT	S35	South of Selçik	+	−	−	+	+	−	−	−
LPT	S35; S37−S38	South of Selçik	+	−	−	+	+	−	−	−
LPT	S5− S5/1	South of Selçik	−	−	−	+	+	+	−	−
HPT	B20; B21	South of Ballık	−	+	−	−	−	+	−	−
HPT	B22−B24	South of Ballık	−	+	−	+	−	−	−	+
HPT	B6	Alılı	−	+	+	−	−	−	−	−
HPT	B31	South of Ballık	+	−	−	+	−	−	−	−
HPT	B303	South of Ballık	+	+	−	+	−	−	+	−
HPT	K32; K33	Küfeke	+	−	−	+	+	−	−	−
HPT	K22	Küfeke	−	+	+	−	−	−	−	−
HPT	K23	Küfeke	+	−	−	+	−	−	−	−
HPT	K335	Küfeke	+	+	−	−	−	+	+	−
HPT	O25	West of Ömer-kuyu	−	+	−	−	−	+	−	−
HPT	O26; O27	South of Soğucak	−	+	−	+	−	−	−	+
HPT	K28	Küfeke	−	+	−	−	−	+	−	−
HPT	K29; K31	Küfeke	−	+	−	+	−	−	−	+
HPT	K30	Küfeke	−	+	−	+	−	+	−	+
HPT	O313	Soğucak	−	+	−	+	−	−	+	−
Purified zeolites samples										
LPT	SZ2; SZ6	Selçik	+	−	−	+	+	+	−	−
LPT	SZ3	Selçik	+	−	−	+	+	−	−	−
LPT	SZ8	Selçik	+	−	−	+	−	−	−	−
HPT	OZ5	Soğucak	−	+	−	+	−	−	−	−
HPT	OZ7	Soğucak	−	+	−	−	−	+	−	−
HPT	OZ22/2	Soğucak	−	−	−	+	−	+	−	−
HPT	BZ1; BZ4	Ballık	+	+	−	−	−	+	−	−

Cha; chabazite, Phi; phillipsite, Ana; analcime, San; sanidine, Q; Quartz, Cal; calcite, Bio; Biotite, Aug; augite.

amounts of calcite (Figure 3a; Table 1). The LPT has variable, small pyroclasts with microlitic and micro-porphyritic textures. Although biotite, chlorite, and opaque minerals were not detected by XRD, they are occasionally observed by optical microscopy. Plagioclase and augite were also found as microlite and phenocrysts in the pyroclasts. The LPT is less lithified, containing many cavities and pores, resulting in greater porosities than the HPT. The HPT contain phillipsite, chabazite, sanidine, and minor amounts of analcime, calcite, biotite, and augite (Figure 3b,c; Table 1). Although chlorite and opaque minerals were not detected by XRD, they are occasionally determined by optical microscopy. The XRD patterns contain a broad background, which is interpreted to be a glassy matrix. Small amounts of analcime were found in two samples (B6 and B22) from the Alılı and Küfeke areas. A representative XRD pattern of a sample with analcime (B6) is shown in Figure 3d.

Chabazite is confined to the vesicles and appears as transparent crystal aggregates. Chabazite rhombohedra grew on phillipsite rims. Generally, chabazite is found together with calcite and grown in pyroclasts including remnant leucite forms (Figure 4a). The rhombohedra range from 10 to 30 μm in diameter. Phillipsite is always found as a thin rim inside the vesicles. Phillipsite occurs mainly as white rosettes of radiating and spherulitic crystal aggregates (Figure 4c). Phillipsite is also present as isolated stout euhedral prisms. Crystals range from 30 to 60 μm in length and spherulites are 50 μm in diameter. The smallest phillipsite crystals were found to have formed with alteration of volcanic glass and in the vitric-rich fragments located in HPT (Figures 4b). Phillipsite is occasionally found within cracks of sanidine and leucite, and around the leucite crystals (Figure 4c−d). Calcite occurs as coarse-grained cements filling central parts of vesicles and intergranular spaces. Calcite appears to have formed as the latest secondary mineral (Figure 4a).

Large leucite crystals (1−2 cm) were hand picked for XRD investigation from HPT and HPL. The XRD data indicated that analcime formed in the HPT and generally

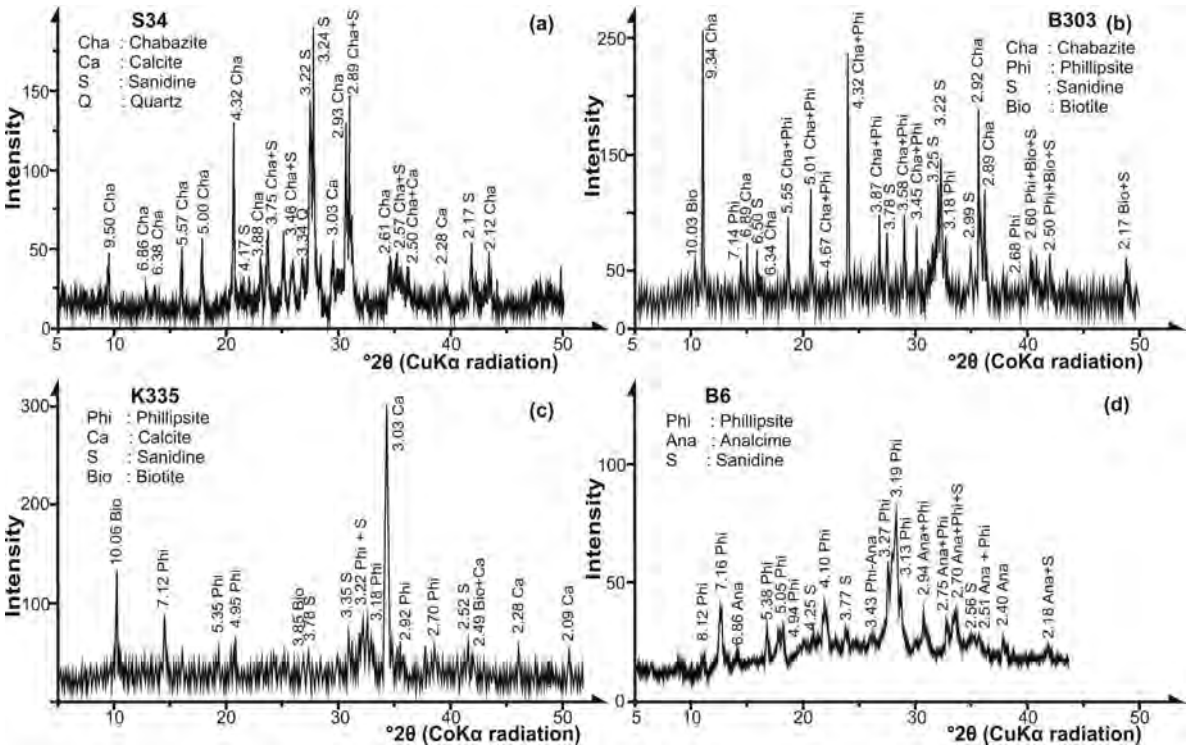

Figure 3. Mineralogical composition of the samples determined by XRD using CuKα and CoKα radiation. (a) LPT in the Selçik area (sample no. S34), (b) HPT in the Ballık area (sample no. B303), (c) HPT in the Küfeke area (sample no. K335), (d) HPT in the Alılı area (sample no. B6).

occurs together with leucite, which is found as a pyrogene mineral (Figure 5a) and leucite replacement by analcime. Analcime was probably formed by alteration of volcanic glass and of leucite. Analcime did not crystallize directly from a silicate melt and was not detected in the leucite crystal taken from HPL (Figure 5b). These rocks reveal an abundance of sanidine and leucite minerals.

The zeolite minerals were concentrated from zeolitic tuff by using heavy liquid (tetrabromoethane) (as per Minato, 1992). The small particulates (<2 μm) were dispersed in distilled water by ultrasonic vibration in a beaker and then filtered and dried at 60ºC. Zeolite particles were separated from the suspended small particulates using the heavy liquid tetrabromoethane. Concentrated zeolite grains were filtered on filter paper (Whatman™ Grade 541), washed with acetone, and dried. In the purified zeolite samples, XRD analysis showed the presence of chabazite and sanidine minerals in LPT (Figure 5c) and chabazite, phillipsite, and calcite minerals in HPT (Figure 5d). The zeolite content is defined as the weight percent retained during the separation process. The zeolite content in LPT (in the Selçik area) is up to 25 wt.% (Figure 6b). The zeolite content in HPT (in other areas) reaches up to 70 wt.% (Figure 6a,c,d). The zeolite content of the tuffs also varies vertically through the section. The LPT contains a maximum of 25% pyrogene minerals (sanidine, quartz, biotite, and ±augite) and the HPT contains a maximum of 8% pyrogene minerals (leucite, clinopyroxene, ±sanidine, and ±phlogopite).

Scanning electron microscopy and electron microprobe

Scanning electron microscopy (SEM) combined with energy-dispersive X-ray analysis (EDX) was carried out for all samples from HPT. Chabazite and phillipsite were the most abundant zeolite minerals observed (Figure 7a,b).

Chabazite appears as grouped rhombohedral crystals, often exhibiting 'pseudocubic' habit. Crystals from the study areas range in dimensions from 10 to 30 μm. Chabazite from the Ballık area, as in Figure 7a, formed in volcanic glass and cavities with dimensions ranging between 2 and 20 μm. The EDX analysis of chabazite crystals indicates a large Ca content in both sites (Figure 7a). Chabazite and phillipsite often occur together (Figure 7b). Phillipsite displays a spherulitic, radiating prismatic crystal habit infilling pores and ranges from 30 to 60 μm long, with a few of the crystals up to 120 μm long. Radiating prismatic K- and Ca-bearing phillipsite crystals from the Küfeke area are shown in Figure 7b. The EDX analysis revealed that all crystals contain mainly Si, Al, Ca, and K, similar to those observed by Tschernich (1992), but also contain minor amounts of Fe and Mg. Analcime occurrences are restricted to the Ballık and Küfeke localities. They

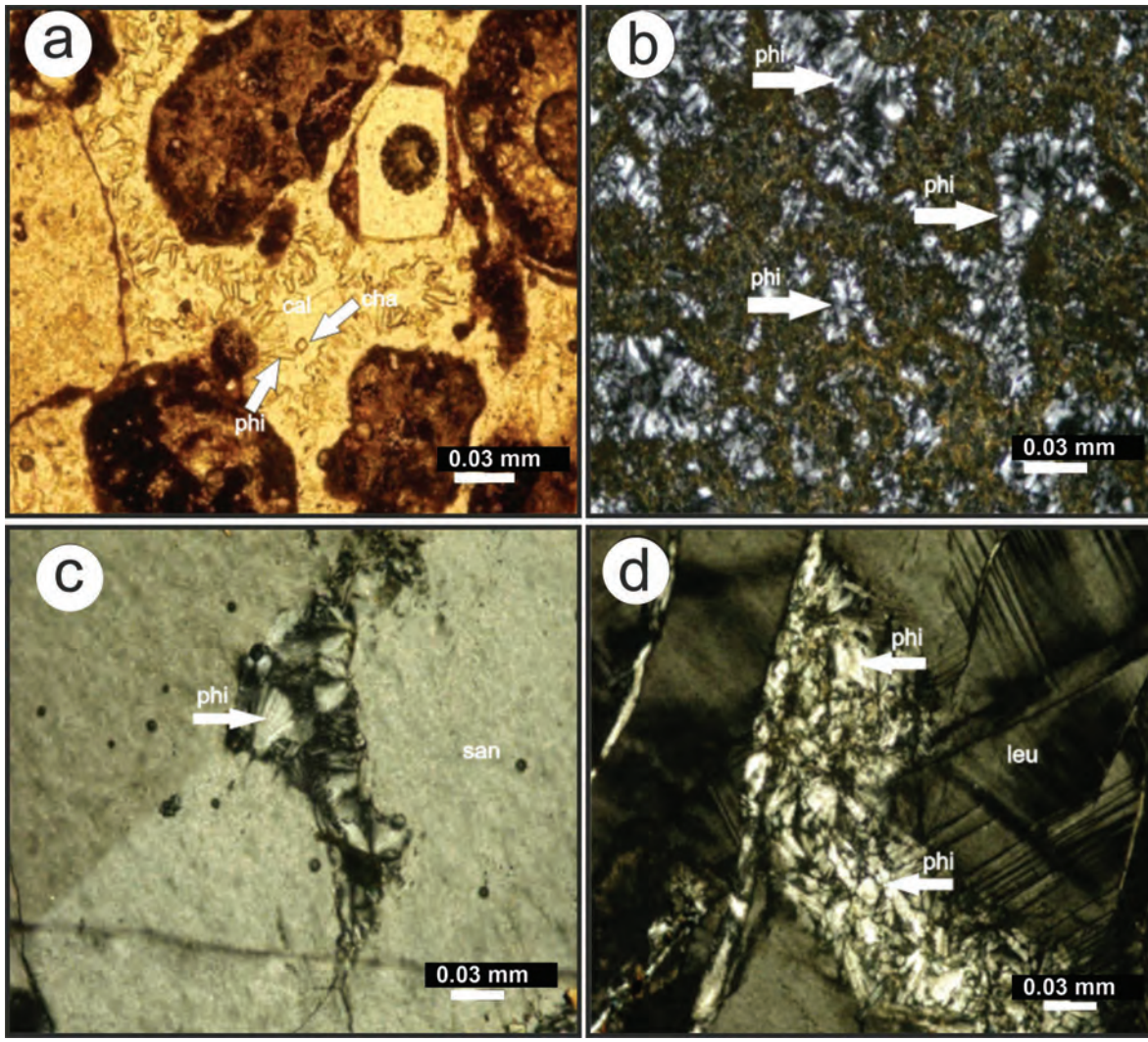

Figure 4. Photomicrographs of characteristic petrographic features of zeolites in HPT from Sandıklı regions: (a) chabazite and phillipsite at the border of pyroclasts from the Ballık area (sample no. B133; PPL); (b) phillipsite in matrix from the Ballık area (sample no. B521; XPL); (c) phillipsite in a crack in sanidine from the Ballık area (sample no. B520; XPL); (d) phillipsite around leucite from the Ömerkuyu area (sample no. O142; XPL). Scale bars shown in mm (cal, calcite; phi, phillipsite; cha, chabazite; leu, leucite; san, sanidine).

appear as isolated euhedral and colorless polygonal crystals. The EDX data for analcime show large Na contents (Figure 7c).

Electron Microprobe (EMPA) backscatter electron images suggest a paragenetic sequence whereby phillipsite crystals grew from the leucite and sanidine (Figure 8a,b; Table 2). Elemental analysis by wavelength dispersive spectroscopy (WDS) of zeolite aggregates (Table 3) were recalculated to structural formulae on the basis of 32 and 24 oxygens for phillipsite and chabazite, respectively. The low totals are due to the presence of structural water. The stoichiometric Si/Al ratio of phillipsites in HPT ranges from 1.99 to 2.62 (Table 3), with small Na contents (<0.1 a.p.f.u.) and large Ca and K contents (0.8−1.4 and 1.3−1.6 a.p.f.u.), respectively. The stoichiometric Si/Al ratios in HPT resemble those of the phonolitic tuffs in the Germany Laach volcanic area, which have been characterized by abundant K and Ca and small Si/Al ratios of 2.33−2.72 (Bernhard and Barth-Wirsching, 2002). The EMPA of chabazite samples in the LPT and HPT showed relatively large SrO contents, which range from 0.46 to 0.79 wt.%. The composition of the chabazite appears to be closely related to the original host-rock composition. The Si/Al ratios of chabazite range from 1.89 to 2.21 (Table 3), which is slightly lower than the phillipsite-rich sample. The Si/Al ratio of chabazite in the tephriphonolitic tuffs of study area also resemble those in the phonolitic tuffs in the Laach volcanic area though they are more abundant in K and Ca and have Si/Al ratios that range

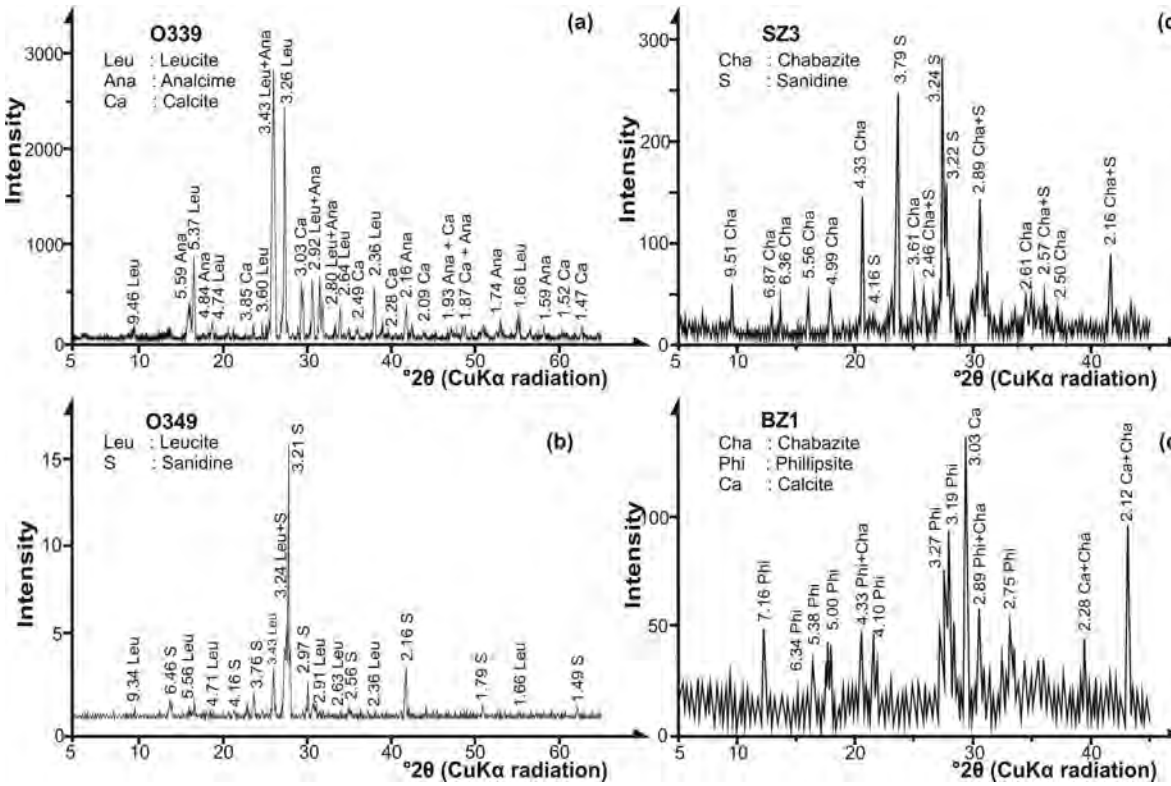

Figure 5. XRD patterns of handpicked leucite crystals and purified zeolite samples: (a) HPT (sample no. O339 from the Soğucak area); (b) HPL specimen including an abundance of sanidine and fewer leucite crystals (sample no. O349 from the Soğucak area); (c) purified zeolite from Selçik area (sample no. SZ3); (d) purified zeolite from the Ballık area (sample No BZ1).

from 2.33 to 2.50 (Bernhard and Barth-Wirsching, 2002).

A triangular plot of (Mg+Ca+Sr), Na, and K (Figure 9a) allows for comparison with other zeolitic terrains (de'Gennaro *et al.*, 2000; Weisenberger and Spürgın, 2009). Zeolites in the present study plot mostly as K-phillipsite ($K_{1.58}Na_{0.10}Ca_{1.33}Al_{5.26}Si_{10.87}O_{32}\cdot 12.90H_2O$) and rarely Ca-chabazite ($Ca_{1.39}Na_{0.06}K_{0.51}Al_{4.01}Si_{8.00}O_{24}\cdot 23.64H_2O$). The phillipsites are Na-depleted and Ca- and K-enriched (Figure 9a). Phillipsites plot near the middle of the K-(Ca+Mg+Sr) line. Chabazites plot closer to the (Ca+Mg+Sr) line. When recast as (Na+K)/(K+Na+Ca+Ba) *vs.* Si/Al (Figure 9b), samples fall in the phillipsite–chabazite field of Chipera and Apps (2001) (see their figure 3). Phillipsites from volcanic rocks have low Si/Al ratios, which are similar to mafic igneous rocks. Phillipsites from deep-sea sediments and saline lake deposits have larger Si/Al ratios and more first-group alkali cations (Sheppard *et al.*, 1970; Oba and Yoshikawa, 1994).

Bulk geochemistry

Representative bulk-chemical analyses of lavas and tuffs from this study are given in Table 4. The samples are classified as trachyte and trachyandesite (HPL, LPT, and HPT) on a Zr/TiO_2 *vs.* Nb/Y diagram like that proposed by Winchester and Floyd (1977) (Figure 10a). Lavas and tuffs were also plotted on a K_2O *vs.* Na_2O diagram (Figure 10b) and show their potassic character, which falls around the dashed line between ultrapotassic and shoshonitic fields. The HPT show high potassic character and fall into the ultrapotassic area of Figure 10b. The LPT show shoshonitic characteristics.

Trachytic and phonolitic rocks have intermediate silica contents and a high percentage of alkali cations (Na^+ and K^+). High proportions of alkali cations indicate that highly alkaline (*i.e.* high pH) pore waters occurred in the tuff vesicles. Under alkaline conditions, the mechanism of zeolite genesis is influenced by excess Si and Al, elements which are rapidly dissolved from volcanic glass and provide the main constituents of zeolites (Hernandez *et al.*, 1993). A similar case is seen in the pyroclastic rocks of Campi Flegrei (southern Italy), which have a narrower range of Si/Al compositions, between 2.59 and 2.86 (*i.e.* from trachyte to phonolite), greater K and Na contents, and moderate concentrations of alkaline earth cations (de' Gennaro *et al.*, 1999). The compositions of pyroclastic rocks of the Sandıklı district vary with broader Si/Al ratios of between 2.49 and 2.99, more K ranging between 2.72 and 7.79, and larger Na contents ranging between 0.40 and 2.12. The secondary minerals in the Sandıklı district are relatively silica poor and

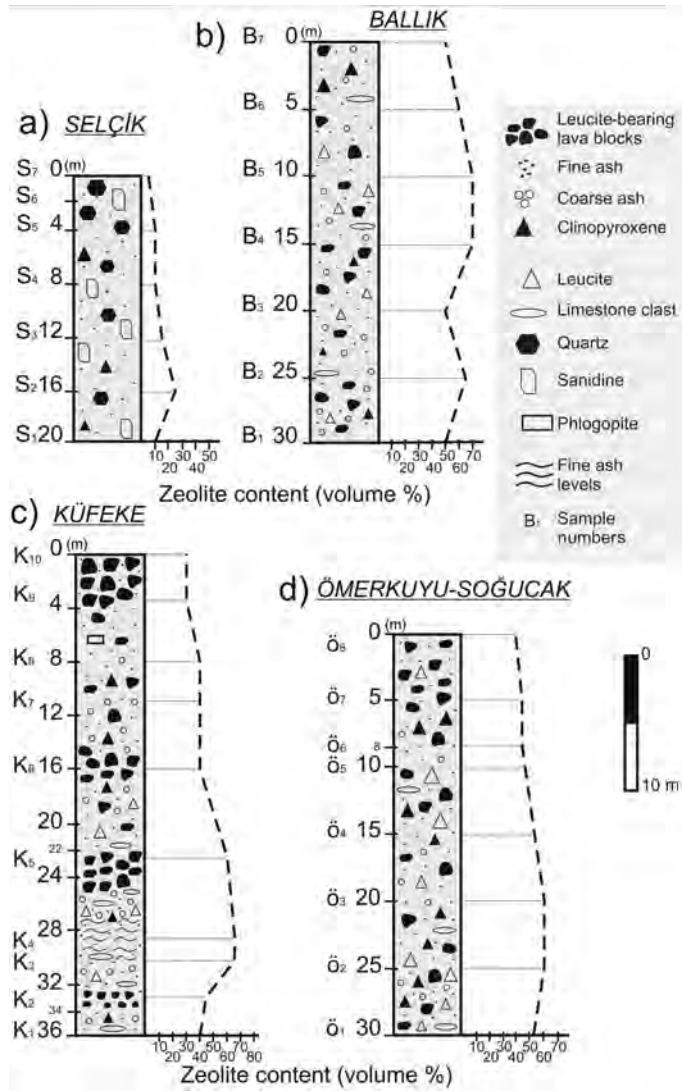

Figure 6. Zeolite contents from lower to upper levels in tuffs of the study area: (a) LPT containing chabazite (Selçik area); (b) HPT containing chabazite and phillipsite (Ballık area); (c) HPT containing phillipsite (Küfeke area); (d) HPT containing phillipsite (Ömerkuyu area). The zeolite content is defined as the mass recovered from heavy liquid separation.

consist mostly of phillipsite and chabazite that formed in K- and Na-rich environments.

DISCUSSION

Controls on zeolitization of pyroclastic rocks

Zeolitization of the pyroclastic deposits of the Sandıklı district was found within two main lithologic units. Chabazite is the dominant zeolite mineral in LPT and both chabazite and phillipsite are dominant in HPT. Zeolitization in the pyroclastic deposits of the Sandıklı district was controlled by processes that depend on: (1) the chemical composition of the source rocks; (2) the deposit thickness and degree of lithification; (3) emplacement temperatures; (4) eruptive dynamics and depositional mechanism and chilling rates; (5) extent of post-depositional meteoric flushing experienced (*i.e.* climatic regime); and (6) the chemistry of the basin sediments into which the deposits accumulated (*i.e.* freshwater *vs.* marine *vs.* hyper-alkaline).

A general summary of the main features of the controls on zeolitization of pyroclastic rocks is given in Table 5. The depositional characteristics of LPT developed from ash-fall deposits while the HPT developed from ash-flow deposits. De'Gennaro *et al.* (2000) suggested that fall processes promoted an effective gas-phase separation and clast dispersion in the atmosphere. In contrast, during flow deposition the steam was retained during the prior transport. When the steam condensed during flow transport the steam was retained and the resulting deposits are relatively wetter and cooler than ash-fall deposits. Both the abundance and

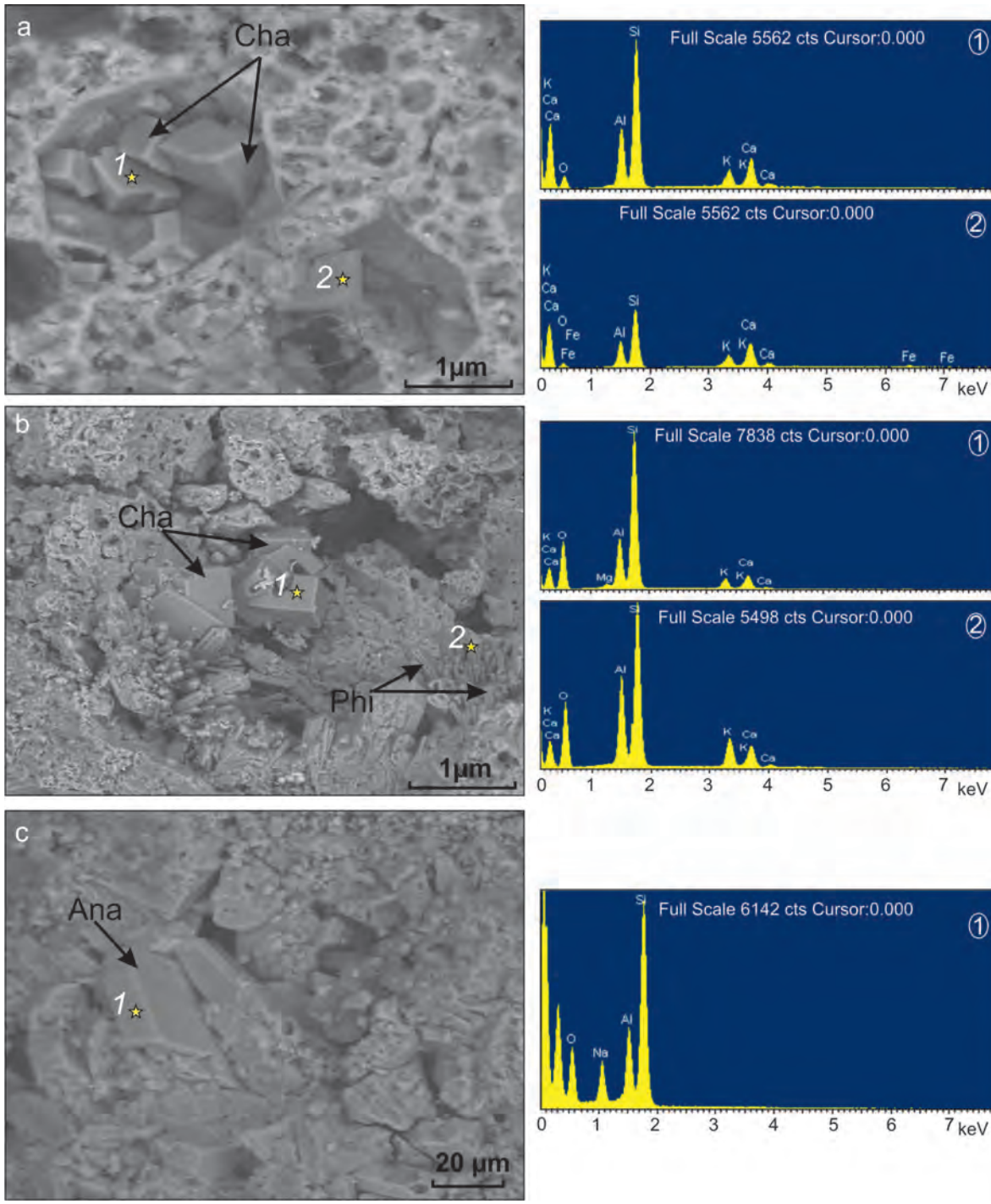

Figure 7. SEM images (left) and the corresponding EDX spectrum (right) of zeolite occurrences in the Sandıklı regions: (a) rhombohedral chabazite crystals formed in cavities from the Ballık area (sample no. B303); (b) rhombohedral chabazite crystals associated with spherulitic radiating prismatic phillipsite crystals from the Soğucak area (sample no. O313); (c) isolated euhedral analcime crystals (sample no. K339). (Arrows indicate examples of different minerals. Stars indicate EDX spectrum points.)

out-fluxing mechanisms of volatile phases in moving pyroclastic flows depend on the initial magma properties and eruptive conditions. Degassing and the cooling processes of a pyroclastic deposit further depend on the initial emplacement conditions, such as deposit thickness. The thickness and porosity of pyroclastic deposits

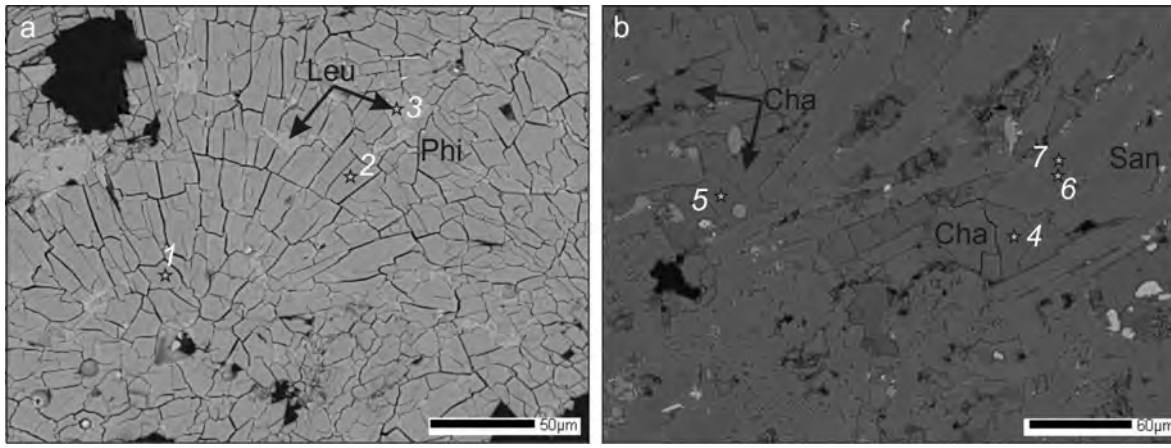

Figure 8. BSE images of chabazite and phillipsite occurrences in the Sandıklı regions: (a) Radiating clusters of phillipsite crystals in the leucite mineral from the Ballık area (sample no. B522); (b) chabazite crystals in sanidine from the Ballık area (sample no. B718). (Analysis numbers (1−7) are the same as those in Table 3. Arrows indicate examples of different minerals.)

decrease with time due to volatile out-fluxing, compaction, and welding. The Sandıklı pyroclastic succession ranges between 20 and 50 m thick. The lithification processes began by the formation of zeolites (mainly chabazite and phillipsite) and in the case of Sandıklı, the extent of lithification in LPT is less than that of HPT. The thicknesses and emplacement temperatures of pyroclastic rocks were lower in the LPT. The LPT was formed as an ash-fall deposit that did not entirely fill the pre-existing deepest valley. Hence the emplacement

Table 2. Microprobe analyses of K-phillipsite and leucite (sample no. B522) and Ca-chabazite and sanidine (sample no. B718) of the Sandıklı volcanics.

Sample No	B522			B718			
	– K-Phillipsite –		Leucite	Ca-Chabazite		– Sanidine –	
Analysis no.	1	2	3	4	5	6	7
SiO_2	53.15	51.15	55.60	38.47	43.80	63.86	65.00
TiO_2	0.25	0.34	0.07	0.07	0.01	0.04	0.07
Al_2O_3	23.02	20.59	22.77	23.03	18.88	19.79	19.04
MgO	0.07	0.10	0.00	0.06	0.01	0.00	0.00
FeOt	0.30	0.17	0.64	0.15	0.02	0.51	0.73
MnO	0.00	0.13	0.08	0.08	0.08	0.21	0.08
CaO	6.34	6.26	0.04	8.95	9.76	1.29	0.15
K_2O	5.66	6.17	20.17	2.92	2.22	9.72	13.27
Na_2O	0.18	0.22	0.10	0.05	0.10	3.38	1.96
BaO	1.14	0.57	0.24	0.63	0.64	0.07	0.13
SrO	0.38	0.31	0.20	0.93	0.84	n.d.	n.d.
Total	90.48	86.01	99.91	75.33	76.37	99.49	100.78
Σ cations:	– 32 oxygens –		6 oxygens	– 24 oxygens –		— 8 oxygens —	
Si	10.700	10.849	2.017	7.085	7.856	2.932	2.971
Ti	0.037	0.054	0.002	0.009	0.002	0.001	0.002
Al	5.462	5.147	0.974	4.999	3.991	1.071	1.026
Mg	0.020	0.032	0.000	0.016	0.002	0.000	0.000
Fe	0.051	0.030	0.019	0.023	0.003	0.020	0.028
Mn	0.000	0.023	0.002	0.012	0.012	0.008	0.003
Ca	1.368	1.423	0.002	1.766	1.876	0.063	0.008
K	1.453	1.669	0.933	0.687	0.509	0.569	0.774
Na	0.070	0.090	0.007	0.017	0.035	0.301	0.174
Ba	0.090	0.048	0.003	0.045	0.045	0.001	0.002
Sr	0.044	0.038	0.004	0.099	0.087	n.d.	n.d.
Total	19.294	19.403	3.964	14.759	14.418	4.966	4.988

n.d. not detected.

Table 3. Representative electron microprobe analyses [mean values; ( ): number of analyses used] of phillipsite and chabazite from the zeolitic tuffs of the Sandıklı area.

Mineral sample no.	MDL	– Chabazite –		Phillipsite					
		B718 (4)	K334 (3)	B718 (2)	B718 (2)	B518 (6)	B518 (5)	B522 (2)	B522 (1)
	wt.%	wt.%	wt.%	wt.%	wt.%	wt.%	wt.%	wt.%	wt.%
SiO_2	0.0856	44.69	47.52	57.05	51.91	51.12	51.31	52.15	51.26
TiO_2	0.1020	0.12	0.18	n.d.	0.11	0.10	n.d.	0.29	0.10
Al_2O_3	0.0796	20.25	18.53	18.49	21.68	21.63	21.92	21.81	20.78
FeO	0.3152	0.17	0.63	n.d.	0.45	0.33	0.26	0.24	n.d.
MnO	0.2739	n.d.	n.d.	n.d.	n.d.	n.d.	n.d.	n.d.	n.d.
MgO	0.0902	n.d.	0.88	n.d.	n.d.	n.d.	n.d.	0.08	0.12
CaO	0.0618	8.99	5.41	3.79	6.34	6.12	6.26	6.30	5.69
Na_2O	0.1185	0.22	0.12	0.43	0.13	0.25	0.19	0.20	0.30
K_2O	0.0608	2.37	2.23	5.00	5.98	6.09	6.07	5.92	5.76
BaO	0.2178	0.55	0.27	2.41	1.12	0.75	0.71	0.86	0.85
SrO	0.1458	0.79	0.46	0.26	0.25	0.22	0.23	0.34	0.19
Total		76.45	76.24	87.49	88.03	86.66	87.05	88.25	85.16
Si		7.778	8.288	11.731	10.781	10.759	10.728	10.774	10.922
Al		4.179	3.807	4.482	5.307	5.362	5.420	5.305	5.219
Ti		0.015	0.024	0.000	0.017	0.015	0.007	0.046	0.017
Fe		0.025	0.093	0.009	0.078	0.059	0.046	0.040	0.000
Mn		0.006	0.000	0.000	0.002	0.004	0.007	0.012	0.019
Mg		0.011	0.228	0.002	0.013	0.011	0.006	0.026	0.037
Ca		1.685	1.011	0.835	1.411	1.380	1.407	1.395	1.299
Na		0.072	0.041	0.171	0.053	0.100	0.077	0.080	0.125
K		0.530	0.496	1.313	1.584	1.634	1.623	1.561	1.565
Ba		0.038	0.019	0.194	0.091	0.062	0.059	0.069	0.071
Sr		0.080	0.047	0.031	0.030	0.027	0.028	0.041	0.023
Oxygens =		24	24	32	32	32	32	32	32
Ca+Mg		1.696	1.240	0.837	1.424	1.391	1.413	1.421	1.336
Na		0.072	0.041	0.171	0.053	0.100	0.077	0.080	0.125
K		0.530	0.496	1.313	1.584	1.634	1.623	1.561	1.565
Si/Al		1.893	2.208	2.617	2.032	2.020	1.994	2.033	2.093
(K+Na)/K+Na+Ca)		0.264	0.341	0.639	0.537	0.557	0.547	0.540	0.565
Tsi=Si/(Si+Al)		0.651	0.685	0.724	0.670	0.667	0.664	0.670	0.677

MDL, minimum detection limit; n.d. not detected

temperature reduced more quickly and resulted in smaller zeolite contents and less lithification. The absence of columnar jointed blocks in both LPT and HPT suggests that the emplacement temperature was not high (Francis *et al.*, 1974). The degree of lithification in the lower and middle sections of both LPT and HPT were noted (Özpınar *et al.*, 2002) to have been greater than in the upper levels. The LPT have average porosity of 31% and a compressive strength of 9 Mpa. In contrast, HPT (with chabazite and phillipsite) have a similar average porosity of 29%, but much higher compressive strengths of up to 18 Mpa. The HPT, dominated by phillipsite alone, have a similar average porosity of 28% and compressive strengths of up to 18 Mpa.

In a closed hydrologic system where the basin was without effluent streams, a saline alkaline lake typically formed at its center (Gottardi, 1989). Geomorphological conditions support the migration of both surface and pore waters toward the deepest part of the basin. Evaporation plays an important role in modifying the composition of water that eventually becomes connate. Concentric zoning of waters resulting from evaporation and shrinkage of the water-filled portion of the basin is reflected in the patterns of authigenic mineral deposits. What appears is progressive formation of an outer and upper ring of fresh or altered glass, an intermediate ring with zeolites, and a final central ring with alkali feldspar (Langella *et al.*, 2001). In contrast to open hydrologic systems that have meteoric waters percolating slowly through the thick tuff layers, the compositions of closed systems change progressively and become more alkaline and saline (and higher in pH). As the water descends near the surface, the glass is altered to clay minerals; a little deeper it alters to zeolite (chabazite and phillipsite); more deeply still it alters to analcime; and at the lowest level it alters to alkali feldspar (Gottardi, 1989; Sheppard and Hay, 2001).

In both the LPT and HPT from Sandıklı, concentric zoning of authigenic minerals was not seen. The zeolitization shows much less distinctive vertical

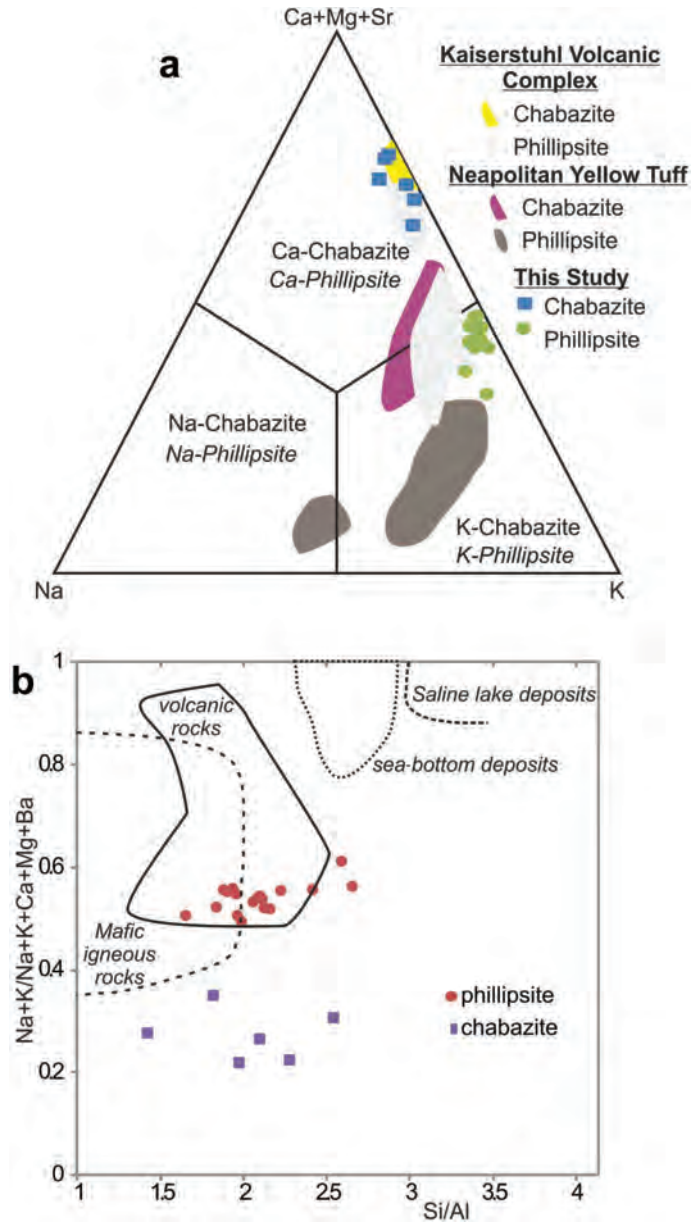

Figure 9. (a) Zeolite compositions from microprobe analyses plotted on a ternary Na-K-(Ca+Mg+Sr) composition diagram. The bounded areas are from de'Gennaro *et al.* (2000) and Weisenberger and Spürgın (2009); (b) plot showing the proportion of (Na+K)/(K+Na+Ca+Mg+Ba) *vs.* the Si/Al ratios of the investigated area. The bounded areas represent compositional fields for phillipsites from Oba and Yoshikawa (1994). Samples B718, B518, B522, and S335 are pyroclastic rocks from the areas of Ballık (samples B718, B518, and B522) and Selçik (sample S335 only).

zonation than seen in other areas (Table 5). Authigenic K-feldspar (sanidine) was not observed. Sanidine seen in thin section and observed with XRD is related to the original pyroclasts and pyrogene mineralization within tuffs. Back-scattered electron images showing chabazite transformed from primary sanidine (Figure 8b) further support this notion. The lack of evaporite minerals in the study area is also an indicator of an open hydrologic system. When combined, the Upper Jurassic–Lower Cretaceous permeable limestone Akdağ Formation underlying the pyroclastic rocks enhanced the alkaline nature of the subsurface environment while at the same time produced a conduit for water to migrate away.

The occurrence of analcime formation based on experimental studies is explained as coming from a primary magmatic source (*i.e.* formation from a fluid phase) and from a secondary transformation of leucite to analcime. Primary formation produces aggregates of well formed crystals with smooth surfaces, while secondary formation produces a micron-sized

Table 4. Major (wt.%), trace (ppm), and rare-earth element (ppm) compositions of the Sandıklı volcanics.

	Lavas								Tuffs						
	O314	O310	S110	S126	S132	O141	K200	S824	B303	O311	O321	O331	S338	S811	S817
SiO_2	54.02	51.13	61.19	59.91	61.79	50.88	59.69	62.29	47.80	48.07	45.90	56.36	54.05	54.49	50.32
Al_2O_3	17.15	16.94	14.84	15.51	14.68	17.14	14.6	14.54	16.32	16.99	14.67	18.02	16.12	16.06	17.49
Fe_2O_3	4.43	5.62	4.93	5.46	5.50	7.07	5.15	4.80	4.97	5.23	7.72	3.80	3.90	3.55	5.40
MgO	1.51	2.13	2.49	2.64	2.15	1.36	2.94	3.03	0.92	0.84	2.72	0.46	1.09	1.30	1.17
CaO	5.10	6.54	4.53	4.48	3.97	6.19	4.35	3.95	4.90	4.96	6.78	3.49	4.92	4.12	3.24
Na_2O	1.53	1.85	3.12	3.57	2.86	2.49	2.35	3.33	0.55	0.54	0.32	2.86	2.17	1.92	0.69
K_2O	10.12	7.73	4.87	4.51	5.03	8.10	4.85	5.09	6.04	7.33	7.90	7.73	3.69	3.28	9.31
TiO_2	0.74	0.86	1.04	1.09	0.92	1.29	1.10	0.99	0.84	0.91	1.26	0.66	0.57	0.65	0.97
P_2O_5	0.33	0.45	0.66	0.53	0.63	0.21	0.77	0.59	0.14	0.22	0.51	0.09	0.25	0.30	0.19
MnO	0.09	0.10	0.10	0.19	0.10	0.13	0.07	0.09	0.09	0.09	0.15	0.10	0.08	0.07	0.09
Cr_2O_3	0.006	0.006	0.015	0.02	0.015	0.004	0.01	0.026	n.d	0.002	0.006	n.d	0.004	0.09	0.06
LOI	4.1	5.6	1.8	1.5	2.0	3.8	3.4	0.8	16.2	13.7	10.9	5.3	12.2	13.3	10.3
Total	99.14	98.93	99.62	99.54	99.67	98.74	99.61	99.52	98.80	98.90	98.83	98.87	99.05	99.30	99.23
Pb	36.5	33.7	5.0	16.0	6.0	75.0	7.0	9.0	58.6	60.4	74.0	5.8	34.6	32.0	62.0
Zn	41	50	32	62	29	42	47	39	65	63	67	27	58	59	78
Ni	6.8	8.4	21.0	22.0	24.0	<20	22.0	25.0	3.6	6.1	10.6	4.7	12.1	23.0	19.0
Ba	2545	3397	1756	2000	1961	5582	1856	1687	4392	4862	6095	2217	4636	3797	4421
Co	16.9	16.2	16.9	18.3	20.1	17.8	17.1	17.2	10.2	12.0	22.4	13.8	10.0	9.6	9.4
Hf	17.4	27.3	13.1	9.8	11.0	21.4	15.4	12.3	16.8	16.9	17.0	15.9	9.8	10.4	15.8
Nb	33.9	34	45.5	40.7	32.6	52.5	47.6	43.4	41.2	41.7	36.8	36.9	42.7	57.1	41.6
Rb	638.8	1042	180.8	161.1	292.9	1776	194.6	216.4	381.1	415.6	351.4	248	156.7	167.5	393.2
Sr	2910	3460	1208	1452	1020	3246	1320	1237	4287	2615	1786	5783	2094	1954	1552
Ta	1.9	1.7	3.3	3.2	3.0	3.7	3.8	3.9	2.2	2.4	2.0	2.5	2.3	3.3	2.8
Th	49.4	46.7	29.8	45.0	53.4	54.5	34.0	40.1	49.1	47.6	45.8	41.3	45.7	47.9	43.9
V	121.0	153.0	92.0	11.4	127.0	216.0	11.0	81.0	88.0	154.0	155.0	74.0	61.0	61.0	132.0
W	53.5	20.9	6.0	4.0	7.0	4.0	8.0	5.0	7.5	8.1	9.7	64.1	18.7	6.0	3.0
Zr	655.4	630.3	457.8	327.6	343.7	774	520.4	419.9	640.4	636.8	597.1	593.2	389.8	419.2	517.9
Y	21.1	19.3	26.7	26.3	28.6	28.3	31.2	25.0	20.0	28.5	24.3	22.7	19.2	30.0	23.0
La	74.4	84.3	103.8	135.0	76.7	104.7	121.7	103.3	76.4	94.6	81.2	79.2	124.0	147.9	85.5
Ce	135.3	142.1	184.5	239.7	129.9	179.3	219.8	186.1	143.3	164.5	160.4	135.2	214.1	222.4	142.7
Pr	13.8	16.1	20.2	26.39	14.74	19.74	24.5	20.45	14.58	17.66	17.56	14.44	19.52	21.85	15.14
Nd	50.2	59.0	73.5	97.6	56.6	69.4	88.4	72.3	49.4	64.5	64.0	53.3	62.9	71.9	54.0
Sm	7.40	8.90	12.00	15.20	9.40	12.10	14.60	11.20	7.65	9.36	10.83	7.79	8.11	9.80	8.60
Eu	1.87	2.16	3.35	4.15	2.39	3.10	4.10	3.10	1.89	2.33	2.59	1.95	1.90	2.53	1.19
Gd	5.07	5.88	7.6	8.76	6.88	7.92	9.76	7.35	5.11	6.45	7.37	5.53	5.25	6.045	5.53
Tb	0.73	0.81	0.9	1.01	0.86	1.00	1.13	0.9	0.77	0.91	1.00	0.77	0.68	0.73	0.70
Dy	3.74	3.71	4.71	5.10	4.85	5.15	5.73	4.56	3.66	4.35	4.71	4.00	3.26	4.15	3.81
Ho	0.68	0.61	0.88	0.87	0.94	0.93	1.01	0.70	0.68	0.78	0.82	0.70	0.60	0.86	0.69
Er	1.92	1.81	2.58	2.52	3.01	2.8	2.99	2.32	1.96	2.14	2.16	2.02	1.74	2.77	2.24
Tm	0.30	0.26	0.33	0.32	0.38	0.37	0.39	0.30	0.30	0.33	0.32	0.30	0.26	0.38	0.29
Yb	1.97	1.78	2.30	2.24	2.69	2.53	2.7	2.13	1.92	2.14	2.04	1.99	1.74	2.82	2.02
Lu	0.31	0.27	0.33	0.30	0.39	0.35	0.35	0.31	0.28	0.30	0.29	0.31	0.26	0.44	0.28

microporous texture (Putnis *et al*., 1994; Line *et al*., 1995; Abdioğlu, 2012) showing the typical leucite habit of deltoid-icositetrahedron with well developed {211} faces. A proposed reaction is leucite + Na^+_{aq} + H_2O = analcime + K^+_{aq}, which involves a 10% molar-volume increase that produces the cracking around the analcime aggregate (Putnis *et al.*, 2007; Weisenberger and Spürgın, 2009). Laboratory simulations using this reaction path suggest that analcime is the most stable phase, often resulting from metastable phillipsite and chabazite (de'Gennaro *et al.*, 2000). In the Sandıklı area, the transformation of leucite into analcime probably occurred under neutral to moderately alkaline conditions after the deposition of the tuffs. X-ray diffraction analysis shows leucite in glass and volcanic rock fragments (volcanic clasts) within HPT.

The formation of phillipsite and chabazite requires K, whereas Ca is less important in most zeolite crystallization in trachytic-phonolitic glasses. Unlike other zeolite occurrences around the world, the chabazite in both LPT and HPT are Ca-enriched which probably occurred by both direct formation in Ca-bearing solutions and by post-zeolitization cation exchange. The concentration of K or the K/(Ca+Na) ratio needs to be sufficiently high to precipitate phillipsite at the initial stage of zeolitization. At Sandıklı, the concentration of

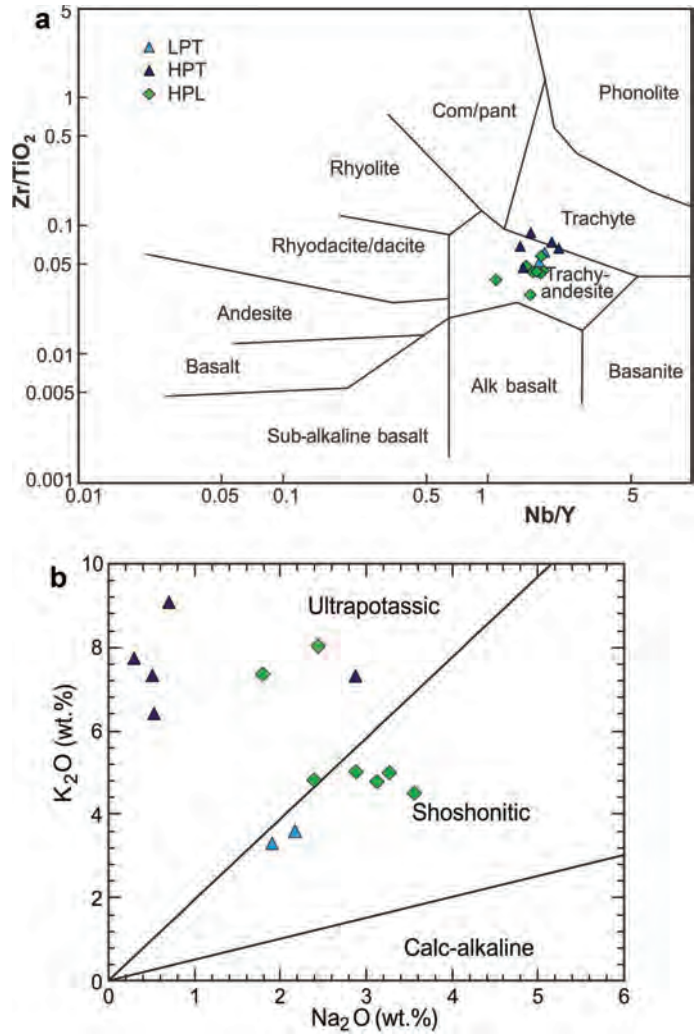

Figure 10. (a) Zr/TiO_2 *vs*. Nb/Y chemical classification diagram for lavas and tuffs from the study area. (b) K_2O *vs.* Na_2O diagram for lavas and tuffs. Stars are tuffs (LPT, HPT) and squares are volcanics/lavas (PL, PAL, HPL).

Na appears to have increased downward as the excess Na was derived from glass dissolution with percolating water through porous tuffs. As the K/(Ca+Na) decreases with phillipsite precipitation, the chabazite begins to crystallize (Iıjima and Harada, 1969). Increasing the fugacity of CO_2 can further influence the formation of zeolites by lowering the activity of H_2O and by providing the carbonate ions by hydrolysis reactions. Carbonate ions can combine with Ca to form calcite, thus creating a Ca sink, which otherwise is used in forming Ca zeolites (Hay, 1986; İbrahim, 2004). The absence of calcite and enrichment of Ca, therefore, suggests lower CO_2 fugacity during zeolitization.

The order of paragenesis of the authigenic minerals in the zeolitization in the pyroclastic deposits is indicated as [analcime/phillipsite → chabazite → calcite]. Analcime/phillipsite was not found together with chabazite in LPT. Analcime appears along with minor calcite only in the Ballık and Soğucak areas.

CONCLUSIONS

Field, petrographic, and petrochemical investigations performed to understand the conditions of formation of the Sandıklı zeolite deposits revealed two different lithologic units: LPT and HPT. The parent materials of these units have been transformed to zeolite minerals by percolating meteoric water, probably in an open hydrological system. The LPT are shoshonitic in character and Ca-chabazite formed as a result. The HPT are more highly potassic in character and characterized by the predominance of K-phillipsite and lesser amounts of Ca-chabazite and analcime. The zeolite contents of the middle and lower sections (both of LPT and HPT) are more abundant than in the upper sections, with zeolite contents for the LPT of as much as 25% and 70% for HPT. These deposits are slightly more potassic and more calcic in composition than typical zeolitic deposits derived from volcanic tuffs in other regions of the world. Exploration and exploitation of zeolitic deposits

Table 5. Comparison of zeolite assemblages.

Zeolitization factors	Sandıklı	Italy[1]	Spain[2]	Germany[3]	Turkey[4]
Source rock	Trachyte, tephriphonolite	Trachyte and phonolite	Trachytic and phonolitic rocks	Phonolite	Basaltic rocks
Zeolite type	Phillipsite, chabazite, minor analcime	Phillipsite, minor chabazite	Phillipsite with lesser chabazite and analcime	Chabazite, phillipsite and analcime	Natrolite, analcime, disordered thomsonite, laumontite and phillipsite
Deposit thickness (m)	20–50	20–30	–	0.15–10	–
Emplacement temperature (ºC)	Not high	Not lower than 375	Lower	100–200	100
Eruptive dynamics and mechanisms	Ash-flow and ash-fall deposits	Pyroclastic-flow and minor air-fall deposits	Ash flows and rare ash falls	Pyroclastic ash flow	Brecciated lavas, tuff-lapilli tuff
Meteoric flushing	Meteoric waters	Meteoric waters	Water vapor trapped within the pores of the glass particles	Stagnant fringe water zone immediately above the groundwater table	Mixture of seawater and meteoric water with magmatic water
Open or closed system conditions	Open hydrologic system	Alteration in an open hydrologic system	Closely related to the hydro-thermal system	Relatively closed system	Closed system

[1]de' Gennaro *et al*. (2000); [2]Hernandez *et al*. (1993); [3]Bernard and Barth-Wirsching (2002); [4]Abdioglu (2012).

hosting analcime, chabazite, and phillipsite might consider using the factors of magmatic source-rock composition, temperature/cooling history, emplacement mechanism, and deposit thickness in development strategies.

ACKNOWLEDGMENTS

The authors extend thanks to Jianguo Fan (Center for Advanced Ultrastructural Research, University of Georgia) for his help with the scanning electron microscopy and Chris Fleshier (Department of Geology, University of Georgia) for his help with the electron microprobe analysis. Murat Kalkan (Aksaray University) is acknowledged for his assistance during the fieldwork. The editorial team and two anonymous reviewers are thanked for their comments which significantly improved the manuscript.

REFERENCES

Abdioğlu, E. (2012) Mineralogy and chemistry of zeolites and associated minerals in Tertiary alkaline volcanics from the Eastern Pontides, NE Turkey. *Neues Jahrbuch für Mineralogie*, **189**, 35–47.

Armstrong, J.T. (1988) Quantitative analysis of silicate and oxide materials: comparison of Monte Carlo, ZAF, and phi-rho-z procedures. *Microbeam Analysis* **23**, 239–246.

Bernhard, F. and Barth-Wirsching, U. (2002) Zeolitization of a phonolitic ash flow by groundwater in the Laach volcanic area, Eifel, Germany. *Clays and Clay Minerals*, **50**, 710–725.

Besang, C., Eckahtrdt, F.J., Harre, W., Kreuzer, H., and Müller, P. (1977) Radiometricshe Altersbesttimmungen der Türkei. *Jahrbuch der Geologischen Bundesanstalt*, **25**, 3–5.

Bish, D.L. and Carey, J.W. (2001) Thermal behavior of natural zeolites. Pp. 403–452 *in: Natural Zeolites: Occurrence, Properties, Applications* (D.L. Bish and D.W. Ming, editors). Reviews in Mineralogy and Geochemistry, **45**, Mineralogical Society of America, Washington, D.C.

Cappelletti, P., Cerri, G., Colella, A., de' Gennaro, M., Langella, A., Perrotta, A., and Scarpati, C. (2003) Post-eruptive processes in the Campanian Ignimbrite. *Mineralogy and Petrology* **79**, 79–97.

Chipera, S.J. and Apps, J.A. (2001) Geochemical stability of natural zeolites. Pp. 117–161 *in: Natural Zeolites: Occurrence, Properties, Applications* (D.L. Bish and D.W. Ming, editors). Reviews in Mineralogy and Geochemistry, **45**, Mineralogical Society of America, Washington D.C.

de'Gennaro, M., Langella, A., Cappelletti, P., and Colella, C. (1999) Hydrothermal conversion of trachytic glass to zeolite. 3. Monocationic Model Glasses. *Clays and Clay Minerals*, **47**, 348–357.

de'Gennaro, M., Cappelletti, P., Alangella, A., Perrotta, A., and Scarpati, C. (2000) Genesis of zeolites in the Neapolitan Yellow Tuff: Geological, volcanological and mineralogical evidence. *Contributions to Mineralogy and Petrology*, **139**, 17–35.

Ercan, T. (1986) Orta Anadolu'daki Senozoyik Volkanizması. *MTA Dergisi*, **107**, 119–141 (in Turkish).

Esenli, F. and Sirkecioglu, A. (2005) The relationship between zeolite (heulandite-clinoptilolite) content and the ammonium-exchange capacity of pyroclastic rocks in Gördes, Turkey. *Clay Minerals*, **40**, 557–564.

Folk, (1962) Classification of carbonate rocks. *American Association of Petroleum Geologists Memoirs*, **1**, 62–82.

Francis, P.W., Roobol, M.J., Walker, G.P.I., Cobbold, P.R. and Coward, M. (1974) The San Pedro and San Pablo Volcanoes and their hot avalanche deposits. *Geologische Rundschau*, **63**, 357–388.

Gottardi, G. (1989) The genesis of zeolites. *European Journal of Mineralogy*, **1**, 479–487.

Gundogdu, M.N., Yalcin, H., Temel, A., and Clauer, N. (1996) Geological, mineralogical and geochemical characteristics of zeolite deposits associated with borates in the Bigadic Emet and Kirka Neogene lacustrine basins, western Turkey. *Mineralium Deposita*, **31**, 492–513.

Hay, R.L. (1986) Geologic occurrence of zeolites and some associated minerals. *Pure and Applied Chemistry*, **58**, 1339–1342.

Helvacı, C., Stamatakis, M.G., Zagouroglou, C., and Kanaris, J. (1993) Borate minerals and related authigenic silicates in northeastern Mediterranean late Miocene continental basins. *Exploration and Mining Geology*, **2**, 171–178.

Hernandez, J.E.G., Notario del Pino, J.S., Gonzalez Martin, M.M., Hernan Reguera, F., and Rodriguez Losada, J.A. (1993) Zeolites in pyroclastic deposits in southeastern Tenerife (Canary Islands). *Clays and Clay Minerals*, **41**, 521–526.

Ibrahim, K. (2004) Mineralogy and chemistry of natrolite from Jordan. *Clay Minerals*, **39**, 47–55.

Iıjima, A. and Harada, K. (1969) Authıgenic zeolites in zeolitic palagonite tuffs on Oahu, Hawaii. *American Mineralogist*, **54**, 182–198.

Kaçmaz, H. and Koktürk, U. (2004) Geochemistry and mineralogy of zeolitic tuffs from the Alacatı (Ceşme) area, Turkey. *Clays and Clay Minerals*, **52**, 705–713.

Langella, A., Cappeletti, P., and de'Gennaro, M. (2001) Zeolites in closed hydrologic systems. Pp. 235–260 in: *Natural Zeolites: Occurrence, Properties, Applications* (D.L. Bish and D.W. Ming, editors). Reviews in Mineralogy and Geochemistry, **45**, Mineralogical Society of America, Washington, D.C.

Line, C.M.B., Putnis, A., Putnis, C., and Giampaolo, C. (1995) The dehydration kinetics and microtexture of analcime from two paragenesis. *American Mineralogist*, **80**, 268–279.

Minato, H. (1992) Investigation methods of zeolite, *Natural Zeolite and its Utilization*, Edited By No. 111 Committee, JSPS, Tokyo University Press, Tokyo, pp. 281–376.

Oba, T. and Yoshikawa, K. (1994) Note on rock-forming minerals in the Joetsu district, Niigata Prefecture, Japan. (7) Phillipsite from Yoneyama. *Bulletin Joetsu University of Education*, **13**, 399–406.

Özen, S. and Göncüoğlu, M.C. (2011) Origin of analcime in the Neogene Arıklı tuffs, Biga Peninsula, NW Turkey. *Neues Jahrbuch für Mineralogie*, **189/1**, 21–34.

Özpınar, Y., Çobanoğlu, I., and Bozkurt, R. (2002) Sandıklı zeolitik tüflerin petrografik ve petrokimyasal ve teknolojik özelliklerinin incelenmesi, TÜBİTAK-YDABÇAĞ-198Y102, Ankara, pp 268 (in Turkish).

Özpınar, Y. (2008) The mineralogic, petrographic and ion exchange capacity features of tuffs containing chabazite and phillipsite in Sandıklı (Afyon) region and their usage in agriculture (southwest Anatolia, Turkey). *Bulletin of the Mineral Research and Exploration*, **137**, 29–48.

Özpınar, Y. (2011) Use of zeolitic tuffs as cement additives, building stone and removal of heavy metal cations. *Carpathian Journal of Earth and Environmental Science*, **6/1**, 147–158.

Putnis, A., Putnis, C., and Giampolo, C. (1994) The microtexture of analcime phenocrysts in igneous rocks. *European Journal of Mineralogy*, **6**, 627–632.

Putnis, C.V., Geisler, T., Schmid-Beuermann, P., Stephan, T., and Giampaolo, C. (2007) An experimental study of the replacement of leucite by analcime. *American Mineralogist*, **92**, 19–26

Schmid, R. (1981) Descriptive nomenclature and classification of pyroclastic deposits and fragments: Recommendations of the IUGS Sub-commission on the Systematics of Igneous Rocks. *Geology*, **9**, 41–44.

Semiz, B., Schroeder, P.A., and Özpınar, Y. (2011) Zeolitization of Miocene tuffs the Saphane-Gediz-Hisarcık regions, Kutahya-western Anatolia, (Turkey). *Euroclay 2011*, Antalya, Turkey, 232 pp.

Sheppard, R.A. and Hay, R.L. (2001). Formation of zeolites in open hydrologic systems. Pp. 261–271 in: *Natural Zeolites: Occurrence, Properties, Applications* (D.L. Bish and D.W. Ming, editors). Reviews in Mineralogy and Geochemistry, **45**, Mineralogical Society of America, Washington, D.C.

Sheppard, R.A., Gude, A.J. 3rd, and Griffin, J.J. (1970) Chemical composition and physical properties of phillipsite from the Pacific and Indian Oceans. *American Mineralogist*, **55**, 2053–2062.

Snellings, R., van Haten, T., Machiels, L., Mertens, G., Vandenberghe, N., and Elsen, J. (2008) Mineralogy, geochemistry and diagenesis of clinoptilolite tuffs (Miocene) in the central Simav graben, Western Turkey. *Clays and Clay Minerals*, **56**, 622–632.

Tschernich, R.W. (1992) *Zeolites of the World*. Geoscience Press, Phoenix, Arizona, USA.

Weisenberger, T. and Spürgın, S. (2009) Zeolites in alkaline rocks of the Kaiserstuhl volcanic complex, SW Germany, new microprobe investigation and the relationship of zeolite mineralogy to the host rock. *Geologica Belgica*, **12**, 75–91.

Winchester, J.A. and Floyd, P.A. (1977) Geochemical magma type discrimination: application to altered and metamorphosed basic igneous rocks. *Earth and Planetary Science Letters*, **28**, 257–272.

(*Received 17 October 2012; revised 12 April 2013; Ms. 719; A.E. S. Kadir*)

Clays and Clay Minerals, Vol. 61, No. 3, 193–203, 2013.

SYNTHESIS, CHARACTERIZATION, AND EVALUATION OF A FERROMAGNETICALLY MODIFIED NATURAL ZEOLITE COMPOSITE FOR REMOVAL OF Cs^+ AND Sr^{2+}

HOSSEIN FAGHIHIAN[1,*], MOHAMMAD MOAYED[1], ALIREZA FIROOZ[1], AND MOZHGAN IRAVANI[1,2]

[1] Department of Chemistry, University of Isfahan, 81746-73441, Isfahan, Iran
[2] Nuclear Fuel Cycle Research School, Nuclear Science and Technology Research Institute, Isfahan, Iran

Abstract—The high fission yield and long half life of cesium and strontium make them the two most high-risk products from nuclear fission, so their separation from radioactive wastes is an important step in mitigating their harmful effects. Clinoptilolite, because of its thermal stability, high radiation resistance, and selectivity, was considered as the adsorbent for this purpose. In order to then separate the adsorbent-adsorbate complex from aqueous solution, the clinoptilolite was prepared as a magnetized composite with nanomagnetite. This magnetically modified zeolite enabled the efficient and quick separation of the adsorbent from solution using magnetic separation. The ability of this composite to remove Cs^+ and Sr^{2+} from aqueous solutions was assessed and characterized using X-ray diffraction, X-ray fluorescence, Fourier-transform infrared spectroscopy, differential thermogravimetric analysis, and vibrating-sample magnetometry. Variables such as initial ion concentration, pH, contact time, and temperature in the sorption process were studied and optimized. The maximum adsorption capacities of the composite were 188.7 and 36.63 mg g^{-1} for Cs^+ and Sr^{2+}, respectively. Investigation of the kinetics revealed that the adsorption process onto the composite was quicker than in the case of the zeolite alone. The equilibrium data were analyzed using the Langmuir, Freundlich, and Dubinin-Radushkevich (D-R) isotherm models. The mean free energy of sorption (E) for both ions was in the range 8−16 kJ mol^{-1}, confirming that an ion-exchange mechanism had occurred. Positive ΔH° and negative ΔG° values were indicative of the endothermic and spontaneous nature of the removal of Cs^+ and Sr^{2+}. The saturation magnetization of the composite was measured (17.46 Am^2/kg), implying fast magnetic separation of the sample after adsorption. The results obtained revealed that the natural Iranian zeolite nanomagnetite composite was a good ion exchanger in the removal of Cs^+ and Sr^{2+}.

Key Words—Cesium, Clinoptilolite, Composite, Nanomagnetite, Natural Zeolite, Strontium.

INTRODUCTION

Radioactive wastes containing radionuclides are considered to be the most hazardous environmental pollutants and their treatment has received much attention. Because of their high fission yields and long half-life properties, ^{137}Cs and ^{90}Sr are the two most notable fission products. Ion exchange, precipitation, liquid-liquid extraction, and adsorption are the traditional methods used for removal of cesium and strontium from liquid wastes, with ion exchange being the most effective technique (Balarama Krishna *et al.*, 2004; Shakir *et al.*, 2007; Wu *et al.*, 2012; Zhang *et al.*, 2009).

Zeolites, as inorganic ion exchangers with high thermal, mechanical, and radiation stability, and with good selectivity and exchange-capacity properties, are generally preferred over other adsorbents for removal of radionuclides from aqueous solution (Abdel Rahman *et al.*, 2010; Borai *et al.*, 2009; El-Naggar *et al.*, 2008). Radioactive wastes have been treated using natural zeolites such as mordenite, erionite, chabazite, and clinoptilolite. The last one is the most abundant natural zeolite with large selectivity and adsorption capacity (Kabiri-Tadi and Faghihian, 2011).

In clinoptilolite, AlO_4 and SiO_4 tetrahedra are linked together by sharing their oxygen atoms in the zeolite framework. In the substitution of Al(III) for Si(IV) in the structure of zeolites, a negative charge appears which is neutralized by exchangeable cations such as Na^+, K^+, Ca^{2+}, and Mg^{2+}. The selectivity and ion-exchange ability depend greatly on the numbers, types, and locations of these exchangeable cations in the zeolite framework, which may vary from one deposit to another and even within the same deposit. The clinoptilolite selected for the present study was obtained from the Aftar deposit located northwest of Semnan in northeast Iran.

After the ion-exchange process, one of the greatest challenges with zeolite powders is their separation from solution, a time-consuming and laborious procedure. This problem could be overcome by using a magnetic-separation technique. Magnetic modification offers a new methodology with efficient, precise, and quick separation of zeolite to which a magnetic field is applied. Magnetic composites have been used for the removal and preconcentration of ions from aqueous solution. Ashtari *et al.* (2005) used neocuproine-

* E-mail address of corresponding author:
h.faghih@sci.ui.ac.ir
DOI: 10.1346/CCMN.2013.0610303

modified magnetic microparticles for separation of Cu^{2+}. Bachir *et al.* (2009) studied the properties of magnetic Ti-pillared clay minerals. Gutierrez *et al.* (2010) prepared a magnetic composite by wet impregnating a powder of natural zeolite with a magnetic Fe oxide-containing synthetic material. Nah *et al.* (2006) prepared a composite of clinoptilolite, magnetite, and urethane for removal of Pb^{2+}. Oliveira *et al.* (2004) prepared a magnetic zeolite-Y composite for removal of Cr^{3+}, Cu^{2+}, and Zn^{2+}. Bourlinos *et al.* (2003) decorated the external surface of zeolite-Y with maghemite, and used it for adsorption of Hg^{2+}.

In the present study, the adsorption feature of natural clinoptilolite with magnetic properties of iron oxide was combined to prepare a nanomagnetite zeolite composite. The composite prepared was used to remove Cs^{+} and Sr^{2+} from aqueous solution and subsequently was separated from solution by simple magnetic separation. Different variables such as contact time, temperature, pH, and initial ion concentrations were investigated and optimized. The kinetics, thermodynamic, and isotherm parameters of the process were also evaluated.

EXPERIMENTAL

Materials and reagent

All chemical reagents used in this study were of analytical reagent grade (AR Grade). $FeCl_3{\cdot}6H_2O$ (Sigma-Aldrich, Germany, 98%) and $FeCl_2{\cdot}4H_2O$ (Sigma-Aldrich, Germany, 99%) were used for magnetic particle preparation. Cesium and strontium were supplied as cesium chloride and strontium chloride by Merck, Germany. Natural clinoptilolite was collected from the Aftar deposit located northwest of Semnan, Iran. In order to remove soluble salts, the zeolite was dispersed in distilled water and stirred for 12 h at 343 K in a round-bottom flask under reflux conditions. The purified zeolite was separated by centrifugation, dried at 110ºC in air, crushed and pulverized in a mortar, and the particle size between 200 and 400 μm collected by dry sieving. The powder was stored in a desiccator over saturated NaCl solution in order to maintain constant water content throughout the experiments.

Synthesis of the nanomagnetite zeolite composite

The magnetic zeolite composite (MZC) was prepared through co-precipitation of Fe^{3+} and Fe^{2+} in the presence of zeolite powder. Aqueous ammonia solution (100 mL of 1 M NH_4OH) was placed in a round-bottom flask with three access ports (one for N_2 gas, one for $FeCl_3$ and $FeCl_2$ solution, and one for the stirrer shaft) to which 3.5 g of zeolite powder was added. The mixture was stirred vigorously using a mechanical stirrer and deoxygenated by bubbling N_2 gas (99.99%) for 30 min. Solutions of ferric chloride (1 M $FeCl_3$ in water) and ferrous chloride (2 M $FeCl_2$ in 2 M HCl) with a volume ratio of 4:1 were prepared and mixed together. The Fe^{3+}/Fe^{2+} solution was added drop-wise to the zeolite/ammonia mixture while the mixture was stirred vigorously under N_2 atmosphere. The resulting composite was then separated from solution with the aid of a permanent magnet. Finally, the separated product was washed four times with deionized-deoxygenated water and then dried at 50ºC for 5 h (the product was protected from exposure to the atmosphere by applying a magnetic field under nitrogen atmosphere).

Characterization of the samples

The structural phase identification of samples was examined using a Bruker (Germany) D8 ADVANCE X-ray diffractometer (XRD). The chemical composition of the samples was determined using a PANalytical (The Netherlands) Magix X-ray fluorescence (XRF) spectrometer. The Fourier-transform infrared (FTIR) spectra were obtained using a Shimadzu (Japan) IR Prestige-21 Model spectrophotometer. Thermal analysis was performed using a Mettler (USA) TG-50 thermal analyzer with a heating rate of 10ºC min^{-1}. A vibrating-sample magnetometer (Meghnatis Daghigh Kavir Co., Kashan, Iran) was used to characterize the magnetic properties of the composite (the magnetic field applied was between 0 and 10,000 Oe). The concentration of cesium and strontium ions was determined using an inductively coupled plasma-atomic emission spectroscopy (ICP-AES) technique (GBC integra XL, Australia).

The cation exchange capacity (CEC) of the natural zeolite and the magnetic composites was determined by shaking 1.0 g of the samples with 100 mL of 1 M NH_4NO_3 solution at 25ºC for 72 h. The ammonium concentration was determined by the Kjeldahl method (Archibald and Seligson, 1957). Theoretical cation exchange capacity (TCEC) was calculated from chemical composition of the samples as a sum of exchangeable cations present in 1.0 g of zeolite.

Metal ion-uptake experiments

Adsorption experiments were carried out by stirring 0.2 g of zeolite sample or magnetic composite with 20 mL of 0.01 N Cs^{+} and Sr^{2+} solution at 298 K in a controlled-temperature rotary shaker (Pars Azma Co., Isfahan, Iran). After equilibration, the zeolite samples were separated by centrifugation while the composite was separated using a permanent magnet. The effect of pH on the sorption process was studied by adjusting the initial pH at 3−8 using 0.1 N HNO_3 and 0.1 N NaOH solutions. To study the kinetics, the samples were placed in contact with ion solutions for different periods of time (between 2 and 48 h). All experiments were conducted with 0.01 N ion solutions at 298 K except for temperature-dependence studies where the temperature varied between 298 and 343 K. The ion-exchange isotherms were constructed from the data obtained at different initial concentrations for Cs^{+} and Sr^{2+} (0.001−0.1 N).

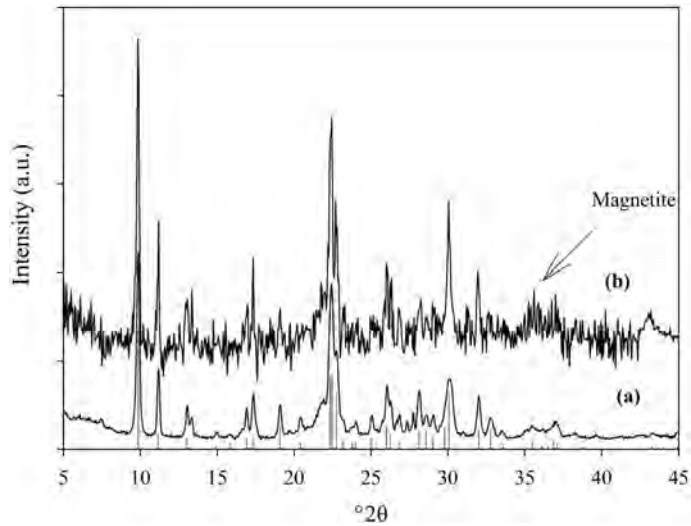

Figure 1. XRD patterns of the natural zeolite (matched with reference pattern of clinoptilolite) (a) and MZC (b).

The amount of ions adsorbed per unit mass of the adsorbent, q (meq g^{-1}), was calculated as:

$$q = (C_i - C_f) \times V/m \quad (1)$$

The distribution coefficient k_d (mL g^{-1}) was also calculated as:

$$k_d = (C_i - C_f)/C_f \times (V/m) \quad (2)$$

where C_i and C_f were the initial and final concentrations (meq mL^{-1}), respectively; m was the amount of the adsorbent (g), and V was the volume of the solution (L).

RESULTS AND DISCUSSION

Characterization of the adsorbents

The XRD patterns of the MZC and natural zeolite (Figure 1) correspond with reference patterns of clinoptilolite (Treacy and Higgins, 2007) demonstrating that clinoptilolite was the prevalent phase in the zeolite-rich rock. The line positions and relative intensities of the composite remained intact, showing that the crystal structure of zeolite was not changed during preparation of the composite. The XRD diffraction line at 35.55°2θ of the composite (Figure 1) corresponded to magnetite (Maity and Agrawal, 2007). Using Scherrer's equation (Klug and Alexander, 1974), the particle size of the nanomagnetite was found to be 24.7 nm

The chemical composition of the composite and natural zeolite (Table1) was obtained using XRF. The composite consisted of 19.86 wt.% Fe_2O_3. The Si/Al ratio of the present zeolite sample was 4.85, which is consistent with previous findings placing the ratio within the range of 4−5.5 (Breck, 1974). The theoretical cation exchange capacity (TCEC) was estimated as the sum of exchangeable ions, including Na^+, K^+, Ca^{2+}, and Mg^{2+}, in the zeolite. The difference between TCEC and CEC (Table 1) was ascribed to the fact that some of the counter-ion sites in the zeolite particles were unavailable for cation exchange.

The FTIR spectrum of the natural zeolite and MZC were recorded over the range 400−4000 cm^{-1} (Figure 2). Zeolites are significantly hydrated materials, and water absorption bands at 1636 cm^{-1} and in the range 3000−3600 cm^{-1} confirmed it. The band at 1070 cm^{-1} was assigned to asymmetric stretching vibration modes of internal T−O bonds in TO_4 tetrahedra (T = Si and Al). The bands at 794 and 465 cm^{-1} arise from the stretching vibration modes of O−T−O groups and the bending vibration modes of T−O bonds, respectively (Bekkum *et al.*, 2001). The

Table 1. Chemical compositions (wt.%) of natural zeolite and the MZC.

Compound	SiO_2	Al_2O_3	Na_2O	TiO_2	K_2O	CaO	MgO	SrO	Fe_2O_3	LOI[a]	Total	Si/Al	TCEC[c]	CEC[c]
Zeolite	67.41	11.82	2.258	0.201	2.143	1.812	0.912	0.128	0.623	12.64	99.95	4.848	1.736	1.561
MZC	53.21	9.280	1.922	0.096	1.482	1.249	0.705	n.d.[b]	19.86	12.01	99.81	4.874	1.335	1.218

[a] Loss on ignition
[b] Not detected
[c] (meq g^{-1})

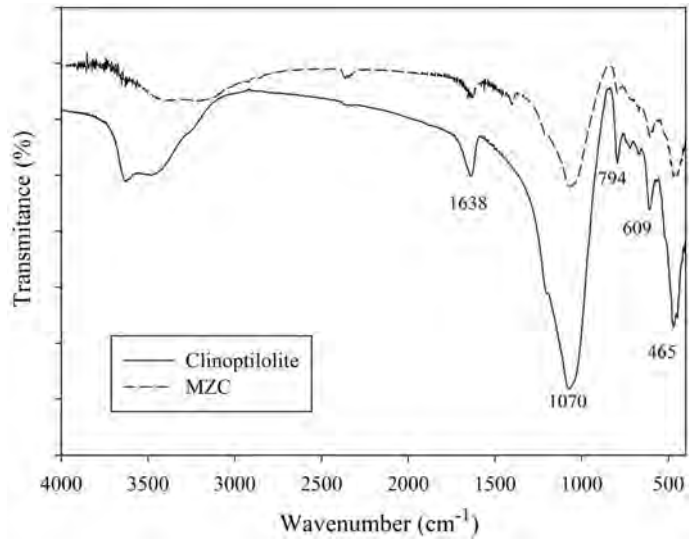

Figure 2. FTIR spectra of clinoptilolite and MZC.

characteristic band related to the Fe−O−Fe bond of Fe oxide must appear at 584 cm^{-1}, but this band was overlapped by the bands assigned to the double-ring stretching mode of zeolite (Maity and Agrawal, 2007).

In the DTG curves of the natural zeolite and composite, two weight-loss peaks were observed at temperatures below 100ºC (Figure 3). These dehydration peaks are attributed to the evaporation of water molecules which are located in different positions in the zeolite structure. At temperatures above 200ºC and up to 800ºC, the samples exhibited no weight-loss peaks, indicating that the samples were thermally stable.

Magnetic properties of the composite

The magnetic curve of the composite with 20% Fe oxide at 298 K (Figure 4) exhibited no hysteresis loop and no remanence which would indicate that the composite had satisfactory superparamagnetic properties. Consequently, the composite did not remain magnetized after exposure to an external magnetic field, and can be redispersed when the magnetic field is removed. The composite confirmed a saturation magnetization of ~17.46 Am^2/kg at 298 K, indicating sufficiently good magnetic property to be attracted by a permanent magnet. Because of the desirable magnetic properties and adsorption capacity, the composite with 20% Fe oxide was selected for adsorption experiments.

Effect of experimental condition on the adsorption process

Effect of pH. The evaluation of the pH effect (Figure 5) indicated that an acidic medium has an inhibitory effect on the uptake process. The lower uptake in acidic media was attributed to the competition by hydronium ions

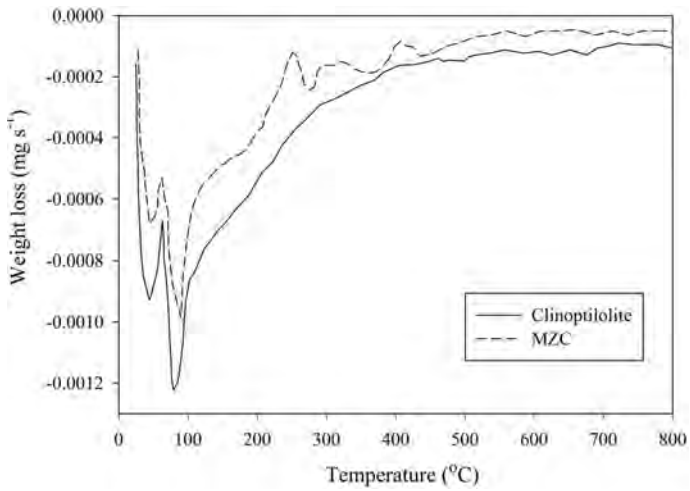

Figure 3. DTG curves of clinoptilolite and MZC.

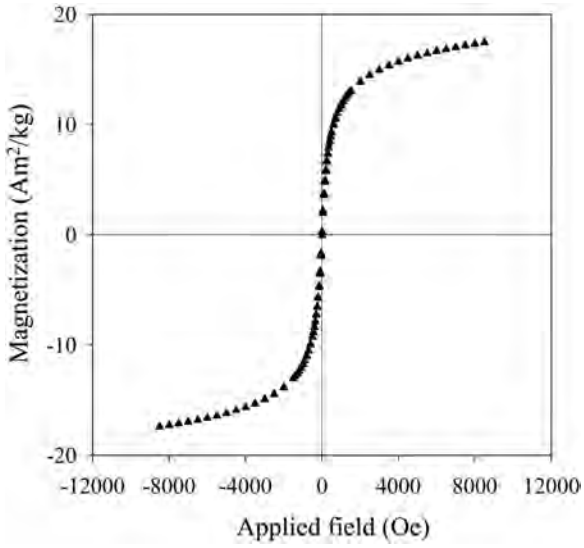

Figure 4. The hysteresis loops of MZC.

with Cs^+ and Sr^{2+} for the exchange sites. In addition, Fe oxide, as a weak acid or a weak base, participated in the cation exchange process according to the following reaction:

$$\text{Fe oxide}-\text{OH} + M^+ \rightarrow \text{Fe oxide}-\text{O}-M + \text{H}^+ \qquad (3)$$

Therefore, the total exchange capacity of the composite consisted of the exchangeability of both the zeolite and Fe oxide.

The concentration of deprotonated surface sites of Fe oxide increased with increasing pH value; therefore, the adsorption capacity of the composite increased with increasing pH and the maximal adsorption was observed at pH 8. In the present study, the pH was adjusted to 8.

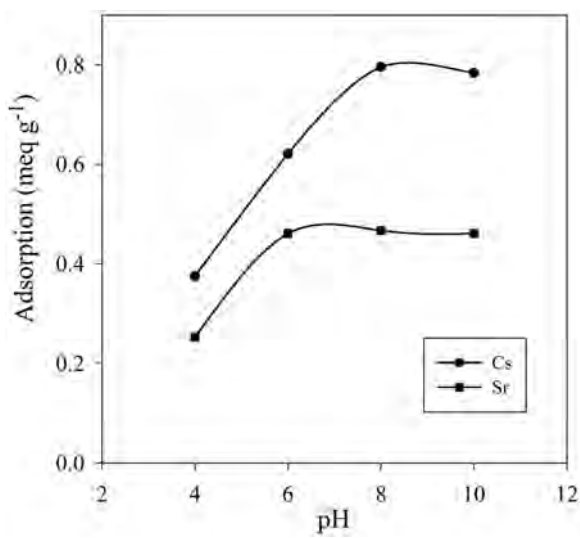

Figure 5. Effect of pH on sorption of Cs^+ and Sr^{2+}.

Effect of contact time. The effect of contact time on the cation adsorption capacity of the composite (Figure 6) was studied. The slope of the curves indicated that the adsorption rate was fast at the outset, but this initial rapid sorption subsequently gave way to a slow approach until equilibrium and saturation were reached after ~24 h. Based on the results collected, 24 h was taken as the equilibrium time in adsorption experiments.

Effect of temperature. The effect of adsorption temperature on removal of Cs^+ and Sr^{2+} (Figure 7) was studied over the temperature range 298−343 K. The adsorption capacity increased with increasing temperature, proving that the sorption process was endothermic. An increase in temperature caused progressive weakening of the ion-dipole forces between the cations and the solvent dipoles (water molecules), reducing the kinetic diameter of the ingoing ions. Therefore, greater numbers of hidden exchange sites within the zeolite framework participated in the sorption process. The data were used to estimate the thermodynamic variables.

Evaluation of thermodynamic variables

In order to identify the thermodynamic nature of the adsorption process, the value of enthalpy change (ΔH°) and entropy change (ΔS°) (Table 2) was calculated from the slopes and the intercepts of the linear plot of the Van't Hoff equation (Figure 8).

$$\ln k_d = -(\Delta H^\circ/\text{R}T) + (\Delta S^\circ/\text{R}) \qquad (4)$$

where k_d is the distribution coefficient, R is the universal gas constant (8.314 J mol^{-1} K^{-1}), and T is the absolute temperature (K). The change in Gibbs free energy of the adsorption (ΔG°) was then calculated from:

$$\Delta G^\circ = \Delta H^\circ - T\Delta S^\circ \qquad (5)$$

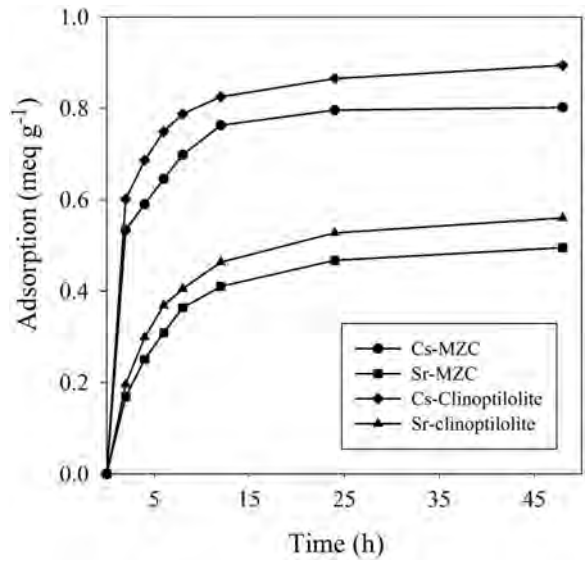

Figure 6. Effect of contact time on adsorption of Cs^+ and Sr^{2+} onto clinoptilolite and MZC.

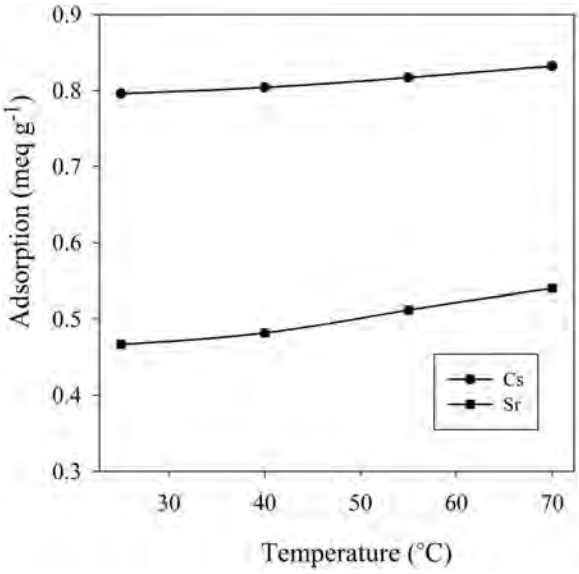

Figure 7. Effect of temperature on Cs^+ and Sr^{2+} adsorption.

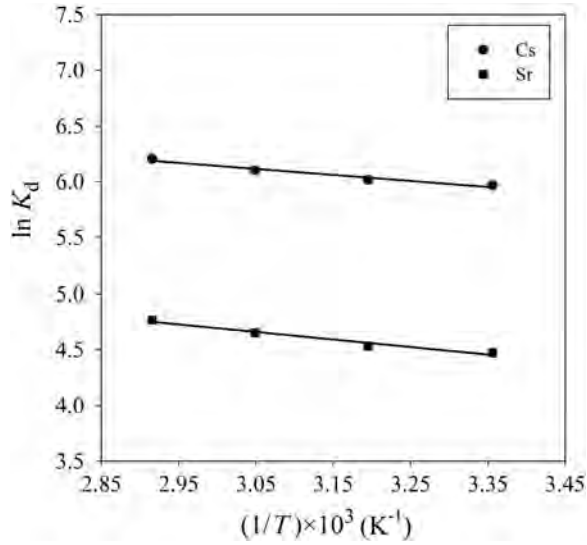

Figure 8. Van't Hoff plot for adsorption of Cs^+ and Sr^{2+}.

The adsorption process was endothermic because the ΔH° values were positive. The positive values of ΔS° showed that the randomness of the system was increased during the sorption process. The ΔG° values were negative, indicating that an adsorption process occurred spontaneously. Also, for both ions, ΔG° became more negative with increasing temperature, suggesting the favorable nature of sorption at higher temperature. Similar results have been found for Sr and Ba removal by dolomite (Ghaemi *et al.*, 2011) and Zr removal by clinoptilolite (Faghihian and Kabiri-Tadi, 2010). Greater absolute values of ΔG° for Cs^+ indicated that its adsorption is more favored than that of Sr^{2+}.

Kinetics study

Both pseudo-first order and pseudo-second order kinetics models were used to estimate the kinetics parameters. The conformity between experimental data and kinetics models was expressed by the correlation coefficients (R). Also, the values of calculated q_e were compared with the experimental data.

The linear forms of the pseudo-first order model of Lagergren and pseudo-second order model are, respectively:

$$\ln (q_e - q_t) = \ln q_e - k_1 t \quad (6)$$

$$t/q_t = 1/(k_2 q_e^2) + (1/q_e)t \quad (7)$$

and the initial sorption rate, h (mmol g^{-1} min^{-1}), was obtained from:

$$h = k_2 q_e^2 \quad (8)$$

where q_e and q_t are the amount of ions adsorbed per unit mass of composite at equilibrium and at any time, t (mmol g^{-1}), respectively. k_1 and k_2 are the rate constants of the pseudo-first order (min^{-1}) and pseudo-second order (g mg^{-1} min^{-1}) models (Table 3). The value of the correlation coefficients (R^2) and agreement of calculated q_e with experimental data indicated that the sorption process can be described well by the pseudo-second order equation. Therefore, the overall rate constant of both sorption processes appears to be controlled by chemical sorption (McKay and Ho, 1999; Karadag *et al.*, 2007).

For comparison, experimental data from natural clinoptilolite were also fitted to pseudo-first and -second order models (Table 3). The rate constant for the composite was greater than that for zeolite, which was attributed to the nanosize and large surface area of the magnetite on the surface of zeolite contributing to

Table 2. Thermodynamic variables calculated for the sorption of Cs^+ and Sr^{2+} onto MZC.

Ion	E_a (kJ mol^{-1})	ΔH° (kJ mol^{-1})	ΔS° (kJ mol^{-1})	ΔG° (kJ mol^{-1})			
				298K	313K	328K	343K
Cs^+	3.633	4.496	0.0645	−14.725	−15.692	−16.660	−17.627
Sr^{2+}	4.319	5.616	0.0559	−11.042	−11.880	−12.719	−13.558

Table 3. Kinetics of Cs^+ and Sr^{2+} adsorption onto MZC.

Sorbent	Ion	$q_{e(exp.)}(\times 10^{-1})$ (mmol g^{-1})	pseudo-first order model			pseudo-second order model			
			$k_1(\times 10^{-2})$ (min^{-1})	$q_{e(theor.)}(\times 10^{-1})$ (mmol g^{-1})	R^2	$k_2(\times 10^{-1})$ (g $mmol^{-1}$ min^{-1})	$q_e(\times 10^{-1})$ (mmol g^{-1})	$h(\times 10^{-2})$ (mmol g^{-1} min^{-1})	R^2
Zeolite	Cs^+	8.940	0.169	2.867	0.9534	0.1418	9.163	1.1902	0.9999
	Sr^{2+}	2.800	0.177	1.942	0.9856	0.1373	3.043	0.1272	0.9999
MZC	Cs^+	8.020	0.297	4.092	0.9930	0.1497	8.277	1.0256	0.9996
	Sr^{2+}	2.470	0.186	1.809	0.9864	0.1453	2.702	0.1069	0.9995

sorption process. The k_2 values were selected for evaluation of E_a using the Arrhenius equation (Figure 9).

$$\ln k_2 = \ln A - E_a/RT \quad (9)$$

where k_2 and A are the rate constant and temperature independent factor (g $mmol^{-1}$ min^{-1}), respectively; E_a is the activation energy of the sorption (J mol^{-1}). The values of E_a were calculated from the slope of ln k_2 *vs.* $1/T$ (Table 2). The values of E_a were <42.0 J mol^{-1}, suggesting that adsorption of Cs^+ and Sr^{2+} proceeded with a low potential energy (Scheckel and Sparks, 2001).

Sorption isotherm study

The effect of ion concentrations on the uptake behavior of the magnetic composite was investigated in the concentration range 0.001−0.1 meq mL^{-1}. The relationship between the amount of ions adsorbed per unit mass of the composite, and the concentration of the ions remaining in solution at equilibrium represented the sorption isotherm (Figure 10a,b). Three isotherm models (Langmuir, Freundlich, and D-R) were used to evaluate the experimental data.

Langmuir isotherm model

The Langmuir isotherm assumes that the sorption occurs at specific homogeneous sites within the adsorbent. The linearized form of this model is given by:

$$C_e/q_e = 1/(Q_0 b) + C_e/Q_0 \quad (10)$$

where Q_0 is the monolayer saturation adsorption capacity (mg g^{-1}) and b is the constant related to the enthalpy of adsorption, which were calculated from the slope and the intercept of equation 10 (Figure 11). The Langmuir model can be used to estimate the maximum adsorption capacity corresponding to complete monolayer coverage of the adsorbent. The values of Q_0

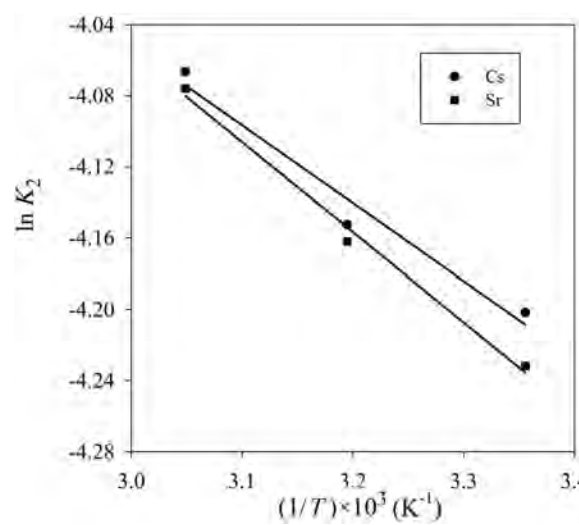

Figure 9. Arrhenius plot for adsorption of Cs^+ and Sr^{2+}.

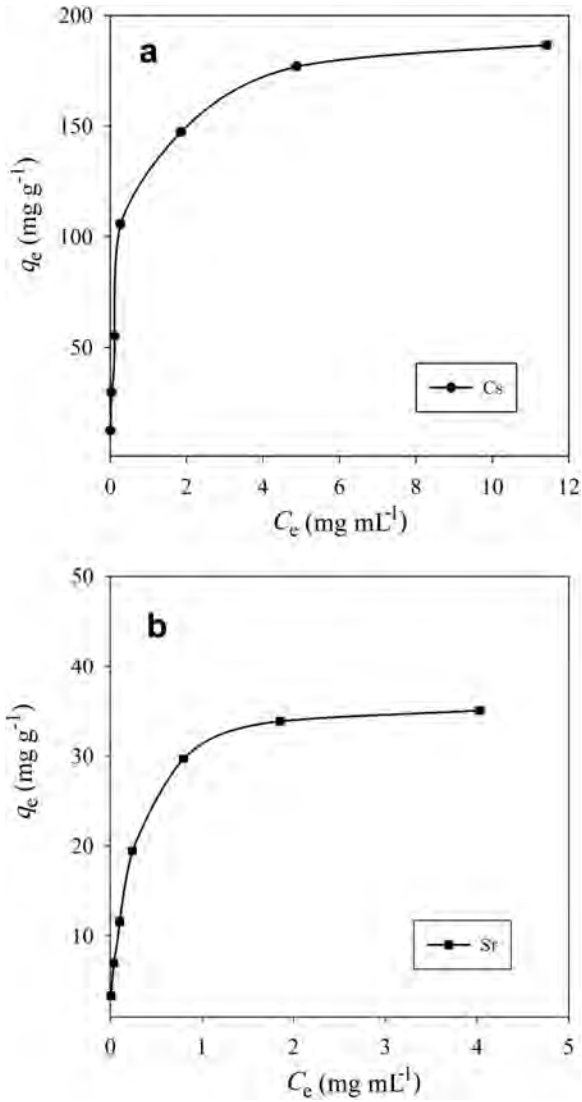

Figure 10. Effect of different initial ion concentrations on sorption of Cs^+ (a) or Sr^{2+} (b).

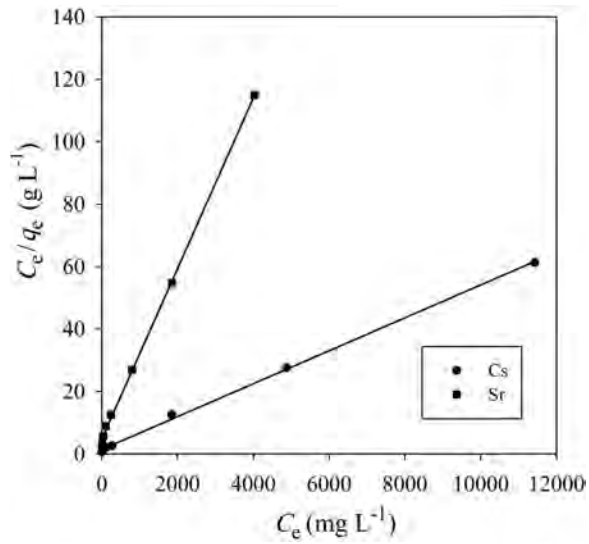

Figure 11. Langmuir isotherm plots for adsorption of Cs^+ and Sr^{2+}.

confirmed the large adsorption capacity of the composite prepared for Cs^+ and Sr^{2+} (Table 4).

The important parameter of the Langmuir isotherm model is the dimensionless constant, R_L, which could be calculated from:

$$R_L = 1/(1 + bC_0) \quad (11)$$

where C_0 is the largest initial ion concentration (mg L^{-1}). The value of R_L gives an indication of whether the process is unfavorable ($R_L > 1$), linear ($R_L = 1$), favorable ($0 < R_L < 1$), or irreversible ($R_L = 0$) (Mohan and Chander, 2006). The data obtained confirmed that adsorption was favorable for Cs^+ and Sr^{2+}.

The maximum adsorption capacities of MZC for the removal of Cs^+ and Sr^{2+} were compared with those of some natural adsorbents reported in the literature (Table 5). The MZC exhibited significant adsorption capacity for these ions. Most importantly, the separation of the magnetic composite from solution was easily achieved using a permanent magnet.

Table 4. Adsorption isotherm parameters for Cs^+ and Sr^{2+} adsorption onto MZC.

		Model parameters			
Isotherm	Ion	q_0 (mg g^{-1})	$b \times 10^3$ (L mg^{-1})	$R_L \times 10^3$	R^2
Langmuir	Cs^+	188.7	3.759	19.62	0.9991
	Sr^+	36.63	5.716	38.40	0.9992
		n	K_f (mg g^{-1})	R^2	
Freundlich	Cs^+	2.705	8.147	0.916	
	Sr^+	2.455	1.604	0.9492	
		$\beta \times 10^{-9}$ (mol^2 kJ^{-2})	q_m (mmol g^{-1})	E (kJ mol^{-1})	R^2
D-R	Cs^+	5.174	1.992	9.831	0.9799
	Sr^{2+}	6.321	1.144	8.894	0.9913

Table 5. Adsorption capacity, q_m, of Cs^+ and Sr^{2+} by various adsorbents.

Adsorbent	q_m (mg g^{-1})		Reference
	Cs^+	Sr^{2+}	
Natural clinoptilolite	132.9	–	(Borai *et al.*, 2009)
Montmorillonite	57.04	13.26	(Ma *et al.*, 2011)
Phosphate-modified montmorillonite	93.87	12.56	(Ma *et al.*, 2011)
Taiwan laterite	39.87	–	(Wang *et al.*, 2008)
Dolomite	–	1.172	(Ghaemi *et al.*, 2011)
Natural zeolite	205.8	41.36	Present study
Magnetic zeolite composite	188.7	36.63	Present study

Freundlich isotherm model

The Freundlich isotherm model assumes that sorption occurs at heterogeneous surfaces on which the adsorption energy changes exponentially with surface coverage. This model was used to estimate the intensity of the adsorption process and relative sorption capacity. The linearized form of the Freundlich model is written as

$$\log q_e = \log K_f + 1/n \log C_e \quad (12)$$

where K_f is the Freundlich constant related to the adsorbent capacity, and n is a constant, indicative of the intensity of the absorption process. The values of the constants n and K_f were calculated from the slope and the intercept of equation 12 (Figure 12). The value of n was >1, illustrating that significant adsorption had taken place even at high ion concentrations. The value for K_f for MZC was greater for Cs^+ than for Sr^{2+}, indicating that the composite had a greater affinity for Cs^+ (Table 4).

D-R isotherm model

The D-R isotherm model distinguishes between the physical and chemical nature of the sorption process. This equation is given as follows:

$$\ln q_e = \ln q_m - \beta\varepsilon^2 \quad (13)$$

where q_m is the maximum adsorption capacity (meq g^{-1}), β is the constant related to the adsorption energy (mol^2 kJ^{-2}), and ε is the Polanyi potential:

$$\varepsilon = RT \ln (1 + 1/C_e) \quad (14)$$

where R is the gas constant (8.314 kJ mol^{-1} K^{-1}) and T is absolute temperature (K). The experimental data were fitted to this isotherm model (Figure 13). The mean internal energy of adsorption, E (kJ mol^{-1}), is defined as the change in internal energy when 1 mole of ions is transferred to the surface of the composite from infinity of the solution, and is calculated from:

$$E = (2\beta)^{-1/2} \quad (15)$$

The E value in the range 8–16 kJ mol^{-1} indicates that the sorption process is achieved *via* exchange.

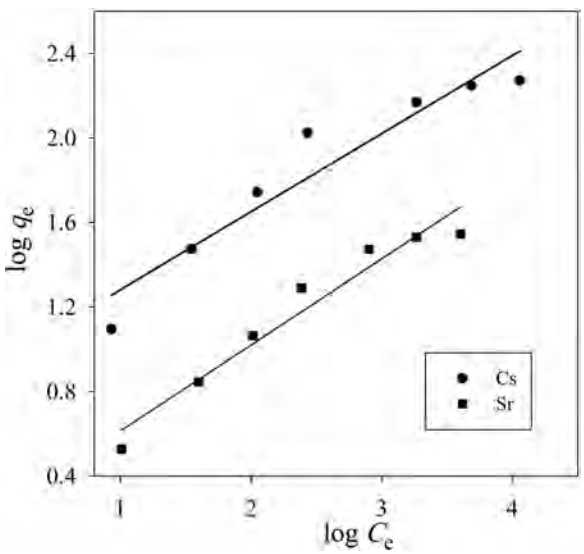

Figure 12. Freundlich isotherm plots for adsorption of Cs^+ and Sr^{2+}.

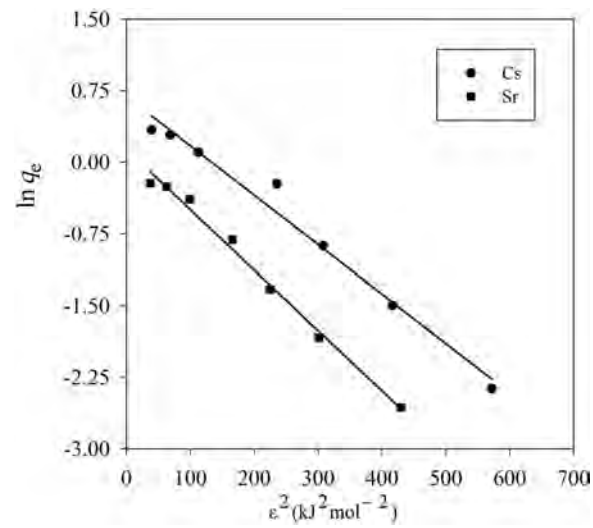

Figure 13. D-R isotherm plots for adsorption of Cs^+ and Sr^{2+}.

Physical force is involved in the sorption process if E<8 kJ mol^{-1} (Helfferich, 1962). The E values obtained for adsorption of Cs^+ and Sr^{2+} were in the range 8−16 kJ mol^{-1}, indicating that both ions were taken up *via* an ion-exchange, or chemical adsorption, process (Table 4).

CONCLUSIONS

In the present study, a natural zeolite nanomagnetite composite was synthesized, characterized, and evaluated for removal of Cs^+ and Sr^{2+} from aqueous solutions. The crystal structure of zeolite was not changed during the magnetic modification. The VSM results confirmed that the composite was sufficiently magnetic to be attracted by a magnetic field. A pseudo-second order model gave better correlation with the experimental kinetics data than pseudo-first order, confirming that chemical sorption was the dominant process. The rate-constant values for sorption by MZC were greater than the values obtained for natural zeolite, indicating a faster rate of adsorption by the composite. The negative ΔG° value and positive ΔH° value indicated that the adsorption of both ions was spontaneous and endothermic. The R_L values obtained were in the range 0−1, indicating that adsorption of Cs^+ and Sr^{2+} were favored. The composite demonstrated large CEC capacity and fast adsorption kinetics for Cs^+ and Sr^{2+}, as well as good magnetic behavior, making it easy to separate from the aqueous solution.

ACKNOWLEDGMENTS

Financial support of this work by the Center of Excellence of Chemistry and Research Council of the University of Isfahan is gratefully appreciated.

REFERENCES

Abdel Rahman, R.O., Ibrahim, H.A., Hanafy, M., and Abdel Monem, N.M. (2010) Assessment of synthetic zeolite Na A−X as sorbing barrier for strontium in a radioactive disposal facility. *Chemical Engineering Journal*, **157**, 100−112.

Archibald, R.M. and Seligson, D. (1957) *Standard Methods of Clinical Chemistry*. Academic Press, New York.

Ashtari, P., Wang, K., Yang, X., Huang, S., and Yamini, Y. (2005) Novel separation and preconcentration of trace amounts of copper (II) in water samples based on neocuproine modified magnetic microparticles. *Analytica Chimica Acta*, **550**, 18−23.

Bachir, C., Lan, Y., Mereacre, V., Powell, A.K., Bender Koch, C., and Weidler, P.G. (2009) Magnetic titanium-pillared clay (Ti-M-PILC): Magnetic studies and Mössbauer spectroscopy. *Clays and Clay Minerals*, **57**, 433−443.

Balarama Krishna, M.V., Rao, S.V., Arunachalam, J., Murali, M.S., Kumar, S., and Manchanda, V.K. (2004) Removal of ^{137}Cs and ^{90}Sr from actual low level radioactive waste solutions using moss as a phyto-sorbent. *Separation and Purification Technology*, **38**, 149−161.

Bekkum, H.V., Flanigen, E.M., and Janson, J.C. (2001) *Introduction to Zeolite Science and Practice*. Elsevier, Amsterdam.

Borai, E.H., Harjula, R., Malinen, L., and Paajanen, A. (2009) Efficient removal of cesium from low-level radioactive liquid waste using natural and impregnated zeolite minerals. *Journal of Hazardous Materials*, **172**, 416−422.

Bourlinos, A.B., Zboril, R., and Petridis, D. (2003) A simple route towards magnetically modified zeolites. *Microporous and Mesoporous Materials*, **58**, 155−162.

Breck, D.W. (1974) *Zeolite Molecular Sieves, Structure, Chemistry and Uses.* Wiley, New York.

El-Naggar, M.R., El-Kamash, A.M., El-Dessouky, M.I., and Ghonaim, A.K. (2008) Two-step method for preparation of NaA-X zeolite blend from fly ash for removal of cesium ions. *Journal of Hazardous Materials*, **154**, 963−972.

Faghihian, H. and Kabiri-Tadi, M. (2010) Removal of zirconium from aqueous solution by modified clinoptilolite. *Journal of Hazardous Materials*, **178**, 66−73.

Ghaemi, A., Torab-Mostaedi, M., and Ghannadi-Maragheh, M. (2011) Characterizations of strontium(II) and barium(II) adsorption from aqueous solutions using dolomite powder. *Journal of Hazardous Materials*, **190**, 916−921.

Gutierrez, M., Escudey, M., Escrig, J., Denardin, J., Altbir, D., Fabris, J., Cavalcante, L., and García-González, M.T. (2010) Preparation and characterization of magnetic composites based on a natural zeolite. *Clays and Clay Minerals*, **58**, 585−595.

Helfferich, F. (1962) *Ion exchange.* McGraw Hill, New York.

Kabiri-Tadi, M. and Faghihian, H. (2011) Removal of ruthenium from aqueous solution by clinoptilolite. *Clays and Clay Minerals*, **59**, 34−41.

Karadag, D., Koc, Y., Turan, M., and Ozturk, M. (2007) A comparative study of linear and non-linear regression analysis for ammonium exchange by clinoptilolite zeolite. *Journal of Hazardous Materials*, **144**, 432−437.

Klug, H.P. and Alexander, L.E. (1974) *X-ray Diffraction Procedures: for Polycrystalline and Amorphous Materials.* John Wiley & Sons, New York.

Ma, B., Oh, S., Shin, W.S., and Choi, S.J. (2011) Removal of Co^{2+}, Sr^{2+} and Cs^+ from aqueous solution by phosphate-modified montmorillonite (PMM). *Desalination*, **276**, 336−346.

Maity, D. and Agrawal, D.C. (2007) Synthesis of iron oxide nanoparticles under oxidizing environment and their stabilization in aqueous and non-aqueous media. *Journal of Magnetism and Magnetic Materials*, **308**, 46−55.

McKay, G. and Ho, Y.S. (1999) Pseudo-second order model for sorption processes. *Process Biochemistry*, **34**, 451−460.

Mohan, D. and Chander, S. (2006) Single, binary and multi-component sorption of iron and manganese on lignite. *Journal of Colloid and Interface Science*, **299**, 57−76.

Nah, I.W., Hwang, K.Y., Jeon, C., and Choi, H.B. (2006) Removal of Pb ion from water by magnetically modified zeolite. *Minerals Engineering*, **19**, 1452−1455.

Oliveira, L.C.A., Petkowicz, D.I., Smaninotto, A., and Pergher, S.B.C. (2004) Magnetic zeolites: a new adsorbent for removal of metallic contaminants from water. *Water Research*, **38**, 3699−3704.

Shakir, K., Sohsah M., and Soliman, M. (2007) Removal of cesium from aqueous solutions and radioactive waste simulants by coprecipitate flotation. *Separation and Purification Technology*, **54**, 373−381.

Scheckel, K.G. and Sparks, D.L. (2001) Temperature effects on nickel sorption kinetics at mineral water interface. *Soil Science Society of America Journal*, **65**, 719−728.

Treacy, M.M.J. and Higgins, J.B. (2007) *Collection of Simulated XRD Powder Patterns for Zeolites.* Elsevier, Amsterdam.

Wang, T.H., Li, M.H., Yeh, W.C., Wei, Y.Y., and Teng, S.P. (2008) Removal of cesium ions from aqueous solution by adsorption onto local Taiwan laterite. *Journal of Hazardous*

Materials, **160**, 638–642.

Wu, P., Daia, Y., Long, H., Zhu, N., Li, P., Wu, J., and Dang, Z. (2012) Characterization of organo-montmorillonites and comparison for Sr(II) removal: equilibrium and kinetic studies. *Chemical Engineering Journal*, **191**, 288–296.

Zhang, C., Gu, P., Zhao, J., Zhang, D., and Deng, Y. (2009) Research on the treatment of liquid waste containing cesium by an adsorption–microfiltration process with potassium zinc hexacyanoferrate. *Journal of Hazardous Materials*, **167**, 1057–1062.

(*Received 6 December 2012; revised 26 March 2013; Ms. 733; AE: S.M. Kuznicki*)

Clays and Clay Minerals, Vol. 61, No. 3, 204–217, 2013.

CLAY MINERALOGY, OXYGEN ISOTOPE GEOCHEMISTRY, AND WATER/ROCK RATIO ESTIMATES, TE MIHI AREA, WAIRAKEI GEOTHERMAL FIELD, NEW ZEALAND

RYAN B. LIBBEY[1,*,†], FRED J. LONGSTAFFE[1], AND ROBERTA L. FLEMMING[1]

[1] The University of Western Ontario, Department of Earth Sciences, Biology and Geological Sciences Bldg., London, Ontario, Canada, N6A 5B7

Abstract—Dioctahedral clays from an active continental geothermal system have been studied to assess their usefulness as proxies of paleo-hydrological and thermal conditions in the subsurface. Drill cuttings from Well WK244 in the Te Mihi area of the Wairakei Geothermal Field, New Zealand, were analyzed to determine the mineralogical, morphological, and isotopic characteristics of hydrothermal clays in these samples. Mixed-layer illite-dioctahedral smectite (I-S) and R0 chlorite-trioctahedral smectite are the main clay minerals, with I-S clays varying downward from R1 to R3 ordering and 50 to >90% illite over 160 m. The proportion of illite in I-S correlates positively with downhole temperature (r = 0.98) and I-S morphology changes from high aspect ratio ribbons, laths, and hairy fibers to pseudo-hexagonal plates with depth. Swelling clay percentages determined using the methylene blue method show a strong positive correlation with %S in I-S (r = 0.91), validating use of methylene blue as a rapid field tool for characterizing the smectite to illite transition in this active geothermal environment. The oxygen isotopic composition of I-S ($\delta^{18}O_{I\text{-}S}$) decreases systematically with depth, and mostly reflects a progressive increase in subsurface temperature during clay formation. Estimates of water/rock ratios calculated using $\delta^{18}O_{I\text{-}S}$ values display stratigraphic variability that corresponds to variations in permeability. Oxygen isotopic measurements of I-S are a useful tool for understanding reservoir and permeability evolution in such geothermal systems and their related fossil analogs.

Key Words—Clay Minerals, Hydrothermal, Geothermal, Illite-smectite, Methylene Blue, pXRD, New Zealand, Oxygen Isotopes, SEM, Taupo Volcanic Zone, Wairakei, Water/Rock Ratio.

INTRODUCTION

The transition from smectite to illite through mixed-layer illite-smectite (I-S) clays is well documented in upper crustal environments that have been affected by hydrothermal alteration, low-grade metamorphism, burial diagenesis, and contact metamorphism (Inoue *et al.*, 2005). Variables affecting the development of this clay transitional series are time, temperature, fluid chemistry (including availability of K), and water/rock ratios (Hower *et al.*, 1976; Nadeau and Reynolds, 1981; Whitney, 1990; Altaner and Ylagan, 1997). The compositional dependence of I-S clays on these variables permits their use as tools for physicochemical evaluation in a variety of geologic environments.

Several studies have described the isotopic systematics of structural oxygen in smectite, illite, and I-S in diagenetic and pedogenic environments (*e.g.* Savin and Epstein, 1970; Yeh and Eslinger, 1986; Longstaffe and Ayalon, 1991; Ryan *et al.*, 1998; Vitali *et al.*, 2002) and during laboratory experiments (James and Baker, 1976; Savin and Lee, 1988; Bechtel and Hoernes, 1990). Fewer studies have examined active geothermal environments (*e.g.* Ohaki-Broadlands – Eslinger and Savin, 1973; Kakkonda – Inoue *et al.*, 2004). The present study adapted methods described in the aforementioned studies to examine the oxygen isotope systematics of the Te Mihi area of the Wairakei geothermal field, and suggests how such data can be used to characterize the properties and evolution of such geothermal resources.

Geologic setting

The Taupo Volcanic Zone (TVZ) is a 200 km long, 30–50 km wide, SSW–NNE trending area of active rifting within the North Island of New Zealand, with NW–SE extension rates (7–16 mm y^{-1}) increasing northward toward the Bay of Plenty (Cole, 1990; Harrison and White, 2006). This extension is a continental expression of the Tonga–Kermadec oceanic backarc spreading center, resulting from the westward subduction of the Pacific Plate. As a result, the North Island of New Zealand has experienced rhyolitic volcanism for ~12 million years, with active andesitic and rhyolitic volcanism now confined to the TVZ (Stratford and Stern, 2006).

The Wairakei geothermal field, which is situated ~8 km northeast of Taupo in the southerly region of the TVZ, was globally the first liquid-dominated geothermal resource to be exploited for electricity generation. The

* E-mail address of corresponding author:
ryan.libbey@mail.mcgill.ca
† Present address: McGill University, Department of Earth & Planetary Sciences, Frank Dawson Adams Bldg., 3450 University Street, Montreal, Quebec, Canada, H3A 2A7
DOI: 10.1346/CCMN.2013.0610304

subsurface geology at Wairakei comprises ~2.5 km of Pliocene–Pleistocene volcaniclastic, volcanic, and lacustrine deposits resting on a downfaulted block of Jurassic greywacke (Rosenberg *et al.*, 2009).

The Te Mihi area constitutes the westernmost division of the Wairakei geothermal field (Figure 1). This area is interpreted as a major zone of convective upflow, as indicated by discharge fluids containing some of the highest gas contents, temperatures, and chloride contents within the Wairakei field (Harvey and Browne, 1991). Samples for this study were obtained from production Well WK244, which was drilled to a depth of 1100 mRF (meters below rig floor), with no cuttings returned below 811 mRF. Downhole lithologies intersected by Well WK244 are identical to those intersected by WK245 (see cross-section in Rosenberg *et al.*, 2009) and have been described by Rosenberg *et al.* (2009) and the Institute of Geological and Nuclear Sciences (pers. comm.). In ascending stratigraphic order, these lithologies include: the Karapiti IIb (rhyolite lava); Waiora W_{3-4} (tuffaceous sandstone, mudstone); Waiora W_5 (ignimbrite, tuff); Rautehuia Breccia (muddy lithic volcaniclastic breccia); Huka Falls Formation (HFF, tuffaceous lacustrine sediments); Oruanui Formation (ignimbrite); and post-26 ka surficial deposits (unaltered coarse tuff). The Rautehuia Breccia is considered a basal sub-unit of the Huka Falls Formation (Rosenberg *et al.*, 2009). Significant circulation losses during drilling of Well WK244 indicate the presence of highly permeable zones within the Waiora and Karapiti IIb units (Rosenberg *et al.*, 2009; GNS, pers. comm.).

ANALYTICAL METHODS

Clay fraction

Nineteen samples of drill cuttings were crushed to <~2 mm and dispersed ultrasonically in distilled water. The <~10 μm supernatant of dispersed samples was transferred to 30 cm high, 1000 mL glass columns and the <2 μm fraction separated using settling times determined by Stokes Law. Each sample underwent resuspension and collection of the <2 μm fraction four times. 50 mL of 6% sodium hypochlorite was added to glass beakers containing the <2 μm fractions to assist with flocculation and to oxidize organic matter. The samples were then placed in a water bath overnight at ~60ºC and subsequently washed with distilled water *via* centrifugation. Separate aliquots of each Na-saturated <2 μm fraction then underwent Ca and K saturation, followed by additional washing with distilled water. All

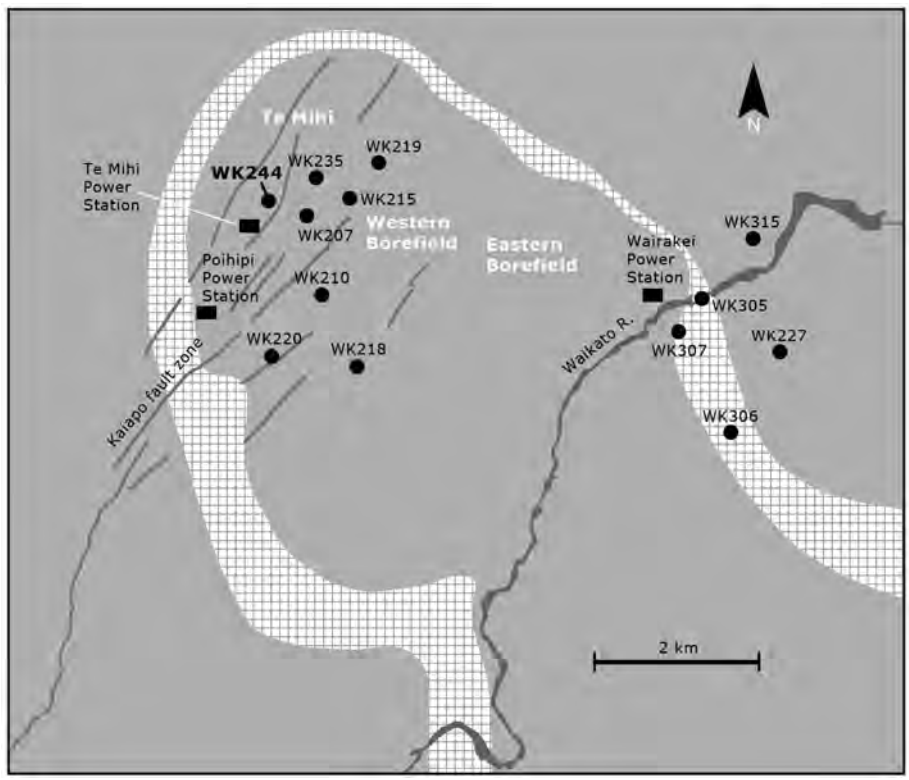

Figure 1. Map of the Wairakei geothermal field showing selected wells (circles) and deviation path of WK244, power-plant locations (rectangles), dominant faults in the Te Mihi area (gray lines), the Waikato River, and the resistivity boundary of the geothermal system (cross-hatched) (modified after Rosenberg *et al.* (2009) and Bixley *et al.* (2009)).

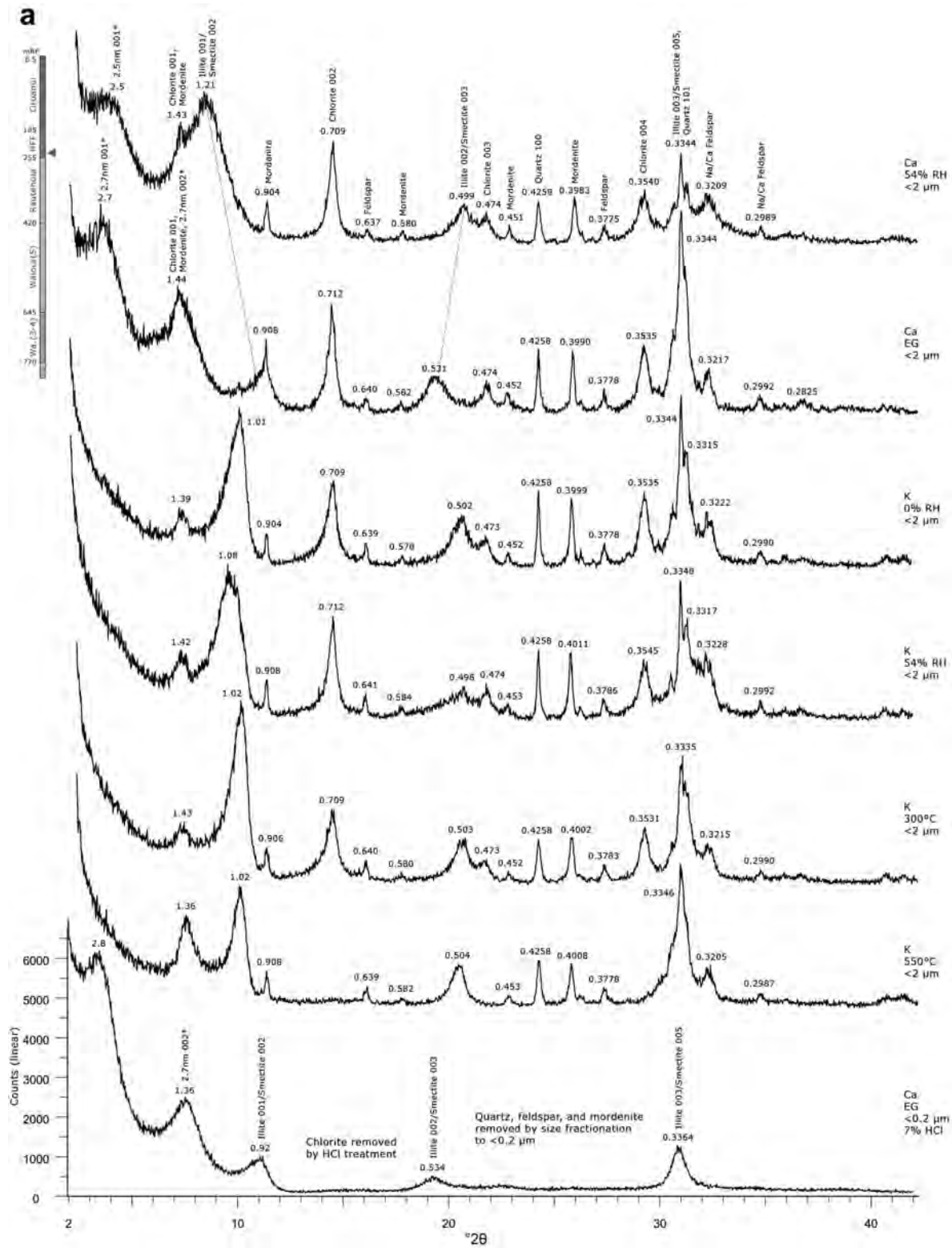

Figure 2. Representative pXRD patterns for oriented clay-size fractions of drill cuttings from (a) 245 mRF and (b [*facing page*]) 710 mRF in WK244. Size fractions, cation saturation, and treatment (ethylene glycol (EG), humidity, heating, acid) are indicated adjacent to each XRD pattern. All scans were corrected to the quartz 100 peak (0.4258 nm) except <1/<0.2 µm fractionations where no quartz was present. Stratigraphic columns showing sample locations (arrows) are provided to the top left of the diagram.

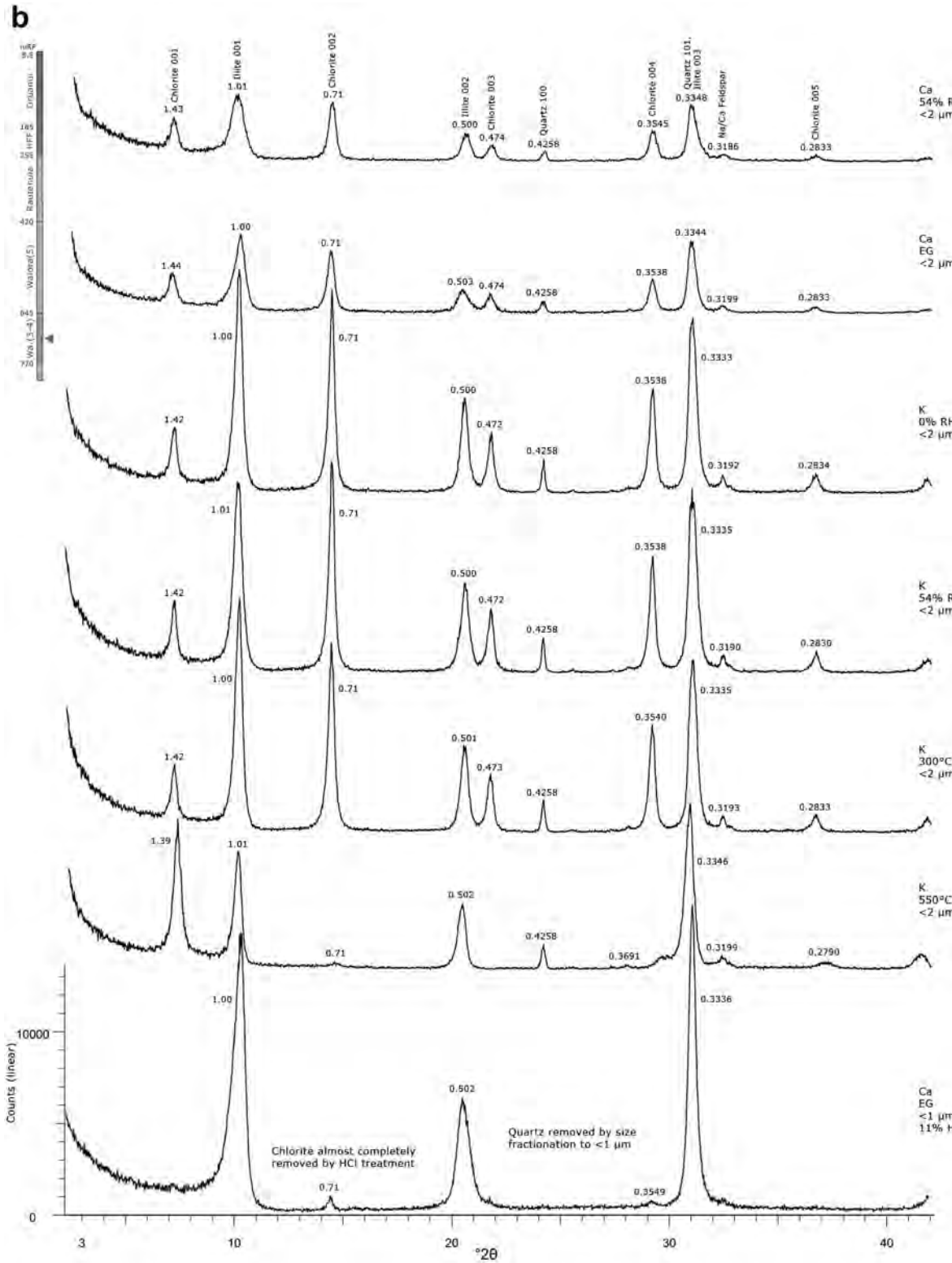
b
Chlorite 001
Illite 001
Chlorite 002
Illite 002
Chlorite 003
Quartz 100
Chlorite 004
Quartz 101, Illite 003
Na/Ca Feldspar
Chlorite 005
Ca 54% RH <2 µm
Ca EG <2 µm
K 0% RH <2 µm
K 54% RH <2 µm
K 300°C <2 µm
K 550°C <2 µm
Ca EG <1 µm 11% HC
Chlorite almost completely removed by HCl treatment
Quartz removed by size fractionation to <1 µm
Counts (linear)
°2θ

aliquots were then freeze dried. Ceramic tile mounts (~30 mg) of the freeze-dried Ca- and K-saturated samples were prepared using suction to obtain a preferred basal orientation of the clay minerals for powder X-ray diffraction (pXRD).

While some <2 μm size fractions consisted almost entirely of clay minerals, others also contained non-phyllosilicates. To remove non-phyllosilicates, finer size fractionations (<1, <0.5, and/or <0.2 μm, as required) were obtained by centrifugation of the <2 μm fraction, following Jackson (1969). Glass slides of these size fractionations were prepared using the pipette method for examination by pXRD. Once a separated fraction consisting of only clay minerals was obtained, heated HCl (7% or, if required, 11%) was used to reduce or eliminate the presence of chloritic clays, as described by Ayalon and Longstaffe (1990). This acidification does not affect the isotopic composition of the remaining silicate mineral residues (Longstaffe, 1986). Pure I-S and/or illite samples were obtained by the end of this process (Figure 2).

XRD and SEM

The ceramic and glass mounts of the clay samples were analyzed at the Laboratory for Stable Isotope Science (The University of Western Ontario) using a high-brilliance Rigaku Rotaflex RU-200B series diffractometer, equipped with a rotating anode (CoKα source operated at 160 mA and 45 kV) and a graphite monochromator. Scans were performed at 2º2θ/min with a step size of 0.02º2θ. K-saturated samples were analyzed at 0% and 54% relative humidity, and additionally after heating at 300 and 550ºC (for 3 h and 2 h, respectively). Ca-saturated samples were analyzed at 54% relative humidity and after glycolation. A randomly oriented front-pack mount of each Ca-saturated sample was also prepared and analyzed from 58 to 78º2θ at 5º2θ/min to determine 060 band positions. Calculated XRD data of Moore and Reynolds (1997), adapted for CoKα radiation, were utilized to determine phase proportions and ordering of mixed-layer clays (illite-smectite and chlorite-smectite); *NEWMOD*© software (Reynolds, 1985) was used to confirm these determinations. The % illite (%I) values were considered to be accurate within ±5%.

The non-clay mineralogy was determined for unfractionated, powdered rock material at the Wairakei Research Centre, New Zealand, using randomly oriented front packs and a Philips X'Pert X-ray diffractometer equipped with CoKα radiation. Each sample was scanned from 2 to 80º2θ at 1.2º2θ/min, with a total step count of 3900. Scans were interpreted using Bruker *DiffracPlus*™ *EVA* evaluation software at the University of Western Ontario.

To identify phases present in small amounts, μXRD analysis of individual grains was performed using a Bruker™ D8 Discover diffractometer, equipped with a CuKα source (40 kV, 40mA), theta-theta geometry, Gobel mirror parallel optics system, and a general area detector diffraction system. Samples were mounted on an XYZ stage oriented to target predetermined points (with an accuracy of 12.5 μm; Flemming, 2007). Crystal morphologies and mineral-mineral relationships for samples from each depth interval were examined using an Hitachi S-4500 field emission SEM with a Quartz XOne EDS system at Surface Science Western, The University of Western Ontario, and a JEOL JSM-7400F high-resolution field emission SEM at the Laboratory for the Study of Calcified Tissues and Biomaterials, at the Université de Montréal.

Oxygen isotope analysis

The oxygen isotopic compositions of illite-smectite and illite ($\delta^{18}O_{I\text{-}S}$) were analyzed at the Laboratory for Stable Isotope Science, The University of Western Ontario, Canada. About 8 mg of each sample was placed in spring-loaded sample holders, and heated while pumping under vacuum overnight at 150ºC to remove sorbed and interlayer water. The samples were then loaded into Ni-reaction vessels under dry nitrogen, and heated while pumping under vacuum at 150ºC for an additional 3 h to eliminate any remaining non-hydroxyl water from the system. Structural oxygen was then liberated using chlorine trifluoride; this oxygen was then reacted with incandescent carbon to produce carbon dioxide gas, following Clayton and Mayeda (1963), as modified by Borthwick and Harmon (1982). Isotopic measurements were conducted using a Prism II, dual-inlet, triple-collecting stable isotope ratio mass-spectrometer. The results are reported in δ-notation relative to Vienna Standard Mean Ocean Water (VSMOW). Analyses of NBS-30 (n = 6) and KGa-1 (n = 3) produced $\delta^{18}O$ values of +5.1±0.1‰ and +21.5±0.1‰, respectively, which compares well with their accepted values of +5.1‰ and +21.5‰, respectively. Duplicate analyses of samples (n = 10) were reproducible to better than ±0.2‰. No significant difference was observed in $\delta^{18}O$ values between samples that underwent treatment with sodium hypochlorite and those that did not (n = 7).

Bulk-rock swelling clay percentages

Methylene blue (MeB) is an organic dye that is preferentially incorporated into the interlayer sites of smectitic clays, and can be used for rapid, semi-quantitative determination of the smectitic component of a crushed rock sample. The method set out by Harvey *et al.* (2000) for active geothermal environments was utilized in this study as follows. Dry-crushed samples were fractionated through a <3 Ø (0.125 mm) sieve. 1 g of the recovered material was added to a well stirred and warmed (~50ºC) 10 mL solution of 1% H_2SO_4. A 3.74 g/L MeB solution was then titrated into the sample in 1 mL aliquots until all expandable clay interlayers were saturated. Interlayer saturation was tested by pressing a

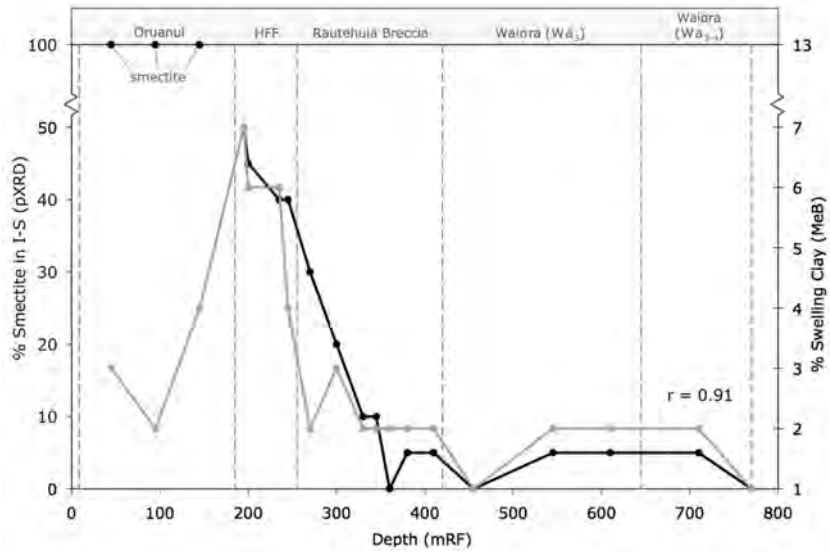

Figure 3. Smectite proportions in I-S and occurrence of end-member smectite and illite (black data series; primary Y axis) as determined by powder XRD analyses and bulk rock %swelling clay estimates (gray data series; secondary Y axis) as determined by MeB methods. The two data series (exclusive of samples from the Oruanui Formation) exhibit a strong positive correlation (r = 0.91).

drop of the solution onto filter paper after the addition of each MeB aliquot. Once sample saturation is achieved, excess MeB in solution creates a diagnostic blue halo about the spot where the solution droplet touched the filter paper. All samples were analyzed in duplicate.

RESULTS AND DISCUSSION

Clay and zeolite mineralogy

The pXRD analysis of the <2 μm size fraction indicates progressive illitization with increasing depth (Figure 3). Smectite is present in all samples from the Oruanui Formation (<185 mRF). The I-S transition occurs between 195 and 360 mRF within the Huka Falls Formation and the Rautehuia Breccia. This I-S transition is similar to that observed in the nearby Wairakei Well WK207, where it occurs between 146 and 297 mRF (Harvey and Browne, 1991). The total interval thickness over which the I-S transition occurs is similar in Wells WK244 and WK207 (165 and 151 m, respectively), but the actual depths are ~50–60 m deeper in WK244. This difference is a result of hotter downhole conditions in Well WK207 (as reported by Harvey and Browne, 1991) relative to WK244.

The composition of mixed-layer illite-dioctahedral smectite in WK244 changes from $I_{0.5}$ to $I_{>0.95}$ over the 165 m interval. Compositions of $I_{\geqslant 0.95}$ are present between 360 and 770 mRF within the Rautehuia Breccia, the Waiora, and the boundary zone between the Waiora and the Karapiti IIb Rhyolite. The I-S has R1 ordering at $I_{<0.85}$ and R3 ordering at $I_{\geqslant 0.85}$. A strong positive correlation (r = 0.98) exists between illite proportions in the I-S and downhole temperature (Figure 4) (57–221ºC; Contact Energy, pers. comm.). Linear regression of these data yields the following I-S 'geothermometer' for the Te Mihi area:

$$T\ (^{\circ}\mathrm{C}) = (I - 0.30839)/(0.00296) \qquad (1)$$

where I is the fractional component of illite in the mixed-layered I-S. Chi and Browne (1991) reported a similar relationship for other boreholes in the Wairakei geothermal field (Figure 4). Such empirical 'geothermometers' can be very useful for intra-field geothermal prospecting as they provide subsurface temperature estimates for comparison with other wells in a given field, before reliable downhole measurements are available. However, they do not necessarily reflect the original formation temperatures of the clay minerals and they are generally insensitive to field-wide thermal changes that have occurred since clay formation.

Swelling clay percentages obtained for bulk samples using MeB organic-dye testing range from ~7 to <1% in Well WK244. Swelling clay phases within the bulk rock are predominantly pure smectite and the smectitic component of I-S (the contribution from smectite interlayers within trioctahedral clays is considered negligible). The downhole trend of decreasing swelling clay percentage from the upper Huka Falls Formation to the boundary of the Karapiti IIb Rhyolite shows a strong positive correlation with decreasing %S in I-S, as determined by pXRD (r = 0.91; Figure 3). This pattern suggests that the abundance of hydrothermal I-S is approximately constant at all depths $\geqslant$195 mRF, an observation supported by illitic clay abundance estimates from pXRD of bulk samples. This strongly suggests that the swelling component in these samples is contained mostly in I-S. The slight decoupling between the two datasets probably arises from the

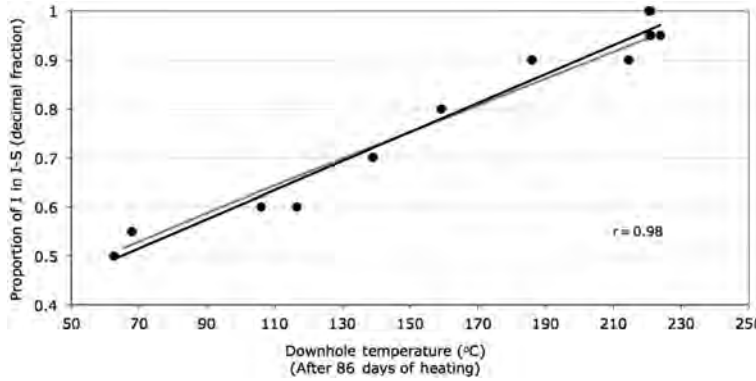

Figure 4. Illite proportions in I-S *vs*. downhole temperatures (Contact Energy, pers. comm.). The I-S geothermometer proposed for WK244 (black line; linear regression, r = 0.98) is very similar to the I-S geothermometer (gray) determined previously for the Te Mihi area (Chi and Browne, 1991; with data from Harvey and Browne, 1991).

assumption of a constant abundance for I-S across the sample intervals. Overall, the comparison of the two methods shows that the MeB method is useful for rapid, field-based estimation of %S in I-S within the Te Mihi area, and perhaps other similar geothermal settings.

The pXRD data for glycolated and dehydrated samples suggest that R0 chlorite$_{(>0.95)}$-smectite is also generally present throughout the sampled portion of Well WK244. In addition, poorly developed diffractions observed throughout the Oruanui Formation may indicate the additional presence of a chloritic (possibly detrital) trioctahedral clay.

The XRD and SEM results indicate a depth/temperature-dependent sequence of zeolites in Well WK244. Clinoptilolite is present in the shallowest sample studied (45 mRF). Mordenite appears within the lower Oruanui and Huka Falls formations. Laumontite and wairakite are present at depths greater than 410 and 455 mRF (>220ºC), respectively.

Clay morphologies

The commonly used terminology for describing illite/I-S morphologies (*e.g.* Guven, 2001) is adopted herein. Lath and fibrous morphologies are characterized by mineral length/width aspect ratios of 3–50 and >50, respectively, and flexible laths and fibers are referred to as ribbons and filaments or hairs, respectively.

Smectite occurs in a typical 'cornflake'-type morphology (*e.g.* Keller *et al.*, 1986) in all samples from the Oruanui Formation (Figure 5a). The appearance of I-S ribbons and hairs at 145 mRF indicates the presence of minor illitic clay not detected by pXRD.

Within the Huka Falls Formation and Upper Rautehuia Breccia (corresponding to samples from 195–345 mRF), I-S appears as laths, ribbons, fibers, and hairs (Figure 5b,c), with flexibility negatively correlated to crystal thickness. These high-aspect-ratio morphologies could arise from illite supersaturation and rapid mineral growth rates paired with relatively low diffusion rates (*e.g.* in a low-porosity environment; Inoue and Kitagawa, 1994). Alternatively, they could reflect inhibition of mineral growth in the *b* crystallographic direction (due to organic or inorganic functional groups reacting with exposed hydroxl ligands on the illite (010) crystal face; Surdam *et al.*, 1984; Guven, 2001).

Experimental studies have shown that high-aspect-ratio illites are metastable (Bauer *et al.*, 2000; Champion, 1989; and Lanson and Champion, 1991), and eventually coalesce and transform through Ostwald ripening into flakes and end-member pseudo-hexagonal plates – a phenomenon previously documented in hydrothermal systems (*e.g.* Keller *et al.*, 1986; Inoue *et al.*, 2004; Meunier, 2005). In Well WK244, I-S laths and fibers have coalesced into flakes with 'scalloped' edges, probably because of the variable lengths of the amalgamated laths and fibers (Figure 5c,d,e). This ripening process seems to have progressed with increasing depth within the Huka Falls Formation and Upper Rautehuia Breccia (Figure 5c,d,e).

At greater depths in Well WK244, within the Waiora Formation, high-aspect-ratio morphologies were not observed and pseudo-hexagonal crystallites prevail (Figure 5f). Greater porosities in the Waiora Formation probably contributed to an increased fluid flux, which may well have facilitated the ripening process from laths/fibers to platelets.

Oxygen isotopic systematics

The $\delta^{18}O_{I\text{-}S}$ values in Well WK244 decrease systematically with depth, from +5.4 to +0.5‰ (Figure 6). This pattern is consistent with increasing temperature of clay formation.

Hydrothermal fluids in Wairakei originate from local meteoric water with a $\delta^{18}O$ of ~–6‰ (Eslinger and Savin, 1973; Giggenbach, 1995) but are enriched in ^{18}O during heating by isotopic exchange with host rocks in the Wairakei subsurface. However, assuming present downhole temperatures for clay formation and using the oxygen isotope illite-smectite–water geothermometer of Savin and Lee (1988), calculated $\delta^{18}O_{water}$ values appear

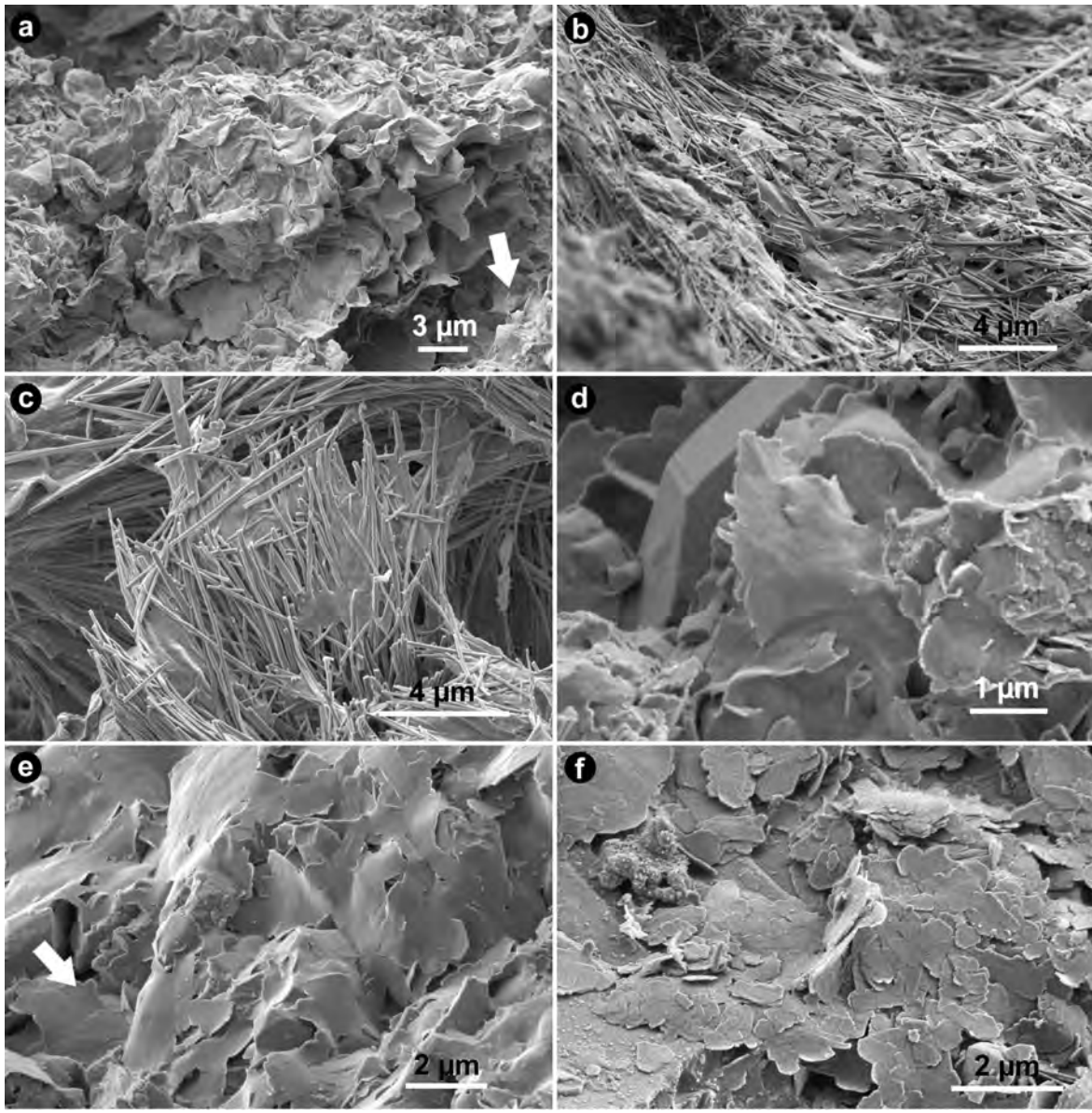

Figure 5. SEM images of hydrothermal clays from Well WK244 in the Te Mihi area, Wairakei geothermal field. Mineralogical identifications were made using morphological characteristics, EDS, and µXRD. (a) 'Cornflake'-textured dioctahedral smectite from the Oruanui Formation, 145 mRF. Submicron illite filaments extending from coalesced flakes are visible in the bottom right quarter of the image (arrow). (b) Strands of 'hairy' illite coalescing into flakes near the center of the image, 195 mRF. (c) Coalescence of hairs and ribbons of illite, 195 mRF. (d) Flakes of coalesced illite ribbons of varying original length displaying scalloped edges, 235 mRF. (e) Flakes of well coalesced illite ribbons, 345 mRF. Evidence of amalgamated ribbons is provided by scalloped edges and faint ribbon impressions on flake surfaces (arrow). (f) Well developed pseudo-hexagonal illite platelets, 610 mRF.

to be as low as −12.6‰ in the upper portions (195−300 mRF) of Well WK244. Such compositions are unlikely, and suggest instead that shallower parts of this system were hotter during clay formation. This observation is supported by the presence of R1 and R3 ordered I-S within this interval (Table 1), for which minimum temperatures of 100 and 200ºC, respectively, are normally required (Nadeau and Reynolds, 1981).

Heat transfer by convecting fluids is the primary control on thermal gradient in geothermal systems, with maximum subsurface temperature generally governed by the thermal buffering properties of the H_2O liquid-vapor transition. Active geothermal systems commonly exhibit temperature-depth profiles that approach the 'boiling point with depth' (BPD) curve of water – implying hydrostatic control on pressure in the upper few hundred

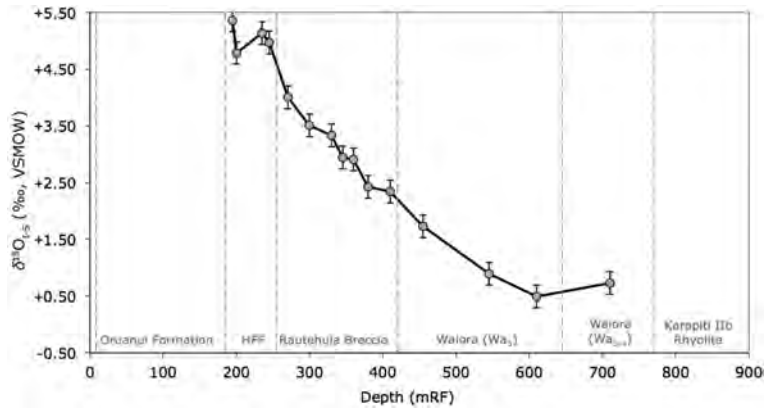

Figure 6. Oxygen isotopic composition of I-S in WK244. Error bars shown for the $\delta^{18}O$ values are ±0.2‰.

meters and, thus, a hydrothermal system that is connected (through permeable networks) to the surface (Haas, 1971). In Well WK244, the temperature change from 345 to 195 mRF follows a remarkably linear trend (Figure 7), which is inferred to represent increasing interaction between cool groundwater and hydrothermal fluids up-section. Temperatures throughout this interval have been adjusted upward toward the BPD curve using 345 mRF as a pivot point. Constraints governing this correction were that: (1) the minimum $\delta^{18}O_{water}$ value was fixed at −6‰, and (2) a linear trend was required for the adjusted depth-temperature profile on the assumption that mixing with cooler groundwaters also attenuated temperature increases in the upper 330 m at the time of clay formation (Figure 7). With this adjustment, agreement was produced with the expected thermal thresholds for R1 and R3 ordered I-S, which were first observed at 195 and 330 mRF, respectively.

Other support for a reduction in temperature and fluid pressures between the time of clay formation and present conditions is provided by overprinting of previously established propylitic assemblages in Wairakei by lower temperature and/or pH phases (Rosenberg *et al.*, 2009). Radial anhydrite present on open pore surfaces at 545 mRF in Well WK244 may have formed in a recent boiling zone below the Rautehuia Breccia, as documented elsewhere in the Wairakei (Bixley *et al.*, 2009; Rosenberg *et al.*, 2009) and Kakkonda, Japan, (Muramatsu *et al.*, 2000) geothermal fields. The occurrence of clinoptilolite at 45 mRF, well below its typical occurrence at >60ºC in the Wairakei geothermal field (Braithwaite, 2003), provides further evidence of temperature depression at the current time in the upper portions of Well WK244.

Measured temperatures below 345 mRF are within ~15−40ºC of the boiling-point curve (Figure 7).

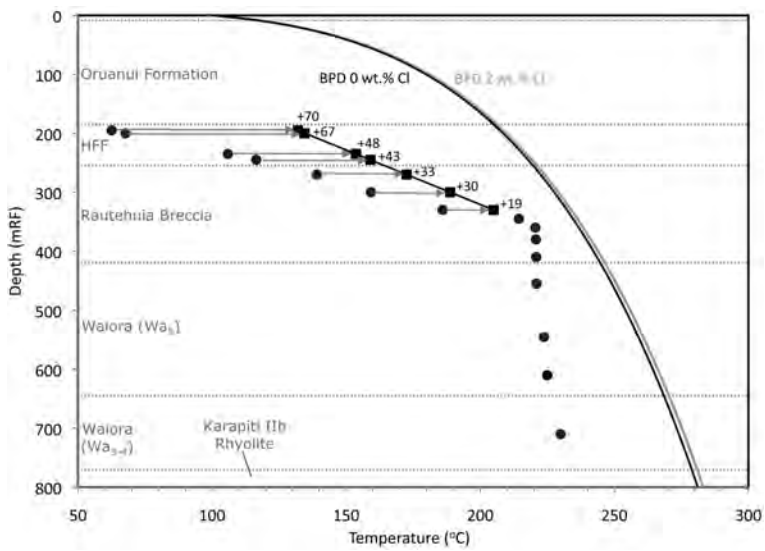

Figure 7. Measured downhole temperatures (filled circles) in Well WK244. Temperature-corrected values (squares) have been fitted to a linear trend, which lies closer to the 'boiling point with depth' (BPD) curve for water (Hass, 1971). Hydrothermal fluids at Wairakei generally contain 1−2 wt.% Cl (Giggenbach, 1995; Kissling *et al.*, 1996).

Wairakite, which is commonly used as an indicator of temperatures above 210ºC (Browne and Ellis, 1970; Steiner, 1977), first appears in Well WK244 at 455 mRF and a present temperature of 221ºC. Based on these observations, the present authors have assumed that the illite$_{>0.9}$-smectite is close to thermal equilibrium under present conditions. No temperature adjustments were made for samples from 345 to 710 mRF.

Using the adjusted temperature profile, $\delta^{18}O_{water}$ values calculated using the I-S data range from −6.0 to −2.7‰ and have a mean of −4.1‰ (Table 1), 0.8‰ higher than the average $\delta^{18}O_{water}$ value of Wairakei reservoir fluids reported by Clayton and Steiner (1975).

Water/rock ratios in Well WK244

Estimates for water/rock (W/R) ratios in the study area can be calculated using both closed- and open-system models. In the former case, a package of fluid makes an infinite number of passes through a convective system; in the latter case, the package of fluid makes only a single pass. Fluids in natural geothermal systems operate between these two end-members, with many documented systems behaving more like closed systems (Taylor, 1977). However, some consider that the hydrological system at Wairakei may be an exception, given its relatively large W/R (by mass) ratio of 4.3 (Clayton and Steiner, 1975) and its considerable natural fluid discharges of 400 kg/s (Banwell, 1963).

Closed system

Water/rock ratios under closed-system conditions for the Kakkonda geothermal field using $\delta^{18}O_{I\text{-}S}$ values were estimated by Inoue *et al.* (2004), who developed a simplified model for clay formation based on dissolution of volcanic glass of albitic composition (similar to the volcanic rocks dominating Wairakei) followed by precipitation of I-S (beidellite composition for the smectitic layers). This model was applied in the present study and the mineral compositions, as described in equation 2 (see Inoue *et al.*, 2004 for details), to the present samples from the Te Mihi area:

$$W/R \text{ (atomic)} = [\delta^{18}O_i^r - \delta^{18}O_f^w - (0.6435 - 0.126I)\Delta_{I/S\text{-}w}]/(\delta^{18}O_f^w - \delta^{18}O_i^w) \quad (2)$$

where $\delta^{18}O_i^r$ is the isotopic composition of unaltered (initial) rock; $\delta^{18}O_i^w$ and $\delta^{18}O_f^w$ are the isotopic compositions of unreacted (initial) and reacted (final) water, respectively; $\Delta_{I/S\text{-}w}$ is the difference between $\delta^{18}O_{I\text{-}S}$ and $\delta^{18}O_f^w$; and I is the fractional proportion of illite in I-S. Values of $\delta^{18}O_i^r$ and $\delta^{18}O_i^w$ for the Wairakei geothermal field were assumed to be +7.5 to +9.7‰ (Clayton and Steiner, 1975) and −6.0‰ (Eslinger and Savin, 1973), respectively. Values of $\delta^{18}O_f^w$ were taken from Table 1, as described earlier. W/R (atomic) ratios, as given by equation 2, were then converted to W/R (mass) ratios, assuming a starting material of albitic composition.

The calculated W/R (mass) ratios for Well WK244 range from 1.2−1.6 to 5.3−6.5 and have an average of 2.6±0.3. This average lies between the previously suggested ratios for the Wairakei geothermal field of 2 (Stewart, 1978) and 4.3 (Clayton and Steiner, 1975). Such relatively high ratios are consistent with the high permeability of some host rocks at Wairakei. Henley and Ellis (1983) suggested that W/R (mass) ratios in Wairakei are near the maximum for a convecting geothermal system; such ratios for other active geothermal systems are commonly (though not exclusively; Christidis, 1998) <2 (Inoue *et al.*, 2004; Larson and Taylor, 1986; White *et al.*, 1992).

The calculated W/R ratios can be divided into two groups that correspond well with the variations in relative permeability of the formations intersected by Well WK244. In this area, 'high' *vs.* 'low' permeability is identified by the extent of drilling fluid losses during production drilling (GNS, pers. comm.; Rosenberg *et al.*, 2009). The Huka Falls Formation and Rautehuia Breccia (Group 1, Figure 8) have average W/R (mass) ratios of 1.4−2.5, excluding samples at 195 and 200 mRF (for which the largest temperature corrections had to be made). Such W/R ratios are consistent with the lower permeability of these lacustrine and volcaniclastic units, which are considered to be aquitards within the Wairakei geothermal field. The lowest values occur in the mid to lower portions of the Rautehuia Breccia, which is more massive and compacted than its upper portions (Rosenberg *et al.*, 2009; Bixley *et al.*, 2009). The high W/R ratios calculated for the upper half of the Huka Falls Formation may be related to shallow steam zones that are known to occur within this unit (Rosenberg *et al.*, 2009).

The highly permeable ignimbrite, tuff, and tuffaceous sandstone and mudstone of the Waiora Formation in the Te Mihi area (Group 2, Figure 8) have greater calculated W/R ratios (2.5−5.9) than Group 1. This unit contains the main producing hot aquifers at Wairakei. The lithological boundary between the Rautehuia Breccia (*i.e.* lower Huka Falls Formation) and the upper Waiora Formation is gradational (Rosenberg *et al.*, 2009), which may explain the corresponding gradient in W/R ratios (Figure 8).

Open system

Open-system W/R ratio calculations assume the unlikely scenario that a unit of water makes a single pass through the hydrothermal system. Nevertheless, such calculations can be used to provide a lower limit for W/R ratios in convective hydrothermal systems.

Water/rock ratios calculated for a closed system can be adapted to an open-system model using the equation provided by Taylor (1977):

$$W/R = \ln[(W/R)_{closed} + 1] \quad (3)$$

As expected, the calculated W/R ratios for the open-system model yield a very subdued version of the pattern obtained for the closed-system model (Figure 8).

Table 1. Temperature, pXRD, isotopic, and MeB data for samples from Well WK244. % Illite and interlayer ordering were determined following Moore and Reynolds (1997) and confirmed using *NEWMOD©* (Reynolds, 1985). The $\delta^{18}O_{fluid}$ values were calculated using the oxygen isotope illite-smectite–water geothermometer of Savin and Lee (1988). Water/rock (mass) ratios were calculated using the closed-system model described by Inoue *et al*. (2004).

Depth	Formation	Measured temperature (ºC)	Corrected temperature (ºC)	% Illite	R	% Swelling clay (MeB)	$\delta^{18}O_{mineral}$ (‰, VSMOW)	$\delta^{18}O_{fluid}$ (‰, VSMOW)	W/R closed system (avg.)	W/R open system (avg.)
45	Oruanui	15		–		<3%				
95	Oruanui	18		–		<2%				
145	Oruanui	30		–		<4%				
195	Huka Falls	63	132.06	50	R1	<7%	+5.4	–5.6	12.2	2.2
200	Huka Falls	68	134.5	55	R1	<6%	+4.8	–6.0	–	–
235	Huka Falls	106	153.67	60	R1	<6%	+5.1	–4.2	2.4	1.4
245	Huka Falls	116	159.07	60	R1	<4%	+5.0	–4.1	2.2	1.3
270	Rautehuia	139	172.58	70	R1	<2%	+4.0	–4.2	2.5	1.4
300	Rautehuia	159	188.78	80	R1	<3%	+3.5	–3.7	2.0	1.3
330	Rautehuia	186	205.00	90	R3	<2%	+3.3	–3.0	1.5	1.1
345	Rautehuia	214		90	R3	<2%	+2.9	–3.0	1.6	1.1
360	Rautehuia	221		>95	R3	<2%	+2.9	–2.7	1.4	1.1
380	Rautehuia	221		95	R3	<2%	+2.4	–3.2	1.8	1.2
410	Rautehuia	221		95	R3	<2%	+2.4	–3.2	1.8	1.2
455	Waiora W5	221		>95	–	<1%	+1.7	–3.9	2.5	1.4
545	Waiora W5	224		95	R3?	<2%	+0.9	–4.6	4.2	1.7
610	Waiora W5	225		95	R3?	<2%	+0.5	–5.0	5.9	1.9
710	Waiora W3-4	230		95	R3?	<2%	+0.8	–4.6	3.9	1.6
770	Karapiti 2B	–		>95	–	<1%				

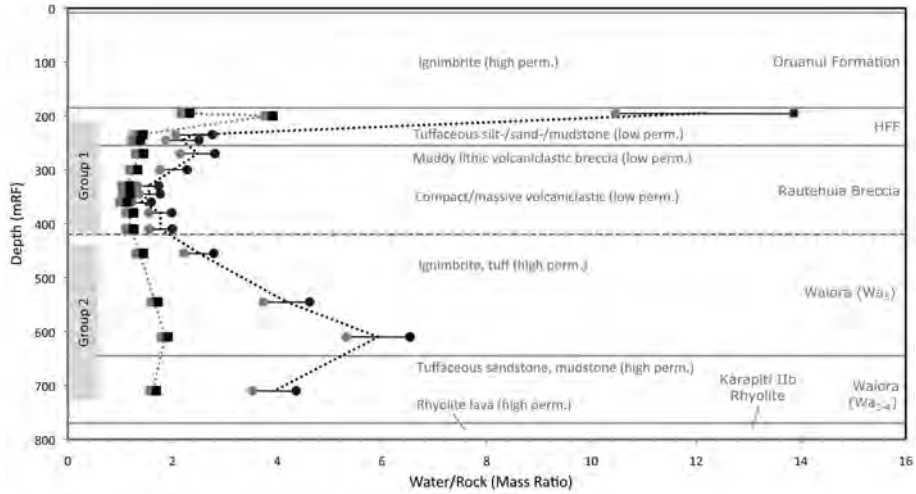

Figure 8. Calculated W/R ratios as a function of depth in Well WK244. Values for closed (circles) and open (squares) system models are shown for upper (black) and lower (gray) estimates of $\delta^{18}O_i^r$ (Clayton and Steiner, 1975). Closed-system calculations follow Inoue *et al.* (2004) and assume that a unit of water makes an infinite number of passes through the hydrothermal system. Open-system calculations following Taylor (1977) assume that a unit of water makes a single pass through the hydrothermal system. Average W/R ratios are illustrated as black (closed system) and gray (open system) dotted lines. Horizontal lines denote lithological boundaries, with the dashed horizontal line representing a gradational boundary.

CONCLUSIONS

Mixed-layer I-S in Well WK244 from the Te Mihi area, Wairakei geothermal field, displays a systematic change from R1 to R3 ordering and from 50 to >90% illite over a 160 m interval within the Huka Falls Formation and associated Rautehuia Breccia. High-aspect-ratio hairs and ribbons of illitic clay have coalesced through Ostwald ripening to form flakes and pseudo-hexagonal platelets, with the degree of ripening increasing with depth. Estimates of the swelling clay percentage obtained using the methylene blue method show a strong positive correlation with %S of I-S ($r = 0.91$) as determined by pXRD. This result further validates use of the methylene blue method for delineating illitization sequences and estimating temperatures in active geothermal environments. Values of $\delta^{18}O_{I\text{-}S}$ become progressively lower with depth, reflecting increasing temperature of clay formation. W/R ratios calculated using $\delta^{18}O_{I\text{-}S}$ values and clay-formation temperatures show significant variability that corresponds well with permeability differences among the units that host this geothermal system.

The general agreement between calculated W/R ratios and empirically documented variations in host-rock permeability in Well WK244 suggests that oxygen isotopic compositions of hydrothermally produced I-S, combined with determinations of % illite layers and ordering, are useful in delineating hydrogeologic variability and thermal evolution in such environments. The W/R ratios calculated assuming both open and closed systems for the Wairakei field provide reasonable upper and lower limits for actual conditions at depth. While the open-system model is probably unrepresentative of conditions persisting in active geothermal environments, the possibility of such lower limits should not be overlooked for systems operating at high fluid fluxes, such as Wairakei.

ACKNOWLEDGMENTS

The authors acknowledge K. Law, L. Munro, J. Potter, and G. Yau for their assistance at the Laboratory for Stable Isotope Science (The University of Western Ontario, Canada); the Institute of Geological and Nuclear Sciences and Contact Energy for supplying samples; K. Elliston, M. Elliston, B. Mountain, G. Bignall, A. Rae, and B. Carey of the Wairakei Research Center for on-site assistance; and K. Coverdale, A. Libbey, B. Libbey, P. Haughian, M. Haughian, and F. Haughian for their continued support. This manuscript benefited from thoughtful reviews and suggestions by Dr Atsuyuki Inoue and Dr Joseph W. Stucki. This work was supported by a Natural Sciences and Engineering Research Council of Canada (NSERC) Discovery grant and Canada Foundation for Innovation and Ontario Research Fund (ORF) infrastructure awards to F.J. Longstaffe, and also made possible, in part, through release time provided to F.J. Longstaffe under the Canada Research Chairs Program. This is 'Laboratory for Stable Isotope Science' Contribution #285.

REFERENCES

Altaner, S.P. and Ylagan, R.F. (1997) Comparison of structural models of mixed-layer illite/smectite and reaction mechanisms of smectite illitization. *Clays and Clay Minerals*, **45**, 517–533.

Ayalon, A. and Longstaffe, F.J. (1990) Isolation of diagenetic silicate minerals in clastic sedimentary rocks for oxygen isotope analysis – a summary of methods. *Israel Journal of Earth Sciences*, **39**, 139–148.

Banwell, C.J. (1963) Oxygen and hydrogen isotopes in New Zealand thermal areas. Pp. 95–138 in: *Nuclear Geology in Geothermal Areas* (E. Tongiorgi, editor). Consiglio

Nationale delle Ricerche, Pisa, Italy.

Bauer, A., Velde, B., and Gaupp, R. (2000) Experimental constraints on illite crystal morphology. *Clay Minerals*, **35**, 587–597.

Bechtel, A. and Hoernes, S. (1990) Oxygen isotope fractionation between oxygen of different sites in illite minerals – a potential single-mineral thermometer. *Contributions to Mineralogy and Petrology*, **104**, 463–470.

Bixley, P.F., Clotworthy, A.W., and Mannington, W.I. (2009) Evolution of the Wairakei geothermal reservoir during 50 years of production. *Geothermics*, **38**, 145–154.

Borthwick, J. and Harmon, R.S. (1982) A note regarding ClF_3 as an alternative to BrF_5 for oxygen isotope analysis. *Geochimica et Cosmochimica Acta*, **46**, 1665–1668.

Braithwaite, R.L. (2003) Geological and mineralogical characterization of zeolites in lacustrine tuffs, Ngakuru, Taupo Volcanic Zone, New Zealand. *Clays and Clay Minerals*, **51**, 589–598.

Browne, P.R.L. and Ellis, A.J. (1970) Ohaki-Broadlands hydrothermal area, New Zealand – mineralogy and related geochemistry. *American Journal of Science*, **269**, 97–131.

Clayton, R.N. and Mayeda, T.K. (1963) The use of bromine pentafluoride in the extraction of oxygen from oxides and silicates for isotopic analysis. *Geochimica et Cosmochimica Acta*, **27**, 43–52.

Clayton, R.N. and Steiner, A. (1975) Oxygen isotope studies of the geothermal system at Wairakei, New Zealand. *Geochimica et Cosmochimica Acta*, **39**, 1179–1186.

Champion, D. (1989) Etude des mécanismes de transformation des interstratifiés illite/smectite au cours de la diagenèse. PhD thesis, Université de Paris XI-Orsay, France, 204 pp.

Chi, M.A. and Browne, P.R.L. (1991) Alteration mineralogy of sediments in the Huka Falls Formation of the Te Mihi area, Wairakei. *Proceedings of the 13th New Zealand Geothermal Workshop*, 185–191.

Christidis, G.E. (1998) Comparative study of the mobility of major and trace elements during alteration of an andesite and a rhyolite to bentonite, in the islands of Milos and Kimolos, Aegean, Greece. *Clays and Clay Minerals*, **46**, 379–399.

Cole, J.W. (1990) Structural control and origin of volcanism in the Taupo Volcanic Zone, New Zealand. *Bulletin of Volcanology*, **52**, 445–459.

Eslinger, E.V. and Savin, S.M. (1973) Mineralogy and oxygen isotope geochemistry of hydrothermally altered rocks of Ohaki-Broadlands, New Zealand geothermal areas. *American Journal of Science*, **273**, 240–267.

Flemming, R.L. (2007) Micro x-ray diffraction (μXRD): a versatile technique for characterization of Earth and planetary materials. *Canadian Journal of Earth Sciences*, **44**, 1333–1346.

Giggenbach, W.F. (1995) Variations in the chemical and isotopic composition of fluids discharged from the Taupo Volcanic Zone, New Zealand. *Journal of Volcanology and Geothermal Research*, **68**, 89–116.

Guven, N. (2001) Mica structure and fibrous growth of illite. *Clays and Clay Minerals*, **49**, 189–196.

Haas, J.L. (1971) Effect of salinity on maximum thermal gradient of a hydrothermal system at hydrostatic pressure. *Economic Geology*, **66**, 940–946.

Harrison, A. and White, R.S. (2006) Lithospheric structure of an active backarc basin: the Taupo Volcanic Zone, New Zealand. *Geophysical Journal International*, **167**, 968–990.

Harvey, C. and Browne, P.R.L. (1991) Mixed-layer clay geothermometry in the Wairakei geothermal field, New Zealand. *Clays and Clay Minerals*, **39**, 614–621.

Harvey, C. and Browne, P. (2000) Studies of mixed-layer clays in geothermal systems and their effectiveness as mineral geothermometers. *Proceedings of the World Geothermal Congress*, pp. 1201–1205.

Harvey, C., Gunderson, R., and Cumming, W. (2000) Methylene Blue adsorption: a real-time rig geologist tool for estimating geothermal reservoir temperatures and forecasting drillhole stability problems. *Proceedings of the 22nd New Zealand Geothermal Workshop*, pp. 151–155.

Henley, R.W. and Ellis, A.J. (1983) Geothermal systems ancient and modern – a geochemical review. *Earth-Science Reviews*, **19**, 1–50.

Hower, J., Eslinger, E.V., Hower, M.E., and Perry, E.A. (1976) Mechanism of burial metamorphism of argillaceous sediment: 1. Mineralogical and chemical evidence. *Geological Society of America Bulletin*, **87**, 725–737.

Inoue, A. and Kitagawa, R. (1994) Morphological characteristics of illitic clay minerals from a hydrothermal system. *American Mineralogist*, **79**, 700–711.

Inoue, A., Meunier, A., and Beaufort, D. (2004) Illite-smectite mixed-layer minerals in felsic volcaniclastic rocks from drill cores, Kakkonda, Japan. *Clays and Clay Minerals*, **52**, 66–84.

Inoue, A., Lanson, B., Marques-Fernandes, M., Sakharov, B.A., Murakami, T., Meunier, A., and Beaufort, D. (2005) Illite-smectite mixed-layer minerals in the hydrothermal alteration of volcanic rocks: I. One-dimensional XRD structure analysis and characterization of component layers. *Clays and Clay Minerals*, **53**, 423–439.

Jackson, M.L. (1969) *Soil Chemical Analysis, Advanced Course, 2nd edition*. Published by the author, Madison, Wisconsin, USA.

James, A.T. and Baker, D.R. (1976) Oxygen isotope-exchange between illite and water at 22 degrees C. *Geochimica et Cosmochimica Acta*, **40**, 235–239.

Keller, W.D., Reynolds, R.C., and Inoue, A. (1986) Morphology of clay minerals in the smectite-to-illite conversion series by scanning electron microscopy. *Clays and Clay Minerals*, **34**, 187–197.

Kissling, W.M., Brown, K.L., O'Sullivan, M.J., White, S.P., and Bullivant, D.P. (1996) Modelling chloride and CO_2 chemistry in the Wairakei geothermal reservoir. *Geothermics*, **25**, 285–305.

Lanson, B. and Champion, D. (1991) The I/S-to-illite reaction in the late stage diagenesis. *American Journal of Science*, **291**, 473–506.

Larson, P.B. and Taylor, H.P. (1986) An oxygen isotope study of hydrothermal alteration in the Lake-City Caldera, San-Juan Mountains, Colorado. *Journal of Volcanology and Geothermal Research*, **30**, 47–82.

Longstaffe, F.J. (1986) Oxygen isotope studies of diagenesis in the basal Belly River sandstone, Pembina I-Pool, Alberta. *Journal of Sedimentary Petrology*, **56**, 78–88.

Longstaffe, F.J. and Ayalon, A. (1991) Mineralogical and O-isotope studies of diagenesis and porewater evolution in continental sandstones, Cretaceous Belly River Group, Alberta, Canada. *Applied Geochemistry*, **6**, 291–303.

Meunier, A. (2005) *Clays*. Springer-Verlag, Berlin, Heidelberg, 472 pp.

Moore, D. and Reynolds, R.C. Jr. (1997) *X-ray diffraction and the Identification and Analysis of Clay Minerals, 2nd edition*. Oxford University Press, New York, 396 pp.

Muramatsu, Y., Komatsu, R., Sawaki, T., Sasaki, M., and Yanagiya, S. (2000) Geochemical study of fluid inclusions in anhydrite from the Kakkonda geothermal system, Northeast Japan. *Geochemical Journal*, **34**, 175–193.

Nadeau, P.H. and Reynolds, R.C. (1981) Burial and contact-metamorphism in the Mancos Shale. *Clays and Clay Minerals*, **29**, 249–259.

Reynolds, R.C., Jr. (1985) NEWMOD: A computer program for the calculation of one-dimensional diffraction patterns of mixed-layered clays. R.C. Reynolds, 8 Brook Rd., Hanover, New Hampshire, USA.

Rosenberg, M.D., Bignall, G., and Rae, A.J. (2009) The geological framework of the Wairakei-Tauhara geothermal system, New Zealand. *Geothermics*, **38**, 72–84.

Ryan, P.C., Conrad, M.E., Brown, K., Chamberlain, C.P., and Reynolds, R.C. (1998) Oxygen isotope compositions of mixed-layer serpentine-chlorite and illite-smectite in the Tuscaloosa Formation (U.S. Gulf Coast): implications for pore fluids and mineralogic reactions. *Clays and Clay Minerals*, **46**, 357–368.

Savin, S.M. and Epstein, S. (1970) Oxygen and hydrogen isotope geochemistry of clay minerals. *Geochimica et Cosmochimica Acta*, **34**, 25–42.

Savin, S.M. and Lee, M. (1988) Isotopic studies of phyllosilicates. Pp. 189–223 in: *Hydrophyllosilicates (Exclusive of the Micas)* (S.W. Bailey, editor). Reviews in Mineralogy, **19**, Mineralogical Society of America, Washington, D.C.

Steiner, A. (1977) The Wairakei geothermal area, North Island, New Zealand: its subsurface geology and hydrothermal rock alteration. *New Zealand Geological Survey, Bulletin*, **90**.

Stewart, M.K. (1978) Stable isotopes in waters from the Wairakei geothermal area, New Zealand. Stable Isotopes in the Earth Sciences. *New Zealand Department of Scientific and Industrial Research Bulletin*, **220**, 113–120.

Stratford, W.R. and Stern, T.A. (2006) Crust and upper mantle structure of a continental backarc: central North Island, New Zealand. *Geophysical Journal International*, **166**, 469–484.

Surdam, R.C., Crossey, L.J., and Lahann, R. (1984) Mineral oxidants and porosity enhancement. *American Association of Petroleum Geologists Bulletin*, **68**, 532–532.

Taylor, H.P., Jr. (1977) Water/rock interactions ad the origin of H_2O in granitic batholiths. *Journal of the Geological Society of London*, **133**, 509–558.

Vitali, F., Longstaffe, F.J., McCarthy, P.J., Plint, A.G., and Caldwell, W.G.E. (2002) Stable isotopic investigation of clay minerals and pedogenesis in an interfluve paleosol from the Cenomanian Dunvegan formation, NE British Columbia, Canada. *Chemical Geology*, **192**, 269–287.

White, A.F., Chuma, N.J., and Goff, F. (1992) Mass-transfer constraints on the chemical evolution of an active hydrothermal system, Valles Caldera, New Mexico. *Journal of Volcanology and Geothermal Research*, **49**, 233–253.

Whitney, G. (1990) Role of water in the smectite-to-illite reaction. *Clays and Clay Minerals*, **38**, 343–350.

Yeh, H.W. and Eslinger, E.V. (1986) Oxygen isotopes and the extent of diagenesis of clay minerals during sedimentation and burial in the sea. *Clays and Clay Minerals*, **34**, 403–406.

(*Received 13 August 2012; revised revised 24 April 2013; Ms. 699; AE: W. Huff*)

Clays and Clay Minerals, Vol. 61, No. 3, 218–230, 2013.

STRUCTURE DETERMINATION OF TRIMETHYLSULFOXONIUM-EXCHANGED VERMICULITE

CANDICE A. JOHNS[1], RUBÉN MARTOS-VILLA[2], STEPHEN GUGGENHEIM[1,*], AND C. IGNACIO SAINZ-DÍAZ[3]

[1] Department of Earth and Environmental Sciences, University of Illinois at Chicago, 845 W. Taylor St., mc 186, Chicago, Illinois 60607, USA

[2] Facultad de Ciencias del Mar y Ambientales, Universidad de Cádiz, Av. República Saharaui s/n, 11510, Puerto Real, Spain

[3] Instituto Andaluz de Ciencias de la Tierra, CSIC-Universidad de Granada, Av. De las Palmeras, 4, 18100, Armilla, Granada, Spain

Abstract—The structure of trimethylsulfoxonium-exchanged vermiculite has been examined to compare it with other onium-exchanged structures, such as tetramethylammonium- and tetramethylphosphonium-exchanged vermiculite. The three organic cations are tetrahedral in shape, but trimethylsulfoxonium [$(CH_3)_3SO^+$] has an oxygen atom replacing a methyl group at one apex. This study describes the effect this substitution and the larger S atom have on the site location in the interlayer and the effect on the vermiculite 2:1 layer. These clay minerals may be commercially useful as adsorbents.

Na-exchanged crystals of vermiculite from Santa Olalla, Spain, were intercalated with trimethylsulfoxonium [$Me_3SO^+ = (CH_3)_3SO^+$] molecules by refluxing in an aqueous 0.25 M trimethylsulfoxonium iodide solution at 80ºC for 14 days. The resulting Me_3SO^+-exchanged vermiculite crystals were studied by single-crystal, X-ray diffraction methods and by computer modeling (density functional theory). Cell parameters are a = 5.349(2), b = 9.270(3), c = 13.825(8) Å, and β = 97.40(4)º, the space group is $C2/m$, and the polytype is 1M. Refinement results (R = 0.073, wR = 0.080) show that in the average structure of $C2/m$, the S atoms of the Me_3SO^+ molecules form two partially occupied planes [2.066(2) Å from each basal oxygen plane] between the 2:1 layers, and the S atoms show considerable positional disorder. The O atom of the Me_3SO^+ molecule occurs in the central plane of the interlayer, as far away from each 2:1 layer as possible. In projection down the c* axis, the Me_3SO^+ molecule resides within the center of the silicate rings from each adjacent 2:1 layer. In the ideal (static) model of the Me_3SO^+-exchanged vermiculite structure, the Me_3SO^+ molecule is oriented such that two methyl groups point toward charge-deficient bridging oxygen atoms of the basal plane; thus, the organic pillars charge compensate the bridging oxygen atoms of the 2:1 layer that are charge deficient. In projection, the oxygen atom of the Me_3SO^+ molecule projects over a tetrahedron containing Si. Computer modeling showed that if H_2O is not included in the model, the Me_3SO^+ molecule (S and O atoms) is in the center of the interlayer, but with the addition of randomly placed H_2O, two partially occupied planes similar to the X-ray derived model are formed.

Key Words—Computational Modeling, Organoclay, Trimethylsulfoxonium-exchanged Vermiculite, Vermiculite, X-ray Structure Determination.

INTRODUCTION

Pillared clays were originally defined as containing small, organic cations that hold the silicate layers apart, allowing for an accessible interlayer region for additional intercalation (Barrer, 1984; see also Guggenheim, 2013, for an updated definition). The pillaring organic cation is required to charge compensate the net negative charge on the silicate layer. Pillared clays are commonly derived from swelling clays, smectite, and vermiculite, and result in a fixed or nearly fixed layer-to-layer distance. Two potentially important properties for commercial use are: (1) depending primarily on the size and spacing of the pillar in the interlayer and the presence of adsorbed H_2O, a pillared clay may accept additional (sorbate) molecules selectively, based on size (*e.g.* Barrer, 1989; Lee *et al.*, 1990); and (2) these sorbates may be uncharged, polar, or non-polar molecules (e.g. Barrer and Millington, 1967; Barrer and Perry, 1961), presumably because of the van der Waals interactions provided by the pillaring organic cation. Thus, pillared clays are organophilic, whereas the original non-pillared clay may not be.

To understand the pillaring system in swelling clays better, single-crystal, X-ray structure determinations were made using a well crystallized and homogenous vermiculite sample. Onium-pillared structures included exchanges with tetramethylammonium (TMA^+) (Vahedi-Faridi and Guggenheim, 1997), tetramethylphosphonium (TMP^+) (Vahedi-Faridi and Guggenheim, 1999a), and monomethylammonium (MMA^+) and dimethylammonium (DMA^+) (Vahedi-Faridi and Guggenheim, 1999b). Two structural series are provided by these substitutions, with one series involving systematic addition of pillar complexity (MMA, DMA, and TMA pillars) to the vermiculite substrate. This series not only showed that interlayer sites were positioned much differently for the various pillars, but showed also that

* E-mail address of corresponding author:
xtal@uic.edu
DOI: 10.1346/CCMN.2013.0610305

the 2:1 layer was affected by the type of pillar present, with systematic differences in tetrahedral and octahedral bond lengths and angles. The other series, TMA- *vs*. TMP-exchanged vermiculite, involved a variation in pillar size (and charge density) for pillars with tetrahedral geometry. This series showed that size and charge density influences how the pillar may satisfy the net negative charge on the 2:1 layer, with the smaller cation (TMA) positioning itself near the center of the silicate ring of the 2:1 layer and the larger cation (TMP) associating with individual basal oxygen atoms.

The present study continues with a series approach. Trimethylsulfoxonium [$(CH_3)_3SO^+$, simplified to Me_3SO^+] is an organic cation of tetrahedral shape, but unlike TMA or TMP, it contains an oxygen atom at one of the tetrahedral apices around the centrally located sulfur atom. Thus, a change in the charge distribution is observed about the central cation. Therefore, the influence of this charge variation on the Me_3SO^+ cation and how it affects the site location in the interlayer can be evaluated and compared to the TMA- and the TMP-exchanged forms.

EXPERIMENTAL AND RESULTS

Sample and preparation

Vermiculite from Santa Olalla, Spain, was used. The structural formula determined after Ca intercalation and ignition is $Ca^{2+}_{0.85}(Mg_{5.05}Ti_{0.03}Mn_{0.01}Fe^{3+}_{0.58}Al_{0.28})(Si_{5.48}Al_{2.52})O_{22}$ (Norrish, 1973). Sections were cut to ~0.7 mm × 0.7 mm × 0.1 mm from the same crystal used by Vahedi-Faridi and Guggenheim (1997, 1999a, 1999b). Untreated crystals show that 0*kl*, $k \neq 3n$ (n = integer) reflections are streaked along the [001]* direction, indicating lack of three-dimensional periodicity and stacking disorder. One hundred crystals were Na-exchanged for 8 days in an aqueous 1 M NaCl solution at 80ºC. The solution was refreshed every 2 days. After exchange, the crystals were removed, rinsed three times in deionized water, and air dried for 24 h. Na exchange was monitored periodically using a Siemens D-5000 powder X-ray diffractometer with CuKα radiation. Na exchange resulted in a d_{001} value of ~14.7 Å. The purpose of the Na exchange was to increase the layer-to-layer distance to allow more rapid exchange with the large organo-cation.

The Na-exchanged crystals were refluxed in an aqueous 0.25 M trimethylsulfoxonium (Me_3SO^+) iodide solution at 80ºC for 14 days. The solution was refreshed every four days. Crystals were removed, rinsed three times in deionized water, and air dried for 24 h before examination on the powder X-ray diffractometer. A spacing of 13.47 Å was observed for the d_{001} reflection. Examination of 100 crystals showed that ~17% of the crystals were twinned, 20% of the crystals were very thin owing to cleavage along 001 during the exchange, 45% of the crystals were split partially on the (001) plane, and 9% showed too much stacking disorder for a structure determination. Fewer than 9% of the crystals were considered to be of sufficient quality for structure refinement, and the best was chosen for additional study, which showed three-dimensional order after the organic treatment. The 0*kl* and *h*0*l* reflections showed that suitable crystals were monoclinic with the presence of $h + k = 2n$ reflections, which define a *C*-centered cell, and an apparent mirror plane and two-fold axis. Space-group symmetry of *C*2/*m* was assumed initially, and *Cm* and *C*2 symmetries were considered also. The polytype is 1*M*. The nominal composition after Norrish (1973) and assuming complete exchange is: $[(CH_3)_3SO^+]_{1.7}(Mg_{5.05}Ti_{0.03}Mn_{0.01}Fe^{3+}_{0.58}Al_{0.28})(Si_{5.48}Al_{2.52})O_{20}(OH)_2$.

Data collection and refinement

The crystal was placed on a Picker four-circle diffractometer equipped with a graphite monochromator using MoKα (Kα = 0.71069 Å) radiation. Unit-cell dimensions were refined from 17 reflections in eight octants (136 reflections total) and values obtained were a = 5.349(2), b = 9.270(3), c = 13.825(8) Å, and β = 97.40(4)º. A total of 1426 reflections were collected from $h = -7$ to 7, $k = -12$ to 0, and $l = -10$ to 10 from 2θ = 2 to 70º. A total of 73 reflections was removed owing to irregular peak shapes or owing to very high intensity, the latter being of the type $k = 3n$ reflections. Reflections were measured at a scan rate of 2θ = 1º/min with a 2º scan window adjusted as a function of 2θ, and a background-time count equal to one half the scan time. Three standard reflections were monitored approximately every 2 h to check electronic and temperature stability. Data were corrected for Lorentz polarization and absorption effects and symmetry averaged using a locally written program (*Fobs-P*). After symmetry averaging, 576 observations above 4σ were obtained. Absorption effects were determined empirically from psi scans around the [010] direction taken at psi intervals of 10º for 0*k*0 reflections at various values of 2θ. For comparison to Vahedi-Faridi and Guggenheim (1997), the refinement proceeded as described in that paper.

Starting atomic coordinates for the 2:1 layer were taken from Vahedi-Faridi and Guggenheim (1997) for TMA-exchanged vermiculite in *C*2/*m* symmetry, but adjusted for differences in the *c*-cell parameter for the two crystals. Initially, no atomic parameters were included for interlayer material. Initial site occupancies were determined from the chemical formula of Norrish (1973), which indicated substitution in the tetrahedral and octahedral sites. Atomic scattering factor curves for half-ionized atoms were determined using the I*nternational Tables for X-ray Crystallography* (1965). Reflections were assigned unit weights and a single scale factor. The scale factor was allowed to vary at all stages of the refinement. All atomic coordinates, x, y, and z, were varied except those fixed by symmetry, which brought the residual index to R = 0.309 and wR = 0.313,

where $R = \Sigma(||F_o|-|F_c||)/\Sigma|F_o|$, $wR = [\Sigma w\ (|F_o|-|F_c|)^2/\Sigma w|F_c|^2]^{1/2}$, F_o = observed structure factor amplitude, F_c = calculated structure factor amplitude, $w = 1.0$. The isotropic thermal displacement parameter, B, was then refined for each atom in the 2:1 layer, which decreased the R values to $R = 0.174$ and $wR = 0.196$. Then, x, y, z, and B values were refined together. Positive and negative electron-density peak locations were determined using a difference-Fourier map. A possible sulfur peak in the interlayer was identified at x, y, z fractional coordinates of 0.4570, 0.5000, 0.3945 with an electron density of 3.49 electrons/Å^3 (e$^-$/Å^3). Introduction of the sulfur atom produced $R = 0.146$ and $wR = 0.151$.

Additional difference-Fourier maps were made and a possible oxygen atom peak was identified at 0.6660, 0.5000, 0.4785 fractional coordinates with an electron density of 1.58 e$^-$/Å^3. This atom position was determined to be that of a Me_3SO^+ oxygen and after refinement the R values were reduced to $R = 0.134$ and $wR = 0.144$. A second possible Me_3SO^+ oxygen position at 0.5000, 0.3945, 0.5039 with electron density of 0.989 e$^-$/A^3 was located. Placement of this atom in the model gave an occupancy value of 0.05, did not decrease the R values, and this peak was excluded in the refinement. As the last phase of the refinement, isotropic thermal displacement parameters were refined anisotropically (in U_{ij}) to better define atomic shapes, but the Me_3SO^+ oxygen position did not produce physically meaningful results. An anisotropic refinement with the Me_3SO^+ oxygen atom defined isotropically and with all parameters refined together resulted in final residual-index values of $R = 0.073$ and $wR = 0.080$. A final difference-Fourier map was used to try to locate methyl groups of the Me_3SO^+ cation and the hydrogen of the OH group of the 2:1 layer. All peaks in the difference map were below the background of $3\sigma = 0.624$ e$^-$/Å^3. Final atomic coordinates, calculated bond lengths and angles, calculated structural parameters for *C*2/*m* symmetry, and a refinement summary are reported in Tables 1, 2, 3, and 4, respectively.

Attempts to refine a model in *Cm* and *C*2 symmetries were unsuccessful. Refinement of x, y, and z coordinates of the 2:1 layer for the *Cm* model, expanded with atom parameters for the reduction in symmetry, resulted in (isotropic refinement) R values of $R = 0.168$ and $wR = 0.177$ (compared to $R = 0.138$ and $wR = 0.150$ for *C*2/*m* symmetry for the isotropic refinement). Attempts to refine displacement parameters did not produce physically meaningful results for the apical oxygen atoms. The *Cm* model showed the existence of a two-fold axis in the 2:1 structure. The model was thus abandoned in favor of the C2/*m* model. In the *C*2 model, refinement of the x, y, and z coordinates as expanded for the additional atom parameters resulted in isotropic refinement R values of $R = 0.136$ and $wR = 0.146$, but the atoms could not be refined anisotropically. Because of the large number of additional varied parameters compared to the

Table 1. Atomic coordinates of Me_3SO^+-exchanged vermiculite in *C*2/*m* symmetry.

Site	x	y	z	frac	B	U (1,1)	U (2,2)	U (3,3)	U (1,2)	U (1,3)	U (2,3)
M(1)	0.5	0	0	0.253(3)*	1.85	0.0057(9)	0.0017(3)	0.0056(3)	0	0.0010(9)	0
M(2)	0	0.1689(3)	0	0.520(4)**	1.96	0.0068(6)	0.0019(2)	0.0059(2)	0	0.0019(6)	0
T	0.3993(3)	0.1666(2)	0.1993(2)	1	2.13	0.0066(4)	0.0018(2)	0.0067(2)	0.0001(5)	0.0031(4)	−0.0002(3)
O(1)	0.445(1)	0	0.2405(7)	0.5**	3.29	0.020(2)	0.0032(6)	0.0084(7)	0	0.002(2)	0
O(2)	0.1465(8)	0.2338(6)	0.2415(5)	1	3.35	0.014(1)	0.0057(5)	0.0085(5)	0.005(1)	0.004(1)	0.0000(8)
O(3)	0.3603(7)	0.1671(4)	0.0809(4)	1	2.11	0.009(1)	0.0027(4)	0.0057(4)	0.000(1)	0.001(1)	0.0000(6)
OH	0.360(1)	0.5	0.0771(6)	0.5**	1.98	0.005(1)	0.0021(6)	0.0061(6)	0	0.002(1)	0
S	0.464(5)	0.5	0.392(2)	0.175(7)**	11.13	0.10(1)	0.027(3)	0.016(2)	0	0.009(8)	0
O(4)	0.607(6)	0.447(3)	0.497(3)	0.16(1)	4.3(8)						

frac indicates refined value of site occupancy.
* indicates an atom located at the center of two symmetry operators where the true site occupancy value is the refined frac value multiplied by 4.
** indicates an atom located on a symmetry operator where the true site occupancy value is the refined frac value multiplied by 2.

Table 2. Selected calculated bond lengths and angles for the *C*2/*m* refined model.

		Distance (Å)			Distance (Å)		Angle (°)
2:1 layer							About *T*
T −O(1)		1.654(4)	O(1) −O(2)′		2.691(5)		108.8(3)
−O(2)′		1.655(5)	−O(2)		2.694(6)		108.6(3)
−O(2)		1.662(5)	−O(3)		2.686(9)		110.1(4)
−O(3)		1.623(6)	O(2) −O(2)′		2.691(5)		108.4(3)
	Mean	1.649	−O(3)		2.698(8)		110.4(3)
			O(2)′−O(3)		2.690(8)		110.2(3)
				Mean	2.692	Mean	109.4
			Shared				About *M*(1)
M(1)−O(3) × 4		2.104(4)	O(3) −O(3) × 2		2.847(7)		85.16
−OH × 2		2.081(6)	−OH × 4		2.813(9)		884.45
	Mean	2.096		Mean	2.824		
			Unshared				
			O(3) −O(3) × 2		3.099(6)		94.84
			−OH × 4		3.099(5)		95.55
				Mean	3.099		
M(2)−O(3) × 2		2.082(5)	Shared				About *M*(2)
−O(3)′ × 2		2.100(4)	O(3) −O(3)		2.847(7)		86.28
−OH × 2		2.086(5)	−O(3)′ × 2		2.843(7)		85.65
	Mean	2.089	OH −O(3)′ × 2		2.813(9)		84.45
			−OH		2.75(1)		82.67
				Mean	2.82		
			Unshared				
			O(3) −O(3)′ × 2		3.084(5)		95.03
			−OH × 2		3.083(5)		94.87
			OH −O(3)′ × 2		3.086(4)		95.53
				Mean	3.084		

Me_3SO^+		Me_3SO^+-nearest 2:1 layer	
S−O(4)	1.63(5)	S−*T*	4.06(2)
		S−O(2)	3.52(2)
		S−O(2)′	3.24(2)
		S−O(3)	5.26(2)
		S−OH	4.32(3)
		S−*M*(1)	5.66(3)
		S−*M*(2)	5.67(3)

*C*2/*m* model and the inability to refine the *C*2 model successfully, the *C*2 model was abandoned also.

Computational methods

Calculation procedures. Quantum mechanical calculations of an isolated Me_3SO^+ molecule were performed using the Hartree-Fock approximation with the second-order Moeller-Plesset (MP2) method for describing the electron exchange correlation for all electrons. The molecular electronic structure was calculated with a triple-ζ basis set with polarization functions for all atoms including H atoms (MP2/6−311G** level) as implemented in the *Gaussian03* program (Frisch *et al.*, 2004). No geometry constraint was applied to the molecule, which was optimized fully using the Berny analytical gradient method. Normal vibration modes were calculated from the force-constant analysis to confirm the nature of the stationary points, which resulted in only positive eigenvalues for the minimum. The molecular structure of Me_3SO^+ as a gas produced S−O and S−C distances of 1.454 Å and 1.775 Å, respectively, with the O−S−C angle of 113.7º.

Ab initio total energy calculations of the periodic crystal model were performed using density functional theory (DFT) methods based on the numerical atomic orbital (NAO) methodology implemented in the *SIESTA* program (Soler *et al.*, 2002). The generalized gradient approximation (GGA) was used with the Perdew-Burke-Ernzerhof (PBEsol) parameterization of the exchange-correlation function optimized for solids (Perdew *et al.*, 2008). Core electrons were replaced by norm-conserving pseudopotentials (Troullier and Martins, 1991). Calculations were restricted to the Γ point in the irreducible wedge of the Brillouin zone. In all model

Table 3. Calculated structural parameters for Me_3SO^+-exchanged vermiculite.

Parameter	Value
$\alpha(^o)$*	6.40
$\psi(^o)$**	59.68 (*M*1)
	59.57 (*M*2)
$\tau_{tet}(^o)^\dagger$	110.28
Sheet thickness‡	
Octahedral (Å)	2.116
Tetrahedral (Å)	2.202
Interlayer separation (Å)	7.099
$\beta_{ideal}(^o)^\S$	97.41
Cation distance to basal oxygen plane (Å)	2.073

* α (º) = ½[120 − mean $O_b-O_b-O_b$ angle]
** ψ (º) = $\cos^{-1}$[(oct. thickness)/(2(M−O)$_{ave}$)]
† τ_{tet} (º) = mean O_b-T-O_a
‡ Octahedral sheet thickness includes OH
§ β_{ideal}(E) = 180 − $\cos^{-1}$[a/3c]

structures, each atom was relaxed by conjugate gradient minimizations at constant volume. In *SIESTA*, the basis sets consist of strictly localized numerical atomic orbitals (NAOs) with a localization cut-off radius corresponding to an energy shift of 270 meV. The basis sets used here are double-Z polarized (DZP) following the perturbative polarization scheme. This approach was used successfully in previous calculations on phyllosilicates (Hernández-Laguna *et al.*, 2006).

A uniform mesh with certain plane-wave cut-off energy was used to represent the electron density, the local part of the pseudopotential, and the Hartree and exchange-correlation potentials. Calculations were performed with cut-off energy values of 150 Ry. These conditions are consistent with previous studies with phyllosilicates (Sainz-Díaz *et al.*, 2005).

Model development and the basic 2:1 layer. Model development involved defining each component of the phyllosilicate and then assembling these components. Analyses were made using increasingly complex assemblages. A periodic model of the crystal structure of vermiculite was generated from the experimental atomic coordinates and cell parameters given in Vahedi-Faridi and Guggenheim (1997). To create a supercell of a reasonable size for modeling, the structural formula of the vermiculite 2:1 layer was simplified to: $(Mg_{5.25}Al_{0.75})(Si_{5.5}Al_{2.5})O_{20}(OH)_4$ per unit cell, where the layer charge per unit cell is −1.75. Maximum separations between cation substitutions in the tetrahedral and octahedral sheets are used because these configurations are most stable (Sainz-Díaz *et al.*, 2003). Each model consisted of a supercell of $2 \times 2 \times 1$ vermiculite unit cells. To compensate the layer charge in this supercell, Me_3SO^+ cations, as optimized by quantum mechanical calculations (see above), were placed in the supercell to explore the different possible arrangements in the interlayer.

Models involving intercalated Me_3SO^+. The Me_3SO^+ molecule, initially optimized at the MP2/6-311G** level, was placed in the vermiculite crystal lattice based on the experimental X-ray diffraction (XRD) data and re-optimized using the DFT-*SIESTA* approach before intercalation. Seven Me_3SO^+ molecules are within the $2 \times 2 \times 1$ supercell of vermiculite, three of which are located within the upper-layer tetrahedral-ring cavity and four in the lower-layer, alternately choosing the tetrahedral-ring cavities with greatest local charge. One pair of cavities is without Me_3SO^+. In the optimization calculations of the dry (no H_2O) model, all Me_3SO^+ molecules are displaced to the center plane of the interlayer region, with the S and O atoms in the center of the interlayer and the methyl groups pointing to the basal oxygen atoms of the tetrahedral sheet (Figure 1).

Table 4. Summary of parameters.

Formula	$[(CH_3)_3SO^+]_{1.7}(Mg_{5.05}Ti_{0.03}Mn_{0.01}Fe^{3+}_{0.58}Al_{0.28})(Si_{5.48},Al_{2.52})O_{20}(OH)_2$
Z	1
Polytytpe	1M
CEC[1]	140 meq/100 g
Crystal size (mm)	~$0.7 \times 0.7 \times 0.1$
Cell parameters	a = 5.349(2), b = 9.270(3), c = 13.825(8) Å, and β = 97.40(4)º
Crystal system	monoclinic
Space group	$C2/m$
hkl range and theta	h = −7 to 7, k = −12 to 0, and l = −10 to 10 from 2θ = 2 to 70º
Number of reflections	total measured: 1426, independent: $I > 4\sigma$, 576
Absorption correction	empirical, *via* psi scan
R (on F)	= $\Sigma(\|\|F_o\|-\|F_c\|\|)/\Sigma\|F_o\|$ = 0.073
wR (on F)	=$[\Sigma w\ (\|F_o\|-\|F_c\|)^2/\Sigma w\|F_c\|^2]^{1/2}$ = 0.080
Largest difference peak	< 0.624 $e^-/Å^3$

[1] Measured on Mg-vermiculite, Santa Olalla, sample (Ruiz-Conde *et al.*, 1997).

Models involving H_2O + Me_3SO^+. Different numbers of H_2O molecules were added to Me_3SO^+-vermiculite models in a disordered fashion. For example, the W3 model: three H_2O molecules are located in each cavity at the opposite site to each Me_3SO^+ (13.6 % w/w of total water content); W4: the same as W3, but adding four H_2O molecules per Me_3SO^+ (16.1% total water content); W5: adds five H_2O molecules per Me_3SO^+ (20.7% total water content). In each case, seven Me_3SO^+ molecules and eight pairs of tetrahedral-ring cavities are in each supercell, and the cavity pair without Me_3SO^+ is filled with five to ten H_2O molecules.

Geometry optimizations for the W3 models place Me_3SO^+ molecules at the center of the interlayer (Figure 1b). Density profiles of the S atom along the [001] direction show a maximum at 3.58 Å from the lower basal-oxygen plane of the tetrahedral sheet (Figure 2). However, density profiles of the O atom from Me_3SO^+ molecules shows two peaks, corresponding to different positions of Me_3SO^+ molecules in the interlayer (Figure 3). For the W4 model, Me_3SO^+ molecules are located closer to the basal-oxygen planes of the tetrahedral sheets (Figure 1c) than in the W3 model. Density profiles of S atoms show two peaks from Me_3SO^+ molecules at an average distance of 2.83 Å from the lower basal-oxygen plane and 3.10 Å from the upper plane (Figure 2c). Similar to the W3 model, O atoms of the Me_3SO^+ molecule form two separate planes (Figure 3c). For the W5 model, Me_3SO^+ molecules are located to form two planes in the interlayer (Figure 1d), but more separated from each other than in W4. The S atom has an average distance of 2.70 Å from the lower basal-oxygen plane and 2.16 Å from the upper plane (Figure 2d). Oxygen atoms of the Me_3SO^+ molecule form one plane in the center of the interlayer (Figure 3d).

DISCUSSION

Space-group determination and refinement

The determination of the symmetry to use in a least-squares refinement can be problematic. The problem is especially severe in Me_3SO^+-exchanged vermiculite

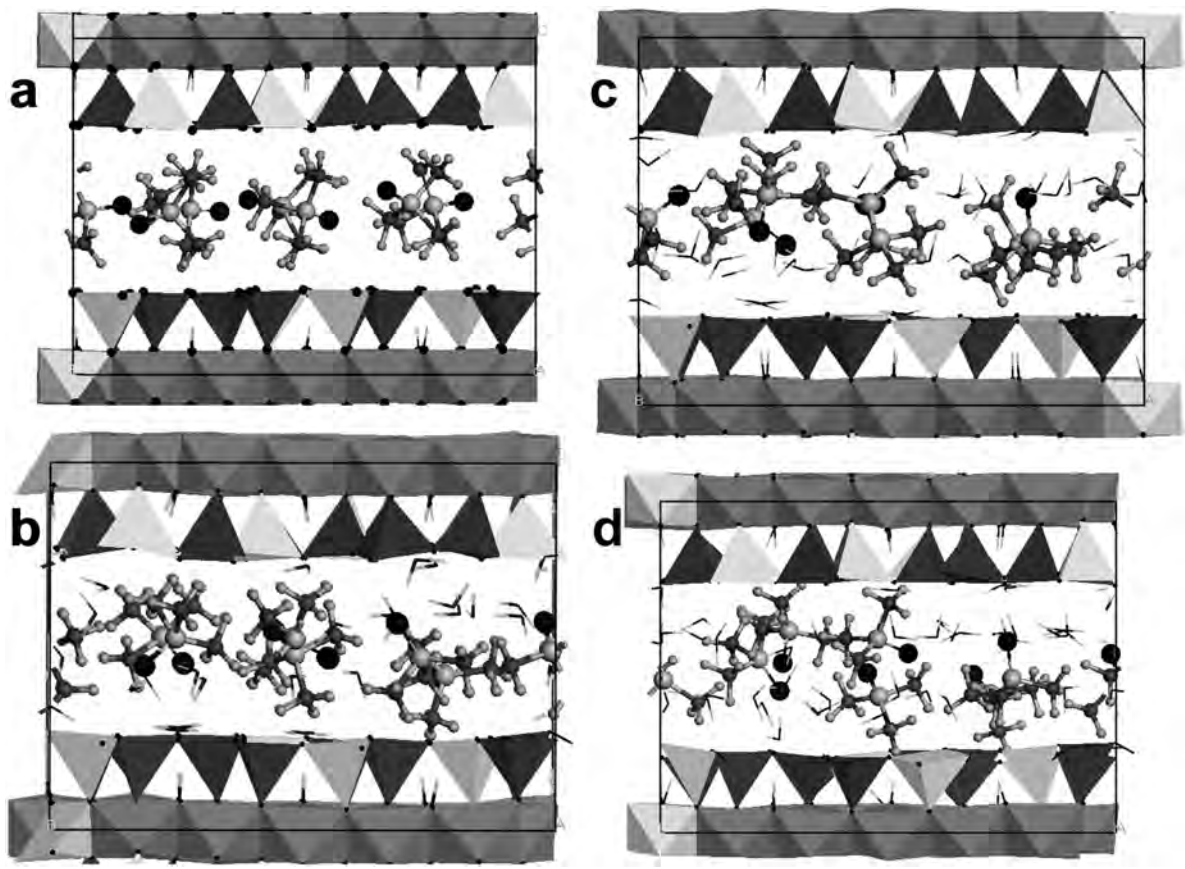

Figure 1. Optimized crystal structure of Me_3SO^+-exchanged vermiculite models: (a) vermiculite- model; (b) vermiculite-W3 model; (c) vermiculite-W4 model; (d) vermiculite-W5 model. Vermiculite 2:1 layers are represented as follows: Mg atoms are octahedral polygons, Al atoms are light-gray octahedral and tetrahedral polygons, and Si atoms are dark gray tetrahedral polygons. H and O atoms from water molecules are represented by light gray and black sticks, respectively. S, O, C, and H atoms from Me_3SO^+ molecules are represented by light gray, black, dark gray, and small light gray balls, respectively.

where the majority of atoms (*e.g.* those in the 2:1 layer) show high symmetry (*i.e. C*2 and C*m*) and dominate the diffraction pattern, and where a relatively small number of atoms (*e.g.* Me_3SO^+) is present that may not follow the same symmetry. In addition, the Me_3SO^+ molecules show positional disorder and have relatively low electron density per site occupied, thereby making the determination of symmetry more difficult. One approach is to make trial refinements in lower symmetry using plausible subgroups, as was done here. For example, one possible subgroup symmetry, *Cm*, is plausible if the Me_3SO^+molecule occurs on the mirror plane, with this plane bisecting the central S atom and the O atom of the Me_3SO^+ molecule. This refinement was unsuccessful.

Single-crystal, XRD methods provide data on the average structure of the material studied, because the least-squares method involves atom-position information over all the unit cells in the crystal. Another possible subgroup symmetry, *C*2, is plausible on a statistical basis with the 2-fold axis relating two sites with

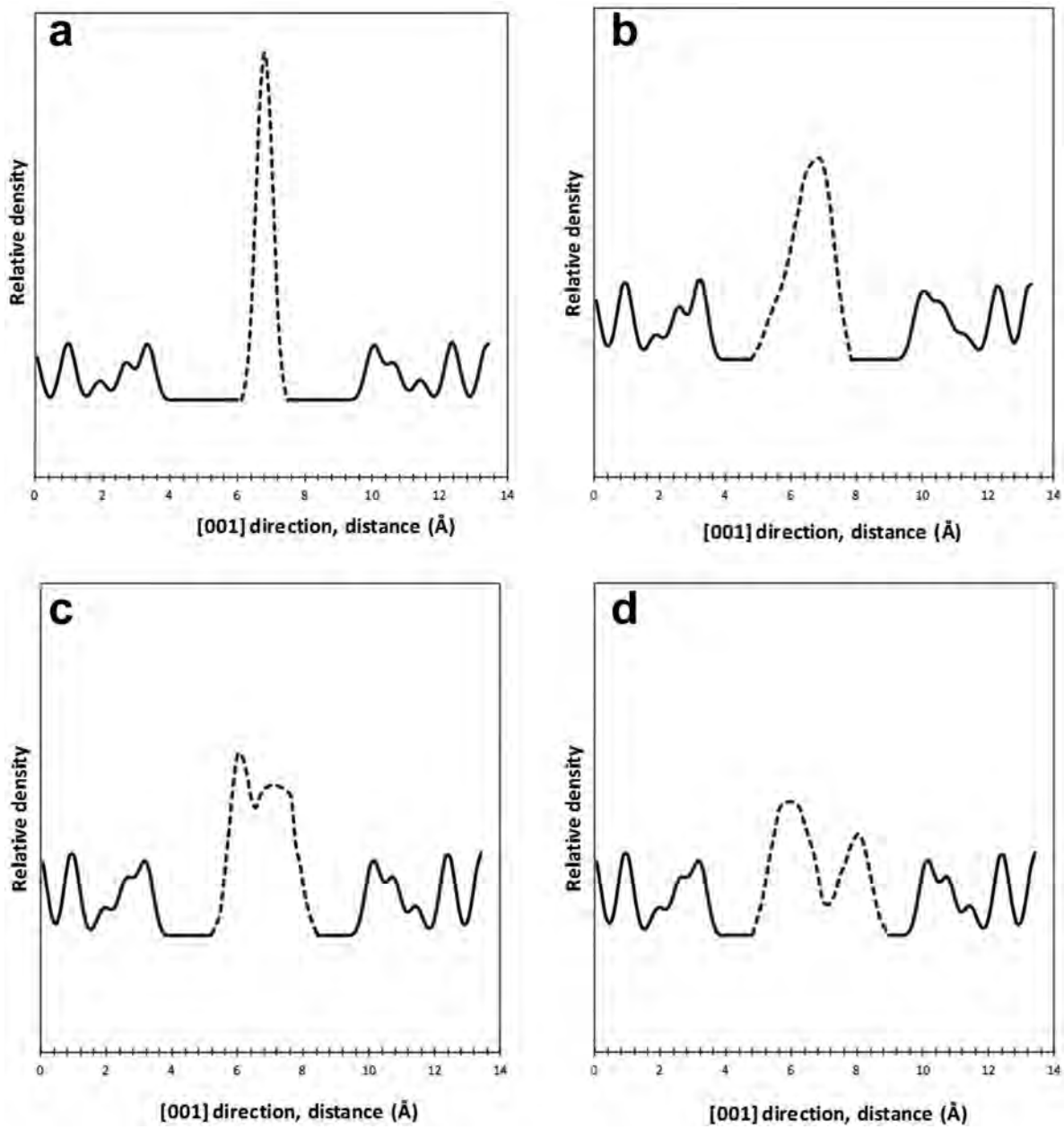

Figure 2. Electron density profiles along the *c* axis of the interlayer of vermiculite models: (a) vermiculite model; (b) vermiculite-W3 model; (c) vermiculite-W4 model; (d) vermiculite-W5 model. Dashed lines represent S atoms from molecules; black lines represent the 2:1 layer electron density of vermiculite.

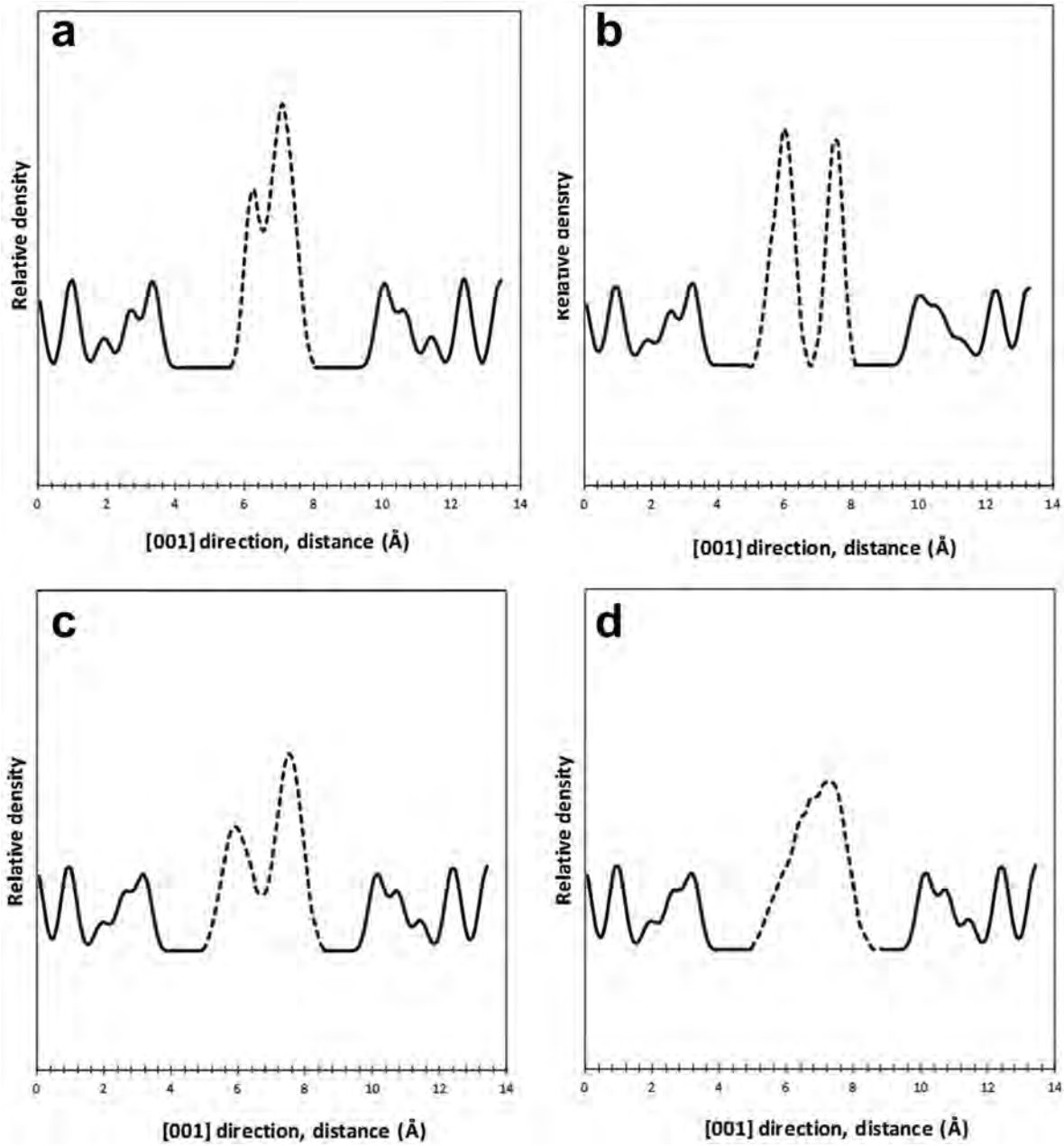

Figure 3. Electron density profiles along the *c* axis of the interlayer of vermiculite models: (a) vermiculite model; (b) vermiculite-W3 model; (c) vermiculite-W4 model; (d) vermiculite-W5 model. Dashed lines represent O atom from the molecules; black lines represent 2:1 layer electron density profiles of vermiculite.

Me_3SO^+molecules that are partially occupied in such a way that both sites are not occupied simultaneously. This refinement was also unsuccessful. Failure to obtain a successful refinement in *Cm* and *C*2 subgroup symmetries suggests that the parent space group of *C*2/*m* best describes the X-ray data. A third subgroup model, $C\bar{1}$, was not considered in detail and is considered to be very unlikely based on the results of the other subgroup models.

In space group *C*2/*m*, the resultant position for the sulfur atom (Table 1) shows a high isotropic displacement parameter near 11 $Å^2$. For inorganic crystal structures, a value this high may be an indication of a misplaced atom, but in this case there are several reasons why this may not be the case: (1) organic molecules often have high displacement factors relative to inorganic species (Stout and Jensen, 1968); (2) the residual *R* value dropped significantly when the S atom

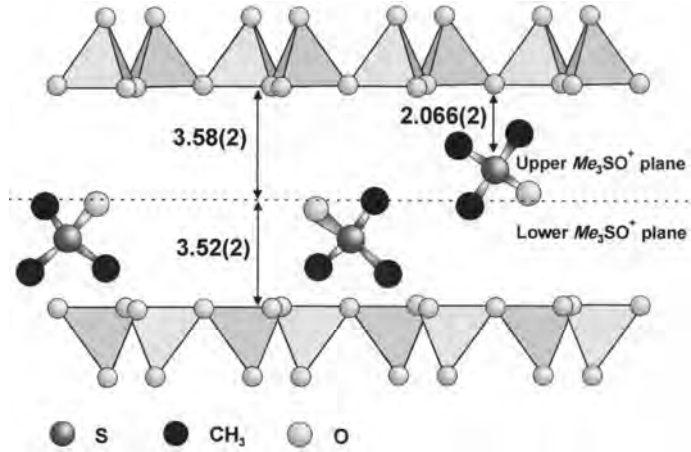

Figure 4. Diagram showing the Me_3SO^+ molecules in two distinct planes in the interlayer as projected down the [100]* direction. Various Me_3SO^+ orientations are shown. Sulfur-atom and oxygen-atom distances (Å) to the basal oxygen atom plane are given. Numbers in parentheses indicate estimated standard deviations, where 3.58(2) indicates 3.56 to 3.60 Å. The 2:1 layer is incomplete as shown.

was included in the refinement (wR = 0.196 to 0.151); (3) the high displacement parameter is probably indicative of the considerable positional disorder (see below) expected where electrostatic interactions exist between the interlayer molecule and substitutional disorder (Al *vs*. Si) within the silicate ring of the 2:1 layer; and (4) the S site location is crystallochemically reasonable.

The average interlayer structure and disordered H_2O

Because interlayer water molecules could not be located from the X-ray data, computer modeling was used to determine the effect of disordered H_2O on the position of the Me_3SO^+ molecule. Without H_2O present, models indicated that the Me_3SO^+ molecule would reside in a central plane between two adjacent 2:1 layers. This is the configuration found in the single-crystal X-ray refinement of TMA-exchanged fluorhectorite (Seidl and Breu, 2005). However, Vahedi and Guggenheim (1997), in TMA-exchanged experiments in water similar to the Me_3SO^+ sample preparation procedures used here, found that the Me_3SO^+ cation occurred in two planes in the interlayer, and the results were supported by the computational methods described by Martos-Villa *et al.* (2013).

Sulfur of the Me_3SO^+ molecule is offset by 0.160(4) Å from the center of the six-member ring of Si,Al tetrahedra of the 2:1 layer. The S is 2.066(2) Å from the basal-oxygen atom plane of each adjacent 2:1 layer; thus, Me_3SO^+ molecules are located in two planes in the interlayer (Figure 4). The planes are referred to as 'upper' and 'lower' Me_3SO^+ planes as labeled in Figure 4. The sulfur atom has an average distance of 4.06(2) Å from each tetrahedral cation of the nearest tetrahedral ring and 3.38(3) Å from each basal oxygen atom (O_b), nearest the plane in which the Me_3SO^+ resides (Figure 4). Three basal oxygen atoms (inner) are closer to the sulfur [S−O_b distance of 3.24(2) Å], and three (outer) are further away [S−O_b of 3.52(3) Å]. The S−O4 bond distance (where O4 is part of the Me_3SO^+ molecule) is 1.63(5) Å, as compared to 1.439(2) Å in trimethylsulfoxonium perchlorate (Kolinsky *et al.*, 1994). The short S−O bond distance in the trimethylsulfoxonium perchlorate structure is probably a consequence of repulsions between the oxygen atom of the Me_3SO^+ molecule and ClO_4^-.

The oxygen atom of each Me_3SO^+ molecule is located at the center of the interlayer, at 3.52(2) Å (lower Me_3SO^+ plane) or 3.58(2)Å (upper Me_3SO^+ plane) from the basal-oxygen plane of the tetrahedral sheet (Figure 4). Table 1 includes only one oxygen-atom position for the Me_3SO^+ group, but an electron-density map at the final stage of the refinement suggests considerable positional disorder around the sulfur atom for the oxygen atom, and the significance of this is discussed below for the ideal structure. Because the axis of the Me_3SO^+ tetrahedron is established by the S and O4 positions, methyl-group positions can be inferred. Possible methyl-group positions are discussed below. No H_2O molecules were found, but the possibility exists that they occur randomly in the interlayer because the crystal was exchanged in an aqueous solution and air dried. In the simulations, some water molecules are joined tightly to the tetrahedral O atom, forming strong hydrogen bonds of 1.45−1.70 Å to the basal O atoms and 1.48−1.79 Å to the H atom of the octahedral OH group. Hence, these strong interactions would make the release of water from the mineral particle more difficult. In addition, the interactions between water molecules and the Me_3SO^+ cations would make the release of H_2O from the interlayer even more difficult, and this is consistent with the standard hygroscopicity of the Me_3SO^+ halide salts.

The 2:1 layer

Calculated structural parameters for the Me_3SO^+-exchanged vermiculite are defined and given in Table 3. These determined values are similar to those obtained for the 2:1 layer (*i.e.* sheet thicknesses, α, ψ, and τ_{tet}) for the other onium-exchanged vermiculites (*cf.* table 5 of Vahedi-Faridi and Guggenheim, 1999b). The most notable deviation is the tetrahedral rotation angle, α, which describes the in-plane rotation of adjacent tetrahedra around the silicate ring that results in a ditrigonal distortion of that ring. The α value in the Me_3SO^+-exchanged vermiculite is 6.4º (*cf.* TMA, 7.1º; TMP, 6.75º), consistent with the TMA molecule being positioned more deeply in the silicate ring than the Me_3SO^+ molecule (TMA, N to basal-plane distance = 1.91 Å; Me_3SO^+, S to basal-plane distance = 2.07Å). Differences in positioning occur because of the smaller size of TMA relative to the Me_3SO^+ molecule and the effects of an oxygen atom apex of the Me_3SO^+ molecule (see below). Thus, the TMA molecule can better attract first nearest neighbor basal oxygen atoms than the Me_3SO^+ molecule, to produce a greater α value. Because, on average, TMP-exchanged vermiculite has TMP molecules associated with each bridging basal oxygen atom, a direct comparison with Me_3SO^+ in Me_3SO^+-exchanged vermiculite is limited.

The ideal (static) interlayer structure

Three important aspects of the 2:1 layer in developing a static model for the interlayer include: (1) a ditrigonal silicate ring is formed; (2) ditrigonal rings in adjacent sheets across the interlayer superimpose (hereafter referred to as 'paired rings') when viewed down the [001]* direction, and (3) Al cations may randomly substitute for Si in the tetrahedral sites. Because the average unit cell apparently contains multiple Me_3SO^+ locations, a model must involve two S sites that occur near one another, although not necessarily occupied simultaneously. The S−S and O(4)−O(4) distances between adjacent Me_3SO^+ molecules are given in Table 5. The O(4)−O(4) distances shown in Table 5 are the minimum and maximum distances between neighboring oxygen atoms with different apex orientations (*e.g.* Figure 4).

The favored model has S−S distances of 5.34(3) Å and O(4)−O(4) distances ranging from 4.38(5) to 5.43(4) Å. Alternatively (Figure 4), Me_3SO^+ molecules occur in side-by-side ditrigonal rings but alternate between Me_3SO^+ planes [*e.g.* S−S = 6.10(3) Å, O(4)−O(4) = 4.19(4)−4.30(4) Å]. The models involve one molecule per paired ring in either the same or opposite Me_3SO^+ planes. Thus, the Me_3SO^+ tetrahedron is 3.5 Å from the oxygen apex to the methyl group triad base, and the interlayer separation is 7.099 Å. Sufficient space is present for the occupation of two planes of Me_3SO^+ pillars with alternate occupancy of planes. Rejected models include cases where S−S and O(4)−O(4) distances are too short (*e.g.* where S−S occurs within a paired ring or where two Me_3SO^+ molecules occur in the same Me_3SO^+ plane but at side-by-side ditrigonal rings occurring in the same 2:1 layer).

Me_3SO^+ orientation. The S atom is the source of the positive charge, and it offsets the net negative charge on the 2:1 layer by locating itself, in projection, in the center of the ditrigonal ring of tetrahedra. The oxygen apex of the Me_3SO^+ tetrahedron is located on the central plane of the interlayer owing to electrostatic repulsions from the negatively charged and adjacent 2:1 layers on the margins of the interlayer. In Me_3SO^+ tetraphenyl-borate, Knop *et al.* (1994) found that the Me_3SO^+ orientation is related to lone pairs of electrons on the oxygen atom of the structure and the interaction between the Me_3SO^+ cation and phenyl groups. Likewise, the lone pairs on the oxygen atom in exchanged vermiculite may also affect the Me_3SO^+ orientation relative to the 2:1 layer structure because the oxygen apex of the Me_3SO^+ tetrahedron is located at the center plane of the interlayer. The oxygen atom is probably pointing, in projection, directly toward one of the six tetrahedral sites (Figure 5), presumably if occupied by Si^{4+} and not Al^{3+}.

The refined location of sulfur is an average position with an apparent high thermal displacement parameter (Table 1). This large B value of 11.13 $Å^2$ is explained by positional disorder of the S in response to its bond to the Me_3SO^+ oxygen. Because the oxygen atom is located in any one of six positions (pointing toward the tetrahedral sites) surrounding the sulfur, the sulfur position shifts slightly to accommodate the location of the oxygen.

Methyl-group orientation. The methyl-group orientation is determined from the S−O(4) axis orientation and charge requirements of the bridging oxygen atoms of the tetrahedra, because electron-density maps were unsuccessful in locating either C or H. The substitution of Al

Table 5. Select distances relating possible Me_3SO^+ sites.

Two Me_3SO^+ sites occupying:	S−S (Å)	O4−O4 (Å)
Same set of paired rings and opposite Me_3SO^+ planes	2.95(3)	0.056(3)−1.50(4)
Side-by-side ditrigonal rings in the same 2:1 layer and the same Me_3SO^+ plane	5.34(3)	4.38(5)−5.43(4)
Side-by-side ditrigonal rings but alternating between Me_3SO^+ planes	6.10(3)	4.19(4)−4.30(4)

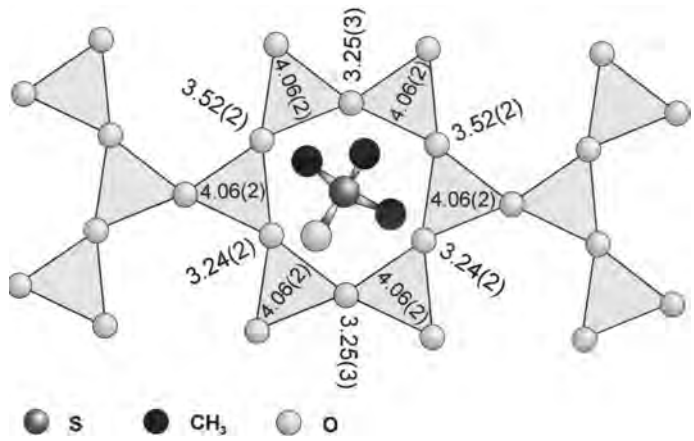

Figure 5. Sulfur-atom distance to the nearest tetrahedral plane of the adjacent 2:1 layer. Sulfur-atom to bridging-oxygen distances and sulfur atom to tetrahedral-cation distances (all distances as Å) are given. As noted in Figure 4, numbers in parentheses indicate estimated standard deviation, the projection is down the [001]* direction, and the 2:1 layer is incomplete.

in a tetrahedral site produces a positive charge deficiency of the associated bridging oxygen atom relative to Si, and a resulting attraction of the organic cation to the bridging oxygen atom. Covalent bonds were suggested by Loudon (1995) as possibly acting to enhance electrostatic effects; he considered the ionic character between atoms and the shared electrons of the covalent bond. For example, an oxygen atom can attract electrons from a covalent bond toward itself and, thus, is assigned a delta negative charge distribution. Equally, carbon atoms tend to repulse electrons from covalent bonds and are assigned a delta positive charge distribution. In Me_3SO^+, the methyl groups have a delta positive charge, and thus, satisfy the electrostatic character of the lone pair of the oxygen atom. Furthermore, the delta positive charge on the methyl groups will also aid in charge compensation of the charge-deficient bridging oxygen atoms in the tetrahedral sheets, and thus methyl groups may associate with these bridging oxygen atoms (Figure 6).

Santa Olalla vermiculite has a Si:^{IV}Al ratio of 5.48:2.52, or 1.33 Al ions per ditrigonal ring. The Me_3SO^+ molecules occupy 58% of the paired ditrigonal rings, and $\leqslant$66% of the rings may contain at least two Al. Where ditrigonal rings contain at least two tetrahedra occupied by Al, these tetrahedra are separated by at least one Si-tetrahedron (Loewenstein, 1954). Thus, ditrigonal rings may contain two Al substitutions (Figure 7). Although many combinations are possible for the locations of Al and Si, Figure 7 shows an arrangement to illustrate how the organic cation probably associates with the tetrahedral ring.

The tilt of the S−O(4) axis orients two methyl groups to point toward charge-deficient bridging oxygen atoms (note the arrows in Figure 7). Where a methyl group points toward a bridging oxygen atom of the tetrahedral sheet, the distance between a methyl hydrogen and the oxygen atom is ~1.84−2.45 Å, taken from the simulation models from the present study, and this may suggest that electrostatic interactions are occurring between the

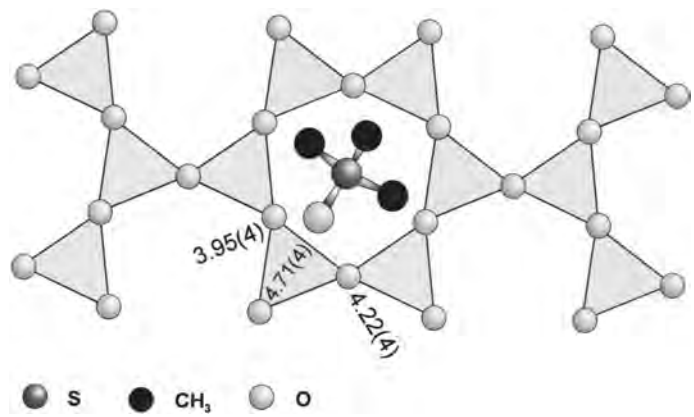

Figure 6. Distances (Å) of the oxygen atoms of the Me_3SO^+ molecule to bridging oxygen atoms of an associated tetrahedral cation site. See Figure 5 for information about the projection.

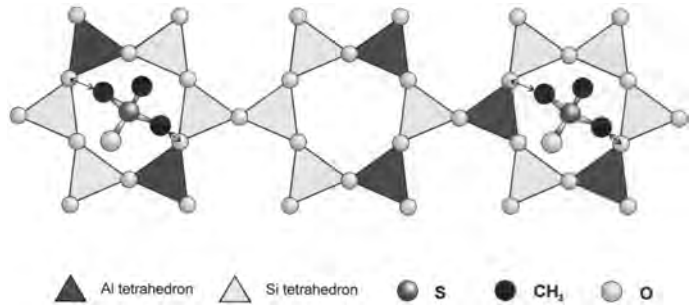

Figure 7. Several examples of Al substitution in the tetrahedral sheet. Each ring, on average, contains two Al atoms separated by at least one Si-bearing tetrahedron. Arrows indicate charge-deficient bridging-oxygen atoms closest to the methyl groups. See Figure 5 for information about the projection.

methyl hydrogen atoms and the bridging-oxygen atoms. When the methyl group is very close to the tetrahedral ring, the octahedral OH group tilts from its standard orientation perpendicular to the 001 plane, due to the repulsive interactions between the H atoms of the methyl and OH groups. The third methyl group is, thus, oriented in the interlayer as shown (Figure 7).

CONCLUSIONS

Organic pillars must charge compensate the bridging oxygen atoms of the 2:1 layer that are deficient in positive charge. Such charge deficiencies may occur either by tetrahedral substitutions, as commonly found in vermiculite, or by other substitutions elsewhere in the 2:1 layer. However, pillars with charge asymmetry, such as the Me_3SO^+ molecule, are required to position themselves such that the negative side of the molecule remains as far away from the 2:1 layer, an additional source of negative charge, as possible. To achieve this, the negative side of the molecule will align so that it resides midway between adjacent 2:1 layers.

In Me_3SO^+-exchanged vermiculite, the position of the Me_3SO^+ molecule is believed to be further stabilized by two methyl groups that can associate with bridging basal oxygen atoms of the ditrigonal silicate ring. Arguments involving lone pairs of electrons interacting within the Me_3SO^+ molecule suggest an electrostatic interaction between the methyl groups of the molecule and associated bridging basal oxygen atoms, rather than by hydrogen bonding. Thus, the ditrigonal aspects of the silicate rings that allow the approach of the methyl groups to the bridging basal oxygen atoms may, in part, be responsible for the alignment of the molecule where two methyl groups associate with the ditrigonal ring rather than an alternate arrangement where three methyl groups of the Me_3SO^+ tetrahedron might align with the ditrigonal ring. That the oxygen atom of the Me_3SO^+ molecule can position itself over a Si-containing tetrahedron may be further evidence of the veracity of the model presented here. The X-ray data suggest that H_2O molecules, if present, must be distributed randomly in the interlayer. The computer modeling confirms this conclusion.

If the asymmetry of charge distribution on the Me_3SO^+ molecule is influenced significantly by unshared electrons, the pillar may be a unique site for interlayer reactions. In addition, the attraction of the Me_3SO^+ molecule for fixing other molecules in the interlayer, such as environmental pollutants, may be enhanced by the effects of the unshared electrons.

ACKNOWLEDGMENTS

Dr A. Vahedi-Faridi is acknowledged and thanked for suggesting the project. The donors of The Petroleum Research Fund, administered by the American Chemical Society, are acknowledged for partial support of this research under grant PRF-32858-AC5. The U.S. National Science Foundation is acknowledged for support under grant EAR-0001122; the Junta de Andalucía is acknowledged for partial support under grant RNM-3581 CADHYS project; and the computational facilities of the Supercomputational Center of Granada University (UGRGRID) and Computing Center of CSIC are acknowledged also for support.

REFERENCES

Barrer, R.M. (1984) Sorption and molecular sieve properties of clays and their importance as catalysts. *Philosophical Transactions of the Royal Society of London*, **A311**, 333–352.

Barrer, R.M. (1989) Shape selective sorbents based on clay minerals: A review. *Clays and Clay Minerals*, **37**, 385–395.

Barrer, R.M. and Millington, A.D. (1967) Sorption and intracrystalline porosity in organo-clays. *Journal of Colloid Interface Science*, **25**, 359–372.

Barrer, R.M. and Perry, G.S. (1961) Sorption of mixtures, and selectivity in alkylammonium montmorillonites. *Journal of the Chemical Society*, 842–858.

Frisch, M.J., Trucks, G.W., Schlegel, H.B., Scuseria, G.E., Robb, M.A., Chesseman, J.R., Zarzewki, V.G., Montgomery, J.A., Stratmann, R.E., Burant, J.C., Dapprich, S., Millam, J.M., Daniels, A.D., Kudin, K.N., Strain, M.C., Farkas, O., Tomasi, J., Barone, V., Cossi, M., Cammi, R., Mennucci, B., Pomelli, C., Adamo, C., Clifford, S., Ochterski, J., Petersson, G.A., Ayala, P.Y., Cui, Q., Morokuma, K., Malick, D.K., Rabuck, A.D., Raghavachari, K., Foresman, J.B., Cioslowski, J., Ortiz, J.V., Stefanov, B.B., Liu, G., Liashenko, A., Piskorz, P., Komaromi, I., Gomperts, R., Martin, R.L., Fox, D.J., Keith, T.A., Al-Laham, M.A., Peng, C.Y., Nanayakkara, A., Gonzalez, C., Challacombe, M., Gill, P.M.W., Johnson, B.G., Chen, W.,

Wong, M.W., Andres, J.L., Head-Gordon, M., Replogle, E.S., and Pople, J.A. (2004) *Gaussian 03* (Revision A.1), Gaussian, Inc., Pittsburgh, Pennsylvania, USA.

Guggenheim, S. (2013) Glossary for clay science. Updated annually and can be down loaded at: http://www.clays.org/GLOSSARY/GlossIntro.html

Hernández-Laguna, A., Escamilla-Roa, E., Timón, V., Dove, M.T., and Sainz-Díaz, C.I. (2006) DFT study of the cation arrangements in the octahedral and tetrahedral sheets of dioctahedral 2:1 phyllosilicates. *Physics and Chemistry of Minerals*, **33**, 655–666.

International Tables for X-ray Crystallography (Volume 4: Revised and Supplementary Tables to Volumes 2 and 3) (1974) J.A. Ibers and W.C. Hamilton, editors. The Kynoch Press, Birmingham, England, pp. 71–147.

Knop, O., Cameron, S., Bakshi, P.K., Linden, A., and Roe, S.P. (1994) Crystal chemistry of tetraradial species. Part 5. Interaction between cation lone pairs and phenyl groups in tetraphenylborates: Crystal structures of Me_3S^+, Et_3S^+, Me_3SO^+, Ph_2I^+, and 1-azoniapropellane tetraphenylborates[1,2]. *Canadian Journal of Chemistry*, **72**, 1870–1881.

Kolinsky, C., Puget, R., de Braver, C., and Jannin, M. (1994) Structures of trimethyloxosulfonium salts VIII. New refinement of the perchlorate $(CH_3)_3SO^+.ClO_4^-$. *Acta Crystallographica*, Section C, 1514–1516.

Lee, J., Mortland, M.M., Chiou, C.T., Kile, D.E., and Boyd, S.A. (1990) Adsorption of benzene, toluene, and xylene by two tetramethylammonium-smectites having different charge densities. *Clays and Clay Minerals*, **38**, 113–120.

Loewenstein, W. (1954) The distribution of aluminum in the tetrahedra of silicates and aluminates. *American Mineralogist*, **39**, 92–96.

Loudon, G.M. (1995) *Organic Chemistry*, third edition. The Benjamin/Cummings Publishing Company, Inc., California, USA.

Martos-Villa, R., Guggenheim, S., and Sainz-Diaz, C.I. (2013) Interlayer water molecules in organocation-exchanged vermiculite and montmorillonite: A case study of tetramethylammonium. *American Mineralogist*, **98**, DOI: 10.2138/am.2013.4370.

Norrish, K. (1973) Factors in the weathering of mica to vermiculite. Pp. 417–432 in: *Proceedings of the International Clay Conference 1972* (J.M. Serratosa, editor). Division de Ciencias, CSIC, Madrid.

Perdew, J.P., Ruzsinszky, A., Csonka, G.I., Vydrov, O.A., Scuseria, G.E., Constantin, L., Zhou, X., and Burke, K. (2008) Restoring the density-gradient expansion for exchange in solids and surfaces. *Physical Review Letters*, **100**, 136406.

Ruiz-Conde, A., Ruiz-Amil, A., Perez-Rodriguez, J.L., Sanchez-Soto, P.J., and Aragan de la Cruz, F. (1997) Interaction of vermiculite with aliphatic amides (formamide, acetamide and propionamide): Formation and study of interstratified phases in the transformation of Mg- to NH_4-vermiculite. *Clays and Clay Minerals*, **45**, 311–326.

Sainz-Diaz, C.I., Palin, E.J., Hernández-Laguna, A., and Dove, M.T. (2003) Octahedral cation ordering of illite and smectite. Theoretical exchange potential determination and Monte Carlo simulations. *Physics and Chemistry of Minerals*, **30**, 382–392.

Sainz-Díaz, C.I., Escamilla, E., and Hernández-Laguna, A. (2005) Quantum mechanical calculations of trans-vacant and cis-vacant polymorphism in dioctahedral 2:1 phyllosilicates. *American Mineralogist*, **90**, 1827–1834.

Seidl, W. and Breu, J. (2005) Single crystal refinement of tetramethylammonium-hectorite. *Zeitschrift für Kristographie*, **220**, 169–176.

Soler, J.M., Artacho, E., Gale, J.D., García, A., Junquera, J., Ordejón, P., and Sánchez-Portal, D. (2002) The SIESTA method for ab-initio order-N materials simulation. *Journal of Physics: Condensed Matter*, **14**, 2745–2779.

Stout, G.H. and Jensen, L.H. (1968) *X-ray Structure Determination: A Practical Guide*. John Wiley and Sons, Inc., New Jersey, USA.

Troullier, N. and Martins, J.L. (1991) Efficient pseudopotentials for plane-wave calculations. *Physical Reviews B*, **43**, 1993–2006.

Vahedi-Faridi, A. and Guggenheim, S. (1997) Crystal structure of tetramethylammonium-exchanged vermiculite. *Clays and Clay Minerals*, **45**, 859–866.

Vahedi-Faridi, A. and Guggenheim, S. (1999a) Structural study of tetramethylphosphonium-exchanged vermiculite. *Clays and Clay Minerals*, **47**, 219–225.

Vahedi-Faridi, A. and Guggenheim, S. (1999b) Structural study of monomethylammonium and dimethylammonium-exchanged vermiculites. *Clays and Clay Minerals*, **47**, 338–347.

(*Received 25 February 2013; revised 26 April 2013; Ms. 744; AE: H. He*)

Clays and Clay Minerals, Vol. 61, No. 3, 231–257, 2013.

MINERALOGICAL AND CHEMICAL PROPERTIES AND THE ORIGIN OF TWO TYPES OF ANALCIME IN SW ANKARA, TURKEY

NECATI KARAKAYA[1], MUAZZEZ ÇELIK KARAKAYA[1,*], AND ABIDIN TEMEL[2]

[1] Selçuk Universitesi Mühendislik Fakültesi, Jeoloji Müh. Böl. Konya, 42079, Turkey
[2] Hacettepe Üniversitesi Mühendislik Fakültesi, Jeoloji Müh. Böl. 06800 Ankara, Turkey

Abstract—Authigenic analcimes were observed in different amounts in Miocene units in central Anatolia, Turkey. Two types of analcime occurrences were defined: (1) as continuous but inhomogeneous concentrations varying from 3 to 75 wt.% in lacustrine sedimentary rocks; and (2) as low concentrations (between 3 and 20%) and discontinuous components in the tuffs and claystones intercalated with tuff. The type 2 analcimes have been investigated by many researchers while the origin and properties of the sedimentary analcimes, which are widespread in different parts of Turkey, have not been clarified. The present study focused on the genesis and the mineralogical and geochemical properties of both types of analcime. The analcimes were investigated using X-ray diffraction, optical microscopy, scanning electron microscopy, and chemical analytical methods. In the first type, other than volcaniclastic material, analcime is the only zeolite mineral. The first type of analcime was associated mainly with montmorillonite, dolomite, and feldspar and sometimes with calcite, and rarely with illite and kaolinite. The second type of analcime was found as an accessory mineral accompanied by montmorillonite, feldspar, and heulandite/clinoptilolite, and more rarely by erionite, kaolinite, and mica. The pyroclastic rocks are chemically classified into two subgroups, dacitic and andesitic rocks, with an intermediate to high silica content and a high percentage of alkali cations. Analcime in the pyroclastics intercalated with clay layers commonly replaced early-formed zeolites, such as clinoptilolite or volcanic materials. The first type of analcime was not formed from precursor zeolites and had a different origin than the second type. Type 1 analcime contains larger amounts of Si (34.19 to 34.68 Si per unit cell) and less Al and Na than in theoretical analcime. The theoretical structural formula of analcime is $Na_{16}(Al_{16}Si_{32}O_{96})H_2O$. The strongly decomposing feldspar and clay minerals (in particular montmorillonite and partially illite) of the older formations and the dissolution of halite and also soda minerals, *e.g.* thenardite and glauberite, allow the authigenic formation of type 1 analcime, dolomite, K-feldspar, and montmorillonite in a saline and highly alkaline environment such as the marginal part of Lake Tuzgölü. Type 2 analcime may have been precipitated directly from solution, pyroclastic material, or precursor zeolite minerals in saline and alkaline lake water.

Key Words—Analcime, Central Anatolia, Clinoptilolite, Zeolite, Turkey.

INTRODUCTION

Specific environmental conditions are required for the formation of zeolites in sedimentary environments, *e.g.* composition of the volcanic material, water temperature (30−45ºC), and pH (between 8 and 9) (Hay, 1966; Sheppard and Gude, 1969; Ataman and Beseme, 1972; Surdam and Parker, 1972; Gündoğdu *et al*., 1996, Temel and Gündoğdu, 1996). In several cases analcime has been identified in lacustrine sediments free of associated volcaniclastic material (Hay, 1966; Sheppard and Gude, 1969; Gall and Hyde, 1989; Remy and Ferrell, 1989; Renaut, 1993; English, 2001; Karakaş and Kadir, 2006; Kadir *et al*., 2008). The physico-chemical conditions necessary to form analcime from non-volcanic materials in lacustrine sediments have been studied (Ataman and Gündoğdu, 1982; English, 2001; Campo *et al*., 2007). English (2001) noted the importance of saline groundwater and a siliceous gel as precursors for analcime precipitation, while Campo *et al*. (2007) suggested that analcime was formed by direct precipitation or through reactions between interstitial brines and either clay or feldspar minerals. The occurrences of analcime, other zeolite minerals, and deposits from volcanic and non-volcanic sediments have been studied in different parts of Anatolia (Ataman and Beseme, 1972; Ataman, 1976; Ataman and Gündoğdu, 1982; Helvacı *et al.*, 1993; Esenli and Özpeker, 1993; Gündoğdu *et al*., 1996; Temel and Gündoğdu, 1996; Kaçmaz and Köktürk, 2004; Esenli and Sirkecioğlu, 2005; Şahin, 2007; Snellings *et al*., 2008; Özen and Göncüoğlu, 2011). The deposits from volcanic sources were formed in saline and alkaline lakes, and some of them cover wide areas and are economically important. The authigenic analcime in saline environments was formed from a saline solution with volcanic materials (Hay, 1966, 1968, 1970; Sheppard and Gude 1968; Iijima and Hay, 1968; Surdam and Paker, 1972; Surdam and Eugster, 1976; Gottardi and Obradovic, 1978; Ataman and Gündoğdu, 1982).

* E-mail address of corresponding author:
mzzclk@hotmail.com
DOI: 10.1346/CCMN.2013.0610306

Analcime-bearing tuffs and sedimentary rocks have been described in Tertiary units in central and western Anatolia (Ataman and Gündoğdu, 1982). Analcime occurrences in both non-volcanic and pyroclastic rocks are widespread in the Neogene grey-greenish marl layer and mudstone west of Ankara (Ataman and Gündoğdu, 1982) according to the above-mentioned authors. The marl layer is 10−20 cm thick, contains >60% analcime, and has been defined as "analcimolite" (Sheppard and Hay, 2001). The analcime is associated with smectite, dolomite, and feldspar and is partially associated with calcite, but rarely with mica, kaolinite, or quartz.

The formation of analcime has been observed in sedimentary rocks as well as in volcanoclastic rocks, but had not previously been studied in the present study area. The origin of the sedimentary analcimes from another part of Turkey has been clarified (Ataman and Gündoğdu, 1982). The lithological properties of the analcimes defined by the above-mentioned authors are similar to those of the analcimes investigated here. Analcime occurrences in the two types of lithologies were identified in the northwestern part of the Tuzgölü (salt lake) basin in central Anatolia, where volcanic rocks are also common. Therefore, Na_2O which is an important oxide for analcime mineralization could have been sourced from a wide variety of origins. Type 1 authigenic analcime was observed in sedimentary rocks, while type 2 was observed in mainly tuff intercalated with clay layers and in clay beds, and in many places with clinoptilolite and rarely erionite minerals from the zeolite group. The present authors suggest that type 1 formed either by direct chemical precipitation or by the reaction of non-zeolite precursors while the type 2 was derived from precursor zeolites and/or volcanic material in the saline, alkaline basin. The present study sought to: (1) determine the mineralogical and morphological characteristics of the two analcimes types; (2) investigate the mineralogical and geochemical properties of type 1 analcime; (3) explain the origins of the two types of analcime; and (4) compare features of the two analcime types.

GEOLOGICAL SETTING

The study area is located in the northwestern part of the Tuzgölü fore-arc basin (Görür *et al*., 1984), which is the largest interior basin in central Anatolia in the eastern Mediterranean. The basin formed on the Menderes–Taurides Platform during the Late Cretaceous–Tertiary (Okay *et al*., 2001; Gürer and Aldanmaz, 2002) (Figure 1). In the study area, an ophiolitic mélange known as Ankara mélange is found as a basement rock and is also the oldest unit in the study area. The mélange comprises peridotite, diorite, serpentinite, metachert, spilite, radiolarite, and recrystallized limestone blocks. The basement rock of the Tuzgölü basin is unconformably overlain by Late Cretaceous–Eocene marine sediments formed from reddish-greenish-gray thin- to medium-bedded siltstone-sandstone at the base and claystone, marl, and sandstone-siltstone interbedded with thin-bedded mudstone in the upper part (Karakaya *et al*., 2012 and references therein). Tectonically, the mélange covers the Küredağ or Aktepe formation in the study area. Limited exposure

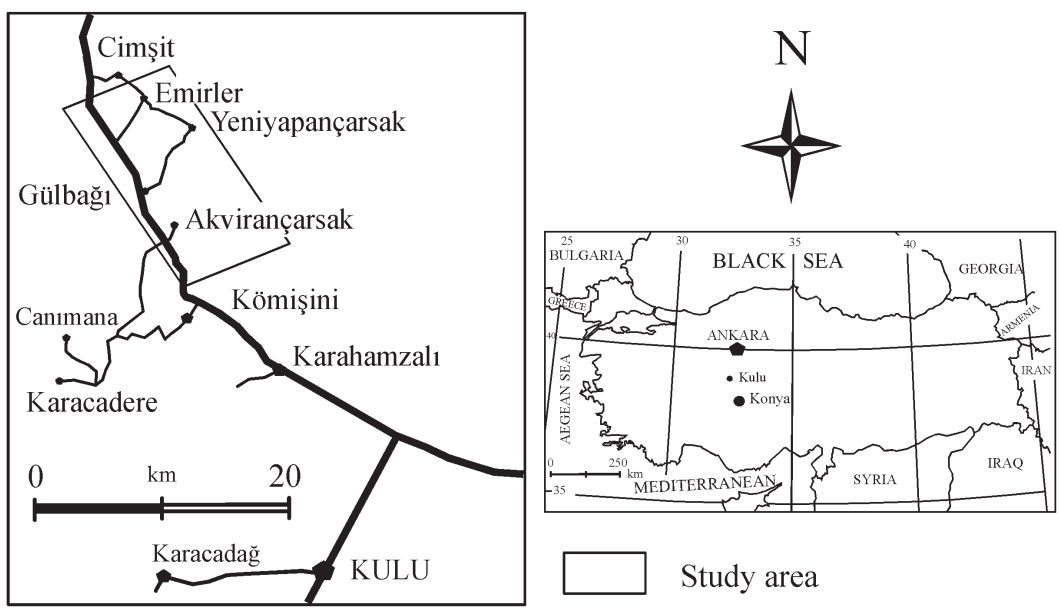

Figure 1. Location map showing Ankara, Konya, Kulu, and other localities in the study area. The area is located in the southeastern part of the Tuzgölü Basin in central Anatolia.

of the Maastrichtian–Paleocene Sarıkaya formation has been noted (Uğuz *et al*., 1999). The formation contains thin- to medium-bedded, greenish-beige-colored fossiliferous clayey limestone, siltstone, and marl. Although, the Küredağı formation rests conformably on the Sarıkaya formation, the boundary of the formations was not observed. The Middle Eocene Küredağı formation consists of wine, green, and greenish-gray colors and thin- to medium-bedded conglomerate, sandstone, siltstone, claystone, and marl interlayers. Tuff, agglomerate, and lava interlayers in the formation were recognized ~50 km NW of the study area (Uğuz *et al.*, 1999), but the volcanics were not observed in the study area. The early Miocene sediments known as the Aktepe formation rest unconformably on the underlying units, but the Ankara mélange overlies tectonically the formation in some part of the study area. The formation consists of conglomerate at the base and is interbedded with sandstone, siltstone, claystone, marl, and limestone. The formation passes laterally and vertically into Karacadağ volcanites in the upper levels of the sequence in the basin. During the Late Miocene–Pliocene period, radical tectonic changes occurred all over Anatolia (Uğuz *et al*., 1999). As a result, the Anatolian plate

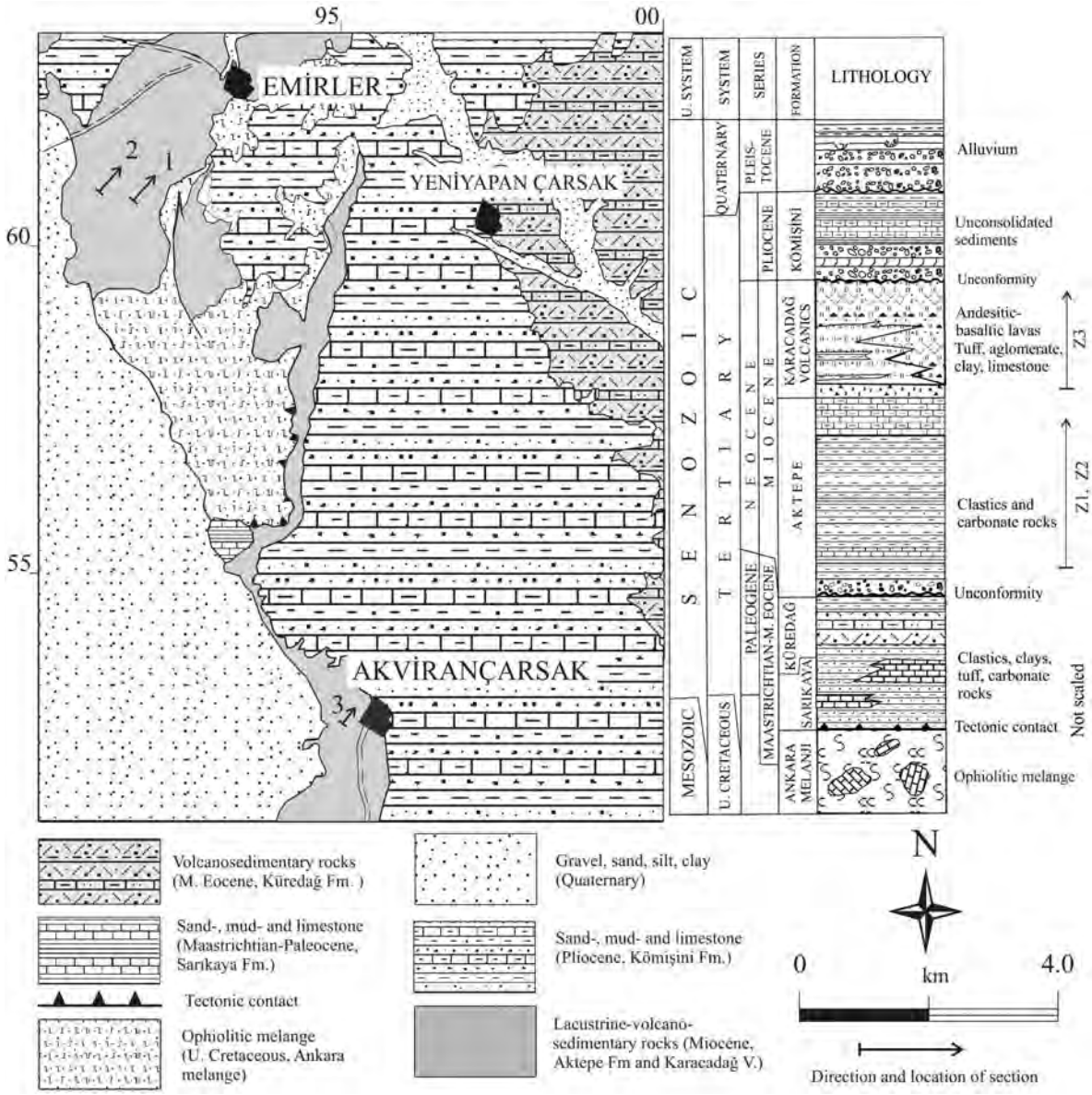

Figure 2. Map showing geology, generalized stratigraphic sections (simplified from MTA 1:100,000 scaled map and Uğuz *et al*., 1999, respectively), and sample localities in the study area.

Table 1. Mineralogy and mineral contents (wt.%) of the samples as inferred from the powder XRD results (rare components were omitted).

Sample number	Sme	Anl	Dol	Cal	Fsp	Bio/Ms	Kln	Qz	Cpt	Eri
Z1-1	46	11	35		5			3		
Z1-2	30	32	6	30				2		
Z1-3		53	43		2			2		
Z1-4	50	17	8	18	3			4		
Z1-5	22	9	41	8	16			4		
Z1-6	38	8	8	16	18	7	6	7		
Z1-7	45	27	12	14				2		
Z1-8	6	15	54		20			5		
Z1-9	6	15	54		20			5		
Z1-10	38	33	21		4			4		
Z1-11	12	40	45					3		
Z1-12	46	20	27		5			3		
Z1-13	48	9	27		11			5		
Z1-14	30	15	25		13	10	4	3		
Z1-15	35	24	26		9			6		
Z1-16	35	8	33		17			7		
Z1-17	77		12		6			5		
Z1-18	42	19	25		8			5		
Z1-19	17	4	17	20	26		4	12		
Z2-1	42	14	5	15	10	6	4	4		
Z2-2	10	65	15		5			6		
Z2-3	23	50		16	8		2			
Z2-4	23	43	10	9	6			4		
Z2-5	29	15	50		3			3		
Z2-6			14	80				5		
Z2-7	52	17		16	8			7		
Z2-8	42	6		21	24			7		
Z2-9	12	41		21	18			8		
Z2-10	18	7	37		30			8		
Z2-11	56	16		11	6		5	6		
Z2-12	37	7	23		16	6	4	9		
Z2-13	41	12	29		6	3	4	5		
Z2-14	44	10	12		12	7		6		
Z2-15	53	11	20		7	2	2	5		
Z2-16	64		6	9	9	6		6		
Z2-17	36	6	27		17	5	2	7		
Z2-18	68		6	10	8	3		5		
Z2-19	38	4	11	21	17			9		
Z2-20	58	13	19		6			4		
Z2-21/1	56	7	19		13			5		
Z2-21/2	45		6		17			32		
Z2-22	67	13	11		5			4		
Z2-23/1	51		25	8	11			5		
Z2-23/2			96	3				1		
Z2-24	55		19		18			8		
Z2-25/1	30	3	24		22	12		9		
Z2-25/2	65	6	20		5			4		
Z2-25/3	79	10			6			5		
Z2-25/4	49	5	24		15			7		
Z2-25/6	50	7		10	20		5	8		
Z2-26	43		26		21			10		
Z2-27		7	47		38			8		
Z2-28	52	3	20		17			8		
Z2-29	44	33			18			5		
Z2-30	46	7	27		15			5		
Z2-31		75	10		5			10		
Z2-31/1	10	70	10		6			4		
Z2-31/2	33	10	18	6	27			6		
Z2-31/3	25	20	7	18	12	10	3	3		
Z2-32	53	22	11	12				2		
Z3-1		8			9		4	2	77	

Table 1 (*contd*.)

Sample number	Sme	Anl	Dol	Cal	Fsp	Bio/Ms	Kln	Qz	Cpt	Eri
Z3-2		12			10			8	61	8
Z3-3	45	20	20	4	7			4		
Z3-4	50	3	18		10			7	12	
Z3-5									60	40
Z3-6/1	63	14			8			6	9	
Z3-6/2	6	5	82		3			4		
Z3-7	33				43	10		14		
Z3-8	8				50			3	16	23
Z3-9/1					16				80	4
Z3-9/2						3		4	47	46
Z3-10										
Z3-11	43	14			35			8		
Z3-12	55	2		9	15		11	8		
Z3-13	46	7			22		21	4		
Z3-14						2			73	25
Z3-15						5		3	92	
Z3-16	44	14	20		9	5		8		
Z4-1		11			8			7	66	8
Z4-2	35	15	20		10			7	10	3
Z11-2	20	26		5	18	6		4	22	

Anl: Analcime, Bio: Biotite, Cal: Calcite, Dol: Dolomite, Eri: Erionite, Cpt: Heulandite/Clinoptilolite, Fsp: Feldspar, Kln: Kaolinite, Ms: Muscovite, Qz: Quartz, Sme: Smectite (abbreviations from Whitney and Evans, 2010).

was created, and predominantly calc-alkaline volcanic rocks developed above the oceanic slab of the Afro-Arabian plate (Innocenti *et al*., 1975; Pasquar *et al*., 1988). Late Miocene volcanites observed west and south-west of the basin are mainly of high-K calc-alkaline composition in the central Anatolian region. The volcanic rocks are predominantly andesitic to dacitic, are partly basaltic in composition, and contain andesite, basalt, basaltic andesite, and basaltic trachyandesite and pyroclastics that were produced by different episodes of Karacadağ volcanism; and they are widespread west to south-west of the study area. Miocene–Pliocene fluvial-lacustrine carbonates and clay beds are intercalated with the pyroclastics mainly in tuff but rarely in lava layers. The age of volcanism was determined to be Middle Miocene (19 to 18 my) by Kurt *et al*. (2008). The real distribution and relation of the lacustrine sediments and volcaniclastics indicate that the Aktepe formation occurred before the Karacadağ volcanism. Volcaniclastics and sometimes thin lava layers (10–30 cm) from the volcanism were observed in the upper levels of the Aktepe formation. All of the older units were covered unconformably by Pliocene–Quaternary alluviums (Figure 2).

MATERIALS AND METHODS

Type 1 analcime was found in marginal lacustrine mudstones and associated sandstones, siltstones, and carbonates, and was studied in outcrops SW of Emirler village. Type 2 consisted of analcime-poor tuff/tuffites associated with mudstones and was studied in outcrops east of Akvirançarsak village (Figure 1). Type 1 is situated stratigraphically below the type 2.

Eighty-five representative samples were collected from three sections, and tuff and lava samples were taken randomly from around section 3 in the study area (Figure 2). All samples were ground gently for 5 min to a size of <20 μm in a Fritsch mill Pulverisette in preparation for X-ray diffraction (XRD) and chemical analysis. Mineralogical analyses (total fraction) of the samples were performed at Hacettepe University (Ankara, Turkey) on randomly oriented samples using XRD (Rigaku D/MAX 2200 PC, CuKα radiation with a tube voltage and current of 40 kV and 40 mA, respectively) with a scanning speed of 2°/min from 2 to 70°2θ. The <2 μm clay fraction was obtained by the gravitational sedimentation of the purified samples. The mineral proportions were determined from the powder XRD patterns following an external standard method developed by Gündoğdu (1982) and combined chemical analysis (Table 1). All samples were similarly mounted according to the Temel and Gündoğdu (1996) and Gündoğdu (1982) methods, and the characteristic peak intensities (*I*) of the minerals (2.89 Å for dolomite, 3.04 Å for calcite, 3.40 Å for aragonite, 3.96 Å for clinoptilolite, 3.42 Å for analcime, 3.34 Å for quartz, 3.18–3.20 Å for feldspar, 4.04 Å for Opal-CT, 10 Å for micas) were normalized to that of the (104) reflection of dolomite. In other words, a K factor for each mineral (including clays with 4.45–4.46 Å peaks between 19 and 20°2θ) was determined by $K = I_{dolomite}/I_{mineral}$ in a 1:1

dolomite-mineral mixture by weight. The mineral percentages were calculated from the following equation:

$$\% \text{ of mineral } a = (100 \times K_a \times I_a)/(K_a \times I_a + K_b \times I_b + \ldots\ldots\ldots K_n \times I_n)$$

where I is the mineral intensity as defined above and K is the ratio of the dolomite to mineral intensities.

The accuracy of the method is reported by the authors to be less than ±15%. The sizes and morphological features of the submicroscopic zeolite minerals of analcimes and their interrelations with other minerals were determined using scanning electron microscopy (SEM); energy dispersive X-ray spectroscopy (EDS) was used for elemental composition. Both sets of analyses took place at Selçuk University (Zeiss Evo LS-10 instrument, Cambridge, UK) and Afyonkarahisar Kocatepe University (LEO 1430 VP Zeiss instrument, Cambridge, UK). The SEM was equipped with EDS and back-scattered electron imaging (BSE), and the accelerating voltage was in the range 15−20 kV with a probe current of 15 mA and a spot size of 5 μm to identify the mineral composition. The sample was dispersed over a sample holder and gold sputtered for EDS analysis. The samples were dried at 50ºC for 1 h and coated with gold to a thickness of 5 μm. A ZAF calculation program was used to calculate the wt.% of major oxides at each point.

The total abundances of the major oxides and the minor, rare-earth, and refractory elements of rock samples were determined by ACME Laboratories (Vancouver, British Columbia, Canada) using inductively coupled plasma optical emission spectrometry and mass spectrometry (Spectro ICP-OES and Perkin Elmer ELAN 9000 ICP-MS, USA, respectively). Samples (0.1 g) were fused in Li-metaborate/tetraborate and digested with nitric acid. Loss on ignition (LOI) was determined by weight difference after ignition at 1000ºC. Total organic carbon (TOC) and sulfur were also measured by ACME Laboratories (Leco CS230). In addition, a separate 0.5 g portion of each sample was digested in Aqua Regia and analyzed by ICP-MS for precious and base metals, *e.g.* Al, Fe, Ti, Co, Cd, Zr, Ga, and Nb.

Microprobe analyses of the first type of representative analcime crystals were performed by wavelength dispersive spectroscopy (WDS) with a JEOL 8600 electron microprobe at the University of Georgia, (Athens, USA). Natural and synthetic orthoclase and labradorite mineral standards were analyzed as primary standards to monitor accuracy and precision. The WDS running conditions included a 15 kV accelerating voltage, 15 nA beam current, and an analytical spot size of ~1 μm. The X-ray intensities were corrected using the *Phi-Rho-Z* matrix correction software of Armstrong (1988).

RESULTS

Field observation

Analcime-bearing lacustrine sediments and volcanosedimentary rocks were identified in the Aktepe formation and Karacadağ volcanites with intercalated clay beds (Figure 2). Alternating psammitic, pelitic, silty, and carbonaceous layers were characterized by spotty or irregularly bedded structures at sections 1 and 2 (Figure 3a). The base of the Aktepe formation was observed and the sections were measured in the bottom levels of the formation. The detailed lithologic properties and thicknesses of the layers are shown in Figure 3. The fine-grained material alternates occasionally with coarse-grained sediments without any noticeable regularity in grain size. The marl-mudstones are pale green to beige, slightly silty, and commonly tightly compacted and they show conchoidal to subconchoidal fracture (Figure 3b). A gradation to limestone and dolostone is inconcpicuous, while silt and sandstone are apparent. Mudstone beds range from a few centimeters to a few

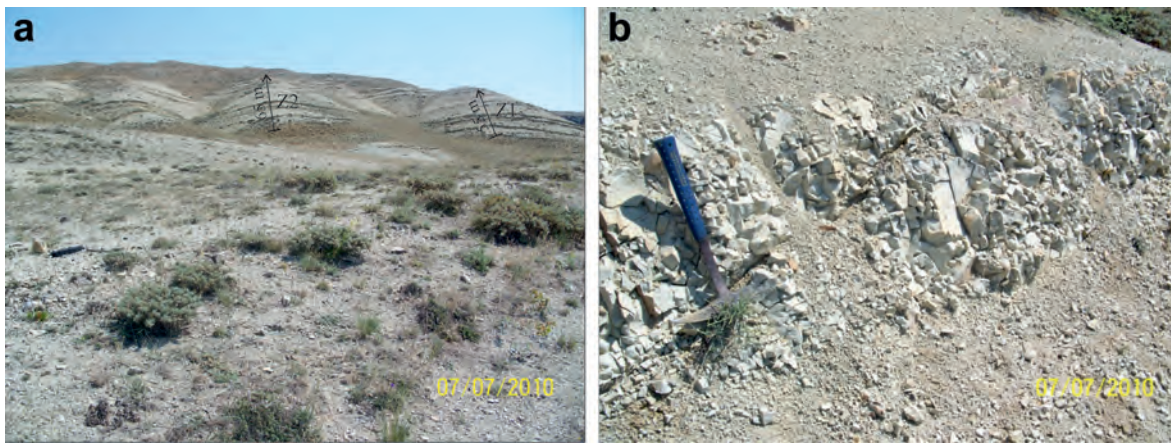

Figure 3. (a) Field photographs showing the locations of the Z1 and Z2 sections of the type 1 analcime-rich sedimentary rocks and (b) photograph showing the Z1 section close up.

meters thick and are commonly truncated, especially by dolostone and limestone. The thicknesses of the limestone layers increase especially toward the upper part of the sequence, and reach maximum thicknesses of up to 3−5 m. The upper levels of the unit are eroded, and thin (*e.g.* 5−10 cm) alluvial sediments cover the sections partially. Although volcanoclastic sediments are absent from the sequence, they are located above the Aktepe formation and depend on spatial distribution and structural state (sequence Z-3, Figure 4).

Poorly sorted, clay-cemented gravelstone was observed at the base of section 3. Gray, greenish, and reddish to dark reddish mudstone is above the gravelstone and alternates with volcanic mud flows, tuff, agglomerate, and lava. However, thin marl and limestone are observed near the bottom of the sequence; a lateral continuation of the layers is truncated. White tuff layers are closely condensed and thin in places; silty and clay layers are found between the tuffs (Figures 4, 5). The clinoptilolite-rich tuff layers are between 0.2 and 4.0 m thick, while the clay layers are between 0.1 and 0.5 m thick. Some of the pale green-, greenish-yellow-, white-, and gray-colored lacustrine marl and siltstone contain thin coal layers (2−10 cm) and small gypsum crystals (1−2 cm).

Mineralogy

A petrographic examination of type 1 analcime in the sand- and mudstone supports the field observation that the rocks are generally massive and structureless. No remnants of volcanic material or its texture exist. The mudstones consist of varying proportions of silt-sized analcime, quartz, feldspar, and micas in a fine-grained matrix of clayey and clayey-carbonate materials. In the marls, analcime is found with smectite, dolomite, rarely calcite, feldspar, and quartz in a carbonate and clay matrix. Both microcrystalline (<0.01 mm in size) and medium-crystalline (~0.5 mm in size) pale brown analcime aggregates are observed in transmitted light. The relatively coarse-grained, mostly euhedral to subhedral analcime crystals are equal in size, clear, and isotropic, but some are slightly birefringent near the edges (Figure 6a). Milky or mottled brown fine inclusions were observed in reflected light in some of the analcime crystals. The analcime content in the rocks ranges from 1 to 75 vol.%.

Mineralogical and petrographical studies showed that the type 2 analcime is found in tuff and intercalated clay beds. The tuffs consist of plagioclase, biotite, quartz, and some amphiboles and oxide minerals. A predominantly

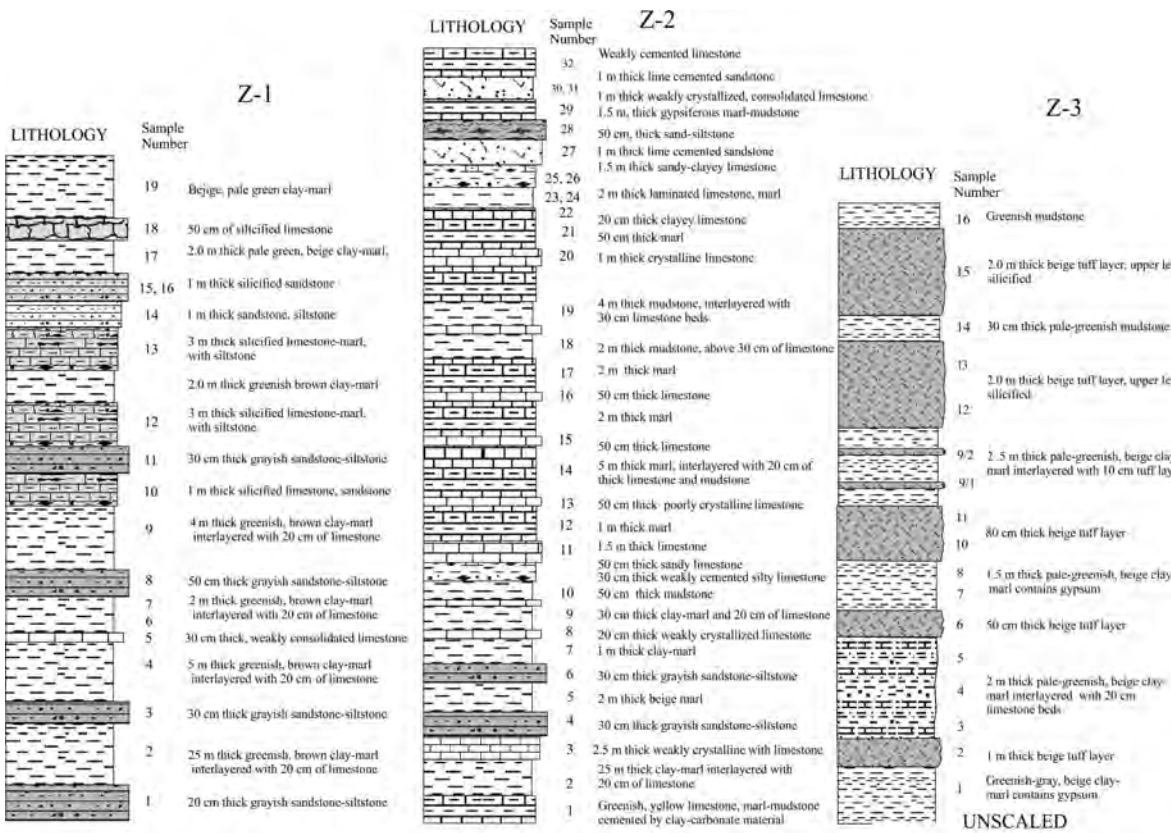

Figure 4. Generalized stratigraphic column of the Aktepe formation and Karacadağ volcano-sedimentary rocks. The figure also shows the detailed section of the stratigraphic interval sampled in the present study.

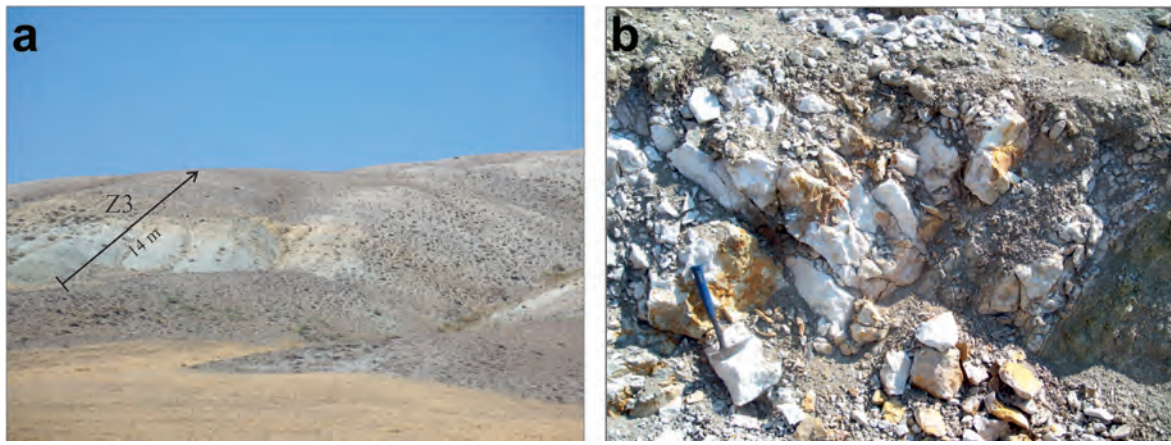

Figure 5. (a) Field photograph showing the location of the Z3 section of the type 2 analcime-containing, clinoptilolite-rich tuff and the intercalated claystones, and (b) a close-up photograph showing the tuff and loosely compacted clay layer.

vitrophyric-porphyric texture was observed in the lava samples. Most of the plagioclases are andesine–oligoclase in composition. The zeolite minerals were found in different percentages in the groundmass and/or replacement of feldspars (Figure 6b). A vitroclastic texture, mostly preserved in tuffs that consist primarily

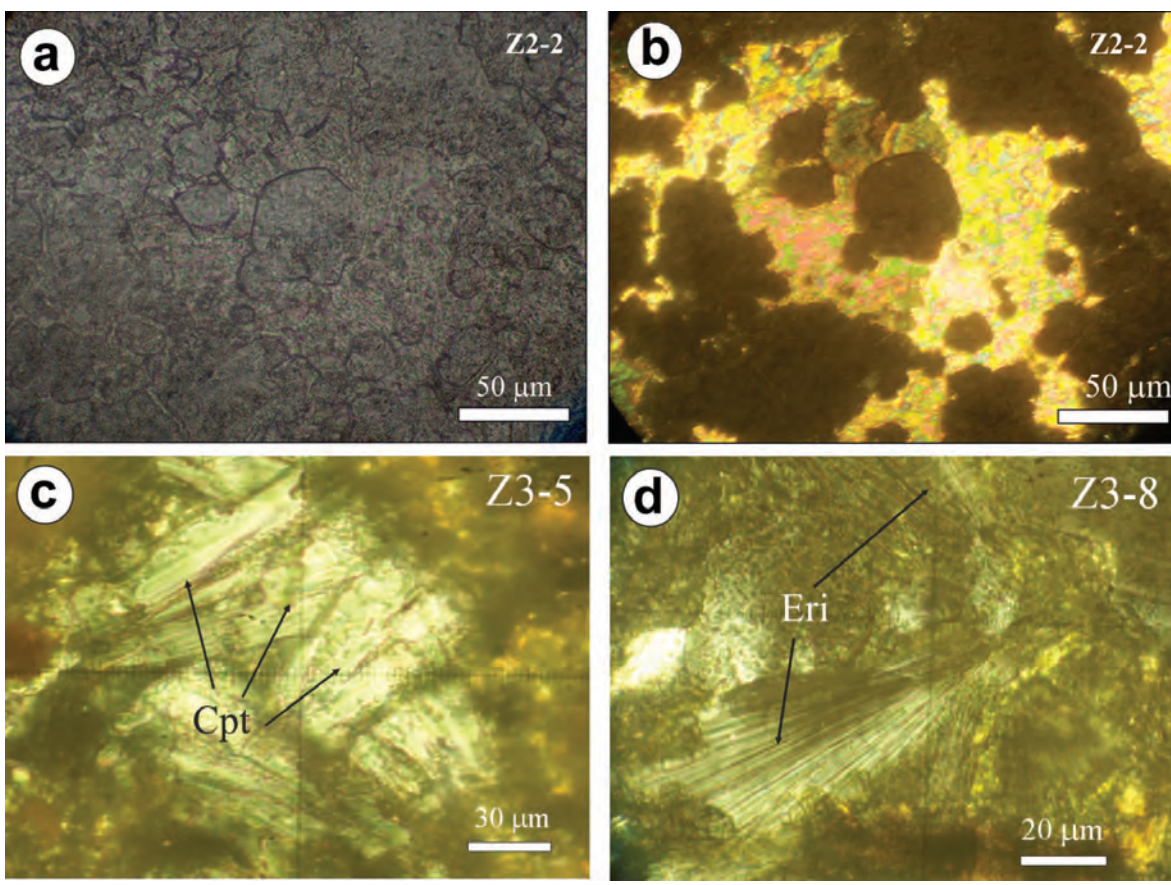

Figure 6. (a) Transmitted light photomicrograph of the analcime trapezohedrons from the analcime-rich samples. The dark outlines around the crystals are hematite and clay. (b) Some of the crystals are mottled by inclusions in reflected light. (c) Reflected-light photomicrographs of the prismatic clinoptilolite and (d) fibrous erionite in tuff (Z3-3). Abbrevations given in Table 1.

of clinoptilolite but also of erionite and chabazite, was observed in thin section. Chabazite was not identified with analcime. Clinoptilolite laths and erionite fibers were clearly defined in thin sections, while analcime was not observed due to its small amount and scattering throughout the matrix. The presence of analcime was only verified by XRD and SEM-EDS analysis.

In the XRD patterns, the characteristic analcime peaks were clearly identified in both types. The XRD patterns of the type 1 analcime were clear and sharp, and the most important analcime lines were defined by the spacing values (Å) 3.43, 5.65, 2.93, and 2.50, in order of their relative intensities (Figure 7). The mineral associations of the first type were classified into two different groups: (1) analcime with dolomite; and (2) analcime with calcite. In type 1, analcime is associated primarily with smectite and dolomite, but it is also associated with plagioclase (mostly albite), K-feldspar, quartz, and calcite. No zeolite-group minerals, except analcime, were identified in this group (Table 1, Figure 7). The mineral types based on the XRD of the first of samples were relatively homogenous, although the mineral proportions are extremely variable (Table 1, Figure 8 – Z1 and Z2). Smectite and feldspar were generally found in both types in different quantities; smectite and the other clay minerals, *e.g.* illite and kaolinite, were identified in clay-sized fractions on oriented and treated samples.

In type 2, clinoptilolite is the main zeolite mineral associated with feldspar, erionite, some analcime, quartz, mica, smectite, calcite, and, more rarely, gypsum. Although it is found both in tuff and in alternating mudstone layers, analcime is not the main zeolite mineral (sample Z4-1 in Figure 7, and the Z3 section in Figure 8). Analcimes are present as euhedral crystals with well developed trapezohedral faces and cube-octahedral crystals or as subhedral, anhedral rounded crystals that are associated with microcrystalline silica or smectitic clays and micritic to microsparitic calcite/dolomite and with microcrystalline silica or smectitic clays, within type 1. Coarse-grained euhedral to partly subhedral analcime crystals are abundant and found as the main components in the first type (Figure 9a–f). Analcime crystals have quite sharp edges, their surfaces are obvious, and their outlined growth traces and dissolution were observed. Analcime-lined voids are commonly filled with dolomite, smectite,

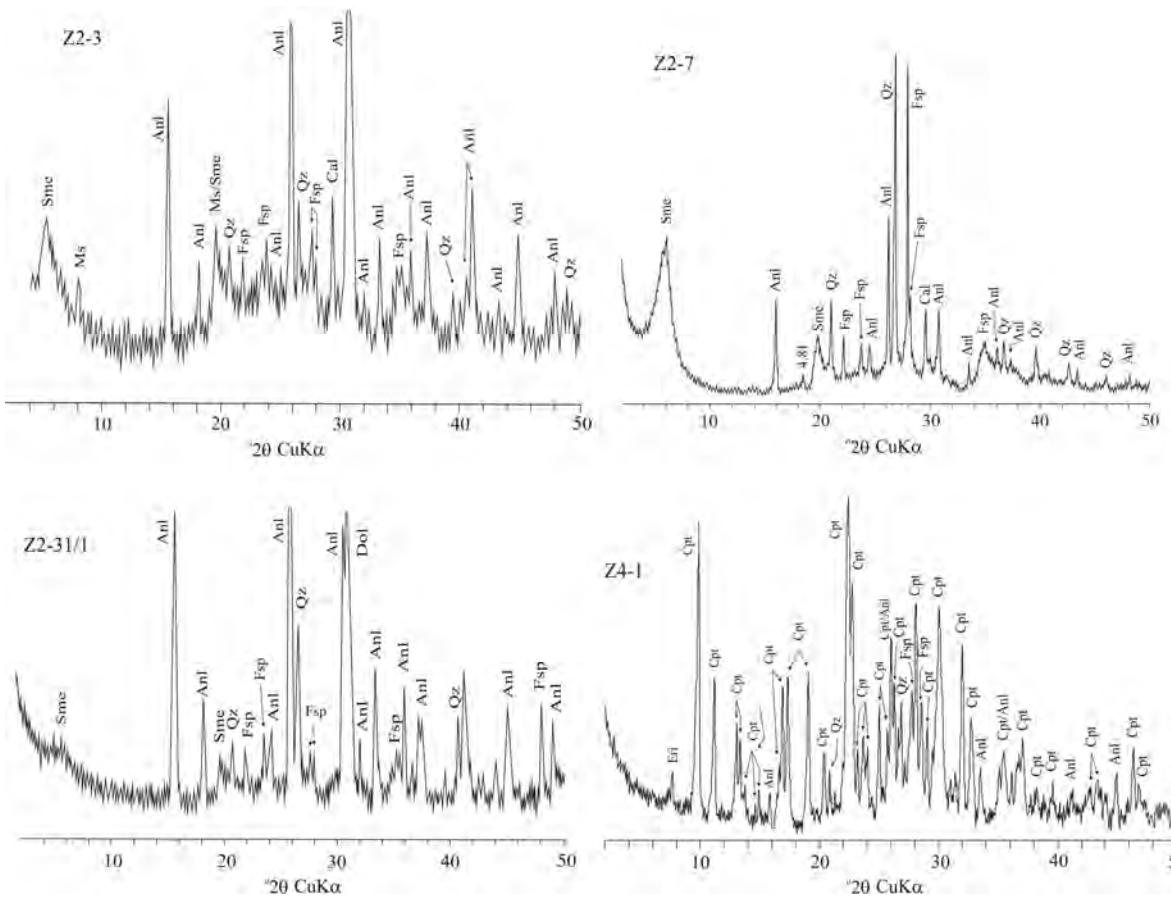

Figure 7. Representative XRD patterns of untreated and air-dried random powder bulk samples of the studied analcime-containing bulk samples from type 1 (Z2-2, 2-7, 31/1) and type 2 (Z4-1) showing the main reflections (Å) (abbreviations given in Table 1).

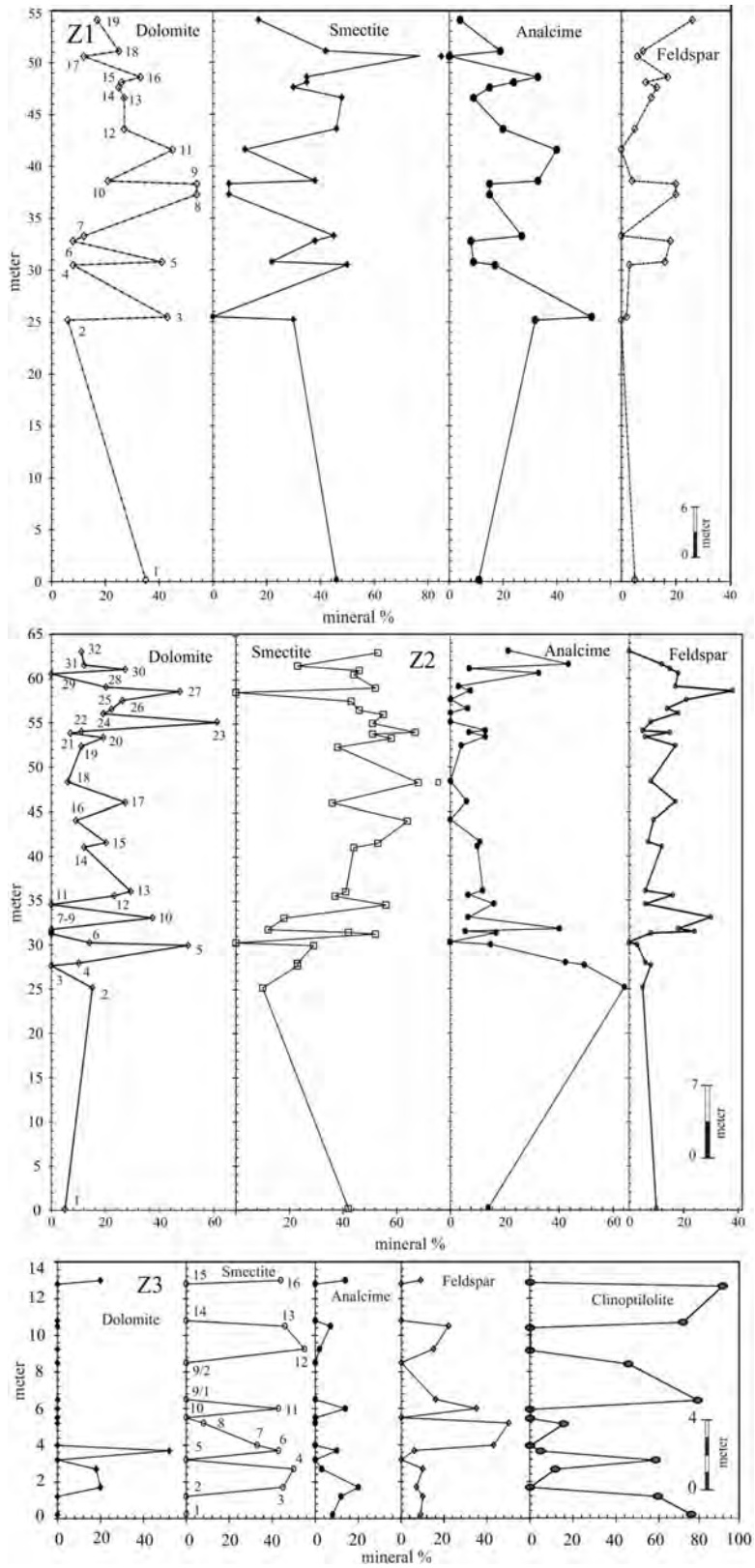

Figure 8. The measured sections compiled at localities 1, 2, and 3, showing the mineral contents of the sampled units.

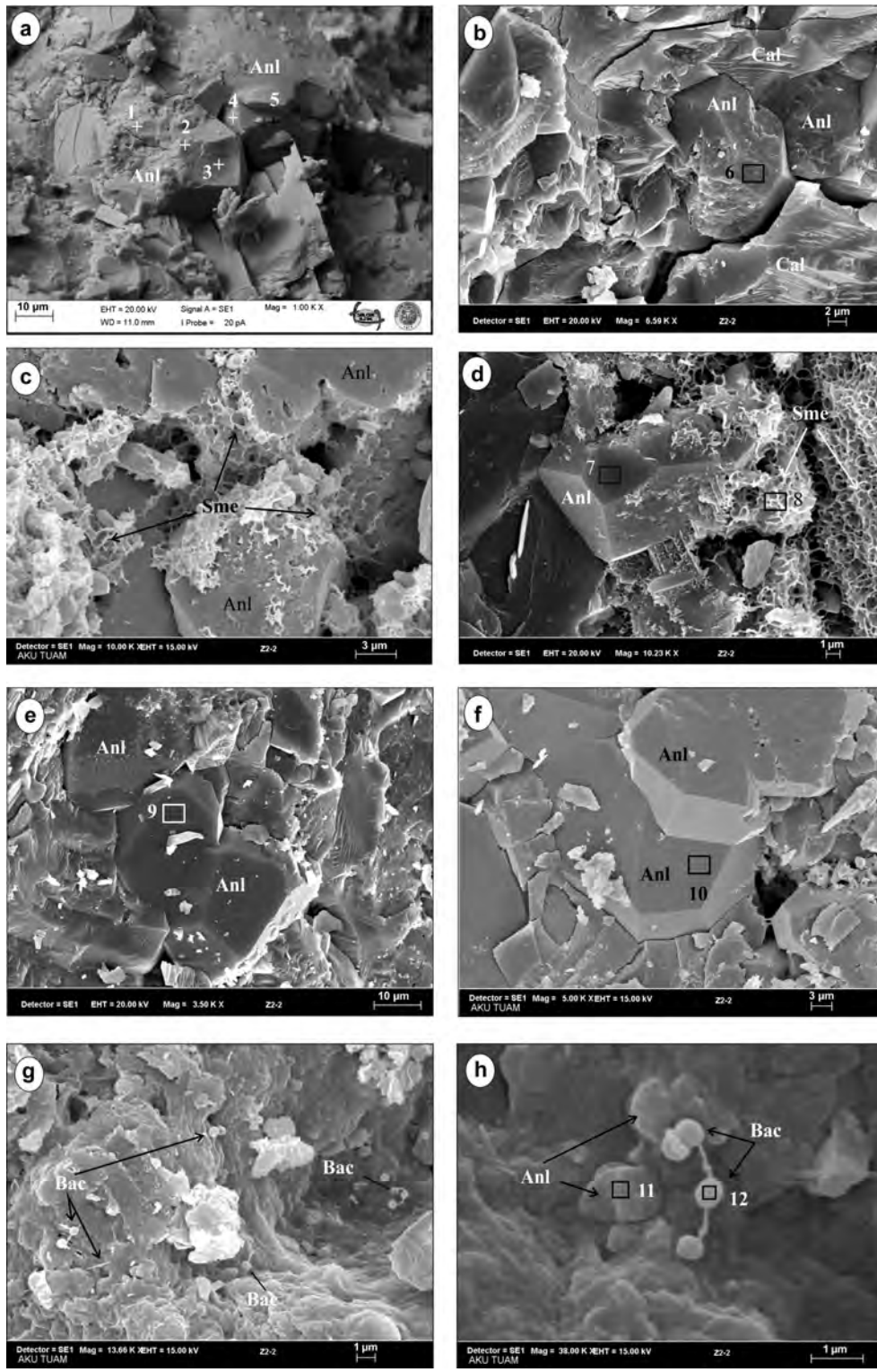

Figure 9. SEM images of the analcimes from type 1 analcime-rich samples. (a,b) Euhedral–subhedral analcime formed from amorphous material. Note the pitted surfaces of the partially dissolved analcime. (c,d) Relationship between authigenic analcime and smectite. The dissolution of analcime is clearly observed and smectite covers the analcime crystals. (e,f) Euhedral analcime crystals. (g) Formation of bacteria in the same samples. (h) Magnified view of the bacteria and analcime-like particles on the top and left sides (abbreviations given in Table 1).

and, more rarely, calcite. The dissolution of analcime crystals and their transformation to smectite was found, while no precursor zeolite or textural evidence of replacement was observed at the SEM scale (Figures 9c,d). However, somewhat similar morphologies are also present in type 2; associated clinoptilolite, erionite, and pumiceous materials, crystal shapes, and crystal surfaces were less prominent. Analcime crystals

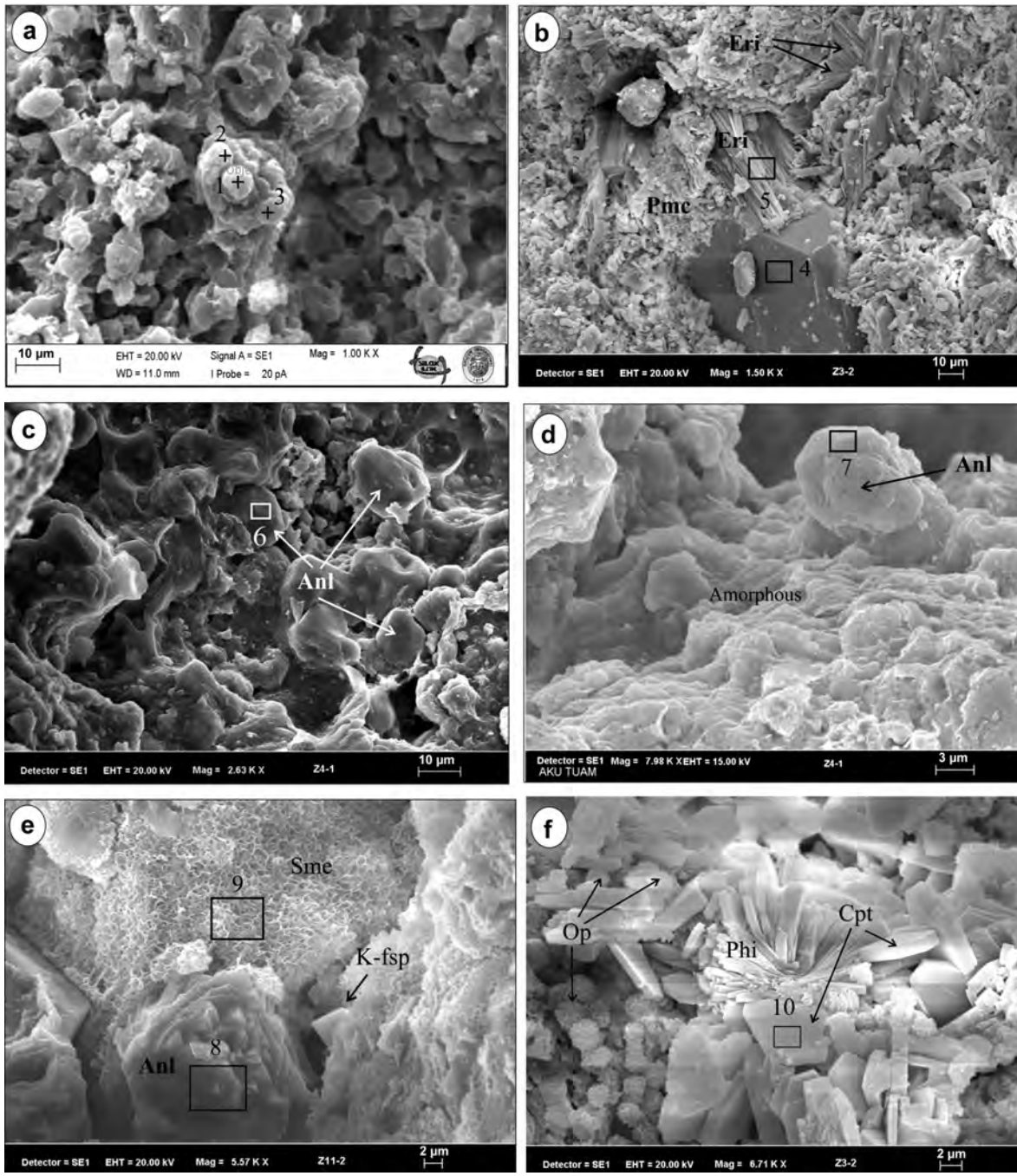

Figure 10. SEM images showing analcimes: (a) globular analcime particles in amorphous material; (b) analcime with fibrous erionite in pumice material; (c,d) globular, subhedral analcime particles in or over amorphous material; (e) growth of authigenic analcime from volcanic material, outlined here to show partially developed, with smectite, and euhedral K-feldspar in the pumice material; and (f) tabular, well developed clinoptilolite crystals with opal-CT and a phillipsite-like mineral (abbreviations given in Table 1).

have different morphologies, and some are globular grains (Figure 10a–e). Globular grains developed from or were covered by the matrix, and outlines of the analcimes are generally conspicuous. The observed morphologies of the type 2 analcimes are compatible with the results of Campo *et al*. (2007) who stated that analcime derived from volcaniclastic materials is commonly observed as subhedral crystals. No evidence of the transformation from zeolite minerals to analcime was observed. The analcime might have been formed gradually directly from volcanic glass and pumice materials. The size of the analcime crystals is coarser in type 1 than in type 2 and ranges from 0.1 to 5.0 μm. Authigenic clinoptilolite and opal-CT are abundant in the type 2. Fibrous erionite was observed on and around the analcime. Clinoptilolite crystals were observed with well developed, tabular shapes, and no relationship was observed between the analcime and clinoptilolite in the samples. Porous and amorphous volcanic glass and pumice fragments were recognized easily using SEM (Figure 10). Analcime crystals grew gradually from the volcanic materials and, thus, present partially developed crystals or globular shapes. The crystal morphology and the crystal-matrix and crystal-crystal relationships indicate that both of the analcimes formed as authigenic minerals from a matrix. According to the EDS analysis, the SiO_2 content of the type 1 analcimes (69.66%) is greater than the second type (mean 63.12 wt.%), while the Al_2O_3 and Na_2O contents are less (Table 2). The alkali cation content (*e.g.* CaO and MgO) was found in almost none of the type 1 analcimes, except points 9 and 10, whereas most of the type 2 analcimes contained both of the alkalis. The smectite composition differed between the two types of analcimes. The Al_2O_3 and Na_2O contents of the smectites in the type 1 analcime are less, and the SiO_2 content is greater (Table 2). The SEM observation and EDS analysis demonstrated that the small Al and Na contents of the analcimes are related to conversion of analcime into smectite. SiO_2, MgO, and some Al_2O_3 contents of clinoptiloite are greater than that of the erionite (Table 2).

Chemistry

Because the tuffs consist mainly of altered volcanic glass, their original chemical composition should approximate that of the volcanic eruptive rocks from which they were derived. Elements that were immobile during alteration may be used to discriminate the effects of hydrothermal alteration of pyroclastic and volcanoclastic rocks and give an indication of the composition of the precursor volcanic rocks (Corfu and Davis, 1991; Rollinson, 1993; Karakaya *et al.*, 2011). A Zr/TiO_2–Nb/Y immobile element ratio plot (Figure 11), which discriminates the fields for volcanic rocks regardless of the effects of post-magmatic alteration (Winchester and Floyd, 1977), shows that the zeolitic tuff analyses cluster around the boundary between trachyte and rhyodacite/dacite, while clays in the rhyolite and tuff and lava plotted mostly in the trachyandesite area and partially in the andesite area (Figure 11). The unaltered vitric tuff from the study area plots in the middle of the cluster of zeolitic tuff analyses. The type 1 analcime was observed in Lower Miocene siltstones, mudstones, and subordinate marls with cavities that are partially or entirely filled with analcime, and carbonate and clay minerals were seen as matrix (Figures 6a, 9). The type 2 analcime formed in clinoptilolite-rich tuffs intercalated with clay beds in Karacadağ volcanites. The Na_2O content of the

Table 2. (a). EDS analysis results (wt.%) of the areas indicated on Figure 9.

	1	2	3	4	5	6	7	8	9	10	11	12
SiO_2	71.17	72.27	73.03	72.62	69.18	69.50	66.43	71.47	66.38	66.36	42.01	42.07
Al_2O_3	20.12	21.03	20.41	20.25	21.07	18.53	22.23	16.15	21.50	19.91	19.80	20.58
Na_2O	8.72	6.70	6.57	7.13	9.75	11.96	11.34	3.97	9.67	11.53	10.50	13.53
K_2O	–	–	–	–	–	–	–	1.98	–	–	–	–
MgO	–	–	–	–	–	–	–	3.69	1.80	1.40	9.88	8.22
CaO	–	–	–	–	–	–	–	2.74	0.65	0.80	13.90	12.01
FeO											3.91	3.55

(b) EDS analysis results (wt.%) of the areas indicated on Figure 10.

	1	2	3	4	5	6	7	8	9	10
SiO_2	61.24	62.62	64.16	62.18	70.88	63.79	64.17	63.70	63.34	75.83
Al_2O_3	18.77	20.42	20.60	22.45	15.38	22.34	21.89	22.30	21.52	15.93
Na_2O	12.90	12.14	10.18	10.50	2.90	12.39	11.96	12.31	7.52	2.48
K_2O	–	–	–	0.62	4.86	–	–	–	1.35	–
MgO	3.02	2.58	2.27	0.99	0.25	1.48	1.37	1.65	3.00	2.39
CaO	4.06	2.28	3.23	3.26	5.63	–	0.61	–	2.15	3.37

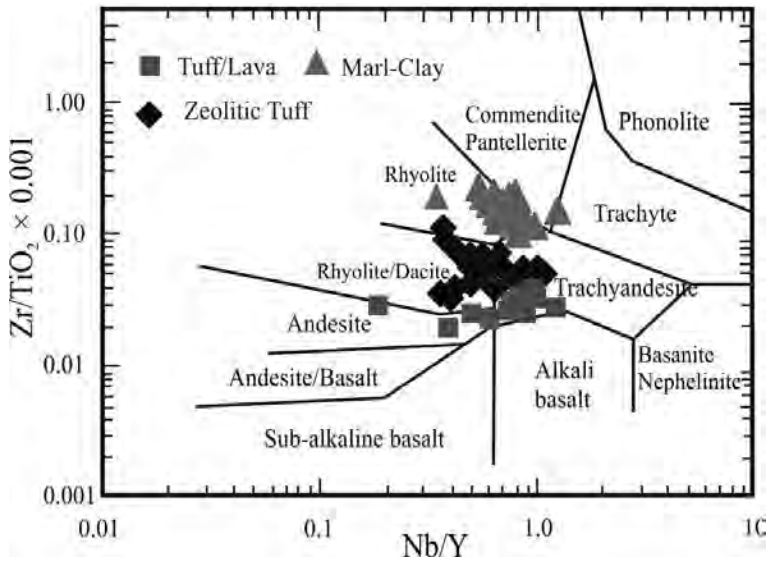

Figure 11. Nomenclature of unaltered and altered samples according to the Nb/Y *vs.* Zr/TiO_2 contents on the diagram of Winchester and Floyd (1977).

analcime-rich samples ranges from 4.17 to 8.02 wt.% (mean 5.83 wt.%) and the positive relationship between the Na_2O content and the analcime clearly shows that most of Na_2O is sourced from analcime (Tables 1 and 3). The fresh/weakly altered lavas contain 2.90−3.81 wt.% Na_2O (mean 3.40 wt.%), 13.45−15.89 wt.% Al_2O_3 (mean 14.70 wt.%), and 65.45−72.23 wt.% SiO_2 (mean 69.70 wt.%). The clay layers in the type 2 analcime samples contain 1.75−2.19 wt.% Na_2O (mean 1.91 wt.%), 8.35−11.56 wt.% Al_2O_3 (mean 9.86 wt.%), and 50.16−55.41 wt.% SiO_2 (mean 50.16 wt.%), while tuffs contain 1.90−2.40 wt.% Na_2O (mean 2.18 wt.%), 12.20−13.70 wt.% Al_2O_3 (mean 12.95 wt.%), and 59.10−64.70 wt.% SiO_2 (mean 62.62 wt.%). The above-mentioned major oxides were more depleted than the lavas, while only Na_2O was clearly enriched in the type 1 analcime-rich samples. Some of trace elements, *e.g.* Sr, Rb, Th, U, Ni, and Sc showed greater enrichment in type 1 analcime samples than in those of the lavas (Table 3). Al_2O_3 shows a slightly positive correlation with Na_2O in nearly all the sample groups, while SiO_2 and Al_2O_3 show strongly positive correlation (R^2 = 0.82) in type 1 analcimic samples (Figure 12). Mean SiO_2/Al_2O_3 ratios of lavas, Z3 section samples (zeolitic tuffs and interlayered clay layers) are 4.76, 4.85, and 5.12, respectively. In sections Z1 and Z2 and in analcime-rich samples, the ratios are 3.97, 4.13, and 3.63, respectively. The SiO_2/Al_2O_3 ratio in analcime-rich samples is less than the samples from section Z3 and lavas (Figure 12a). The correlations are related to silicate minerals in the samples which use SiO_2, Al_2O_3, and also Na_2O. The Na_2O content of sections 1 and 2 plotted in different regions from those of the other samples which show more Na_2O enrichment in type 1 analcime-rich samples (Figure 12a,b). The non-linear relationship between Al_2O_3 and Fe_2O_3 is related to the two elements being found in different silica minerals. Similar non-linear relationships were found between K_2O and other major oxides in mineral associations, *e.g.* feldspar, illite, smectite, and kaolinite. The composition of the zeolitic tuffs with ratios of SiO_2/Al_2O_3 (4.76) and $(Na_2O+K_2O)/(CaO+MgO)$ (9.36) are similar to those of lavas (4.85 and 8.57), while the $(Na_2O+K_2O)/(CaO+MgO)$ ratio (19.24) of the clay samples of section Z3 is greater than that for other samples (Figure 12c), whereas the ratios of the Z1 and Z2 samples are smaller than the section Z3 samples and lavas. Plots of SiO_2/Al_2O_3 *vs.* $(Na_2O+K_2O)/(CaO+MgO)$ discriminates readily between analcime-rich samples from the section Z3 samples (zeolitic tuff and clay) and the lavas (Figure 12c). The Sr contents of sections 1 and 2 range from 334 to 2267 ppm (mean 1356 ppm) and from 583 to 2231 ppm (mean 1345 ppm), respectively. The Sr content in section 3 and lavas varies from 120 to 1239 ppm (mean 674 ppm) and from 333 to 603 ppm (mean 406 ppm), respectively (Table 4) . The weakly positive correlation between Sr and Ca and Mg in the analcimolites suggests a different origin for these elements.

The mean rare-earth elements (*REE*) content of the analcimolites and the section samples Z1 and Z2 are 74, 87, and 85 ppm, respectively. The zeolitic tuffs intercalated with claystones and lavas contain similar amounts of *REE* (mean 85, 77, and 85 ppm, respectively) to each other and to the analcimolites, and are normalized to chondrite (Boynton, 1984). The normalization of all sample groups showed very similar *REE* patterns (Figure 13a). The *REE* in the type 1 analcime-containing sections Z1 and Z2 and clay in the samples in type 2

Table 3a. Major (wt.%), trace (ppm), and *REE* (ppm) elemental compositions and chondrite-normalized ratios from the Z1 section samples.

	Z1-1	Z1-2	Z1-3	Z1-4	Z1-5	Z1-6	Z1-7	Z1-8	Z1-9	Z1-10	Z1-11	Z1-12	Z1-13	Z1-14	Z1-15	Z1-16	Z1-17	Z1-18	Z1-19
SiO_2	48.3	45.0	36.5	36.9	21.4	43.0	42.4	20.4	39.6	37.5	32.9	36.7	34.5	37.7	36.8	33.5	46.1	29.2	44.3
Al_2O_3	12.5	11.7	10.5	9.2	6.0	11.3	11.1	5.9	10.7	9.9	10.3	7.5	8.3	9.5	7.7	7.6	12.2	8.5	8.0
Fe_2O_3	3.8	3.9	1.6	5.6	1.6	5.1	3.1	1.4	6.9	1.5	1.3	2.5	2.9	3.3	2.9	2.9	5.8	4.1	1.7
MgO	5.4	6.6	8.9	3.1	11.0	4.3	5.9	12.1	3.7	9.4	9.5	9.0	9.0	7.8	10.3	9.2	4.9	9.8	3.8
CaO	9.6	6.3	11.6	15.9	22.3	12.2	10.4	22.6	12.9	10.4	13.2	14.0	15.3	13.8	12.4	16.5	7.3	15.8	18.2
Na_2O	2.5	4.7	5.6	2.2	1.6	1.4	2.5	1.6	1.1	4.4	5.7	1.8	1.7	2.2	2.8	1.8	0.8	2.1	2.0
K_2O	1.7	1.8	0.7	1.4	1.7	2.7	1.3	1.7	1.8	0.7	0.4	1.0	1.6	2.1	0.7	1.6	2.2	1.4	1.9
TiO_2	0.3	0.4	0.3	0.4	0.4	0.6	0.4	0.4	0.5	0.1	0.0	0.3	0.5	0.6	0.2	0.5	0.7	0.4	0.5
P_2O_5	0.1	0.1	0.0	0.1	0.1	0.2	0.1	0.2	0.1	0.0	0.0	0.1	0.1	0.2	0.1	0.2	0.7	0.2	0.2
MnO	0.1	0.1	0.0	0.1	0.1	0.1	0.1	0.1	0.1	0.0	0.0	0.1	0.1	0.1	0.0	0.1	0.1	0.1	0.1
Cr_2O_3	0.0	0.0	0.0	0.0	0.0	0.0	0.0	0.0	0.0	0.0	0.0	0.0	0.0	0.0	0.0	0.0	0.0	0.0	0.0
LOI	15.6	19.1	24.2	25.0	33.4	19.0	22.4	33.4	22.4	25.6	26.1	26.5	25.6	22.2	25.8	25.8	18.7	28.2	18.9
Sum	99.8	99.7	100	99.9	99.6	99.8	99.7	99.6	99.8	99.6	99.5	99.6	99.6	99.5	99.6	99.6	99.7	99.6	99.7
TOT/C	7.0	2.8	5.4	4.2	8.5	3.3	3.9	8.9	3.4	5.9	5.9	5.7	5.6	5.0	5.6	6.2	2.2	6.4	4.6
TOT/S	<0.02	0.02	0.31	0.05	0.05	<0.02	<0.02	0.06	0.04	<0.02	0.04	<0.02	0.04	0.03	0.05	<0.02	<0.02	0.03	<0.02
Ba	697	423	224	176	548	398	538	515	425	342	241	529	618	758	300	623	418	448	649
Sc	8.0	1.0	1.0	10.0	9.0	12.0	9.0	7.0	11.0	4.0	2.0	6.0	8.0	9.0	4.0	8.0	14.0	9.0	7.0
Co	5.6	15.0	0.8	9.1	2.7	19.0	4.6	2.0	29.8	1.4	0.7	2.9	5.5	14.1	4.6	4.3	18.0	14.8	8.3
Cs	4.2	4.8	1.3	1.8	1.4	5.3	5.6	1.7	5.6	3.5	2.1	3.5	3.0	3.1	3.9	2.8	6.5	17.0	1.5
Ga	6.3	12.1	7.2	4.4	5.3	12.0	12.0	4.4	12.6	6.6	8.5	8.5	8.2	9.3	7.0	7.1	13.0	7.9	5.9
Hf	1.6	2.4	2.2	0.7	1.8	2.3	2.1	1.6	2.5	1.4	2.6	1.4	1.9	2.6	1.3	1.9	2.4	1.6	2.4
Nb	7.2	11.1	2.8	3.9	7.3	11	10.1	7.1	10.1	5.9	3.1	6	10.1	11.3	4.2	8.9	13	7.4	8.4
Rb	53	67.7	15.2	22.4	30.6	79	56.9	28.3	67	26.4	16.8	45.1	50.9	61.9	24.5	43.6	72	54.4	37.7
Sr	2218	835	1565	334	1281	613	1149	1294	562	1671	2267	1947	1526	1852	1623	1454	837	1193	1548
V	48	<8	10	32	23	101	60	25	105	15	32	42	50	60	32	40	99	70	31
Ta	0.5	0.6	1.5	0.3	0.4	0.7	0.7	0.4	0.6	1.1	1.4	0.5	0.5	0.8	0.6	0.5	0.9	0.5	0.6
Th	6.3	9.3	7	2.9	8.4	8.5	8	8.3	8	4.7	6.3	6.6	7.3	8.6	3.2	7.4	8.4	5.5	6.2
U	1.8	1.8	0.5	1.3	1.3	2.1	1.3	1.1	1.8	0.9	0.7	1.1	2.2	3.8	1.0	1.5	2.8	2.6	1.5
Zr	62.3	90.3	72.1	35.7	70	92	98.7	80.6	90	61.4	93.6	63.5	90.3	102	56.1	90	107	66.8	104
Y	13.9	12.9	10.9	6.3	17.4	15	12.6	18.7	15.6	6.2	4.5	10.4	15.8	20.5	6.5	18	18	11.1	19.1
La	17.8	21.8	7.6	10.9	28.4	21.0	21.2	29.0	25.1	10.0	16.7	16.5	23.1	26.1	14.2	24.3	24.0	16.0	22.5
Ce	33.6	39.2	13.9	20.0	50.8	40.0	38.6	52.2	45.2	16.5	21.8	30.8	42.4	50.5	23.3	44.1	44.0	30.2	41.8
Pr	4.1	4.5	1.8	2.0	6.0	4.8	4.5	6.2	4.9	1.8	2.5	3.4	5.1	6.0	2.5	5.5	5.3	3.4	5.2
Nd	14.6	17.1	7.2	7.3	22.4	17.3	16.1	22.0	17.0	6.6	7.3	13.3	17.6	22.1	8.7	20.5	19.7	13.0	18.7
Sm	2.6	3.1	1.8	1.3	4.3	3.5	3.0	4.4	3.4	1.3	1.1	2.3	3.8	4.4	1.7	3.7	3.8	2.5	4.1
Eu	0.4	0.7	0.4	0.3	1.0	0.9	0.7	1.1	0.8	0.3	0.2	0.6	0.9	1.1	0.4	1.0	0.9	0.6	1.0
Gd	2.5	2.7	1.7	1.1	3.6	3.1	2.5	3.8	3.0	1.1	1.0	2.0	3.3	4.1	1.3	3.8	3.7	2.3	3.9
Tb	0.3	0.4	0.3	0.2	0.6	0.5	0.4	0.6	0.5	0.2	0.1	0.3	0.5	0.6	0.2	0.6	0.6	0.3	0.6
Dy	2.3	2.1	1.6	0.9	3.3	2.6	2.2	3.1	2.5	1.0	0.7	1.8	2.9	3.6	1.2	3.3	3.0	1.7	3.3
Ho	0.4	0.4	0.3	0.2	0.6	0.5	0.4	0.6	0.5	0.2	0.2	0.3	0.5	0.7	0.2	0.6	0.6	0.4	0.6
Er	1.2	1.3	0.9	0.5	1.6	1.4	1.2	1.4	1.5	0.7	0.3	1.0	1.4	1.9	0.5	1.6	1.7	1.0	1.7

Table 3a (*contd*.).

	Z1-1	Z1-2	Z1-3	Z1-4	Z1-5	Z1-6	Z1-7	Z1-8	Z1-9	Z1-10	Z1-11	Z1-12	Z1-13	Z1-14	Z1-15	Z1-16	Z1-17	Z1-18	Z1-19
Tm	0.2	0.2	0.1	0.1	0.3	0.2	0.2	0.3	0.2	0.1	0.1	0.2	0.3	0.3	0.1	0.3	0.3	0.2	0.2
Yb	1.2	1.4	0.9	0.5	1.5	1.6	1.2	1.6	1.3	0.7	0.4	1.0	1.5	1.8	0.7	1.7	1.8	1.3	2.0
Lu	0.2	0.2	0.1	0.1	0.2	0.2	0.2	0.2	0.2	0.1	0.1	0.1	0.2	0.3	0.1	0.2	0.3	0.2	0.3
Ni	49.0	83.0	17.0	98.0	18.1	133	36.0	18.4	110	14.0	11.0	33.0	50.0	65.0	35.0	43.0	166	67.0	49.0
Y/Ni	0.3	0.2	0.6	0.1	1.0	0.1	0.4	1.0	0.1	0.4	0.4	0.3	0.3	0.3	0.2	0.4	0.1	0.2	0.4
Cr/Ni	1.3	0.2	0.8	0.9	3.8	1.0	1.9	4.1	0.9	1.0	1.2	1.9	2.1	2.5	1.6	3.2	1.1	1.6	5.6
Cr/Th	9.8	2.2	2.0	30.7	8.1	16.1	8.6	9.1	12.8	2.9	2.2	9.3	14.1	19.1	17.1	18.5	22.0	19.9	44.1
Th/Sc	0.8	9.3	7.0	0.3	0.9	0.7	0.9	1.2	0.7	1.2	3.2	1.1	0.9	1.0	0.8	0.9	0.6	0.6	0.9
Co/Th	0.9	1.6	0.1	3.1	0.3	2.2	0.6	0.2	3.7	0.3	0.1	0.4	0.8	1.6	1.4	0.6	2.1	2.7	1.3
La/Co	3.2	1.5	9.5	1.2	10.5	1.1	4.6	14.5	0.8	7.1	23.9	5.7	4.2	1.9	3.1	5.7	1.3	1.1	2.7
La/Th	2.8	2.3	1.1	3.8	3.4	2.5	2.7	3.5	3.1	2.1	2.7	2.5	3.2	3.0	4.4	3.3	2.9	2.9	3.6
La/Sc	2.2	21.8	7.6	1.1	3.2	1.8	2.4	4.1	2.3	2.5	8.4	2.8	2.9	2.9	3.6	3.0	1.7	1.8	3.2
La/Lu	89.0	121	69.1	109	142	105	106	145	126	90.9	278	165	116	87.0	142	122	80.0	80.0	75.0
Eu/Eu*	0.5	0.8	0.6	0.8	0.8	0.9	0.8	0.9	0.8	0.7	0.6	0.9	0.8	0.8	0.9	0.9	0.8	0.8	0.8
Ce/Ce*	0.9	1.0	0.9	1.0	0.9	1.0	1.0	0.9	1.0	0.9	0.8	1.0	0.9	1.0	0.9	0.9	0.9	1.0	0.9
REE	81.4	94.9	38.5	45.4	125	97.6	92.4	127	106	40.5	52.4	73.6	104	124	55.1	111	110	73.1	106
HFSE	2074	3270	2022	2877	2933	4375	2884	2978	3384	994	322	2161	3634	5078	1594	4054	7292	3631	3965

Table 3b. Major (wt.%), trace (ppm), *REE* (ppm) elemental compositions and chondrite-normalized ratios from the Z2 section samples.

	Z2-1	Z2-2	Z2-3	Z2-4	Z2-5	Z2-9	Z2-20	Z2-21/1	Z2-21/2	Z2-22/1	Z2-22/2	Z2-23/1	Z2-23/2	Z2-24	Z2-25	Z2-31	Z2-31/1	Z2-31/2
SiO_2	36.5	42.7	43.3	48.9	12.9	46.2	37.7	41.4	28.3	32.4	42.8	29.8	1.31	41.8	34.1	49.8	50.0	43.4
Al_2O_3	8.55	12.2	13.5	12.6	2.92	13.8	9.03	9.05	7.02	7.6	11.3	6.74	0.16	8.77	5.82	13.6	14.3	9.41
Fe_2O_3	2.2	1.32	2.79	3.56	1.87	1.67	4.34	3.19	2.54	2.75	5.58	2.19	1.86	2.63	1.6	2.09	1.35	1.17
MgO	5.12	6.0	4.57	5.52	15.7	4.46	6.76	7.23	10.3	9.38	5.54	9.68	18.8	7.31	10.4	2.08	3.83	8.26
CaO	20.4	8.73	8.81	5.64	24.3	8.94	12.4	12.3	18.7	16.6	8.91	18.8	30.9	13	17.4	6.74	5.84	10.3
Na_{2O}	2.09	6.98	6.02	5.74	0.97	4.99	1.53	1.69	1.49	1.82	1.25	1.31	0.08	1.83	1.6	7.76	8.02	4.17
K_2O	2.05	0.4	2.02	1.17	0.56	0.63	1.38	1.87	1.78	1.59	1.79	1.37	0.03	1.93	1.34	1.04	0.51	0.51
TiO_2	0.57	0.1	0.55	0.54	0.13	0.19	0.43	0.59	0.5	0.45	0.63	0.46	0.01	0.6	0.34	0.33	0.2	0.1
P_2O_5	0.14	0.01	0.27	0.07	0.03	0.08	0.05	0.11	0.13	0.16	0.11	0.14	0.04	0.33	0.15	0.1	0.01	0.04
MnO	0.1	0.02	0.1	0.07	0.12	0.1	0.09	0.1	0.09	0.13	0.13	0.08	0.03	0.1	0.08	0.11	0.03	0.04
Cr_2O_3	0.02	0.01	0.02	0.02	0.01	0.002	0.02	0.04	0.02	0.03	0.02	0.02	0.00	0.03	0.03	0.02	0.002	0.002
LOI	22	21.2	17.7	16.2	39.5	17.4	26	22.1	28.6	26.6	21.7	28.9	46.3	21.3	26.8	16.2	15.9	22.2
Sum	99.7	99.6	99.7	99.9	99.1	99.4	99.6	99.6	99.5	99.5	99.8	99.6	99.5	99.6	99.7	99.8	99.8	99.6
TOT/C	4.83	4.51	3.97	1.83	10.4	3.34	5.12	4.58	7.08	6.41	3.23	6.8	12.2	4.76	7.05	4.98	2.42	4.79
TOT/S	0.02	0.02	<0.02	0.03	<0.02	0.09	<0.02	0.02	<0.02	<0.02	<0.02	<0.02	<0.02	0.03	0.02	<0.02	<0.02	0.03

Ba	478	598	521	464	1396	4366	428	483	488	494	344	379	361	634	611	504	321	249
Sc	8.0	1.0	9.0	4.0	8.0	1.0	11.0	10.0	9.0	7.0	12.0	7.0	1.0	8.0	7.0	2.0	2.0	5.0
Co	7.4	0.5	8.3	15.2	15.2	6.8	8.6	7.1	4.1	6.8	21.7	6.3	3.2	4.5	6.1	5.7	1.0	1.2
Cs	2.6	2.8	3.8	5.3	5.3	2.0	4.5	4.0	2.6	3.3	6.2	2.9	<0.1	4.5	1.7	5.2	2.8	2.8
Ga	8.4	10.4	10.5	13.6	13.6	8.0	9.8	9.6	5.8	6.9	12.2	5.9	<0.5	7.6	4.9	5.8	13.3	7.4
Hf	2.6	3.7	2.0	2.2	2.2	2.4	2.2	3.3	2.4	2.2	2.2	2.2	0.4	2.5	1.3	3.0	4.3	2.6
Nb	12.2	3.9	12.1	11.8	11.8	2.5	24.3	9.8	10.3	8.6	11.3	8.4	0.1	12.7	6.5	6.5	5.2	5.0
Rb	50.4	16.0	67.1	84.0	84.0	17.2	48.8	54.2	43.1	44.1	66.7	39.5	1.0	51.4	34.1	51.5	22.2	21.7
Sr	1348	1883	1395	584	584	1114	1215	1421	1941	1827	793	1845	1585	1293	718	1692	774	2231
V	48.0	<8	54.0	30.0	23.0	<8	81.0	56.0	42.0	37.0	96.0	44.0	11.0	51.0	29.0	24.0	<8	28.0
Ta	0.7	1.7	0.8	0.9	0.3	0.8	0.5	0.7	0.5	0.7	0.7	0.6	0.1	0.8	0.5	0.5	1.9	1.2
Th	9.8	7.5	11.2	7.5	5.2	2.1	5.0	6.0	6.8	6.7	6.9	5.4	0.2	6.7	3.7	5.1	10.6	6.7
U	1.4	0.7	1.9	1.9	2.3	0.9	2.4	1.2	2.4	1.4	1.8	1.1	<0.1	1.5	1.1	2.2	0.6	0.8
Zr	99.9	123	101	91.8	25.3	69.9	72.7	103.2	80.9	111.0	91.1	115.0	44.3	121	94.2	129.2	145.7	85.8
Y	19.0	3.6	17.9	11.0	15.8	9.0	10.6	15.8	18.6	17.7	14.0	14.3	1.4	17.1	10.5	15.9	4.7	5.2
La	28.5	15.6	29.9	18.9	15.4	10.2	15.9	24.5	23.1	24.7	20.3	19.0	1.0	24.0	13.9	19.3	29.6	19.3
Ce	53.7	23.2	55.6	36.1	27.2	17.5	30.9	49.2	45.1	45.7	39.6	36.4	1.7	45.5	26.2	40.1	45.0	18.1
Pr	6.4	2.3	6.5	4.0	3.3	2.1	3.3	5.3	5.0	5.5	4.6	4.4	0.2	5.4	3.1	4.7	4.3	2.5
Nd	23.4	7.6	21.9	14.1	14.4	8.8	13.0	20.0	17.7	20.3	16.8	16.2	0.9	22.0	11.4	17.6	12.4	8.4
Sm	4.7	1.1	4.4	2.8	2.6	1.6	2.1	4.1	3.7	3.9	3.3	3.3	0.2	4.1	2.3	3.6	2.0	1.1
Eu	1.2	0.2	1.1	0.6	0.5	0.5	0.5	1.1	0.9	1.0	0.8	0.8	0.0	1.0	0.5	1.1	0.3	0.2
Gd	4.4	0.9	3.9	2.7	2.6	1.7	2.2	4.0	4.0	3.7	3.0	3.1	0.3	3.8	2.2	3.6	1.3	1.0
Tb	0.6	0.1	0.6	0.4	0.4	0.2	0.3	0.6	0.6	0.5	0.5	0.4	0.0	0.6	0.3	0.5	0.2	0.1
Dy	3.8	0.7	3.5	2.1	2.4	1.5	1.7	3.2	3.4	3.1	2.9	2.5	0.2	3.0	2.0	3.2	1.0	0.8
Ho	0.6	0.1	0.6	0.4	0.6	0.3	0.3	0.8	0.7	0.6	0.5	0.5	0.1	0.6	0.4	0.6	0.2	0.1
Er	1.7	0.4	1.7	1.1	1.6	0.9	0.8	1.8	1.6	1.5	1.3	1.5	0.1	1.5	1.1	1.4	0.5	0.4
Tm	0.3	0.1	0.2	0.2	0.3	0.1	0.2	0.3	0.3	0.3	0.2	0.2	0.0	0.3	0.1	0.2	0.1	0.1
Yb	1.6	0.4	1.6	1.3	1.5	0.9	1.2	1.4	1.4	1.3	1.5	1.4	0.1	1.6	1.1	1.5	0.4	0.5
Lu	0.3	0.0	0.2	0.2	0.2	0.1	0.2	0.3	0.2	0.2	0.2	0.2	0.0	0.2	0.1	0.2	0.1	0.1
Ni	68.0	27.7	57.2	36.7	17.0	16.3	96.0	63.0	44.0	24.0	136.0	75.0	18.0	42.0	39.0	39.8	5.2	12.7
Y/Ni	0.3	0.1	0.3	0.3	0.9	0.6	0.1	0.3	0.4	0.7	0.1	0.2	0.1	0.4	0.3	0.4	0.9	0.4
Cr/Ni	2.3	2.5	1.9	3.2	2.0	0.8	1.1	3.8	3.1	7.7	1.2	1.9	0.8	5.2	4.9	2.6	2.6	1.1
Cr/Th	16.1	9.1	9.8	15.5	6.6	6.5	20.5	39.9	20.1	27.6	23.8	26.6	68.4	32.7	51.8	20.1	1.3	2.0
Th/Sc	1.2	7.5	1.2	1.9	0.7	2.1	0.5	0.6	0.8	1.0	0.6	0.8	0.2	0.8	0.5	2.6	5.3	1.3
Co/Th	0.8	0.1	0.7	2.0	2.9	3.2	1.7	1.2	0.6	1.0	3.1	1.2	16.0	0.7	1.6	1.1	0.1	0.2
La/Co	3.9	31.2	3.6	1.2	1.0	1.5	1.8	3.5	5.6	3.6	0.9	3.0	0.3	5.3	2.3	3.4	29.6	16.1
La/Th	2.9	2.1	2.7	2.5	3.0	4.9	3.2	4.1	3.4	3.7	2.9	3.5	5.0	3.6	3.8	3.8	2.8	2.9
La/Sc	3.6	15.6	3.3	4.7	1.9	10.2	1.4	2.5	2.6	3.5	1.7	2.7	1.0	3.0	2.0	9.7	14.8	3.9
La/Lu	106	390	130	99	73	85	106	94	110	107	88	106	100	109	99	97	493	322
Eu/Eu*	0.9	0.7	0.9	0.7	0.6	1.1	0.8	0.9	0.8	0.9	0.8	0.9	0.6	0.9	0.8	0.9	0.7	0.6
Ce/Ce*	1.0	0.9	1.0	1.0	0.9	0.9	1.0	1.0	1.0	0.9	1.0	1.0	0.9	1.0	1.0	1.0	1.0	0.6
REE	131	52.6	132	84.8	72.8	46.5	72.6	116.5	107.7	112.3	95.6	90.0	4.9	113	64.6	97.6	97.3	52.7
HFSE	4301	839	4701	3766	984	1577	2998	4374	3796	3703	4526	3639	293	5393	2987	2657	1405	882

Table 3c. Major (wt.%), trace (ppm), *REE* (ppm) elemental compositions and chondrite-normalized ratios from the Z3 section and lava samples.

	Section Z3 samples														Lavas					MDL
	Claystone					Zeolitic Tuff														
	Z3-2	Z3-4	Z3-6	Z3-8	Z3-10	Z3-11	Z3-12	Z3-15	Z3-1	Z3-5	Z3-7	Z3-9	Z3-13	Z3-14	Z12-1	Z12-2	Z12-3	Z12-7	Z16-1	
SiO_2	46.9	47.2	52.8	55.4	52.8	49.9	48.9	47.3	64.7	59.1	60.8	62.9	63.9	64.3	71.1	72.2	70.9	68.9	65.5	0.01
Al_2O_3	8.93	8.35	9.8	11.6	9.77	10.24	11.0	9.27	12.20	13.70	13.20	13.40	12.90	12.30	14.96	14.00	13.45	15.89	15.32	0.01
Fe_2O_3	3.59	3.04	3.6	3.85	3.92	3.8	4.44	3.78	0.90	0.80	1.50	0.50	0.70	1.20	2.79	2.35	2.39	2.89	3.68	0.04
MgO	11.1	10.0	10.3	8.04	10.4	8.56	7.18	9.35	1.40	3.10	5.00	1.70	1.70	1.40	0.25	0.41	0.96	0.40	1.67	0.01
CaO	6.87	9.3	3.75	3.6	3.64	5.86	6.96	8.01	2.20	1.70	1.10	1.90	2.60	1.80	3.80	3.65	3.55	3.92	3.71	0.01
Na_2O	1.77	1.86	1.98	1.75	2.00	1.89	2.19	1.80	2.00	3.10	2.10	2.00	1.20	2.30	3.74	3.11	2.90	3.81	3.61	0.01
K_2O	1.68	1.49	1.59	1.81	1.8	2.64	2.78	1.95	1.90	2.10	2.40	2.40	2.20	2.10	1.23	1.38	1.40	1.53	1.75	0.01
TiO_2	0.46	0.37	0.43	0.44	0.51	0.47	0.51	0.47	0.10	0.10	0.10	0.10	0.10	0.10	0.31	0.29	0.25	0.35	0.46	0.01
P_2O_5	0.07	0.2	0.12	0.08	0.06	0.31	0.09	0.09	0.02	0.01	0.01	0.03	0.02	0.03	0.12	0.11	0.11	0.14	0.30	0.01
MnO	0.15	0.08	0.05	0.04	0.07	0.07	0.09	0.11	<0.01	<0.01	0.05	0.03	<0.01	<0.01	0.01	0.01	0.01	0.02	0.03	0.01
Cr_2O_3	0.02	0.02	0.02	0.04	0.02	0.02	0.02	0.02	<0.002	<0.002	<0.002	<0.002	0.01	<0.002	0.01	0.01	0.00	0.00	0.00	0.002
LOI	18.1	17.8	15.3	13.1	14.7	15.9	15.6	17.5	14.4	16.1	13.7	14.9	14.4	14.2	1.60	2.40	4.00	2.00	3.80	5.1
Sum	99.6	99.7	99.7	99.8	99.7	99.7	99.7	99.7	99.8	99.8	99.9	99.8	99.8	99.8	99.9	99.9	99.9	99.9	99.8	
TOT/C	3.08	2.17	0.92	0.83	1.38	1.52	1.7	2.84	0.1	0.2	0.00	0.1	0.00	0.00	<0.02	0.02	0.03	0.03	0.11	0.01
TOT/S	0.03	0.16	0.04	0.03	<0.02	0.04	0.06	0.07	0.00	<0.02	<0.02	<0.02	<0.02	<0.02	<0.02	<0.02	<0.02	<0.02	<0.02	0.02
Ba	264	320	227	328	201	638	609	397	319	768	75	196	382	280	438	340	367	452	752	0.02
Sc	9.0	8.0	19.0	9.0	10.0	9.0	11.0	10.0	3.0	2.0	8.0	3.0	3.0	5.0	3.0	3.0	3.0	4.0	4.0	0.02
Co	12.7	12	13.8	15.1	13.5	14.3	16.5	13.5	1.3	4.6	2.3	3.3	2.2	<0.2	3.4	2.5	5.0	5.2	6.6	0.02
Cs	11.0	6.4	12.9	6	12.6	6.8	9.9	10.6	3.3	2.7	20.6	3.3	2.6	2.7	0.5	0.3	0.3	0.6	0.2	1.0
Ga	10.2	8.6	11.6	14.1	10.2	11.6	12.2	10	16.9	6.6	18.0	18.2	16.9	18.6	15.1	13.8	13.2	15.0	15.7	0.2
Hf	2.2	2.2	2.5	2.9	2.7	2.8	2.6	2.5	4.1	2.6	3.5	4.5	5.7	4	3.7	2.4	2.2	3.0	3.4	0.1
Nb	9.7	9.1	13.4	13.7	10.4	9.9	10.3	10	36.1	2.6	43.1	20.5	31.2	38.8	7.7	5.0	4.6	7.9	12.3	0.5
Rb	92.7	85.6	103	91.1	94.1	131.5	130	97.2	67.2	74.9	189	80.5	86.3	71.7	25.8	18.4	23.5	27.5	34.6	0.1
Sr	1003	475	316	446	376	583.3	495	730	1239	931	120	1017	876	825	351	351	333	394	603	0.1
Ta	0.6	0.7	1.1	0.7	0.7	0.7	0.7	0.7	5.9	1.6	8.2	6.9	7.7	6.2	0.5	0.3	0.4	0.6	0.8	0.1
Th	11.3	7.9	9.4	5.4	8.1	7.3	8.4	10.5	31.2	14.3	32.4	29.7	25.9	38.9	6.3	4.2	4.3	6.9	8.5	0.5
U	11.7	6.1	8.7	3.5	14.1	17.0	4.4	21.5	12.1	0.4	8.4	5.4	3.4	14.4	1.8	0.6	1.0	1.9	2.1	0.1
V	76.0	57.0	127	62.0	86.0	80.0	103.0	86.0	12.0	16.0	9.0	<8	<8	9.0	47.0	57.0	53.0	43.0	63.0	0.1
Zr	88.7	82.2	87.9	97.8	103	95.9	91.5	94.9	74.4	43.0	63.2	73	103	74.4	112.1	91.6	75.2	119.6	145.9	0.2
Y	27.9	10.7	12.8	8.9	16.4	12.6	12.9	17.1	23.5	2.0	23.6	46.5	20.3	81.4	8.0	5.2	5.7	8.2	12.6	0.1
La	15.4	12.8	15.1	14.7	14.9	17.2	19.7	21.5	15.0	6.1	15.6	14.3	11.9	19.2	16.9	14.2	13.3	21.6	36.1	0.1
Ce	29.7	26.0	30.1	26.7	30.0	34.3	38.5	41.4	33.0	12.6	34.5	30.7	26.9	35.2	31.6	25.7	25.2	39.9	70.5	0.1
Pr	3.4	2.8	3.3	3.2	3.3	3.7	4.2	4.6	4.0	1.3	4.1	3.7	3.2	6.6	3.2	2.5	2.5	4.1	7.1	0.1
Nd	12.0	10.5	12.1	11.8	12.1	13.8	15.5	16.8	14.8	4.1	14.3	14.3	11.6	27.2	11.5	8.4	9.3	14.4	25.8	0.02
Sm	2.4	2.0	2.3	2.0	2.3	2.6	2.9	3.1	4.3	0.8	4.9	4.7	3.4	8.9	1.9	1.5	1.5	2.2	3.4	0.3
Eu	0.6	0.5	0.5	0.6	0.6	0.7	0.7	0.8	0.1	0.1	0.1	0.1	0.1	0.2	0.6	0.6	0.6	0.7	0.9	0.05
Gd	2.4	1.9	2.3	1.7	2.0	2.3	2.6	2.8	4.2	0.6	5.2	5.7	3.4	11.3	1.8	1.3	1.4	2.0	3.0	0.02
Tb	0.4	0.3	0.4	0.3	0.4	0.4	0.4	0.5	0.8	0.1	1.0	1.2	0.6	2.4	0.3	0.2	0.2	0.3	0.4	0.05
Dy	2.9	1.7	2.2	1.3	2.2	2.1	2.2	2.6	4.0	0.4	4.6	7.1	3.4	13.6	1.3	1.0	0.9	1.4	2.0	0.01

Ho	0.7	0.4	0.4	0.3	0.5	0.4	0.4	0.6	0.7	0.1	0.8	1.5	0.6	2.7	0.2	0.2	0.2	0.3	0.4	0.05
Er	2.6	1.0	1.1	0.8	1.6	1.2	1.3	1.6	1.9	0.2	1.8	4.2	1.7	7.7	0.7	0.5	0.5	0.8	1.2	0.02
Tm	0.5	0.2	0.2	0.1	0.3	0.2	0.2	0.3	0.3	0.0	0.3	0.7	0.3	1.1	0.1	0.1	0.1	0.1	0.2	0.03
Yb	3.7	1.1	1.2	0.9	2.6	1.2	1.2	2.1	2.0	0.2	1.7	4.3	1.8	7.3	0.7	0.5	0.5	0.7	1.1	0.01
Lu	0.6	0.2	0.2	0.1	0.4	0.2	0.2	0.4	0.3	0.0	0.2	0.6	0.3	1.0	0.1	0.1	0.1	0.1	0.2	0.1
Ni	63.9	79.5	76.4	177	72.7	83	85.3	63.8	3.0	10.1	3.9	1.3	1.5	2.0	12.1	10.1	8.9	9.0	8.6	
Y/Ni	0.4	0.1	0.2	0.1	0.2	0.2	0.2	0.3	7.8	0.2	6.1	35.8	13.5	40.7	0.7	0.5	0.6	0.9	1.5	
Cr/Ni	2.0	1.5	1.3	1.6	2.0	1.7	1.4	1.8					45.6		5.7	6.8	2.3	2.3	3.2	
Cr/Th	11.5	14.7	10.9	51.9	17.7	19.7	14.7	11.1					2.6		0.9	1.6	0.5	0.3	0.4	
Th/Sc	1.3	1.0	0.5	0.6	0.8	0.8	0.8	1.1	10.4	7.2	4.1	9.9	8.6	7.8	2.1	1.4	1.4	1.7	2.1	
Co/Th	1.1	1.5	1.5	2.8	1.7	2.0	2.0	1.3	0.0	0.3	0.1	0.1	0.1		0.5	0.6	1.2	0.8	0.8	
La/Co	1.2	1.1	1.1	1.0	1.1	1.2	1.2	1.6	11.5	1.3	6.8	4.3	5.4		5.0	5.7	2.7	4.2	5.5	
La/Th	1.4	1.6	1.6	2.7	1.8	2.4	2.3	2.0	0.5	0.4	0.5	0.5	0.5	0.5	2.7	3.4	3.1	3.1	4.2	
La/Sc	1.7	1.6	0.8	1.6	1.5	1.9	1.8	2.2	5.0	3.1	2.0	4.8	4.0	3.8	5.6	4.7	4.4	5.4	9.0	
La/Lu	1.7	1.6	0.8	1.6	1.5	1.9	1.8	2.2	5.0	3.1	2.0	4.8	4.0	3.8	5.6	4.7	4.4	5.4	9.0	
REE	77.3	61.3	71.4	64.4	73.1	80.1	90.0	99.0	85.4	26.5	89.1	93.1	69.2	144.0	70.6	56.4	56.0	88.2	151.8	
HFSE	3164	3185	3206	3102	3436	4280	3555	3319	567	497	7295	492	431	630	2506	2318	2061	2840	4229	
Eu*	0.8	0.8	0.8	1.0	0.9	0.9	0.9	0.9	0.1	0.5	0.1	0.1	0.1	0.1	1.0	1.3	1.3	1.1	5.0	
Ce*	1.0	1.0	1.0	0.9	1.0	1.0	1.0	1.0	1.0	1.1	1.0	1.0	1.0	0.8	1.0	1.0	1.1	1.0	1.1	

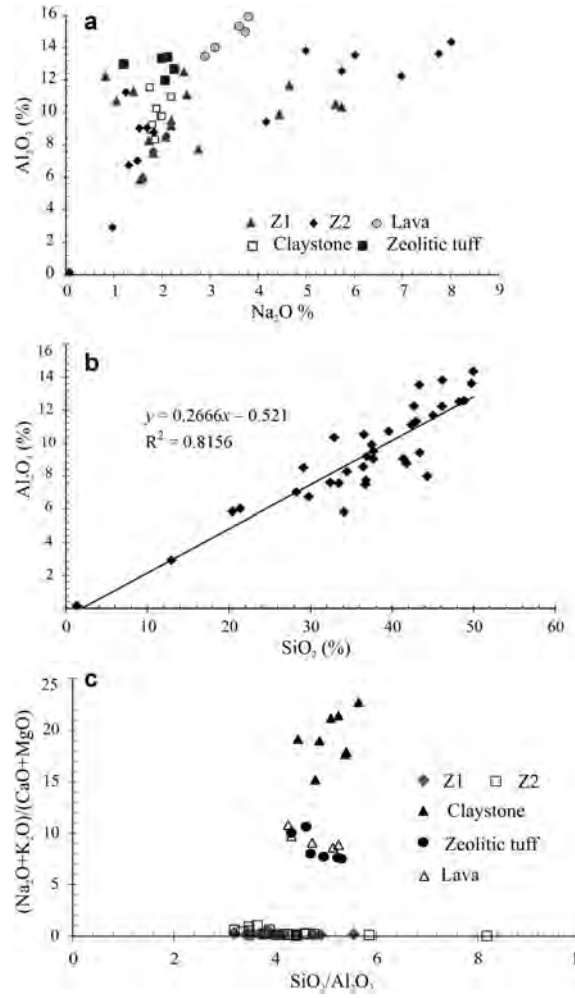

Figure 12. (a) Na_2O *vs.* Al_2O_3 plot of the sample groups investigated. Most of the Z1 and Z2 samples were located in different areas from those of the other sample groups. (b) Al_2O_3 *vs.* SiO_2 plot of the Z1 and Z2 section samples. (c) SiO_2/Al_2O_3 ratio *vs.* $(Na_2O+K_2O)/(CaO+MgO)$ plot (data are from Table 3).

(section Z3), except for some heavy-rare earth elements (*HREE*), were more depleted than those of the tuffs while more enriched than those of the fresh/weakly altered lava samples. All sample groups were enriched compared to chondrite. The Eu anomaly was calculated by the formula $Eu/Eu^* = Eu_N/(Sm_N \times Gd_N)^{1/2}$ (Gromet *et al.*, 1984). Clear Eu/Eu* anomalies were not seen in samples in all sample groups except for analcime-containing tuff samples, which is a strongly negative anomaly ($Eu/Eu^* < 1$) (Table 3a–c). The Ce anomaly denoted Ce/Ce* was calculated by $Ce/Ce^* = Ce_N/(La_N \times Pr_N)^{1/2}$ (Shimizu and Matsuda, 1977). No Ce anomalies were observed in any of the investigated sample groups The enrichment ratios of the light-rare earth elements (*LREE*) were greater than those of the *HREE*, which displayed virtually flat patterns in all samples except the tuffs (Figure 13a). Some of the high

Table 4. Chemical compositions and structural elements and ratios of type 1 analcimes, clinoptilolites, and erionites, as determined by EMPA.

	Z2-9 $n = 4$	Z2-11 $n = 3$	Z2-31 $n = 15$	Z2-31/1 $n = 13$	Mean	Cpt. $n = 12$	Eri. $n = 6$	MDL
SiO_2	59.18	59.01	59.52	60.19	59.50	65.74	61.03	0.09
Al_2O_3	20.36	20.07	19.57	19.67	19.9	13.32	14.80	0.08
CaO	0.21	0.12	0.11	0.37	0.20	2.54	2.99	0.06
K_2O	0.15	0.16	0.23	0.05	0.15	1.55	2.92	0.05
Na_2O	11.40	10.92	11.2	10.78	11.1	0.97	2.24	0.14
Fe_2O_3	0.12	0.13	0.08	0.12	0.11	0.10	0.22	0.32
MgO	0.13	0.18	0.05	0.22	0.15	1.77	0.79	0.09
$^{+}$BaO	0.01	0.01	0.08	0.02	0.03	0.36	0.07	0.22
$^{+}$SrO	0.20	0.18	0.36	0.22	0.24	0.61	0.09	0.15
Sum	91.26	90.71	91.19	91.64	91.2	86.79	85.15	
*%*E*	4.32	7.18	2.96	6.42	7.32	8.24	0.41	
	——— Unit-cell contents based on 96 oxygens ———					– 72 oxygens –		
Si	34.19	34.48	34.48	34.68	34.46	28.99	28.19	
Al	13.86	13.72	13.52	13.36	13.61	6.92	8.06	
Ca	0.13	0.06	0.07	0.23	0.15	0.03	0.08	
Na	12.77	12.21	12.73	12.04	12.44	0.83	2.01	
K	0.11	0.14	0.17	0.04	0.11	0.87	1.72	
Fe	0.16	0.18	0.11	0.16	0.12	1.20	0.98	
Mg	0.11	0.07	0.04	0.19	0.10	1.16	0.56	
Ba	0.00	0.01	0.02	0.01	0.01	0.06	0.01	
Sr	0.07	0.06	0.12	0.07	0.08	0.03	0.03	
Na/(Na+Ca)	0.99	1.00	0.99	0.98	0.99	0.41	0.67	
Na/Al	0.92	0.89	0.94	0.90	0.91	0.12	0.25	
Si/(Si+Al)	0.71	0.72	0.72	0.72	0.72	0.81	0.78	
Si/Al	2.47	2.51	2.55	2.60	2.53	4.19	3.50	
Si/(Al+Fe)	2.44	2.48	2.53	2.57	2.50	4.17	3.47	

$^{+}$ Ba and Sr were omitted in the calculation of the unit cell.
* %*E* calculated using the formula given by Gottardi and Galli (1985).
MDL: method detection limit.

field-strength elements (HFSE), *e.g.* Hf, Nb, Ta, Ti, Zr, and Cr (Saunders *et al*., 1980), and some trace elements, *e.g.* Ba, Sr, Sc, Co, Ni, Cr, Th, and U normalized to chondrite (Anders and Grevesse, 1989), had similar patterns to those of analcimolites, zeolitic tuffs, claystones, and lavas (Figure 13b). All of the above-mentioned elements were enriched compared to chondrite, while Co, Sc, and Ni, which were sourced from

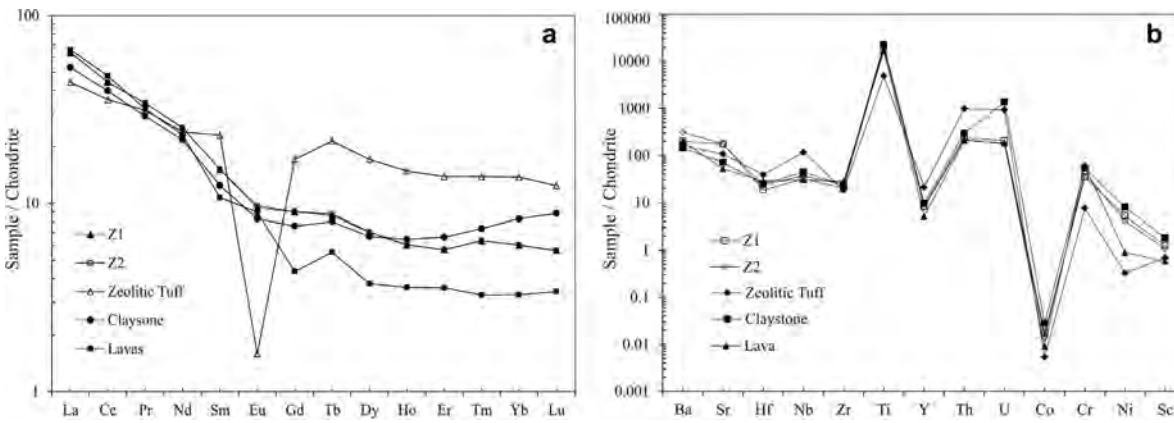

Figure 13. (a) Chondrite-normalized *REE* patterns of the sample groups investigated (normalization values from Boynton, 1984). (b) Chondrite-normalized trace elements of the sample groups (normalization values from Anders and Grevesse, 1989). The data are from Table 3.

mafic rocks, were depleted in the tuff and lavas (Figure 13b).

Quantitative analyses of the type 1 analcimes by electron microprobe analysis (EMPA) were performed for four of the analcime-rich rocks (Table 4). Analcime crystals from type 1 exhibited a range of Si/Al ratios from 2.47 to 2.60 (mean 2.53). In many cases, analcime crystals presented Na/Al ratios of <0.94, while the Si/Al ratio departed considerably from the theoretical value of 2, reaching values near 2.53 in this type. The type 1 analcimes contained more Si (~34.19 to 34.68 atoms per unit cell) and less Al (~13.36 to 13.86 atoms per unit cell) and Na (~12.04−12.77 atoms per unit cell) than the theoretical analcime (32 Si atoms per unit cell). Most of the analyses show Si/Al ratios slightly greater than 2.0; which corresponds to the silica-rich group of Coombs (1998). For the analcimes studied, the mean Si/(Si+Al) and Na/(Na+Ca) ratios were 0.72 and 0.99, respectively. In the sedimentary analcimes, the first and second ratios varied from 0.66 to 0.74 and very close to 1.0, respectively (Passaglia and Sheppard, 2001). The ratios, even though high, are similar to those of sedimentary analcimes, which lay between 0.74 and 0.76, as reported from diagenetically altered silicic tuffs (Passaglia and Sheppard, 2001, and references therein). The mean structural formula of the type 1 analcimes was determined to be $(Si_{34.46}Al_{13.62}Fe_{0.12})(Na_{12.44}Ca_{0.15}Mg_{0.10}Sr_{0.01}Ba_{0.01})$. The analcimes contain small amounts of K and alkaline earths, *e.g.* Mg, Sr, and Ba. Feldspar minerals in first and second section samples were analyzed by EMPA (Table 5). The K content of some feldspar minerals ranges from 10.48 to 14.22 wt.% K_2O, which is the typical K-feldspar composition. The investigated K-feldspar is thought to have formed authigenically. Other K/Na-rich feldspar minerals analyzed also contained much more K and Na than Ca, except for two points, *i.e.* 7 and 12 (Table 5a). Most of the feldspars analyzed contain much more monovalent alkalis than Ca. The smecite minerals were dioctahedral and Al-rich (between 13.45 and 21.29%), and had Na^+ as the main exchangeable cation; they were, therefore, assumed to be montmorillonite, which is also consistent with EDS data. The Na content of the feldspar and montmorillonite may provide Na to the analcime. The Ca and Mg contents of dolomite, the most common matrix mineral, were close to theoretical dolomite compositions (Table 5a). No analcime other than from sections Z1 and Z2 could be analyzed. Section Z3 samples contained K-feldspar and other K- and Na-rich feldspar minerals (Table 5b). Although the K content of some of the K-feldspar minerals ranged from 10.43 to 11.97% K_2O, it was less than in the analcime-rich samples. The chemical composition of K- and Na-rich feldspar was similar to oligoclase and/or andesine, except one sample was albite. The feldspar composition indicates that the host rock tuff is mainly dacite and/or andesite.

DISCUSSION

In the study area, the zeolite mineral types are mainly silicic-alkalic zeolites (analcime), and silicic zeolites with minor analcime. Three mineral associations were determined in the study area: (a) smectite-rich horizons with little or no clinoptilolite + erionite minerals; (b) an analcime-feldspar paragenesis was clear, but clinoptilolite + erionite + feldspar paragenesis was almost non-existent; and (c) clinoptilolite-erionite-rich horizons with little or no analcime. Analcime-rich sequences (Z1 and Z2) of dolomite were the most common carbonate mineral, calcite was found occasionally, and some layers contained nearly pure calcite in the upper parts of the Z1 and Z2 sequences consisting of thick limestone beds.

Textural thin sections and whole-rock and clay-sized fraction examination by XRD and SEM analyses showed that analcime was the only zeolite mineral in the type 1 rocks. There was no trace of the volcanic/pyroclastic input required to produce the analcime detected in the mudstones/sandstones. Detritus of volcanic (pyrogenic) origin, *e.g.* volcanic rock fragments, volcanic quartz, feldspar, amphiboles, and precursor zeolite, was not observed at the SEM scale in the samples. The above-mentioned minerals are also more stable than the volcanic glass in the saline and alkaline lake water. The samples contain different amounts of albite, K-feldspar, and montmorillonite in both the type 1 and type 2 analcimic zeolites (Tables 1, 5; Figures 7, 8). The mineralization period of the type 1 analcime with feldspar and clay minerals (especially montmorillonite and some illite and kaolinite, which were rich in the environment) is related to the alteration of minerals causing an increase in the alkaline ion concentration in the environment, suitable for zeolite-mineral formation (Sheppard and Gude, 1969; Moiola, 1970; Faure, 1998) in the alkaline environment, and it probably provides a source of Na^+, Al^{3+}, and silica. Analcime may form by continuously changing the physical and chemical state of the environment. The Na^+ ion was obtained from three sources: (a) detrital minerals, *e.g.* albite, Na-rich feldspars, montmorillonite; (b) Na-rich saline solutions; and (c) diagenetic evolution of clinoptilolite or volcanic materials. Analcime can be transformed from the albite or Na-rich feldspar by the reaction (Faure, 1998):

$$NaAlSi_3O_8 + 3H_2O \leftrightarrow NaAlSi_2O_6.H_2O + H_4SiO_4$$

or from montmorillonite. Occurrences of analcime which result from weathering of montmorillonite in saline and highly alkaline lake water were explained by Velde (1985) and Sheppard and Hay (2001). Another example of direct formation of analcime in the absence of volcaniclastic material was studied by English (2001) in the Lake Lewis and Maiz Gordo formations described by Campo *et al*. (2007). According to EDS and EMPA results, the Na content of the montmorillonite and Na-

Table 5. (a) Chemical composition (wt.%) of the feldspar, montmorillonite, and dolomite minerals in the first type of analcimes determined by EMPA.

	K-feldspars						K/Na-rich feldspars							Montmorillonites						Dolomites			
	1	2	3	4	5	6	7	8	9	10	11	12	13	14	15	16	17	18	19	20	21	22	23
SiO_2	66.74	66.25	67.17	66.76	64.83	64.93	67.62	66.43	66.23	66.23	66.43	62.54	64.93	51.28	49.24	54.07	50.18	54.30	53.39	0.20	0.89	0.37	0.09
Al_2O_3	18.19	18.22	18.06	18.35	18.58	18.84	20.01	18.92	18.51	18.51	18.92	17.75	20.43	15.01	13.45	16.16	19.63	19.57	21.29	0.05	0.05	0.15	0.00
CaO	0.23	0.34	0.30	0.60	0.51	0.12	0.19	0.51	0.65	0.65	0.51	1.53	0.92	5.24	7.35	5.27	3.48	0.15	2.94	31.16	28.81	28.47	30.75
K_2O	12.49	12.99	11.72	10.48	12.11	14.22	0.27	8.92	9.43	9.43	8.92	4.96	5.97	6.42	4.99	0.08	0.43	0.36	0.81	0.00	0.02	0.00	0.00
Na_2O	1.71	0.94	1.55	3.52	2.42	0.10	10.83	4.84	4.22	4.22	4.84	8.52	5.76	2.86	2.48	8.54	9.04	7.59	6.85	0.00	0.00	0.06	0.00
Fe_2O_3	0.00	0.25	0.04	0.10	0.58	0.00	0.00	0.26	0.18	0.18	0.26	1.97	0.02	0.25	0.53	0.34	0.13	0.08	0.25	0.53	0.38	2.76	0.55
MgO	0.04	0.13	0.07	0.00	0.18	0.04	0.01	0.00	0.00	0.00	0.00	0.19	0.02	3.62	4.86	3.00	2.57	0.01	1.47	18.90	19.50	18.72	21.55
BaO	0.06	0.25	0.08	0.10	0.21	0.24	0.00	0.00	0.29	0.29	0.00	0.27	0.00	0.08	0.25	0.01	0.00	0.00	0.16	0.09	0.00	0.10	0.00
SrO	0.43	0.31	0.39	1.00	0.36	0.40	0.25	0.38	0.13	0.13	0.38	0.42	0.20	0.36	0.61	0.29	0.28	0.18	0.17	0.65	0.93	0.34	0.80
Total	99.88	99.69	99.39	100.9	99.79	98.89	99.19	100.3	99.64	99.64	100.3	98.15	98.25	85.13	83.75	87.75	85.73	84.25	87.33	51.58	50.57	50.97	53.73

(b) Chemical composition of the feldspar minerals in Z3 section samples determined by EMPA.

	K-feldspars											Na/Ca-rich feldspars										MDL
	1	2	3	4	5	6	7	8	9	10	11	12	13	14	15	16	17	18	19	20	21	
SiO_2	66.47	65.55	66.80	66.43	66.50	66.47	66.75	66.15	66.69	66.54	66.01	62.57	61.80	63.48	62.94	62.69	62.62	62.69	62.62	66.14	67.85	0.09
Al_2O_3	19.15	19.48	18.96	18.85	19.17	19.15	18.80	19.00	18.73	18.69	19.13	23.57	22.94	22.94	23.61	22.65	23.49	22.65	23.49	20.98	20.23	0.08
CaO	0.12	0.16	0.05	0.05	0.21	0.12	0.21	0.19	0.21	0.21	0.10	4.66	4.91	4.25	4.65	4.20	4.63	4.20	4.63	2.71	0.04	0.06
K_2O	10.59	10.43	11.53	11.47	11.25	10.59	11.97	11.63	11.52	11.49	11.24	1.64	0.97	1.12	0.99	1.11	0.98	1.11	0.98	1.09	0.04	0.05
Na_2O	3.31	4.01	3.22	3.20	3.25	3.31	2.90	2.90	2.86	2.85	3.52	7.56	7.63	8.20	7.81	8.10	7.77	8.10	7.77	8.46	11.54	0.14
BaO	0.10	0.12	0.10	0.10	0.00	0.10	0.13	0.06	0.12	0.12	0.08	0.07	0.00	0.06	0.05	0.06	0.05	0.06	0.05	0.08	0.00	0.22
SrO	0.18	0.20	0.32	0.32	0.32	0.18	0.41	0.30	0.34	0.34	0.32	0.25	0.32	0.21	0.35	0.21	0.35	0.21	0.35	0.21	0.18	0.15
Total	99.91	99.97	100.6	100.4	100.4	99.91	101.5	100.2	100.5	100.2	100.4	100.3	99.23	100.3	100.4	98.96	99.70	98.96	99.70	99.92	99.97	

MDL: method detection limit

rich feldspars are sufficient for Na-enrichment in the basin. Montmorillonite is one of the main clay minerals associated with type 1 analcimes, and the dissolution/precipitation relation between the two minerals is clearly seen under examination by SEM. Na may also be sourced from salt and soda deposits in the underlying units. Halite and mirabilite/thenardite were deposited in the Tuzgölü basin. During authigenesis of the analcime, the Na-rich deposits could be another source of the Na-rich waters. Castanier *et al*. (1999) suggested that analcime might have occurred as a result of passive precipitation by bacteria when the Ca^{2+} was low and the pH increased (pH = 9) as it formed in Soda Lake, Kenya. Analcime is stable with the increase in Na activities in relation to H, conditions which are typical of saline solutions which are produced by evaporation (Velde, 1985). Euhedral and subhedral analcime crystals may reflect different chemical conditions for crystal growth than the volcanoclastic rocks. The Na and Al contents of all the section samples and lavas clearly show that Na originated from two different sources (Figure 12). Although some of the sample points in sections 1 and 2 are close to those of tuff and clays and some lavas, the Na content of the other samples is greater. Analcime is formed through either direct authigenetic precipitation or the reaction between interstitial fluids and clay minerals or plagioclase soon after deposition of the sediments during the similar conditions repeated in different episodes in the closed system. Analcime associated with sparitic dolomite and calcite may be formed under rather stable conditions with a high degree of water saturation, which is generally required for the development of sparitic carbonate cement. The alkaline earth element content in the first type of analcime-rich samples is related to the high carbonate content of the environment. In the study area, the evolution of saline and highly alkaline pore waters favors the precipitation of analcime, as the study area is the remnant of an ancient salt lake (Tuzgölü). In the absence of volcanic material, analcime from either direct precipitation or the reaction of clay and feldspar minerals with highly alkaline lake water was also proposed by several researchers (Wu, 1970; Ataman and Gündoğdu, 1982; Renault, 1993; English, 2001). The geochemical change in pore water is thought to be influenced by the mineralogy and geochemistry of pyroclastics, detrital-sediment lavas in Eocene rocks within a closed hydrographic basin.

The occurrence of analcime by dissolution and precipitation from detrital sediments (*e.g.* feldspar and clays) can be observed in the remarkable similarity of the *REE* and HFSE trends of the analcime and claystones. The clearly different *REE* trends of the analcime samples from those of the lava and tuffs indicate that the analcime is not sourced from tuff and lavas of the Karacadağ volcanites. Some of the trace element enrichment or depletion may also indicate different sources. The negative Eu anomaly in the tuff samples is related to the removal of Ca from the rocks in response to destruction of plagioclase, the Ca of which hosts most of the Eu. The Ca^{2+} ion is located in exchange sites of montmorillonite and in the structure of carbonate minerals; therefore, the other sample groups show no Eu anomalies.

Dolomite formations are related to solutions rich in Mg and Ca that are derived from the weathering of minerals in the ophiolitic mélange. The noticeably larger Sr content of the type 1 analcime-rich samples than of the other sample groups may be related to warm water (Emelyanov and Shimkus, 1986). The Sr content in magmatic (*e.g.* ultramafic, mafic, intermediate) and sedimentary rocks (*e.g.* argillaceous, shales, sandstones, and carbonate rocks) is lower, ranging from 2 ppm (in ultramafic rocks) to 600 ppm (in intermediate and carbonate rocks), than type 1 analcime-rich samples (Table 3) (Kabata Pendias and Pendias, 1999). A slightly negative correlation between Ca and Sr indicate that Sr is not located in the calcite structure. The Sr derived from a source other than that of Ca and might be precipitated as a $SrCO_3$ mineral (strontianite) when the pH is high (8.5−9.0) (Emelyanov and Shimkus, 1986, and references therein).

The formation of type 2 analcimes in the pyroclastic material may be related to dissolution of the volcanic material in saline-alkaline lakes and is favored by high activities of Na^+ and by low activities of silica and H^+ (Surdam and Sheppard, 1978; Boles and Surdam, 1979). Minerals which coexist with analcime, *e.g.* clinopilolite, erionite, and pumice fragments, support this type of analcime formation. Small, subhedral, globular analcimes in the zeolitic tuffs are indicative of homogeneous nucleation at greater degrees of supersaturation (Wilkin and Barnes, 2000), which is compatible with crystallization from highly reactive volcanic glass in contact with brackish alkaline lake waters which have elevated salinities and pH (Sheppard and Hay, 2001). The zeolite mineral types, contents, and similar content of Na, K, and Ca in the clinoptilolite-rich tuffs indicate that the basin is more alkaline than the Ca-rich clinoptilolite which is stable in diluted water (Chipera and Apps, 2001).

The theoretical structural formula of analcime is $Na_{16}Al_{16}Si_{32}O_{96}.16H_2O$. The ideal Si/Al ratio is 2.0; however, in natural analcime this ratio may vary from 1.5 to 2.9, with the more siliceous phases being found in altered rhyolitic tuffs (Coombs and Whetten, 1967; Iijima and Hay, 1968). The mean SiO_2/Al_2O_3 ratios of the studied lavas, zeolitic tuffs, and interlayered clays were 4.76, 4.85, and 5.12, respectively, while the ratio was 3.63 in the analcime-rich samples. The lower ratio in the analcime-rich samples than in the tuff and the other samples may indicate that their sources were different (Figure 13a). Consequently, the Si/Al ratio of analcime is an important parameter because it provides

information on the conditions or source rocks from which the analcime formed. Iijima and Hay (1968) reported that the Si/Al ratio of the analcime ranged from 1.95 to 2.81 and suggested that this variation might be caused by the reaction of analcime to authigenic feldspar, and may also indicate that analcime associated with authigenic feldspar has a lower Si/Al ratio than in analcime without feldspar with a Si/Al ratio in excess of 2.30. Researchers have suggested that analcime may form as an alteration product of clays deposited in saline and highly alkaline lakes (Hay and Moiola, 1963; Hay, 1970; Ataman and Gündoğdu, 1982; Hay and Guldman, 1986; Remy and Ferrell, 1989; English, 2001; Sheppard and Hay, 2001). Detrital clay minerals are known to react extensively in a saline, alkaline environment (Hay and Moiola, 1963; Hay, 1966; Brobst and Tucker, 1973; Hay and Guldman, 1986). In the analcime-rich samples, the feldspar contents were ~5%, and the Si/Al ratio varied from 2.23 to 2.57. When the feldspar content increased, analcime decreased or disappeared. The analcimolite layer contained much more dolomite and montmorillonite than the other minerals and no fossils or pyroclastics. However, the dissolution of analcime and the formation of smectite were clearly observed in the SEM investigation. Although the analcime-to-feldspar transformation was not observed, analcime may be precipitated after dissolution of the feldspar in different periods.

Analcime-rich sediments cover pillow lavas and dacitic dykes of the ophiolitic mélange. Ataman and Gündoğdu (1982) suggested that the basic rocks of the ophiolitic mélange can supply solutions with suitable compositions, and a closed basin with very weak drainage is suitable for analcime authigenesis.

The *REE* and HFSE patterns of sedimentary rocks may provide an index for the average provenance compositions. The *REE* are particularly useful for studying provenance because of their low solubility during weathering and diagenetic processes (Bhatia and Taylor, 1981). The *REE* trends of rocks may also have been inherited from parent-rock *REE* signatures. All sample groups show slight *LREE*-enriched and relatively flat *HREE* patterns with a negative Eu anomaly (Eu/Eu* = 1.11), except for analcimolite-rich section samples, which have practically no Eu anomaly (Table 3, Figure 12). The characteristic features of the *REE* patterns of the samples investigated (*LREE* enrichment relative to *HREE* and flat *HREE*) may be attributed to the felsic origin of the parent rocks. Nearly parallel patterns and trends of the analcimolites, zeolitic tuffs, and claystones indicate that all of the samples may have originated from a common provenance, not including mafic rocks. The *REE* and some of the HFSE contents of the analcimolites, zeolitic tuffs, and claystones were also similar. All of the analcimolites analyzed, the zeolitic tuff, and the claystone samples had Σ*REE* abundances less than the average Upper Continental Crust (UCC, ~143 ppm; Taylor and McLennan, 1985). Most of the analcimolite samples contained more Sr than the other sample groups, considering that both ions (Eu^{2+} and Sr^{2+}) have comparable ionic sizes and, thus, tend to substitute for Ca^{2+} in calcite (Gao and Wedepohl, 1995).

Analcimolites and zeolitic tuffs show slightly negative Ce* anomalies, suggesting that the environmental conditions were relatively oxygenated in the basin. The *LREE*, especially La and Th, are more abundant in felsic than basic igneous rocks and their weathered products, whereas Co, Cr, V, and Sc are less abundant (Taylor and McLennan, 1985; Wronkiewicz and Condie, 1987). Ratios such as La/Co, (La/Lu)cn, La/Sc, Th/Sc, Th/Co, Cr/Ni, Cr/Th, and Eu/Eu* are significantly different in mafic and felsic source rocks; therefore, the ratios allow constraints to be placed on the average provenance composition (Wronkiewicz and Condie, 1987, 1989, 1990; Cullers *et al*., 1988; Cullers, 1994, 1995; Cox *et al*., 1995). The La/Th ratio of the analcimolites, zeolitic tuffs, and claystones were 2.7, 0.9, and 2.2, respectively, which is similar to the average UCC composition and all samples having a significant felsic component (La/Th = 2.8, Taylor and McLennan, 1985). In the study area, the Eu/Eu*, (La/Lu)cn, La/Sc, Th/Sc, La/Co, Th/Co, and Cr/Th values of the analcimolites, zeolitic tuffs, and claystones were close to the values of sediments derived from felsic (not mafic, *e.g.* ophiolitic mélange) source rocks (Table 4). In addition, the low Cr/Ni ratios were between 1.0 and 3.7 for analcimolites and 0.8 and 1.9 for zeolitic tuffs and claystones (Table 4). The ratios were somewhat higher than in the UCC (1.75) and point to a relative enrichment of ferromagnesian minerals within the clays and sandstones rather than originating from a mafic source.

Tuzgölü was the largest interior basin in central Anatolia. Maastrictian-Oligo-Miocene sedimentation is characterized by shallow marine, marine-deltaic, fluvial-lacustrine, and deltaic−lacustrine deposits (Gürer and Aldanmaz, 2002). Fluctuations in seasonal fresh inflow and temperature caused the lake level, salinity, and alkalinity of the closed Tuzgölü basin to change with time. Calcite precipitated when the lake water was diluted, evaporation/concentration exceeded freshwater inflow, lake water became noticeably more alkaline, and alkaline-earth carbonates precipitated (proto dolomite, dolomite). Increases in alkalinity and temperature caused the basin to become saline. Under the saline and alkaline conditions, the type 1 analcime was derived from weathering of detrital materials, but not from pyrogenic minerals, *e.g.* feldspar and montmorillonite. K-feldspar together with analcime indicates highly saline conditions. The closed basin may have been fed by brine solution from old salt and soda deposits in underlying units.

The Co/Th ratios of the samples were between 0.1 and 3.2 and, thus, close to UCC (0.93), NASC (Average North American Shale, Gromet *et al*., 1984) (2.09), and PAAS (1.58). These ratios indicate that the samples were

of felsic provenance. The average Co content in ultramafic rocks was 105 ppm (Jagoutz *et al*., 1979), whereas Co in the analcime-rich samples ranged from 0.50 to 15.0 ppm. The geochemical differences between elements such as Th and La (indicative of a felsic source) and Sc and Cr (indicative of a mafic source) have been exploited by various researchers to distinguish between felsic and mafic provenance (*e.g.* McLennan *et al*., 1980; McLennan, 1989; Wronkiewicz and Condie, 1990; McLennan and Taylor, 1991). The Th/Sc ratio (1.20−7.5) of the samples studied was related to the more felsic source rocks. The similarity of the depleted *REE* trend of analcimolites and claystone may be related to a cogenetic source.

CONCLUSIONS

Two lines of evidence strongly suggest that type 1 analcime in the lacustrine sediments of the study area was not formed from precursor zeolites derived from vitric material. First, SEM, XRD, and thin-section analyses showed that the analcime is the only zeolite in the rocks. Second, no trace of volcanic material required to produce the analcime was detected in the analcime-rich samples. Based on the textural, mineralogical, and chemical evidence, type 1 analcime was, therefore, not formed by alteration of volcaniclastic materials because of the absence of a precursor zeolite phase, volcanic glass, or volcanic materials. The type 1 silica-rich analcimes formed either by direct chemical precipitation or by the reaction of montmorillonites and Na-rich feldspars or other non-zeolite precursors in a closed basin. Analcime together with K-feldspar indicates that the basin was affected by saline and highly alkaline brine fluids. Partial interlayering of analcime-rich beds with limestone (calcite enrichment) beds related to fluctuation of lake level and increasing seasonal inflow was caused by low evaporation. Type 2 analcimes were apparently formed from precursor zeolites and/or by the reaction of acid with intermediary volcanic material that underwent saline, alkaline lake-water effects, and were favored by high activities of Na^+ and low activities of silica.

ACKNOWLEDGMENTS

The present investigation was made possible through financial support by the TÜBITAK 109Y301 project and the Selçuk University Scientific Research projects support program BAP 10401052. The authors acknowledge Chris Fleisher (Department of Geology, University of Georgia) for his help with the EMPA analyses. The authors are grateful to Prof. Dr. Ö. Işık Ece and two anonymous reviewers for their constructive comments which greatly improved the quality of the manuscript.

REFERENCES

Anders, E. and Grevesse, N. (1989) Abundances of the elements: meteoric and solar. *Geochimica et Cosmochimica Acta*, **53**, 197−214.

Ataman, G. (1976) Türkiye'de yeni bir analsim oluşuğu ve zeolitli serilerle plaka tektoniği arasında muhtemel ilişkiler. *H.Ü. Yerbilimleri*, **2**, 9−23, Ankara.

Ataman, G. and Beseme, P. (1972) Decouverte de I'analcime sedimentaire en Anatolia du Nord-Quest (Turquie), Minerologie, genese, paragenese. *Chemical Geology*, **9**, 203−225.

Ataman, G. and Gündoğdu, N. (1982) Analcimic zones in the Tertiary of Anatolia and their geologic positions. *Sedimentary Geology*, **31**, 89−99.

Armstrong, J.T. (1988) Accurate quantitative analysis of oxygen and nitrogen with a WSi multilayer crystal. Pp. 301−304 in: *Microbeam Analysis* (D.E. Newbury, editor). San Francisco Press, San Francisco, California, USA.

Bhatia, M.R. and Taylor, S.R. (1981) Trace element geochemistry and sedimentary provenances: a study from the Tasman geosyncline, Australia. *Chemical Geology*, **33**, 115−125.

Boles, J.R. and Surdam, R.C. (1979) Diagenesis of volcanogenic sediments in a Tertiary saline lake: Wagon Bed Formation, Wyoming. *American Journal of Science*, **279**, 832−853.

Boynton, W.V. (1984) Geochemistry of rare earth elements: meteorite studies. Pp. 63−114 in: *Rare Earth Element Geochemistry* (P. Henderson, editor). Elsevier, Amsterdam.

Brobst, D.A. and Tucker, J.D. (1973) X-ray mineralogy of the Parachute Creek Member, Green River Formation, in the northern Piceance Creek basin, Colorado. U.S. *Geological Survey Professional Paper* **803**, 53 pp.

Campo, M.D., Papa, D.C., Jiménez-Millán, J., and Nieto, F. (2007) Clay mineral assemblages and analcime formation in a Palaeogene fluvial-lacustrine sequence (Maíz Gordo Formation Palaeogene) from northwestern Argentina. *Sedimentary Geology*, **201**, 56−74.

Castanier, S., Le M′Etayer-Levrel, G., and Perthuisot, J.P. (1999) Ca-carbonates precipitation and limestone genesis − the microbiogeologist point of view. *Sedimentary Geology*, **126**, 9−23.

Chipera, S. and Apps, J. (2001) Geochemical stability of natural zeolites. Pp 117−161 in: *Natural Zeolites: Occurrence, Properties, Applications* (D.L. Bish and D.W. Ming, editors). Reviews in Mineralogy and Geochemistry, **45**, Mineralogical Society of America and the Geochemical Society, Washington, D.C.

Coombs, D.S. (1998) Recommended nomenclature for zeolite minerals − Report of the subcommittee on zeolites of the International Mineralogical Association: *Mineralogical Magazine*, **62**, 533−571.

Coombs, D.S. and Whetten, J.T. (1967) Composition of analcime from sedimentary and metamorphic rocks. *Geological Society of America Bulletin*, **78**, 269−282.

Corfu, F. and Davis, D.W. (1991) Archaean hydrothermal zircon in the Abitibi greenstone belt: constraints on the timing of gold mineralization Comment. *Earth and Planetary Science Letters*, **104**, 545−552.

Cox, R., Lowe, D.R., and Cullers, R.L. (1995) The influence of sediment recycling and basement composition on evolution of mudrock chemistry in the southwestern United States. *Geochimica et Cosmochimica Acta*, **59**, 2919−2940.

Cullers, R.L. (1994) The controls on the major and trace element variation of shales, siltstones, and sandstones of Pennsylvanian-Permian age from uplifted continental blocks in Colorado to platform sediment in Kansas, USA. *Geochimica et Cosmochimica Acta*, **58**, 4955−4972.

Cullers, R.L. (1995) The controls on the major-and trace-element evolution of shales, siltstones and sandstones of Ordovician to Tertiary age in the Wet Mountains region, Colorado, USA. *Chemical Geology*, **123**, 107−131.

Cullers, R.L., Basu, A., and Suttner, L.J. (1988) Geochemical

signature of provenance in sand-size material in soils and stream sediments near the Tobacco Root batholith, Montana, USA. *Chemical Geology*, **70**, 335–348.

Emelyanov, E.V. and Shimkus, K.M. (1986) *Geochemistry and Sedimentology of the Mediterranean Sea*. Reidel, Dordrecht, The Netherlands, 553 pp.

English, P.M. (2001) Formation of analcime and moganite at Lake Lewis, central Australia: significance of groundwater evolution in diagenesis. *Sedimentary Geology*, **143**, 219–244.

Esenli, F. and Özpeker, I. (1993) Zeolitic diagenesis of Neogene basin and the mineralogy of heulandite-clinoptilolite around Gördes. *Geological Bulletin of Turkey*, **8**, 1–18.

Esenli, F. and Sirkecioğlu, A. (2005) The relationship between zeolite (heulandite-clinoptilolite) content and the ammonium-exchange capacity of pyroclastic rocks in Gördes, Turkey. *Clay Minerals*, **40**, 557–564.

Faure, G. (1998) *Principles and Applications of Geochemistry*, Prentice Hall, Upper Saddle River, New Jersey, USA, 600 pp.

Floyd, P.A. and Winchester, J.A. (1978) Identification and discrimination of altered and metamorphosed volcanic rocks using immobile elements. *Chemical Geology*, **21**, 291–306.

Gall, Q. and Hyde, R. (1989) Analcime in lake and lake-margin sediments of the Carboniferous Rocky Brook Formation, western Newfoundland, Canada. *Sedimentology*, **36**, 875–887.

Gao, S. and Wedepohl, K.H. (1995) The negative Eu anomaly in Archean sedimentary rocks: implication for decomposition, age and importance of their granitic sources. *Earth and Planetary Science Letters*, **133**, 81–94.

Gottardi, G. and Galli, E. (1985) *Natural Zeolites*. Springer-Verlag, Berlin, 409 pp.

Gottardi, G. and Obradovic, J. (1978) Sedimentary zeolites in Europe. *Fortschritte der Mineralogie*, **56**, 316–366.

Görür, M.N., Oktay, F.Y., Seymen, İ., and Şengör, A.M.C. (1984) Paleotectonic evolution of the Tuzgölü basin complex, Central Turkey: sedimentary record of a Neo-Tethyan closure. Pp. 467–482 in: *The Geological Evolution of the Mediterranean* (J.E. Dixon and A.H.F. Robertson, editors). Special Publications, **17**, Geological Society, London.

Gromet, L.P., Dymek, R.F., Haksin, L.A., and Korotev, R.L. (1984) The "North American shale composite": its compilation, major and trace element characteristics. *Geochimica et Cosmochimica Acta*, **48**, 2469–3482.

Gündoğdu, M.N. (1982) Neojen yaşlı Bigadiç sedimanter baseninin jeolojik, mineralojik ve jeokimyasal incelenmesi. PhD thesis, Hacettepe University, Ankara, Turkey, 386 pp.

Gündoğdu, M.N., Yalçın, H., Temel, A., and Clauer, N. (1996) Geological, mineralogical and geochemical characteristics of zeolite deposits associated with borates in the Bigadic Emet and Kırka Neogene lacustrine basins, western Turkey. *Mineralium Deposita*, **31**, 492–513.

Gürer, Ö. F. and Aldanmaz, E. (2002) Origin of the Upper Cretaceous-Tertiary Sedimentary Basins within the Tauride-Anatolide Platform in Turkey. *Geological Magazine*, **139/2**, 191–197.

Hay, R.L. (1966) Zeolites and zeolitic reactions in sedimentary rocks. *Geological Society of America Special Paper*, **85**, 130 pp.

Hay, R.L. (1968) Chert and its sodium-silicate precursors in sodium carbonate lakes of East Africa. *Contributions to Mineralogy and Petrology*, **17**, 255–274.

Hay, R.L. (1970) Silicate reactions in three lithofacies of a semi-arid basin, Olduvai Gorge, Tanzania. *Mineralogical Society of America Special Paper*, **3**, 237–255.

Hay, R.L. and Guldman, S.G. (1986) Silicate diagenesis in sediments of Searles Lake, California: in Programme and Abstracts, 23rd Annual Meeting of The Clay Minerals Society, Jackson, Mississippi, USA, p. 15.

Hay, R.L. and Moiola, R.J. (1963) Authigenic silicate minerals in Searles Lake, California. *Sedimentology*, **2**, 312– 332.

Hay, R.L. and Sheppard, R.A. (2001) Occurrence of zeolites in sedimentary rocks: an overview. Pp. 217–234 in: *Natural Zeolites: Occurrence, Properties*, *Applications* (D. Bish and D. Ming, editors). Reviews in Mineralogy, **45**, Mineralogical Society of America and the Geochemical Society, Washington, D.C.

Helvacı, C., Stamatakis, M.G., Zagouroglou, C., and Kanaris, J. (1993) Borate minerals and related authigenic silicates in northeastern Mediterranean late Miocene continental basins. *Exploration and Mining Geology*, **2**, 171–178.

Iijima, A. and Hay, R.L. (1968) Analcime composition in the Green River Formation of Wyoming. *American Mineralogist*, **53**, 184–200.

Innocenti, F., Mazzuoli, R., Pasquare, G., Radicati Di Brozolo, F., and Villari, L. (1975) The Neogene calcalkaline volcanism of central Anatolia: geochronological data on Kayseri–Niğde area. *Geological Magazine*, **112**, 349–360.

Jagoutz, E., Palme, H., Baddenhausen, H., Blum, K., Cendales, M., Dreibus, G., Spottel, B., Lorenz, V., and Wanke, H. (1979) The abundances of major, minor and trace elements in the Earth's mantle as derived from primitive ultramafic nodules. Proceedings of the Lunar and Planetary Science Conference No 10. *Geochimica et Cosmochimica Acta*, *Supplement*, **11**, 2031–2050.

Kabata-Pendias, A. and Pendias, H. (1999) *Biochemistry of Trace Elements*. Wyd Nauk PWN, Warsaw, 398 pp.

Kaçmaz, H. and Koktürk, U. (2004) Geochemistry and mineralogy of zeolitic tuffs from the Alacatı (Ceşme) area, Turkey. *Clays and Clay Minerals*, **52**, 705–713.

Kadir S., Önen-Hall, A.P., Aydın, S.N., Yakıcıer, C., Akarsu, N., and Tuncer, M. (2008) Environmental effect and genetic influence: a regional cancer predisposition survey in the Zonguldak region of Northwest Turkey. *Environmental Geology*, 54, 391–409,

Karakaş, Z. and Kadir, S. (2006) Occurrence and origin of analcime in a Neogene volcano-sedimentary lacustrine environment, Beypazarı-Çayırhan basin, Ankara, Turkey. *Neues Jahrbuch für Mineralogie Abhandlungen*, **182**, 253–264.

Karakaya, M.Ç., Karakaya, N., and Kupeli, Ş. (2011) Mineralogical and geochemical properties of the Na- and Ca-bentonites of Ordu (N.E. Turkey). *Clays and Clay Minerals*, **59**, 75–94.

Karakaya, N., Karakaya, M.Ç., and Yavuz, F. (2012) Investigation of mineralogic, geochemical and some technologic properties of zeolite occurrences in around of Kulu (Konya) and Haymana (Ankara). TÜBİTAK 109Y301, 200 pp. (unpublished report).

Kurt, H., Asan, A., and Ruffet, G. (2008) The relationship between collision-related calcalkaline, and within-plate alkaline volcanism in the Karacadağ Area (Konya-Türkiye, Central Anatolia). *Chemie der Erde*, **68**, 155–176.

McLennan, S. M. (1989) Rare earth elements in sedimentary rocks: influence of provenance and sedimentary processes. Pp. 169–190 in: *Geochemistry and Mineralogy of Rare Earth Elements* (B.R. Lipin and G.A. McKay, editors). Reviews in Mineralogy, **21**, Mineralogical Society of America, Washington, D.C.

McLennan, S.M. and Taylor, S.R. (1991) Sedimentary rocks and crustal evolution: tectonic setting and secular trends. *Journal of Geology*, **99**, 1–21.

McLennan, S.M., Nance, W.B., and Taylor, S.R. (1980) Rare earth element-thorium correlation in sedimentary rocks, and the composition of the continental crust. *Geochimica et Cosmochimica Acta*, **44**, 1833–1839.

Moiola, R.J. (1970) Authigenic zeolites and K-feldspars in the Esmeralda Formation, Nevada. *American Mineralogist*, **55**, 1681–1691.

Okay, A.I., Tansel, İ., and Tüysüz, O. (2001) Obduction, subduction and collision as reflected in the Upper Cretaceous–Lower Eocene sedimentary record of western Turkey. *Geological Magazine*, **138**, 117–142.

Özen, S. and Göncüoğlu, M.C. (2011) Origin of analcime in the Neogene Arıklı tuffs, Biga Peninsula, NW Turkey. *Neues Jahrbuch für Mineralogie*, **189**, 21–34.

Pasquar, G., Poli, S., Vezzoli, L., and Zanchi, A. (1988) Continental arc volcanism and tectonic setting in Central Anatolia, Turkey. *Tectonophysics*, **146**, 217–230.

Passaglia, E. and Sheppard, R.A. (2001) Crystal chemistry of zeolites. Pp 69–116 in: *Natural Zeolites: Occurrence, Properties, Applications* (D.L. Bish and D.W. Ming, editors). Reviews in Mineralogy and Geochemistry, **45**, Mineralogical Society of America and the Geochemical Society, Washington, D.C.

Remy, R.R. and Ferrell, R.E. (1989) Distribution and origin of analcime in marginal lacustrine mudstones of the Green River Formation, south-central Uintsa Basin, Utah. *Clays and Clay Minerals*, **37**, 419–432.

Renaut, R.W. (1993) Zeolitic diagenesis of late Quarternary fluviolacustrine sediments and associated calcrete formation in the Lake Bogoria Basin, Kenya Rift Valley. *Sedimentology*, **40**, 271–301.

Rollinson, H. (1993) *Using Geochemical Data; Evaluation, Presentation, Interpretation.* Longman Scientific and Technical, Harlow, Essex, UK, 352 pp.

Şahin, M.B. (2007) Orta Anadolu'da belirlenen önemli bir şabazit oluşumu ve mineralojik özellikleri. *MTA Dergisi*, **135**, 31–44.

Saunders, A.D., Tarney, J., Marsh, N.G., and Wood, D.A. (1980) Ophiolites as ocean crust: a geochemical approach. Pp. 193–204 in: *Ophiolites: Proceedings of the International Ophiolite Symposium* (A. Panayiotou, editor). Ministry of Agriculture and Natural Resources, Cyprus, 1979. Geological Survey Department, Cyprus.

Sheppard, R.A. and Gude, A.J. (1968) Distribution and genesis of authigenic silicate minerals in tuffs of Pleistocene Lake Tecopa, Inyo County, California. *U.S. Geological Survey Professional Paper*, **597**, 38 pp.

Sheppard, R.A. and Gude, A.J. (1969) Diagenesis of tuffs in the Barstow Formation, Mud Hills, San Bernardino County, California. *U.S. Geological Survey Professional Paper*, **634**, 35 pp.

Sheppard, R.A. and Hay, R.L. (2001) Formation of zeolites in open hydrologic systems. Pp 261–276 in: *Natural Zeolites: Occurrence, Properties, Application*. (D.L. Bish and D.W. Ming, editors). Review in Mineralogy Geochemistry, **45**, Mineralogical Society of America and the Geochemical Society, Washington, D.C.

Shimizu, H. and Masuda, A. (1977) Cerium in chert as an indication of marine environment of its formation. *Nature*, **266**, 346–348.

Snellings, R., Haten van, T., Machiels, L., Mertens, G., Vandenberghe, N., and Elsen, J. (2008) Mineralogy, geochemistry and diagenesis of clinoptilolite tuffs (Miocene) in the central Simav graben, Western Turkey. *Clays and Clay Minerals*, **56**, 622–632.

Surdam, R.C. and Eugster, H.P. (1976) Mineral reactions in the sedimentary deposits of the Lake Magadi region, Kenya. *Geological Society of America Bulletin*, **87**, 1739–1752.

Surdam, R.C. and Parker, R.B. (1972) Authigenic aluminosilicate minerals in the tuffaceous rocks of the Green River Formation, Wyoming. *Geological Society of America Bulletin*, **83**, 689–700.

Surdam, R.C. and Sheppard, R.A. (1978) Zeolites in saline, alkaline-lake deposits. Pp. 145–174 in: *Natural Zeolites: Occurrence, Properties*, *Use* (L.B. Sand and F.A. Mumpton, editors). Pergamon Press, Elmsford, New York.

Taylor, S.R. and McLennan, S.M. (1985) *The Continental Crust: its Composition and Evolution*. Blackwell, Oxford, UK, 312 pp.

Temel, A. and Gündoğdu, M.N. (1996) Zeolite occurrences and the erionite-mesothelioma relationship in Cappadocia, central Anatolia. *Mineralium Deposita*, **31**, 539–547.

Uğuz, F.M, Turhan, N., Bilgin, A.Z., Umut, M., Şen, A.M., and Acarlar, M. (1999) Kulu (Konya)–Haymana (Ankara) ve Kırıkkale dolayının jeolojisi. MTA Rapor No: 10399, Ankara (unpublished report).

Velde, B. (1985) *Clay Minerals: a Physico-Chemical Explanation of their Occurrence*. Elsevier, Amsterdam, 427 pp.

Whitney, D.L. and Evans, B.W. (2010) Abbreviations for names of rock-forming minerals. *American Mineralogist*, **95**, 185–187.

Wilkin, R. and Barnes, H. (2000) Nucleation and growth kinetics of analcime from precursor Na-clinoptilolite. *American Mineralogist*, **85**, 1329–1341.

Winchester, J.A. and Floyd, P.A. (1977) Geochemical discrimination of different magma series and their differentiations products using immobile elements. *Chemical Geology*, **20**, 325–340.

Wronkiewicz, D.J. and Condie, K.C. (1987) Geochemistry of Archean greywackes from Wyoming Supergroup, South Africa: source-area weathering and provenance. *Geochimica et Cosmochimica Acta*, **51**, 2401–2416.

Wronkiewicz, D.J. and Condie, K.C. (1989) Geochemistry and provenance of sediments from the Pongola Supergroup, South Africa: evidence for a 3.0 Ga old continental craton. *Geochimica et Cosmochimica Acta*, *53*, 1537–1549.

Wronkiewicz, D.J. and Condie, K.C. (1990) Geochemistry and mineralogy of sediments from the Ventersdrop and Transvaal Supergroups, South Africa: cratonic evolution during the early Paleozoic. *Geochimica et Cosmochimica Acta*, **54**, 343–354.

Wu, D.C. (1970) Origin of mineral analcite in the upper Flowerpot Shale, northwestern Oklahoma. *Transactions of the Kansas Academy of Science*, **73**, 247–251.

(*Received 25 December 2012; revised 24 April 2013; Ms. 737; AE: S. Kadir*)

Clays and Clay Minerals, Vol. 61, No. 3, 258–276, 2013.

THE RATE AND MECHANISM OF DEEP-SEA GLAUCONITE FORMATION AT THE IVORY COAST–GHANA MARGINAL RIDGE

ANDRE BALDERMANN[1,2], LAURENCE N. WARR[2], GEORG H. GRATHOFF[2], AND MARTIN DIETZEL[1]

[1] Institute of Applied Geosciences, Graz University of Technology, 8010 Graz, Austria
[2] Department of Geography and Geology, Greifswald University, 17493 Greifswald, Germany

Abstract—The environmental conditions and reaction paths of shallow-water glauconititization (<500 m water depth, ~15ºC) close to the sediment–seawater interface are generally considered to be well understood. In contrast, the key factors controlling deep-sea glauconite formation are still poorly constrained. In the present study, green grains formed in the recent deep-sea environment of the ODP Site 959, Ivory Coast–Ghana Marginal Ridge, (~2100 m water depth, 3–6ºC) were investigated by X-ray diffraction and electron microscopic methods in order to determine the rate and mechanism of glauconitization.

Green clay authigenesis at Hole 959C occurred mainly in the tests of calcareous foraminifera which provided post-depositional conditions ideal for glauconitization. Within this organic-rich micro-environment, Fe-smectite developed <10 ky after deposition of the sediments by precipitation from precursor gels containing Fe, Mg, Al, and silica. This gel formation was supported by microbial activity and cation supply from the interstitial solution by diffusion. At a later stage of early marine diagenesis (900 ky), the Fe-smectites reacted to form mixed-layer glauconite-smectite. Further down (~2500 ky), almost pure glauconite with no compositional gaps between the Fe-smectite and glauconite end members formed. This burial-related Fe-smectite-to-glauconite reaction indicates that the glauconitization process was controlled mainly by the chemistry of the interstitial solutions. The composition of the interstitial solution depends heavily on micro-environmental changes related to early diagenetic oxidation of biodegradable (marine) organic matter, microbial sulfate reduction, silicate mineral alteration, carbonate dissolution, and Fe redox reactions. The availability of Fe is suggested as the probable limiting factor for glauconitization, explaining the various states of green-grain maturity within the samples, and this cation may be the most important rate-determining element.

The rate of glauconite formation at ODP Site 959 is given by $\%Gl_{Sed} = 22.6 \cdot \log(age_{Sed}) + 1.6$ ($R^2 = 0.97$) where $\%Gl_{Sed}$ is the state of glauconitization in the sediment and age_{Sed} is the sediment age (in ky). This glauconitization rate depends mainly on continuous cation supply (in particular Fe) and is about five times less than that in shallow-shelf regions, suggesting significantly slower reaction at the lower temperature of deep-sea environments.

Key Words—Deep-sea Sediment, Fe-smectite, Glauconite, Interstitial Solution, Micro-environment, Mixed-layer Clay Minerals, ODP Site 959.

INTRODUCTION

The formation of glauconite, a dioctahedral, green, Fe-rich 2:1 illite mineral and mixed-layer glauconite-smectite (Gl-S) generally takes place in low-latitude, shallow-marine shelf regions at Eh ~0 mV, seawater pH (8.2), and low sedimentation rates (*e.g.* Odin and Fullagar, 1988). The presence of organic-rich, semi-confined micro-environments such as in foraminifera tests and in fecal pellets is considered to be a key factor for glauconitization, providing suitable post-depositional conditions (*e.g.* Odin and Matter, 1981; Baldermann *et al.*, 2012). In this respect, the occurrence of shallow-water glauconites formed in <500 m water depth, at temperatures below 15ºC (Odin and Fullagar, 1988), and close to the sediment–seawater interface (Wiewióra *et al.*, 2001) represents the typical environment of glauconite formation.

In contrast, exotic occurrences of green-clay authigenesis and glauconite formation have been described in some low-temperature (<6ºC), deep-sea (>1000 m water depth) settings (*e.g.* Buatier *et al.*, 1989; Giresse and Wiewióra, 2001; Gaudin *et al.*, 2005; Cuadros *et al.*, 2011). Such cold environments differ significantly from that of the shallow shelf, with reduced hydrodynamic energy, limited supply and reflux of particular (silicate) mineral phases, low reaction rates, and less microbial activity (*e.g.* Schulz and Zabel, 2006). The effects of these parameters on the glauconitization reaction are still poorly known and only a few constraints are placed on the rates and mechanism of green-clay genesis in such recent deep-sea environments. Gaudin *et al.* (2005) proposed that initially formed Fe-montmorillonite alters rapidly towards the glauconite end member during early marine diagenesis in which the availability of Al and K and the low temperature are the most important rate-controlling factors for glauconitization.

* E-mail address of corresponding author:
baldermann@tugraz.at
DOI: 10.1346/CCMN.2013.0610307

Sediments from the ODP Site 959, Ivory Coast–Ghana Marginal Ridge, provide a condensed and undisturbed sedimentary record without long periods of sediment erosion. Since at least the Miocene, foraminifera and nanofossil oozes have accumulated which are mixed with green grains and minor amounts of detrital silicates (*e.g.* Mascle *et al.*, 1996). Based on petrographic, mineralogical, and geochemical analyses on separated bulk green-grain fractions, Giresse and Wiewióra (2001) and Wiewióra *et al.* (2001) established the authigenic nature of the green clay minerals in these sediments and determined their overall composition to be dioctahedral Fe^{3+}-montmorillonite, with minor proportions of interstratified Gl-S (~20% glauconite layers and ~80% Fe-smectite layers) in the more mature, dark green grains. Based on the association of green clay and the occasional periods of sediment erosion, those authors proposed that the authigenic clay formed primarily at the water–sediment interface during phases of intense ion exchange with the seawater. The formation of glauconitic minerals was, therefore, expected to occur immediately after deposition of the sediments and not related to any burial or diagenetic reactions within the sediment pile. The glauconitization mechanism proposed was that of Fe-smectite-to-glauconite alteration *via* the formation of Gl-S.

In the present study, the mineralogical, geochemical, and structural changes that occurred during deep-water glauconitization at the ODP Site 959 were documented in detail and burial-related changes in the development of glauconite are highlighted which have not been described to date in a deep-sea environment. Based on the depth-related changes in the maturity of the green clay minerals and interstitial solution chemistry, the rate and mechanism of glauconite formation are assessed and a reaction model is presented.

GEOLOGICAL SETTING

The Ivory Coast–Ghana continental margin is located in the eastern equatorial Atlantic Ocean (western Africa) and consists of two major segments. The northern segment is known as the Deep Ivorian Basin (synonymous with the Ivory Basin), an extensional margin that includes the eastern Ivorian continental slope and the southwestern Ghanaian upper slope (Figure 1). The southern segment bounds the Ivory Basin toward the south in a NE–SW direction and is referred to as the Ivory Coast–Ghana Marginal Ridge: a feature 130 km long and 25 km wide (Mascle *et al.*, 1996). Owing to its moderate distance from the surrounding coastlines (~120 km), only a minor proportion of the terrigenous sediment input (suspension load) has reached Site 959C (Giresse and Wiewióra, 2001).

Sediment cores from the Ivory Coast–Ghana Marginal Ridge were recovered during the Ocean Drilling Program (ODP) Leg 159, Site 959, in ~2100 m water depth and at 3–6ºC seawater temperature. The sediments are of particular interest because of their slow (~1–2 cm/ky) and continuous sedimentation rate from at least the Miocene to the Holocene (Wagner, 1998). Due to the elevated position of this site (Latitude: 3º37.669‘N, Longitude: 2º44.116‘W), large hiatuses caused by deep-sea bottom currents or gravity-flow activity are almost absent (Figure 1).

The upper 25 m of ODP Site 959, Hole C, consists of thin dark gray to greenish sedimentary layers of

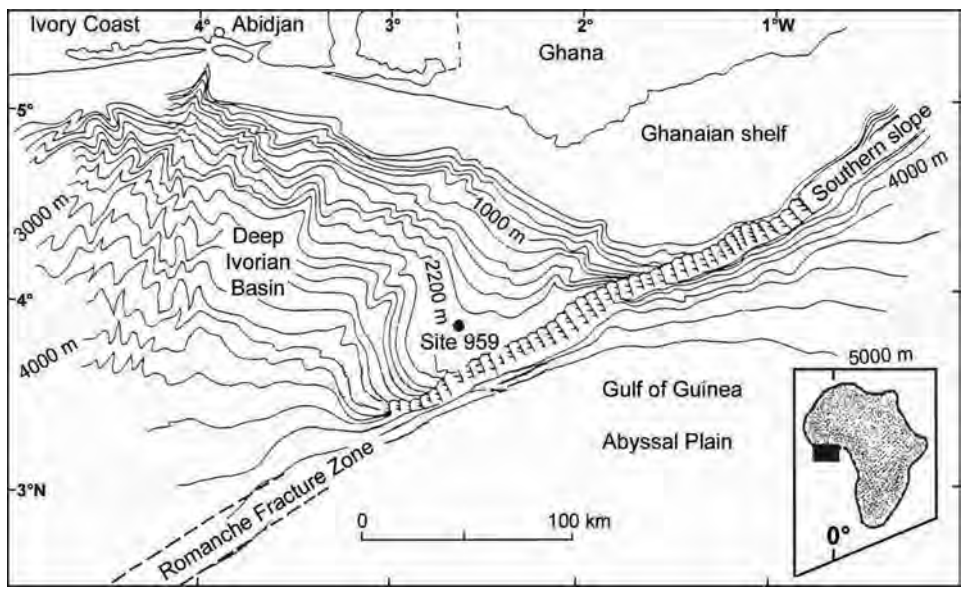

Figure 1. Location map of the ODP Site 959 situated on a small plateau on the Ivory Coast–Ghana Marginal Ridge (western equatorial Africa) (modified after Wiewióra *et al.*, 2001).

interbedded foraminifera and nanofossil oozes mixed with detrital quartz, feldspar, and clay minerals as well as radiolarians (bio-opal) forming darker horizons (Giresse *et al.*, 1998, Wagner, 1998, Wiewióra *et al.*, 2001). The brighter intervals rich in foraminifera tests frequently contain authigenic green clay and also pyrite infillings. Generally, the beds show a lack of sedimentary structures except for two scour contacts and small bioturbation features.

Stratigraphic classification of Hole 959C was derived from stable oxygen isotope records established on the basis of the epibenthic foraminifer *Cibicides wuellerstorfi* (Wagner, 1998). The $\delta^{18}O$ signal provides a nearly complete record over the last 25 oxygen isotope stages corresponding to the last ~1 My, with one notable stratigraphic gap of ~80 ky near 1.5 meters below the sea floor (mbsf). A longer hiatus of ~530 ky occurs at 11.9 mbsf which is slightly below oxygen isotope stage 25 (Wagner, 1998).

Sediments from the Hole 959C are, thus, suitable for high-resolution study of the recent, green-clay authigenesis and for establishing the roles of deep-water chemistry, provenance, and composition of original sediment, and early marine carbonate diagenesis (*e.g.* Giresse *et al.*, 1998; Norris, 1998; Wagner, 1998).

MATERIALS AND METHODS

Sampling and preparation

Bulk-sediment samples (21 in total), ~30 cm^3 in size, were taken from the upper 25 m of Hole 959C, the core of which is stored at the Bremen Core Repository (MARUM), Germany. This sampled section comprises a sedimentary sequence ranging from Early Holocene (0.16 mbsf, ~0.01 My) to Late Pliocene age (24.91 mbsf, ~2.5 My). Four sub-samples from 1.32, 10.23, 11.49, and 24.91 mbsf were impregnated with epoxy resin to study the microstructure of the green clay infillings in the foraminifera tests by optical microscopy of thin sections. For further mineralogical and chemical analyses of the bulk sediment and green-grain fraction, air-dried sediments were treated with 10% acetic acid for 1 h to dissolve carbonates. The proportion of the green-grain fraction was calculated by weighing the carbonate-free >32 μm size fraction which also contained <5 wt.% quartz, radiolarians, and pyrite. In order to investigate the glauconitization process, ~50 mg of green grains were separated by hand picking under a binocular microscope from the pale to light green, the medium green, and the dark green-grain sub-fractions of samples taken at 0.16, 11.69, and 24.91 mbsf.

X-ray diffraction

X-ray diffraction (XRD) analyses were carried out for mineral identification and quantification using a Bruker D8 Advance instrument (Karlsruhe, Germany) equipped with a Cu-target tube (40 kV, 30 mA), Ni-filter, 0.5º divergence slit, and a scintillation detector. Finely ground bulk samples were prepared (side-loaded) for random powder analyses and run over the range 4–65º2θ using a step size of 0.02º2θ/s with a count time of 1 s/step. Rietveld-based phase quantification was carried out using the PANalytical X'Pert *HighScore Plus* software (developed by PANalytical B.V.). The accuracy of these results was verified by comparison with mass-balance calculations based on X-ray fluorescence (XRF) data of the bulk sediment. Idealized compositions for orthoclase, albite, clinochlore (chlorite), Na-montmorillonite (smectite), and muscovite were assumed for the calculations (Baldermann, 2012). The deviation of the XRD and XRF calculations, expressed as error bars, were <5 wt.% for kaolinite, calcite, and quartz, and <3 wt.% for feldspar, smectite, chlorite, and illite/muscovite. The percentage of glauconite layers (%Gl) in Gl-S was determined on the separated green-grain sub-fractions using oriented preparations. Oriented mounts were made by dispersion of 40 mg of green clay matter in 5 mL of ethanol and ultrasonic treatment for 10 min and then pipetting the clay-in-suspension onto 2 cm × 2 cm glass slides which were subsequently left to air dry overnight. Preparations were run over the range 3–30º2θ using a step size of 0.02º2θ/s and a count time of 0.5 s/step. The %Gl was calculated based on XRD patterns of ethylene glycol (EG)-solvated preparations, according to the equation $\%Gl = 60.8 \cdot d_{EG}002 - 504.5$ which was obtained from *NEWMOD*-calculated %illite in illite-smectite *vs.* $d_{EG}002$ peak position relations reported by Moore and Reynolds (1997). The peak reproducibility of the $d_{EG}002$-reflection was 0.01 Å, equivalent to an analytical precision of ±2%Gl in Gl-S. Results were compared with *Sybilla*© (developed by Chevron-Texaco) calculations to verify the accuracy of the %Gl estimations. For *Sybilla*© modeling, an illite-smectite structure with a large Fe content of 1.2 atoms per formula unit (a.p.f.u.) was assumed, based on $O_{10}(OH)_2$, in the octahedral sites.

Scanning and transmission electron microscopy

In order to study mineral alterations and dissolution features related to early marine diagenesis, ~40 hand-picked, C-coated grains from 0.16 (the least altered state) and 24.91 mbsf (the most altered state) were analyzed by scanning electron microscopy (SEM) using a Jeol JXA-840A. For material disaggregation, the bulk sample was first treated with hydrochloric acid (for 1 h) to remove carbonates.

Transmission electron microscopy (TEM) was undertaken to determine the composition, form, and structure of clay-mineral particles in the separated green-grain sub-fractions from 0.16, 11.69, and 24.91 mbsf using a Jeol JEM 1210 instrument equipped with an Oxford Instruments Pentafel Link-Model 6635 detector. The sample preparation was the same as described by Baldermann *et al.* (2012). Imaging, energy-dispersive

X-ray spectroscopy (EDX), and selected area electron diffraction (SAED) analyses were performed on single clay-mineral particles using a 200 kV accelerating voltage and 10 s count time to reduce K^+ migration. The analytical error of elemental analysis depends mainly on particle thickness and size. The standard deviations were <30% for Na, K, and Ca, <10−15% for Al and Mg, and <5% for Si and Fe, equivalent to an analytical error of <2 wt.% for most of the major elements. Structural formulae were calculated on the basis of 22 negative charges, according to Bailey *et al.* (1980), assuming (1) the iron present is ferric Fe, (2) the tetrahedral Si^{4+} + Al^{3+} is equal to 4, (3) Fe^{3+}, Mg^{2+}, and Al^{3+}_{rest} occupying the octahedral sheet, and (4) K^+, Na^+, and Ca^{2+} are located within the interlayer sites.

Focused-ion beam and scanning electron microscope (FIB-SEM) study

The microfabrics of light and dark green clay infillings of the benthic foraminifer *Fursenkoina mexicana* were studied using a Zeiss Auriga CrossBeam FIB-SEM (Oberkochen, Germany). A Pt-coated surface area of ~20 μm × 30 μm was tilted normal to the ion beam. Ion milling was applied to create a cross-sectional surface of ~15 μm × 15 μm that was imaged by the electron beam with a 5 kV accelerating voltage. 3-D information was obtained using a serial sectioning procedure with alternating milling and imaging to acquire a 2-D image sequence across the selected volume (Warr and Grathoff, 2012). The acquired number of secondary electron images ranged between 100 and 300 with a 25 nm slice thickness. 3-D visualization was obtained from the sequence of SEM images using *ImageJ*© (developed by W. Rasband, National Institutes of Health) based on the gray-level contrasts. The distribution of clay matter, pore space, and skeletal calcite was reconstructed using a threshold method slightly modified from that described by Keller *et al.* (2011).

RESULTS

In this section, the results of petrographic, mineralogical, geochemical, and structural studies of the bulk sediment and the green grains are compared in order to investigate the glauconitization process in the recent deep-sea environment of the ODP Site 959C.

Petrographic observations

The uppermost 25 m of sediment consists of slightly bioturbated, olive brown to olive-grayish green horizons of interbedded foraminifera and nanofossil oozes. The laminae which are rich in foraminifera tests are ~1 mm to 1 cm thick and show two scour contacts at ~3.8 and 10.4 mbsf. Giresse *et al.* (1998) interpreted these as resulting from winnowing action or longer breaks in sedimentation. Darker intervals are rich in organic matter (0.7−1.6 wt.%) with a C/N ratio of 8−48 (14 on average), as reported by Baldermann (2012), which indicates the predominance of marine organic matter (Wagner, 1998). These thinner layers also contain large proportions of coccoliths which are mixed with a brownish clay matrix. Sparse occurrences of large detrital quartz and feldspar grains as well as plant debris were recognized over the whole sedimentary sequence whereas the proportions of pyrite and green clay infillings related to glauconitization increase slightly with increasing depth (Baldermann, 2012). No signs of gravity-flow or turbidity deposits are evident, indicating that the green grains were formed *in situ* rather than transported by reworking and re-deposition from the surrounding Ghanaian shelf and slope.

Examples of microfacies and microstructures from 1.32, 10.23, 11.49, and 24.91 mbsf (see Figure 2) reveal that the sediment from 1.32 mbsf consists of nanofossil ooze which is rich in the tests of globigerine and orbuline foraminifera that show a few incomplete, pale to light green clay infillings in addition to some radiolarians (Figure 2a). No pyrite was found, suggesting that the uppermost sediments are the least altered in terms of diagenetic overprinting. At 10.23 mbsf, foraminifera tests mixed with partly dissolved radiolarians dominate in the sediment and some of these tests show immature, light to medium green clay infillings (Figure 2b). Many medium green internal moulds and subordinate pyrite infillings were found within the foraminifera tests at 11.49 mbsf (Figure 2c). Radiolarians are largely absent at ⩾11.49 mbsf, and skeletal calcite (foraminifera tests) has been partly dissolved. Abundant more-mature, medium to dark green grains with a fractured and broken morphology, and many pyrite infillings, were found at 24.91 mbsf (Figure 2d). The section ⩾24.91 mbsf is, thus, considered to reflect the most altered sediment with respect to early diagenesis. An increased state of glauconitization is recognizable in the more deeply buried sediments, together with precipitation of pyrite and dissolution of both carbonate and bio-opal.

Bulk mineralogy of Hole 959C

Quantitative XRD analyses of 21 bulk samples from Hole 959C (see Figure 3) revealed a relatively constant background of siliciclastic input during the last 2.5 My, consisting of poorly crystalline kaolinite (21−34 wt.%), quartz (11−19 wt.%), and feldspar (3−8 wt.% of K-feldspar and albite), and minor proportions of detrital smectite (2−5 wt.%), illite/muscovite (1−5 wt.%), chlorite (1−3 wt.%), and anatase (0.3−0.6 wt.%). In addition to the detrital input, authigenic calcite (27−51 wt.%), Gl-S (1−6 wt.% with an average of 2−3 wt.%), and pyrite (<3 wt.%) were formed. Traces (<1 wt.%) of aragonite, bio-opal, and Fe-(oxyhydr)-oxides as well as secondary halite, gypsum, and hexahydrite were also identified by SEM, most of

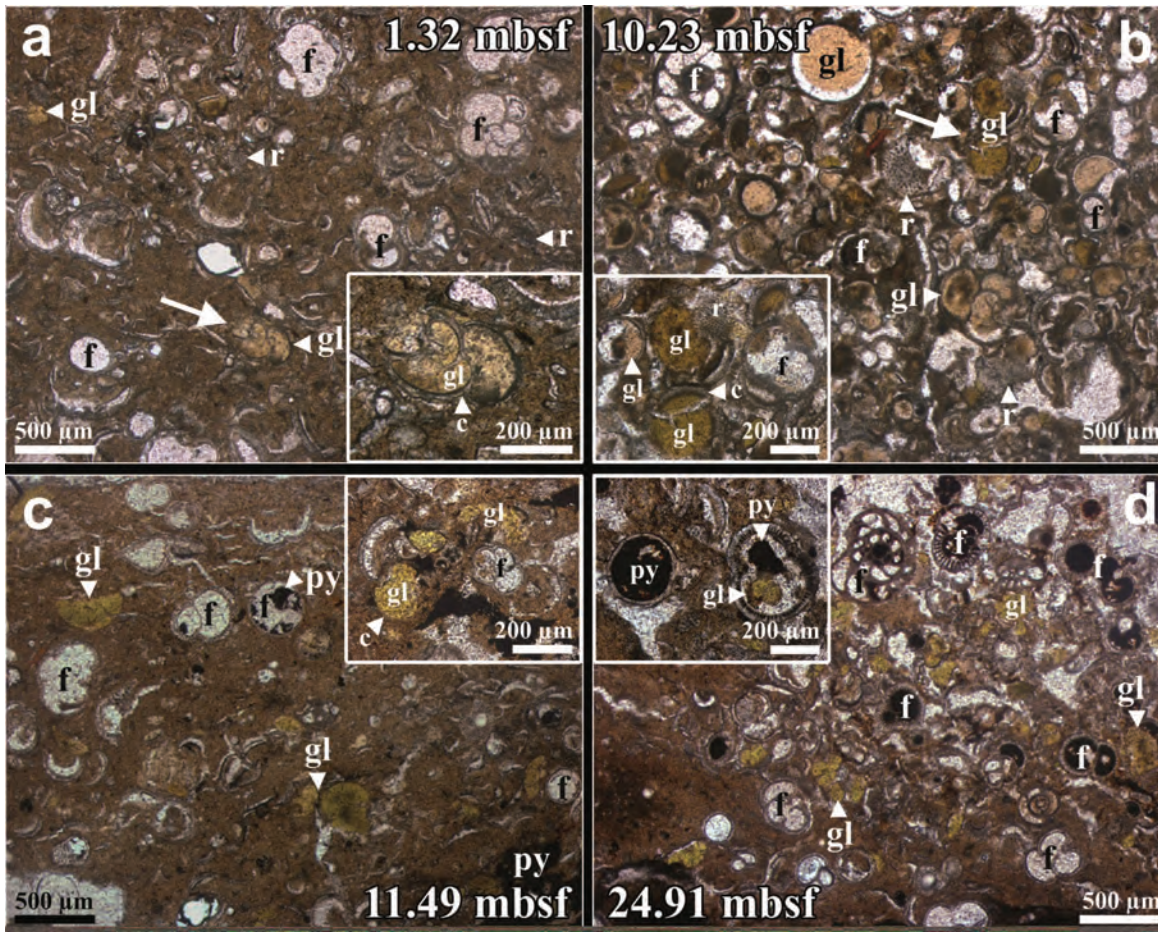

Figure 2. Photomicrographs showing the development of microfacies and microstructure within the upper 25 m of Hole 959C. (a) Clayey nanofossil ooze enriched in foraminifera (f) and radiolarians (r) from 1.32 mbsf. Incomplete, light green clay infillings (gl) are scarce. (b) Immature, light to medium green clay infillings in foraminifera ooze mixed with partly dissolved radiolarians from 10.23 mbsf. (c) Nanofossil ooze containing interbedded laminae of foraminifera tests rich in medium green clay and subordinate pyrite infillings (py). Radiolarians are largely absent at 11.49 mbsf and skeletal calcite (c) is partly dissolved. (d) Foraminifera-rich nanofossil ooze with large proportions of more mature dark green grains showing a modified (broken or cracked) morphology accompanying plentiful pyrite infillings from 24.91 mbsf.

which probably formed as alteration products during storage at the Bremen Core Repository. No general variation with depth in the basic mineral assemblage was detected except an increase in the amount of pyrite (and Gl-S) and a decrease in the proportion of feldspar with increasing depth which can be attributed to diagenetic alterations (Figure 3).

Observations by SEM of carbonate-free sediment from 0.16 mbsf showed it to have slightly rounded quartz grains, in addition to detrital K-feldspar, albite, chlorite, and illite/muscovite particles that show clear cleavage directions and distinct crystal edges with no signs of diagenetic modification (Figure 4). Modified habits, abundant dissolution pits, and decomposition features are evident at 24.91 mbsf, indicating silicate alterations related to progressing marine diagenesis. Fe-(oxyhydr)oxides and unstable bio-opal (fragments of radiolarians, diatoms, and sponge needles) have been almost completely dissolved or have been partly glauconitized at 24.91 mbsf, whereas detrital smectite and kaolinite remained unaltered (Figure 4). Neo-crystallized pyrite with both framboidal and euhedral (octahedral) morphology is most abundant at 24.91 mbsf, together with authigenic Gl-S.

Mineralogy of the green-grain sub-fractions

The material inside the foraminifera shells, namely the green clay infillings, was studied by XRD after removal of the skeletal carbonate and surrounding mud matrix. In order to investigate the state of glauconitization in the more deeply buried sediments, clay matter from the pale to light green, medium green, and dark green-grain sub-fractions from 0.16, 11.69, and 24.91 mbsf was analyzed using oriented clay preparations (Figure 5). Air-dried clay from the light green grains from 0.16 mbsf displayed a d_{001} reflection at

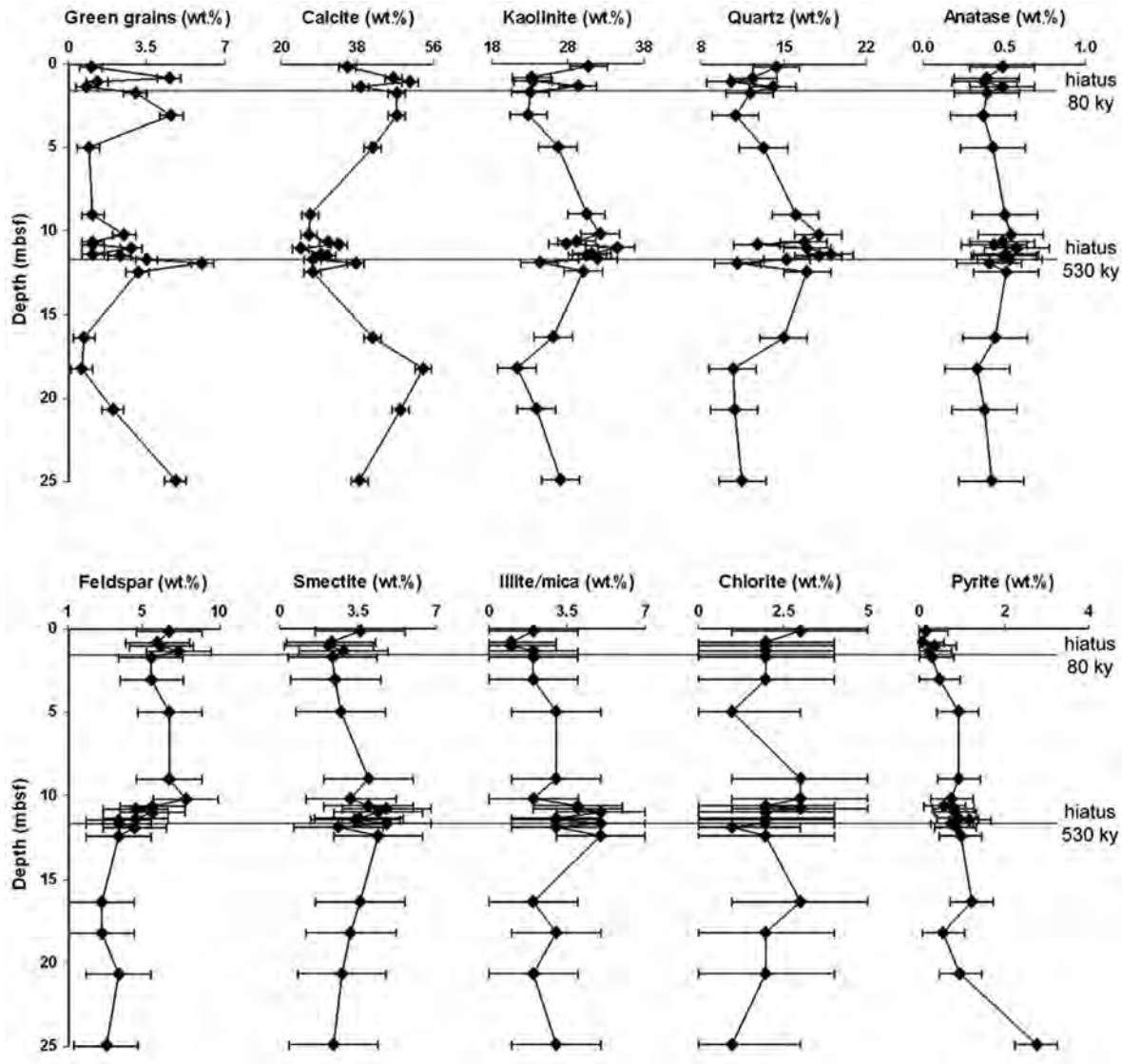

Figure 3. Bulk mineralogy of the upper 25 m of Hole 959C based on XRD. The proportion of the green-grain fractions was determined by weighing.

13.3 Å which shifted to 16.5 Å after EG-solvation with the weak d_{002} reflection at 8.8 Å, typical for immature Fe-smectite-rich Gl-S. In contrast, air-dried clay matter from the buried, dark green grains from 24.91 mbsf showed a d_{001} value at 11.4 Å which increased to 14.8 Å after EG solvation. The d_{002} value was 9.7 Å, indicative of a more mature glauconite-rich Gl-S. After heating to 550ºC for 1 h the basal spacing decreased to 10.0 Å.

Quantitative changes in both the composition of Gl-S and the percentage of each green-grain sub-fraction suggest a sequence of increased glauconitization with increasing burial depth (Figure 5). Using the linear relationship between the %Gl in Gl-S and related shifts in their basal spacings (adapted from Moore and Reynolds, 1997), the d_{002} reflections from EG-solvated clay matter were used to determine the %Gl in each green-grain sub-fraction (Figure 5). *Sybilla*© modeling (Figure 5) of the XRD patterns reveals that the most immature Gl-S from 0.16 mbsf contains ~32% Gl and ~68% Fe-smectite layers (R0 ordered), whereas the most mature Gl-S from 24.91 mbsf contains ~84% Gl and ~16% Fe-smectite layers (R3 ordered). These values are consistent with the %Gl values obtained by using the Moore and Reynolds method. The %Gl increased, together with greening of the grain color, from 32–51% (light green) and 39–74% (medium green) to 61–84% (dark green). The mass fraction (determined by weighing) of the light green grains in the total green-grain fraction decreases with increasing depth, from 70 wt.% at 0.16 mbsf to 20 wt.% at 11.69 mbsf and to 5 wt.% at 24.91 mbsf. Correspondingly, the mass fractions of medium (30 wt.%, 50 wt.%, and 55 wt.%)

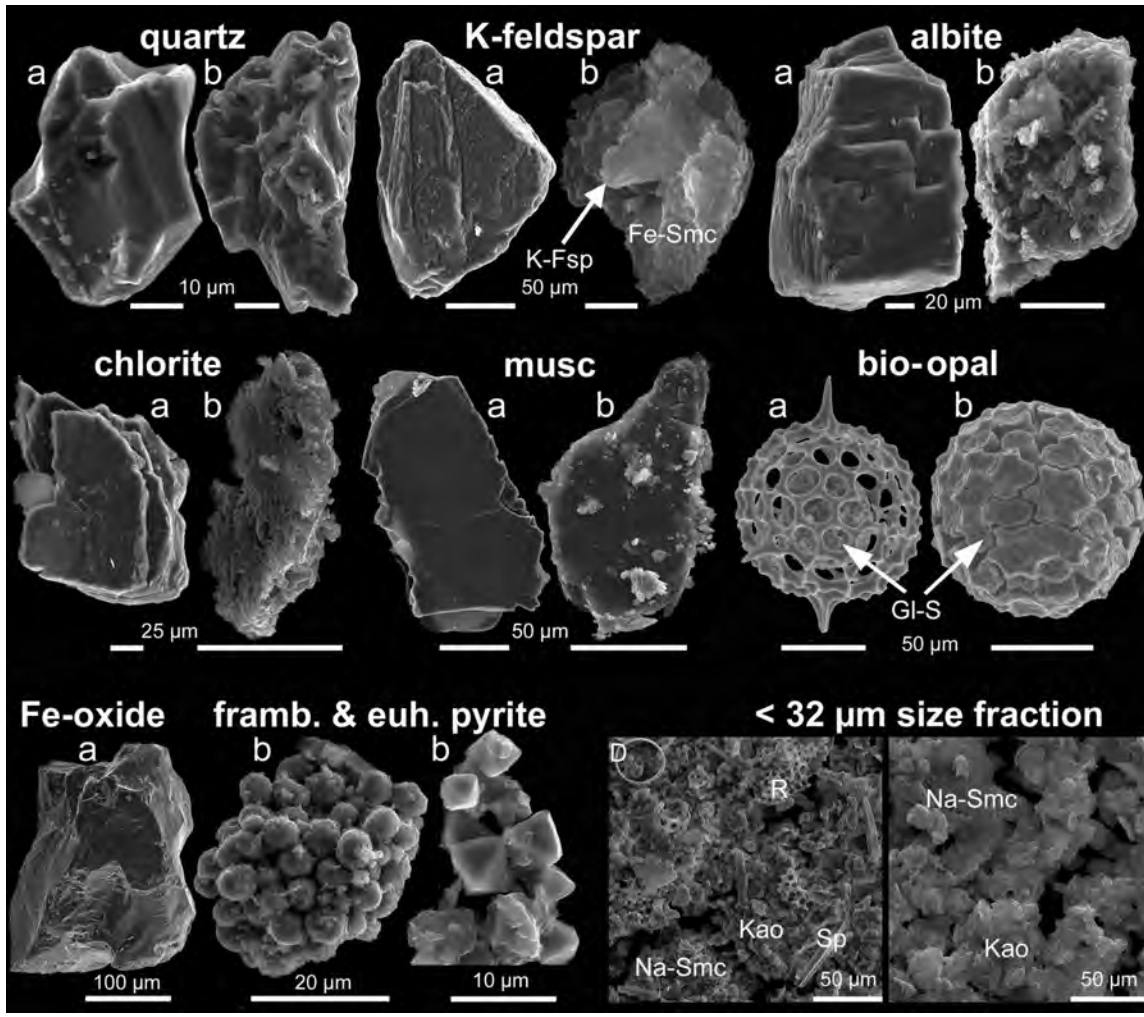

Figure 4. SEM images of less altered selected grains from 0.16 mbsf (a) compared with the more altered grains from 24.91 mbsf (b). Quartz, K-feldspar, albite, chlorite, muscovite (musc), bio-opal (Sp = sponge needles, D = diatoms, R = radiolarians), and Fe-(oxyhydr)oxide show abundant alteration and dissolution features, while detrital Na-smectite (Na-Smc) and kaolinite (Kao) remain unaltered. Glauconite-smectite (Gl-S) and framboidal and euhedral pyrite (framb. and euh. pyrite) were formed *in situ* during early marine diagenesis.

and dark green grains (<5 wt.%, 30 wt.%, and 40 wt.%) increased at the three depths (Figure 5). In each grain color class the %Gl increased with increasing depth, from 32−39% at 0.16 mbsf and 36−61% at 11.69 mbsf to 51−84% at 24.91 mbsf, attributed to ongoing glauconitization related to progressive diagenesis. All %Gl values were notably greater than the value reported by Wiewióra *et al.* (2001) who estimated only ~20% Gl layers for the green-grain assemblages without separation of the light, medium, and dark sub-fractions.

Composition, form, and structure of clay minerals in the green-grain sub-fractions

The composition, form, and structure of clay-mineral particles from the separated light, medium, and dark green-grain sub-fractions from 0.16, 11.69, and 24.91 mbsf of Hole 959C were studied by TEM-EDX and TEM-SAED in order to identify differences attributed to variations in these properties related to burial depth and color of the green clays (Figure 6, Table 1). In total, 332 TEM-EDX analyses were carried out on single clay-mineral particles and structural formulae were calculated, based on average compositions. Nine TEM-EDX analyses were also carried out on biofilm (see below).

Particles of the light green sub-fractions generally have a veil-like or film morphology according to the nomenclature of Buatier *et al.* (1989). These particles consist mainly of Fe-smectites and smectite-rich Gl-S that predominantly display weak diffraction rings reflecting their turbostratic nature (Figure 6a,d,g). Bacteria are frequently present within the light green sub-fractions but they are less abundant in the darker, more mature grains. In close proximity to bacteria,

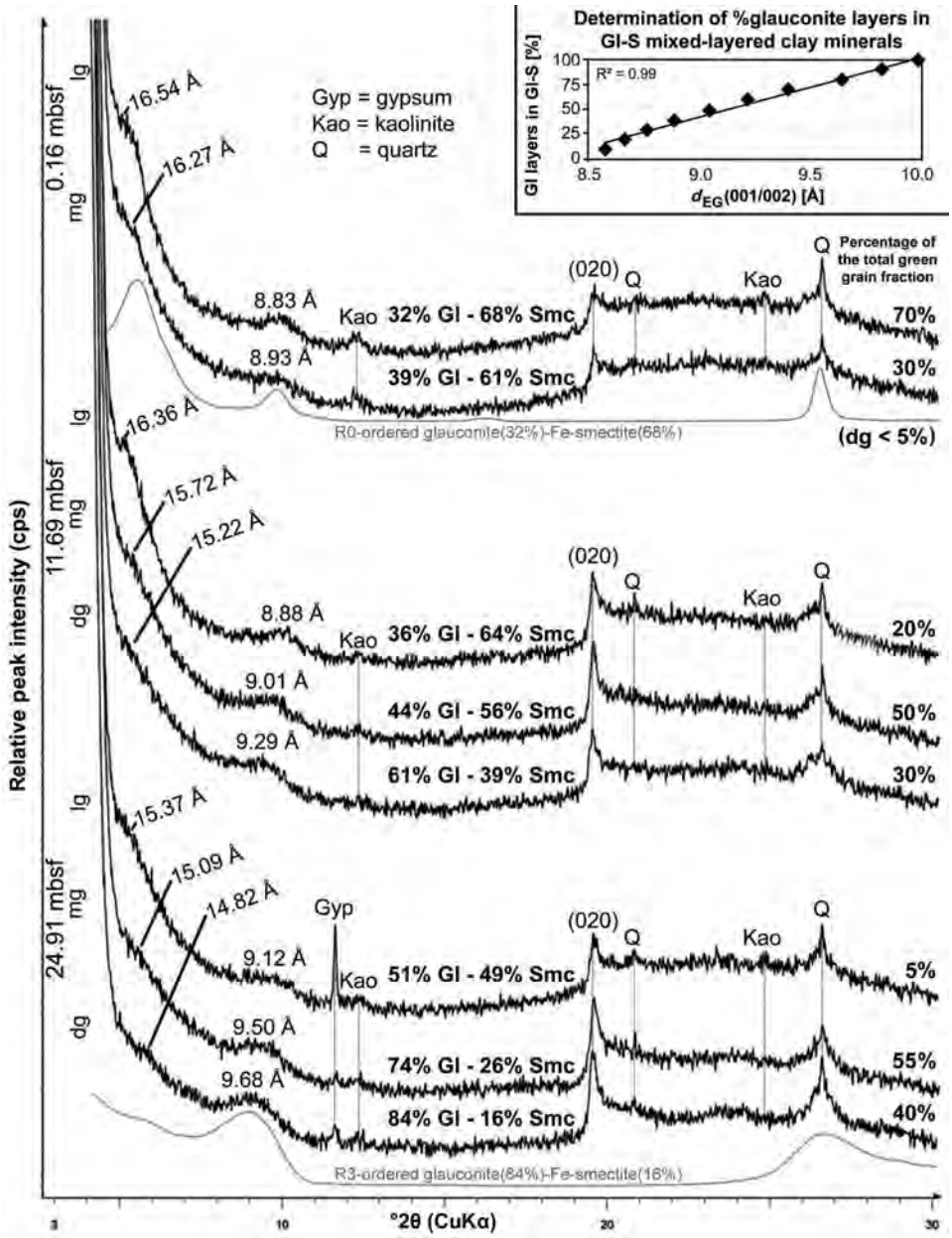

Figure 5. XRD patterns of oriented, glycolated preparations of the separated light (lg), medium (mg), and dark green (dg) grains, collected from 0.16, 11.69, and 24.91 mbsf of Hole 959C. The %Gl in Gl-S was calculated using the linear equation %Gl = 60.8 · $d_{EG}002 - 504.5$ derived from *NEWMOD*-calculated %illite in illite-smectite *vs.* $d_{EG}002$ peak-position relations reported by Moore and Reynolds (1997). The accuracy of the %Gl estimations was verified by comparison with *Sybilla* calculations (gray curves). On the right, the percentage of each green-grain sub-fraction is given in wt.% of the total green-grain fraction (determined by weighing).

biofilm is often mixed with thin Fe-smectite particles, suggestive of bacteria–clay mineral interactions. Intermediate Gl-S particles with both flaky and lath-like morphology occur rarely at 0.16 mbsf but their abundance increases with increasing depth along with greening of the grain color (Figure 6b,e,g,h). Accordingly, minor proportions of Fe-smectite-rich Gl-S with either smeared Bragg spots or unsharp diffraction rings still occur at 11.69 and 24.91 mbsf but lath-like, glauconite-rich Gl-S with discrete Bragg spots predominate. Within the dark green sub-fractions, intermediate and lath-like glauconite particles as well as flake-shaped, glauconite-rich Gl-S are more frequent. The elongated form of these particle types (Figure 6c,f,h, and in the lower right of panel i) is evident from the high aspect ratio of 4:1 to 5:1. Such more evolved, lath-like particles commonly display discrete Bragg spots, documenting a more ordered mineral structure (*e.g.*

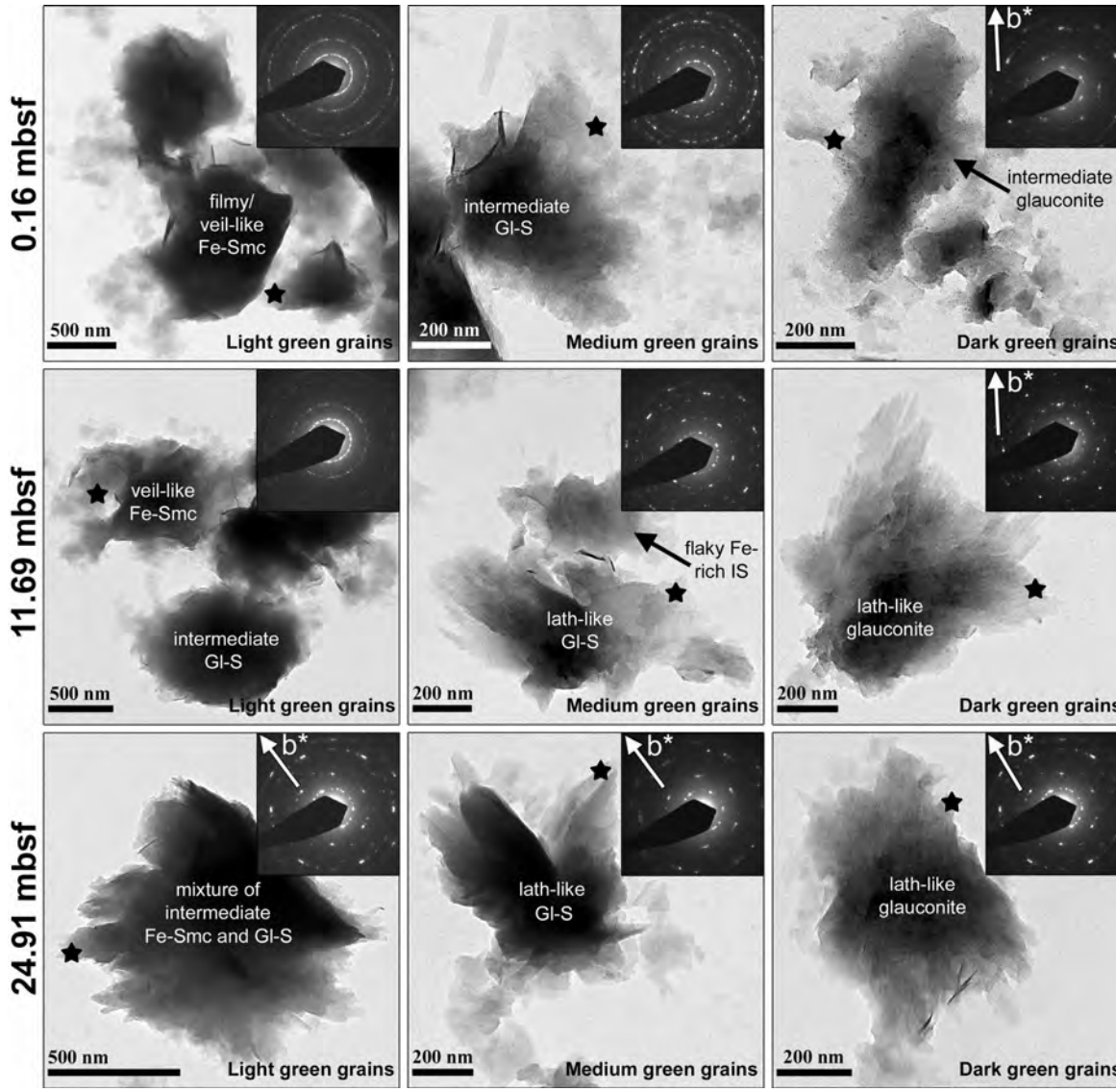

Figure 6. TEM images and TEM-SAED patterns of representative clay mineral particles from the light, medium, and dark green-grain sub-fractions from 0.16 (a–c), 11.69 (d–f), and 24.91 mbsf (g–i) showing the development of particle form and composition at Hole 959C. Initial filmy or veil-like Fe-smectite (Fe-Smc) (a,d) with weak diffraction rings changes into intermediate, flaky, or lath-like Gl-S (b,e,g,h) with weak or smeared Bragg spots and finally into lath-like glauconite (c,f,i). The two diagnostic, non-basal Bragg reflections (b* marks the direction of the *b* axis) indicate a transition from the poorly ordered 1*M*d-polytype to the ordered 1*M*-polytype.

Baldermann *et al.*, 2012) compared to that of Fe-smectite.

According to the chemical composition (based on TEM-EDX analysis), the clay-mineral particles mainly consist of Si, Fe, Al, Mg, K, Ca, and O with small traces of P, S, Ti, and Mn (Table 1). With increasing maturity of the grains, the following changes in elemental chemistry were recognized. Average compositions of the light green clay-mineral particles were rather poor in K_2O (1.8–2.9 wt.%), MgO (3.8–4.4 wt.%), and Fe_2O_3 (24.7–25.2 wt.%), whereas SiO_2 (60.0–61.1 wt.%), Al_2O_3 (7.1–7.6 wt.%), and CaO (0.4–0.8 wt.%) proportions were high. The medium green clay-mineral particles have moderate amounts of K_2O (2.6–4.3 wt.%), MgO (3.7–4.4 wt.%), CaO (0.4–0.8 wt.%), and Fe_2O_3 (25.0–26.0 wt.%), but less SiO_2 (58.8–61.1 wt.%) and Al_2O_3 (6.5–7.1 wt.%). Finally, the dark green clay-mineral particles have the largest amount of K_2O (4.3–5.4 wt.%) and Fe_2O_3 (24.0–27.3 wt.%), moderate MgO (4.2 wt.%) and CaO (0.4–0.8 wt.%), but the smallest amount of SiO_2 (58.2–59.1 wt.%) and Al_2O_3 (5.2–7.3 wt.%). Based on

Table 1. Averaged compositions, excluding water of Gl-S, based on 332 TEM-EDX analyses, with calculated structural formulae of the separated light, medium, and dark green-grain sub-fractions from samples taken at 0.16, 11.69, and 24.91 mbsf.

Depth	—— 0.16 mbsf ——			—— 11.69 mbsf ——			—— 24.91 mbsf ——		
Green-grain sub-fraction	light	medium	dark	light	medium	dark	light	medium	dark
Particles analyzed (*n*)	32	36	30	36	34	38	39	43	44
Averaged elemental chemistry (wt.%) based on TEM-EDX									
MgO	4.0	3.7	4.2	3.8	4.1	4.2	4.4	4.4	4.2
Al_2O_3	7.6	7.1	7.3	7.5	6.5	5.2	7.1	6.1	5.2
SiO_2	61.1	61.1	59.1	61.2	59.8	58.5	60.0	58.8	58.2
K_2O	2.2	2.6	4.6	1.8	3.1	4.3	2.9	4.3	5.4
Fe_2O_3	24.7	25.0	24.0	24.8	25.7	27.3	25.2	26.0	26.7
CaO	0.4	0.5	0.8	0.8	0.8	0.4	0.5	0.4	0.4
Total	100.0	100.0	100.0	100.0	100.0	100.0	100.0	100.0	100.0
Atoms per formula unit (a.p.f.u.) based on $O_{10}(OH)_2$									
^{IV}Al	0.08	0.06	0.14	0.07	0.11	0.14	0.12	0.14	0.14
Si	3.92	3.94	3.86	3.93	3.89	3.86	3.88	3.86	3.86
TC	−0.08	−0.06	−0.14	−0.07	−0.11	−0.14	−0.12	−0.14	−0.14
^{VI}Al	0.50	0.48	0.43	0.49	0.39	0.27	0.43	0.33	0.26
Fe (III)	1.19	1.21	1.18	1.20	1.26	1.36	1.23	1.28	1.33
Mg	0.38	0.36	0.41	0.37	0.39	0.42	0.42	0.43	0.42
$\Sigma(^{VI}Al + Fe (III) + Mg)$	2.07	2.05	2.02	2.06	2.04	2.05	2.08	2.04	2.01
OC	−0.17	−0.21	−0.35	−0.19	−0.27	−0.27	−0.18	−0.31	−0.39
K	0.18	0.21	0.38	0.15	0.26	0.36	0.24	0.36	0.46
Ca	0.03	0.03	0.05	0.06	0.06	0.03	0.03	0.04	0.03
IC	0.24	0.27	0.48	0.27	0.38	0.42	0.30	0.44	0.52

TC = tetrahedral charge, OC = octahedral charge, IC = interlayer charge.

the calculated, average structural formulae (Table 1), the light green clay-mineral particles have an Fe-smectite composition of $(K_{0.18}Ca_{0.03})(Fe^{3+}_{1.19}Al_{0.50}Mg_{0.38})_{\Sigma 2.07}[Al_{0.08}Si_{3.92}O_{10}](OH)_2$ at 0.16 mbsf. Gl-S compositions of $(K_{0.26}Ca_{0.06})(Fe^{3+}_{1.26}Al_{0.39}Mg_{0.39})_{\Sigma 2.04}[Al_{0.11}Si_{3.89}O_{10}](OH)_2$ dominate in the medium green grains from 11.69 mbsf, whereas the most mature, dark green glauconite-rich Gl-S have compositions of $(K_{0.46}Ca_{0.03})(Fe^{3+}_{1.33}Al_{0.26}Mg_{0.42})_{\Sigma 2.01}[Al_{0.14}Si_{3.86}O_{10}](OH)_2$ at 24.91 mbsf. Due to the high Fe-smectite content, especially in the less evolved Gl-S, some of the Mg^{2+} may be located in the interlayer sites of the Fe-smectite which could increase the interlayer charge of Gl-S by a progressively higher octahedral charge deficiency. The greener color of the more mature grains may also reflect the existence of some structural Fe^{2+} which could affect the structural formulae by decreasing the tetrahedral Si content. However, the Fe^{2+}/Fe^{3+} ratio in glauconite is commonly rather low, typically ranging from 0.05 to 0.5 at most (~0.15 is the average, inferred from the data reported by Meunier and El Albani, 2007), and the calculated structural formulae are balanced assuming the Fe is ferric (Table 1). The overall compositional changes mentioned above, thus, support a sequence of increased glauconitization with increasing burial depth, whereby initial Fe-smectites changed continuously into glauconite *via* the formation of Gl-S, as also indicated by the XRD data (Figure 5).

3-D microstructure of light vs. dark green clay infillings

Differences of microstructure, microporosity, and mineralogy between the light and dark green clays were studied by comparison of 3-D reconstructions of infillings in the benthic foraminifer *Fursenkoina mexicana* (Figure 7). At 0.16 mbsf, most of these shells are filled with light green clay matter but at 24.91 mbsf most are filled with dark green clay matter. One shell filled with light green clay matter and one filled with dark green clay matter were selected for the study. The following observations were made on the two varieties:

(1) The light green clay matter from 0.16 mbsf (Figure 7a–c) consisted mainly of sets of Fe-smectite-rich Gl-S ~0.5–1.0 μm across and subordinate Fe-smectite particles. These poorly evolved clay minerals (nomenclature of Odin and Matter, 1981) typically form boxwork-like networks (Figure 7b) with a significant, well connected porosity of ~15–20% (Figure 7c). Fragments of partly dissolved calcite (Figure 7a) which are probably remnants of the foraminifera walls are well preserved between the clayey frameworks.

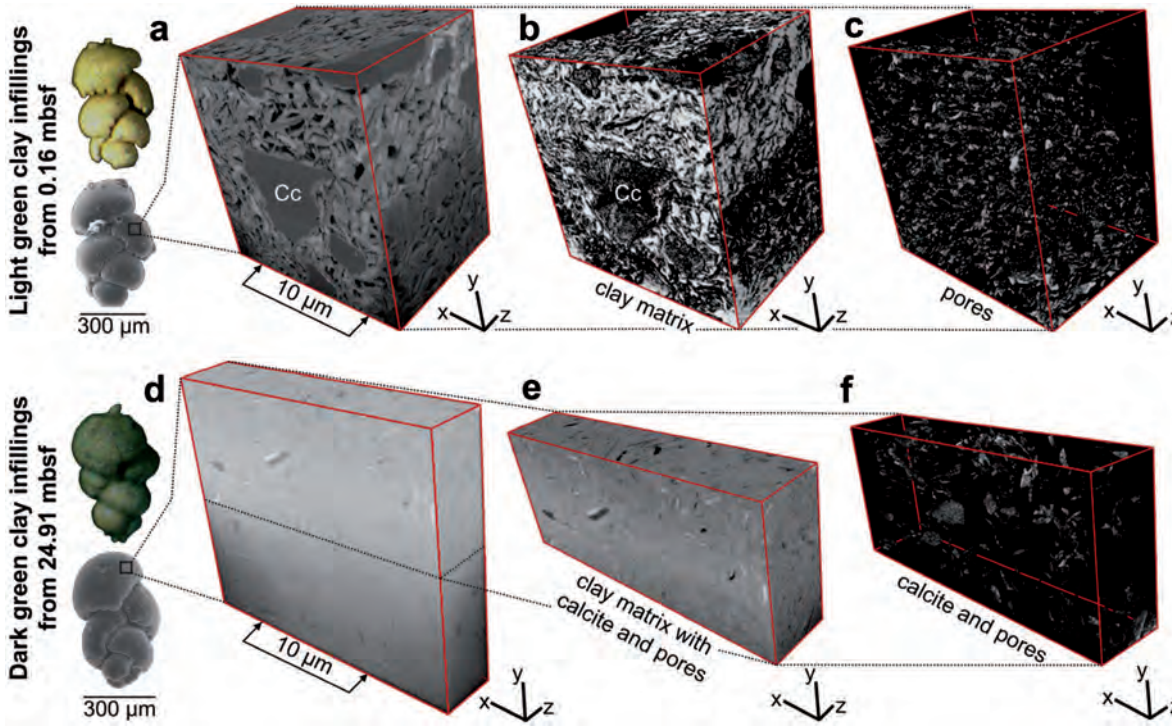

Figure 7. 3-D reconstructions of green clay infillings of the benthic foraminifera, *Fursenkoina mexicana*, based on FIB-SEM images. Optical photomicrographs and SE images of the specimens, filled with either light green clay at 0.16 mbsf (a) or dark green clay at 24.91 mbsf (d), show the locations of the investigated areas. The light green clay matter (a–c) is composed mainly of 0.5–1 µm long Fe-smectite-rich Gl-S (white areas in part b) which forms boxwork-like networks with a high porosity (white areas in part c). Skeletal calcite (dark gray areas in part a marked with Cc) is largely preserved. The dark green clay matter (d–e) is composed of sets of 0.5–2 µm long glauconite-rich Gl-S (gray areas in part e) and forms rosette-like structures with a greater packing density. Pore space and skeletal calcite (white areas in part f) are largely reduced at this state of glauconitization.

(2) The dark green clay matter from 24.91 mbsf (Figure 7d–f) consisted mainly of glauconite-rich Gl-S and showed more complex microstructures than those of the light green clays. Sets of these clay-mineral particles are ~0.5–2.0 µm in size and typically form flame- or rosette-like structures with a high packing density (Figure 7d,e), characteristics associated with the evolved state of glauconitization (Odin and Matter, 1981). At this state, the porosity (5–10%) is reduced and the skeletal calcite has largely been dissolved (Figure 7f). Such (micro)-textures indicate changes in the physicochemical conditions in the foraminifera tests during progressive glauconitization.

DISCUSSION

Previous studies demonstrated that in the deep-water environment of the Ivory Coast–Ghana Marginal Ridge (ODP Hole 959C), authigenic green clay minerals initially formed at the water–sediment interface during phases of enhanced ion exchange with the seawater (Giresse and Wiewióra, 2001; Wiewióra *et al.*, 2001). The reaction mechanism proposed was that of Fe-smectite-to-glauconite alteration by the formation of Gl-S, a feature confirmed in the present study. However, detailed XRD and electron microscope analyses of representative green grains from different depths revealed a number of new features which were not characterized by previous authors: (1) the association of biofilm, gels, and co-precipitated Fe-smectite in less altered grains; (2) the decrease in connected porosity with increasing depth; (3) a greater abundance of glauconite in Gl-S in all samples; and (4) a notable depth-dependent increase in the degree of glauconitization which was observed for all three types of green grains – light, medium, and dark – together with increasing proportions of the dark green grains with increasing burial depth. In this section, the key factors for glauconitization are discussed and a new interpretation of glauconite formation presented. The availability of Fe is suggested to be the most important rate-limiting factor for the glauconitization process in this low-temperature, deep-water setting.

The initial step to glauconitization – formation of Fe-smectite

Comparison of petrographic (Figure 2), mineralogical (Figure 5), and chemical (Table 1) data across the entire range of green clay minerals from the immature light green grains from 0.16 mbsf to the most mature dark

green grains from 24.91 mbsf suggests that a complete, genetically related mineral series from initial Fe-smectite to glauconite exists *via* progressively more glauconitic Gl-S. Thus, the early diagenetic formation of Fe-smectite subsequent to sediment deposition seems to be a key factor for glauconitization of foraminifera tests, as proposed by Giresse and Wiewióra (2001).

Authigenic veil-like Fe-smectite particles ~20−50 nm long are always associated with bacteria-produced biofilm (Figure 8a,b). The biofilm contains, on average, high proportions of volatiles (89.1 wt.% CO_2 and 1.9 wt.% SO_3) and SiO_2 (4.6 wt.%), CaO (1.8 wt.%), P_2O_5 (1.6 wt.%), Fe_2O_3 (0.4 wt.%), MgO (0.4 wt.%), and K_2O (0.1 wt.%) based on nine TEM-EDX analyses (Figure 8). Such a composition is indicative of bacterial biofilm of marine origin with incorporated amorphous gels, rather than that resulting from later contamination, with similarities to biofilm compositions produced in experimental studies of seawater, clay mineral, biofilm, and bacteria interactions (*e.g.* Chaerun and Tazaki, 2005; Warr *et al.*, 2009). According to Konhauser and Urrutia (1999), a Si-rich precursor gel is suggested to promote clay-mineral authigenesis. Smectite precipitation from amorphous gels was proposed previously by Harder (1980), Jiménez-Millán *et al.* (1998), Kloprogge *et al.* (1999), and Gaudin *et al.* (2005). The biofilm can provide an early micro-environment where suitable conditions for the formation of amorphous Fe^{3+}/Mg^{2+}-rich hydrogel with co-precipitated Al^{3+} develop as soon as supersaturation is reached (Konhauser and Urrutia, 1999). Rapid chemisorption of dissolved silica onto this initial precipitate (Martín-Algarra and Sánchez-Navas, 1995) can finally lead to the development of poorly crystalline Fe-smectite-like phases, as found in the surface sediments of ODP Site 959 (Figures 8b, 9). These largely unaltered Fe-smectite particles contain ~8% Gl and ~92% Fe-smectite layers and can be classified as the nascent state of glauconitization (nomenclature of Odin and Fullagar, 1988). The early micro-environment developed within the bacterial biofilm is, therefore, suitable for Fe-smectite formation which is likely to be the first step of the glauconitization process within the Ivory Coast sediments (Figure 9).

With the increased state of glauconitization found in the more deeply buried sediments, the proportion of bacteria present within the internal moulds of the calcareous (pelagic) foraminifera decreased notably, probably reflecting the intense changes in pH and Eh conditions within the micro-environment. As the microbial activity decreases, the interstitial solution of the bulk sediment and its chemistry are expected to become more important and control the ongoing glauconitization

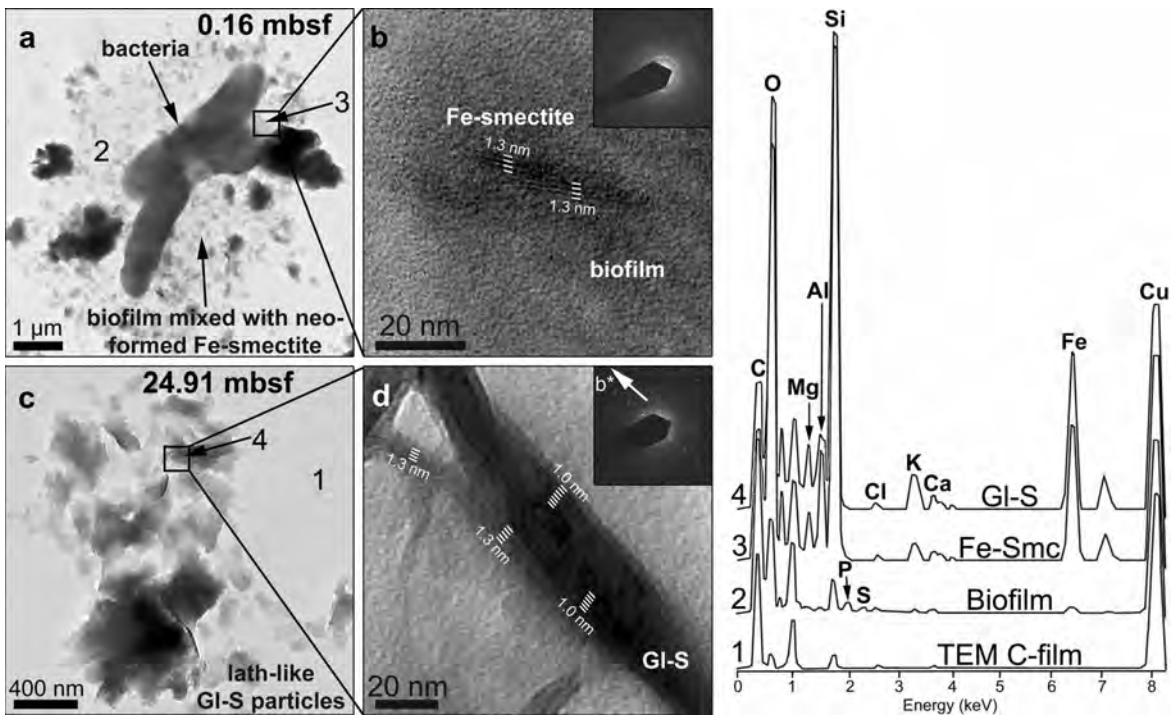

Figure 8. TEM images illustrating the evolution of the green clay minerals at ODP Site 959. (a) Interactions of authigenic Fe-smectites and bacterial biofilm from 0.16 mbsf. (b) An enlarged view of (a) which shows the association of neo-formed Fe-smectite-like phases and biofilm. (c−d) Lath-like Gl-S particles without bacteria from 24.91 mbsf indicative of an ongoing glauconitization process. On the right, TEM-EDX spectra of TEM C-film (1), biofilm mixed with neo-formed Fe-smectite (2), pure Fe-smectite (3), and Gl-S (4) are shown.

process. This interstitial solution-driven Fe-smectite-to-glauconite reaction is evident from the greater degree of glauconitization observed at 24.91 mbsf (Figure 8c,d).

The driving force for glauconitization – interstitial solution chemistry

Recent green-clay authigenesis is commonly restricted to granular siliciclastic and calcareous habitats. The original composition of the sediment and the residence time close to the sediment–seawater interface (Giresse and Wiewióra, 2001) are thought to be the key factors controlling the glauconitization reaction. Such conditions imply continuous cation supply solely from seawater during the whole glauconitization process. Effective cation exchange can only take place in the first centimeters of clayey substrates and in the first meters of granular substrates, depending on the properties of the sediment such as permeability, porosity, tortuosity, and mainly on the sedimentation rate (Meunier and El Albani, 2007). At Hole 959C, the sediment's properties (Mascle *et al.*, 1996) and sedimentation rates (Wagner, 1998) have not changed noticeably over the last 2.5 My, whereas XRD, TEM-EDX, and FIB-SEM data from the present study clearly reveal an increasing state of glauconitization with increasing depth (Figures 6, 9), thus indicating that the glauconitization reaction is not restricted to the seafloor–sediment interface and proceeds further during progressive burial. Furthermore, if the Fe-smectite precursors were precipitated solely from seawater, then an explanation is required for why the mineralogy (Figure 5) and the chemistry of the green grains differ (Table 1), despite a similar residence time close to the sediment–seawater interface at this site (~1 cm/ky) characterized by constant cation supply. These relationships may be explained by the interstitial solution chemistry being modified by microbially catalyzed oxidation of biodegradable (marine) organic matter, causing Fe redox reactions and silicate alterations (Figures 2–4) that promoted the ongoing glauconitization process within the sediment pile.

Microbial oxidation of marine organic matter was suggested by Mascle *et al.* (1996) to have had a major impact on the diagenetic reactions observed at Site 959, namely glauconitization and pyritization. Within the first few meters of sediments, the SO_4^{2-} concentration of the interstitial solution drops below the level of the seawater, owing to microbial sulfate reduction. Thus, dissolved oxygen has been consumed quantitatively (Schulz and Zabel, 2006), followed by Mn^{4+} and Fe^{3+} reduction (Figure 10), *e.g.* from (oxyhydr)oxides. Accompanying ongoing SO_4^{2-} reduction with increasing depth, H_2S accumulated successively in the interstitial solution, providing the anions for framboidal and euhedral pyrite formation (Figures 3, 4). Fe-sulfide precipitation is, thus, a limiting factor for glauconitization because it competes with the primary formation of Fe-smectites by removal of ferrous Fe. As a consequence, the Fe interstitial solution profile displays large variation in Fe content without any systematic depth

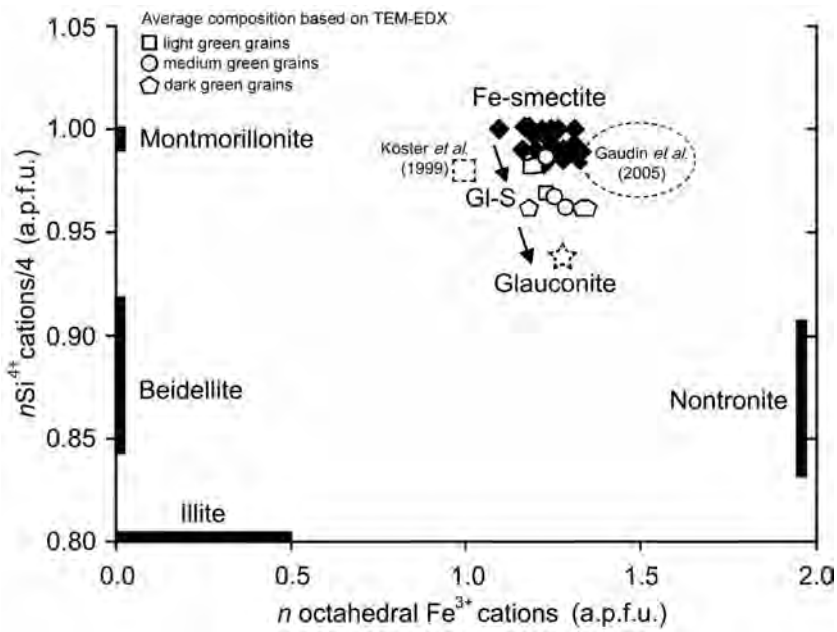

Figure 9. TEM-EDX analyses of unaltered Fe-smectite particles from 0.16 mbsf of Hole 959C (black rhombs) plotted in the $^4Si-\Sigma^{VI}Fe$ diagram of Gaudin *et al.* (2005). Average compositions of the separated green-grain sub-fractions (Table 1) are included to illustrate the ongoing glauconitization process. Reference data of Fe-smectite (dashed circle and square) and of the international GLO (glauconite) standard (dashed star) are included for comparison.

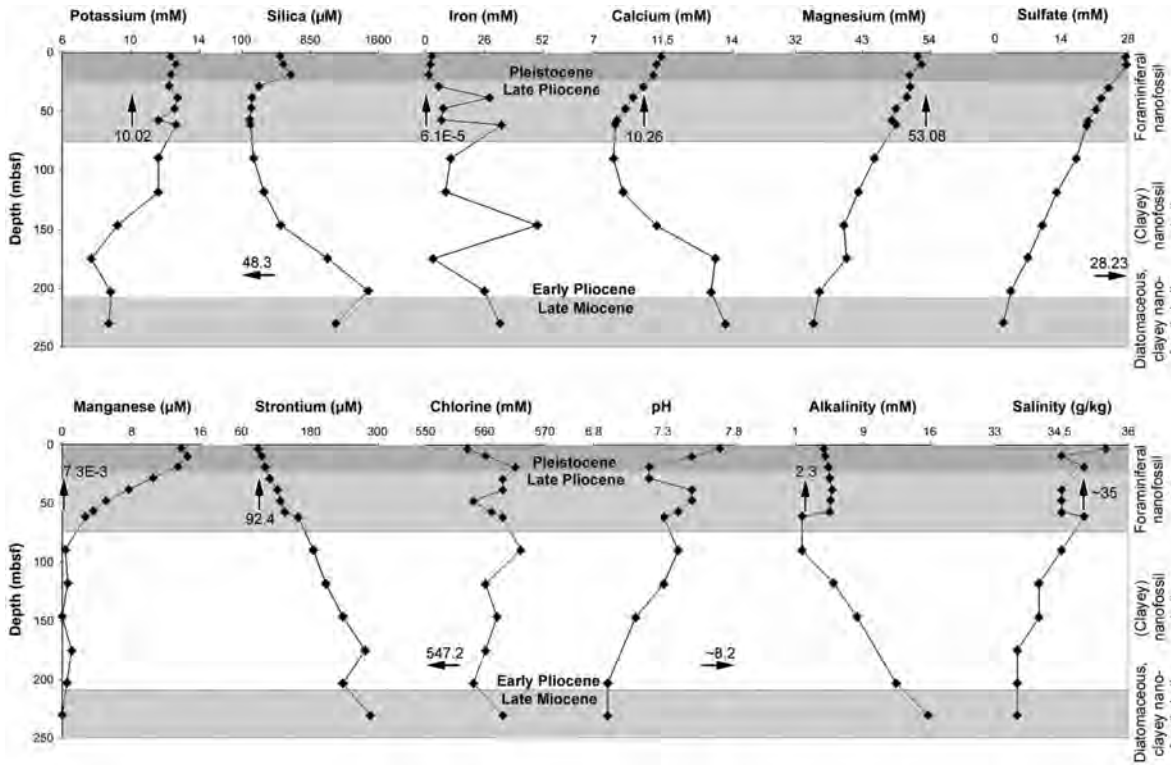

Figure 10. Interstitial solution profiles for ODP Site 959 (data from Mascle *et al.*, 1996). Average seawater composition (black arrows) based on Turekian (1968) and the lithology of Hole 959C are labeled for comparison.

trend which was interpreted by Mascle *et al.* (1996) as a dynamic redistribution of Fe within the sediment column.

The oxidation of marine organic matter and also sulfate reduction are likely to play a key role in regulating the pH of the interstitial solution, as indicated by the drop in pH from 7.7 to 7.2 in the first 20 mbsf (Figure 10) which reflects the formation of *e.g.* carboxylic acids and H_2S (Mascle *et al.*, 1996). At this site, the interstitial solution pH is buffered by calcium carbonate dissolution, as documented by the increase in total alkalinity and Sr^{2+} content. Hence, the pH within organic-rich micro-environments such as in the biofilm within foraminifera tests is probably much lower (pH <5) than that of the interstitial solution. Such locally occurring acidic conditions can promote dissolution of detrital silicates such as feldspar, as documented by the present XRD and SEM data (Figures 3, 4). As a consequence, the concentration of silicic acid in the interstitial solution increases with burial depth (Figure 10), reaching a first maximum at 20 mbsf (~650 μM). Alterations of bio-opal and clay minerals (Figure 4) provide additional ions such as Al^{3+}, Fe^{2+}, Na^{+}, Ca^{2+}, and Mg^{2+} (*e.g.* MacKenzie, 2005) that are required for ongoing glauconitization.

Due to intense silicate weathering, the K^{+} concentration of the interstitial solution (Figure 10) in the first 50 mbsf (12.2−12.7 mM) is ~20−25% greater than that of seawater (10.02 mM) but it decreases continuously below 120 mbsf. An elevated K^{+} concentration of the interstitial solution probably favors the glauconitization reaction by irreversible K^{+} fixation, as indicated by the TEM-EDX data and by previous studies on the illitization of smectite (Hower *et al.*, 1976; Kaufhold and Dohrmann, 2010).

In summary, the interstitial solution chemistry at ODP Site 959 was modified by early diagenetic silicate mineral alteration, microbial sulfate reduction, Fe redox reactions, carbonate dissolution, and oxidation of organic matter, and is probably the driving force for glauconitization within the sedimentary pile.

Rate of deep-water glauconitization

At the ODP Site 959, Fe-smectite formation is considered to be the initial step to glauconitization which occurred in semi-confined, organic-rich micro-environments, as provided within the tests of foraminifera. According to chemical modeling of Fe-smectite formation in deep-sea sediments from the Costa Rica margin (Charpentier *et al.*, 2011), several thousands of years are required to precipitate Fe-smectite in large quantities. Gaudin *et al.* (2005) suggested that these neo-formed Fe-smectites are thermodynamically unstable during early marine diagenesis and alter rapidly into glauconite *via* Gl-S formation. Evidence for such a progressive Fe-smectite into glauconite alteration is

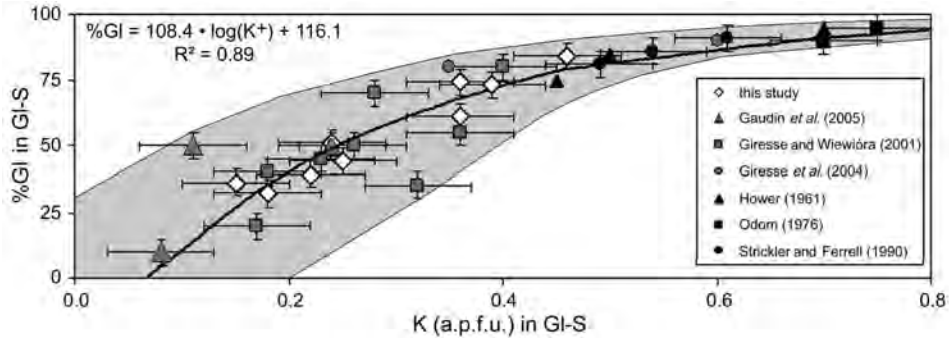

Figure 11. Relationship between %Gl and interlayer K^+ content in Gl-S. Glauconite formation is accompanied by a continuous K^+ uptake.

given by the positive correlation ($R^2 = 0.89$) between the increasing percentage of %Gl in Gl-S and the associated higher K^+ content per a.p.f.u. (Figure 11) with grain maturity, according to the expression:

$$\%Gl = 108.4 \cdot \log(K^+) + 116.1 \text{ for } K^+ < 0.7 \text{ a.p.f.u.} \quad (1)$$

The proportion of %Gl in Gl-S of the total green grains at a given depth, namely, the state of overall glauconitization in the sediment ($\%Gl_{Sed}$), was calculated with equation 1 using the average K content (± 0.05 K a.p.f.u.) of each green-grain sub-fraction (Table 1) multiplied by its percentage (±5%) in the total green-grain fraction from each depth (Figure 5). These calculations revealed 30, 60, and 75% Gl_{Sed}, each ± 10%, at 0.16, 11.69, and 24.91 mbsf which correspond to sediment ages of ~10, 900, and 2500 ky, respectively, given by Giresse and Wiewióra (2001). Assuming that the formation of Fe-smectite with initially little if any %Gl requires ~1 ky (Charpentier *et al.*, 2011), an average glauconitization rate for the ODP Site 959 can be obtained by plotting ($R^2 = 0.97$) the $\%Gl_{Sed}$ against the age of the sediment (age_{Sed} in ky), according to the equation:

$$\%Gl_{Sed} = 22.6 \cdot \log(age_{Sed}) + 1.6 \text{ for } age_{Sed} < 10 \text{ My} \quad (2)$$

The glauconitization rate in this modern deep-sea environment (ODP Site 959) is about five times less than that in the shallow shelf (*e.g.* Odin and Fullagar, 1988) which probably reflects the lower temperatures (~3−6ºC) and the limited supply and reflux of essential cations which are required for glauconitization such as Fe, K^+, Mg^{2+}, and silica. However, the rate of deep-sea glauconite formation is significantly faster than that of smectite illitization that occurs during burial diagenesis (*e.g.* Hower *et al.*, 1976), which may reflect the role of Fe, as shown by the positive linear correlation ($R^2 = 0.98$) between the increasing Fe_2O_3 content and the associated higher percentages of %Gl in Gl-S (Figure 12).

As previously suggested by Baldermann *et al*. (2012), the availability of Fe and subsequently the extent of $Fe^{3+/2+}/Mg^{2+}$ for Al^{3+} substitutions in the octahedral sheet of the neo-formed Fe-smectite and related Gl-S is

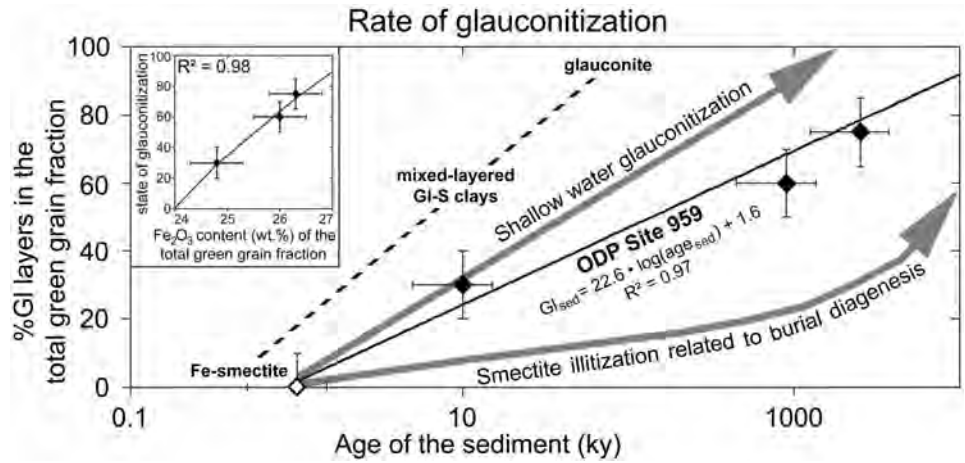

Figure 12. Glauconitization rate for the ODP Site 959. The positive, linear correlation between increasing Fe content and the state of glauconitization implies that Fe could be the overall rate-limiting element (inserted box). The rate of shallow-water glauconitization, as suggested by Odin and Fullagar (1988), and the rate of illitization of smectite, as proposed by Hower *et al*. (1976) for the Gulf Coast sediments, are included for comparison.

expected to have a major impact on the rate of glauconitization. With increasing proportion of bivalent octahedral cations such as Fe^{2+} and Mg^{2+} the octahedral charge increases and K^+ is progressively fixed into the interlayer sites to balance charge, as documented by the TEM-EDX compositions of the Ivory Coast glauconites and Gl-S (Table 1). The proportion of Fe^{2+} in the green grains could not be determined in the present study due to the small amount of green grains available. However, the greening of the grain color with increasing burial depth indicates that some Fe^{2+} in the structural formulae of Gl-S is probable. Thus, the progressive fixation of Fe as well as Fe reduction during glauconitization is considered to be a likely rate-controlling factor, as expressed in the linear relationship of increasing Fe_2O_3 contents and the state of glauconitization (Figure 12).

Model for deep-water glauconite formation

As a result of the petrographic, mineralogical, and chemical observations in the present study, the glauconitization process of foraminifera tests at ODP Site 959 is proposed to occur in three steps (Figure 13):

(1) After sedimentation (~0.01−1 ky), most of the marine organic matter was oxidized. This resulted in locally reducing and slightly acidic conditions ($pH_\mu < pH_{Sed} < pH_{sw}$) in the micro-environment of glauconitization (pH_μ) and the surrounding sediment (pH_{Sed}) compared to the seawater pH (pH_{sw}), as documented by the interstitial solution data (Figure 10). Such conditions favored the dissolution of carbonate, bio-opal, and silicate minerals (*e.g.* Raiswell and Canfield, 2012), making dissolved K^+, Mg^{2+}, and silica readily available at the ODP Site 959. However, the mobilization and transport of Al and (in particular) Fe were probable limiting factors for the advance of glauconitization (Figure 12). Iron and Al are virtually absent from aquatic systems at seawater pH and at the analyzed pH of the interstitial solutions (*e.g.* Turekian, 1968). One key mechanism for the mobilization of Fe and Al is the microbial oxidation of biodegradable (marine) organic matter within the foraminifera tests which is expected to reduce the pH by the supply of *e.g.* carboxylic acids (MacKenzie, 2005). At pH<5 the solubility of FeO-OH and Al-O-OH significantly increases through the predominance of aqueous $Fe(OH)^{2+}$ and $Al(H_2O)_6^{3+}$ species in the Fe_2O_3–Al_2O_3–H_2O system. The occurrence of Fe- and Al-containing organic aquo-complexes is enhanced under such conditions (*e.g.* McBride, 1994; Tipping, 2002).

(2) Immediately after the biodegradable marine organic matter was oxidized, the bacterial activity decreased, as indicated by the TEM observations (Figure 8), and an oxidation front developed in the tests of foraminifera (Gaudin *et al.*, 2005). This initiates a local micro-environment suitable for glauconitization. In the presence of an expanding oxidation front, rapid degradation of Fe- and Al-organic aquo-complexes could take place and Fe^{2+} and Al^{3+} cations were released temporarily. Accompanied by the constant re-oxidation of Fe^{2+} to Fe^{3+} and rapid Al^{3+} supply, the formation of gel occurred contemporaneously with direct precipitation from bacterial biofilm. Subsequently, Fe-smectite formed within the amorphous precursor gels (Figure 8), initiated by the continuous cation supply from the surrounding sediment by chemical diffusion at moderate pH ($pH_\mu \approx pH_{sw} > pH_{Sed}$) (see Martín-Algarra and Sánchez-Navas, 1995). Charpentier *et al.* (2011) suggested that ~1−10 ky are required for the quantitative precipitation of Fe-smectite in deep-sea, low-temperature environments.

(3) The Fe-smectite-to-glauconite reaction was finally promoted by diffusion-controlled cation exchange between the micromilieu and interstitial solutions ($pH_\mu < pH_{Sed}$; Eh ≈ 0 mV), whereby both the initial sediment and the micro-environment of glauconitization became modified by several early diagenetic dissolution and replacement reactions, as described above. As dissolved K^+, Mg^{2+}, and silica are considered to have always been present in the interstitial solutions (Figure 10), the availability of Fe is suggested to be the most important rate-limiting factor for glauconitization of the Ivory Coast sediments. As soon as the Fe supply stopped, *e.g.* by changes in the pH and Eh conditions within the micro-environment of glauconitization, the Fe-smectite-to-glauconite reaction also stopped. Such unsuitable conditions for the formation of glauconite could occur locally within the same micromilieu such as within one single foraminifera test, a feature which explains why green grains with varying color, reflecting a divergent state of maturity, are present within the same horizon.

The physical properties of the sediment such as porosity, permeability, and tortuosity appear to have been additional key factors for glauconitization, by influencing the interstitial solution chemistry and its exchange with the micro-environment *via* diffusion. Changes in the rate of diffusion in the micro-environment, especially that of Fe and K, due to the loss of porosity and connectivity of pore space (Figure 7c,f), may explain why the glauconitization rate slows down with increasing burial depth and aging of the sediment (Figure 12). A reduced diffusion rate may also imply that as glauconization progresses the rate of K^+ fixation in Gl-S is relatively enhanced compared to the rate of formation of new Fe-smectite layers which can explain the logarithmic relationship between increasing %Gl in Gl-S and K content (Figure 11). This feature is probably attributed to the low thermodynamic stability of the Fe-smectite precursors (Gaudin *et al.*, 2005). Thus, the rate of glauconitization does decrease with increasing burial depth and subsequent aging of the original sediments, and at these low temperatures the process requires ~10 My to complete in the deep-water environment of the ODP Site 959, compared to <2 My in a shallow-water setting (Odin and Fullagar, 1988).

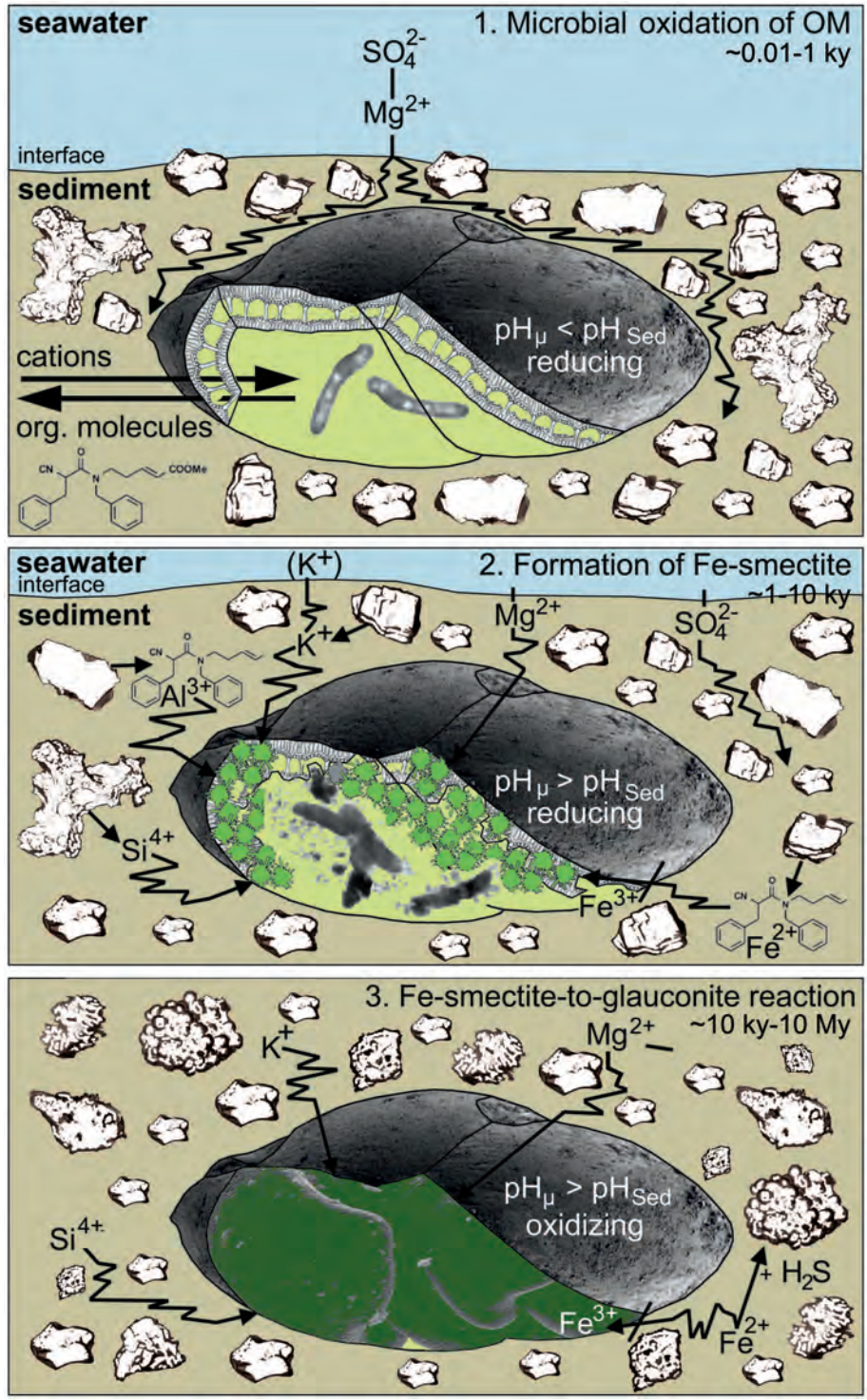

Figure 13. Glauconitization model for ODP Site 959. (1) Microbial oxidation of organic matter (OM) generates locally occurring reducing and acidic conditions in the micro-environment of glauconitization such as in foraminifera tests and the surrounding sediment. These conditions enhance (silicate) mineral dissolution and the formation of cation-organic aquo-complexes. (2) As soon as the OM is consumed, oxidation of the organic complexes and of Fe^{2+} occurs. Subsequently, Fe-smectite formation takes place which is promoted by microbial activity and cation supply from the interstitial solution, while dissolution of skeletal calcite buffers the pH. (3) The Fe-smectite-to-glauconite reaction is controlled by the composition of the bulk interstitial solution and requires ~10 My to complete.

SUMMARY AND CONCLUSIONS

Authigenic, green glauconitic grains, formed in the recent deep-sea environment (~2100 m) of the ODP Site 959, Ivory Coast−Ghana Marginal Ridge, were studied in order to characterize the key factors controlling the rate and mechanism of deep-sea glauconite formation at low temperatures (~3−6ºC). The following conclusions were reached:

(1) Glauconitization occurred mainly in calcareous, planktonic, and benthic foraminifera tests. These semi-confined, organic-rich micro-environments provided the post-depositional conditions suitable for glauconitization. (2) XRD, TEM, and FIB-SEM results of the unaltered light green grains from 0.16 mbsf revealed dioctahedral Fe-smectites as the precursor phases for glauconite formation. These Fe-smectites were formed by precipitation from amorphous gels containing Fe, Mg, Al, and silica generated preferentially from microbial biofilm with cations supplied by diffusion from interstitial solutions. (3) During the later stages of early marine diagenesis, the neo-formed Fe-smectites changed into Gl-S and finally into glauconite with no recognizable compositional gaps between the Fe-smectite and glauconite end members, as identified by combined *Sybilla*© modeling, XRD, TEM-EDX, and TEM-SAED analysis. (4) The composition of the interstitial solution was influenced heavily by microbial oxidation of marine organic matter, Fe-redox reactions, and silicate and carbonate mineral weathering, as indicated by the SEM and hydrochemical results, and all of these early diagenetic alteration processes were important for maintaining glauconitization within the sediment pile. (5) The rate of deep-water glauconite formation depended mainly on continuous Fe supply but, due to the low-temperature conditions, the rate of reaction was about five times less than that in shallow-shelf regions.

ACKNOWLEDGMENTS

The authors are grateful to A. Deditius and C. Nickel (Graz University of Technology) for their helpful contributions and suggestions during preparation of an early version of the manuscript. M. Zander (Ernst-Moritz-Arndt University of Greifswald) is acknowledged for technical assistance with the TEM and FIB-SEM analyses. Special thanks to J. Cuadros, J.M. Wampler, R. Dohrmann, J. Stucki, and an anonymous reviewer for their detailed comments which significantly improved the quality of this paper.

REFERENCES

Bailey, S.W., Alietti, A., Brindley, G.W., Formosa, M.L.L., Jasmund, K., Konta, J., MacKenzie, R.C., Nagasawa, K., Raussell-Colom, R.A., and Zvyagin, B.B. (1980) Summary of the recommendations of the AIPEA nomenclature committee. *Clays and Clay Minerals*, **28**, 73−78.

Baldermann, A. (2012) Recent glauconite formation in a deep sea environment from ODP Site 959, Ivory Caost-Ghana Marginal Ridge. Masters thesis, Univ. Greifswald, Greifswald, Germany, 75 pp.

Baldermann, A., Grathoff, G.H., and Nickel, C. (2012) Micromilieu-controlled glauconitization in fecal pellets at Oker (Central Germany). *Clay Minerals*, **47**, 513−538.

Buatier, M., Honnorez, J., and Ehret, G. (1989) Fe-smectite-glauconite transition in hydrothermal clays from the Galapagos Spreading Center. *Clays and Clay Minerals*, **37**, 532−541.

Chaerun, S.K. and Tazaki, K. (2005) How kaolinite plays an essential role in remediating oil-polluted seawater. *Clay Minerals*, **40**, 481−491.

Charpentier, D., Buatier, M., Jacquot, E., Gaudin, A., and Wheat, C.G. (2011) Conditions and mechanism for the formation of iron-rich montmorillonite in deep sea sediments (Costa Rica margin): Coupling high-resolution mineralogical characterization and geochemical modeling. *Geochimica et Cosmochimica Acta*, **75**, 1397−1410.

Cuadros, J., Dekov, V.M., Arroyo, X., and Nieto, F. (2011) Smectite formation in submarine hydrothermal sediments: samples from the HMS Challenger Expedition (1872−1776). *Clays and Clay Minerals*, **59**, 147−164.

Gaudin, A., Buatier, M., Beaufort, D., Petit, S., Grauby, O., and Decareau A. (2005) Characterization and origin of Fe^{3+}-montmorillonite in deep water calcareous sediments (Pacific Ocean, Costa Rica margin). *Clays and Clay Minerals*, **53**, 452−465.

Giresse, P. and Wiewióra, A. (2001) Stratigraphic condensed deposition and diagenetic evolution of green clay minerals in deep water sediments on the Ivory Coast-Ghana Ridge. *Marine Geology*, **179**, 51−70.

Giresse, P., Gadel, F., Serve, L., and Barusseau, J.P. (1998) Indicators of climate and sediment-source variations at site 959: implications for the reconstructions of paleoenvironments in the Gulf of Guinea through Pleistocene times. *Proceedings of the Ocean Drilling Program, Scientific Results*, **159**, 585−603.

Giresse, P., Wiewióra, A., and Grabska, D. (2004) Glauconitization processes in the northwestern Mediterranean (Gulf of Lions). *Clay Minerals*, **39**, 57−73.

Harder, H. (1980) Synthesis of glauconite at surface temperatures. *Clays and Clay Minerals*, **28**, 217−222.

Hower, J. (1961) Some factors concerning the nature and origin of glauconite. *American Mineralogist*, **46**, 313−334.

Hower, J., Eslinger, E.V., Hower, M.E., and Perry, E.A. (1976) Mechanism of burial metamorphism of argillaceous sediments: 1. Mineralogical and chemical evidence. *Geological Society of America Bulletin*, **87**, 725−737.

Jimenez-Millan, J., Molina, J.M., Nieto, L., Nieto, M., and Ruiz-Ortis, P.A. (1998) Glauconite and phosphate peloids in Mesozoic carbonate sediments (Eastern Subbetic Zone, Betic Cordilleras, SE Spain). *Clay Minerals*, **33**, 547−559.

Kaufhold, S. and Dohrmann, R. (2010) Stability of bentonites in salt solutions: II. Potassium chloride solution − Initial step of illitization? *Applied Clay Science*, **49**, 98−107.

Keller, L.M., Holzer, L., Wepf, R., and Gasser, P. (2011) 3D geometry and topology of pore pathways in Opalinus clay: Implications for mass transport. *Applied Clay Science*, **52**, 85−95.

Kloprogge, J.T., Komarneni, S., and Amonette, J.E. (1999) Synthesis of smectite clay minerals: A critical review. *Clays and Clay Minerals*, **47**, 529−554.

Konhauser, K.O. and Urrutia, M.M. (1999) Bacterial clay authigenesis: a common biogeochemical process. *Chemical Geology*, **161**, 399−413.

Köster, H.M., Ehrlicher, U., Gilg, H.A., Jordan, R., Murad, E., and Onnich, K. (1999) Mineralogical and chemical characteristics of five nontronite and Fe-rich smectites. *Clay Minerals*, **34**, 579−599.

MacKenzie, F.T. (2005) *Sediments, Diagenesis, and*

Sedimentary Rocks, 7: Treatise on Geochemistry. Elsevier Science and Technology, USA.

Martín-Algarra, A. and Sánchez-Navas, A. (1995) Phosphate stromatolites from condensed cephalopod limestones, Upper Jurassic, southern Spain. *Sedimentology*, **42**, 893–919.

Mascle, J., Lohmann, G.P., Clift, P.D., *et al*. (1996) 9. Principal Results. *Proceedings of the Ocean Drilling Program*, *Initial Reports*, **159**, 297–314.

McBride, M.B. (1994) *Environmental Chemistry of Soils*. Oxford University Press, New York.

Meunier, A. and El Albani, A.E. (2007) The glauconite-Fe-illite-Fe-smectite problem: a critical review. *Terra Nova*, **19**, 95–104.

Moore, D. and Reynolds, R.C. Jr (1997) *X-ray Diffraction and the Identification and Analysis of Clay Minerals*. Oxford University Press, USA.

Norris, R.D. (1998) Planktonic foraminifer biostratigraphy: eastern equatorial Atlantic. *Proceedings of the Ocean Drilling Program, Scientific Results*, **159**, 445–479.

Odin, G.S. and Fullagar, P.D. (1988) Geological significance of the glaucony facies. Pp. 295–332 in: *Green Marine Clays* (G.S. Odin, editor). Elsevier, Amsterdam.

Odin, G.S. and Matter, A. (1981) De glauconiarum origine. *Sedimentology*, **28**, 611–641.

Odom, E. (1976) Microstructure, mineralogy and chemistry of Cambrian glauconite pellets and glauconite, central USA. *Clays and Clay Minerals*, **24**, 232–238.

Raiswell, R. and Canfield, D.E. (2012) The iron biogeochemical cycle past and present. *Geochemical Perspectives*, **1**, 1–222.

Schulz, H.D. and Zabel, M. (2006) *Marine Geochemistry*. Springer, Berlin.

Strickler, M.E. and Ferrell, R.E., Jr (1990) Fe substitution for Al in glauconite with increasing diagenesis in the first Wilcox sandstone (Lower Eocene), Livingston Parish, Lousiana. *Clays and Clay Minerals*, **38**, 69–76.

Tipping, E. (2002) *Cation Binding by Humic Substances*. Cambridge University Press, Cambridge, UK.

Turekian, K.K. (1968) *Oceans*. Prentice Hall, New Jersey, USA.

Wagner, T. (1998) Pliocene-Pleistocene deposition of carbonate and organic carbon at Site 959: Paleoenvironmental implications for the eastern equatorial Atlantic of the Ivory Coast/Ghana. *Proceedings of the Ocean Drilling Program, Scientific Results*, **159**, 557–574.

Warr, L.N. and Grathoff, G. (2012) Geoscientific applications of particle detection and imaging techniques with special focus on the monitoring clay mineral reactions. Pp. 667–683 in: *Handbook of Particle Detection* (C. Grupen and I. Buvat, editors). Springer, Berlin.

Warr, L.N., Perdrial, J.N., Lett, M.-C., Heinrich-Salmeron, A., and Khodja, M. (2009) Clay mineral-enhanced bioremediation of marine oil pollution. *Applied Clay Science*, **46**, 337–345.

Wiewióra, A., Giresse, P., Petit, S., and Wilamowski, A. (2001) A deep-water glauconitization process on the Ivory Coast–Ghana Marginal Ridge (ODP Site 959): Determination of Fe^{3+}-rich montmorillonite in green grains. *Clays and Clay Minerals*, **49**, 540–558.

(*Received 24 January 2013; revised 11 May 2013; Ms. 741; AE: R. Dohrmann*)